3-1-2019

# Native and Radiation-Induced Defects in III-V Solar Cells and Photodiodes

George Thomas Nelson IV
gtn1425@rit.edu

R·I·T

# Native and Radiation-Induced Defects in III-V Solar Cells and Photodiodes

by

George Thomas Nelson IV

A dissertation submitted in partial fulfillment of the requirements
for the degree of Doctor of Philosophy in Microsystems Engineering

Microsystems Engineering Program
Kate Gleason College of Engineering

Rochester Institute of Technology
Rochester, New York
March 1, 2019

**Native and Radiation-Induced Defects in III-V Solar Cells and Photodiodes**
**by**
**George Thomas Nelson IV**

## Committee Approval:

We, the undersigned committee members, certify that we have advised and/or supervised the candidate on the work described in this dissertation. We further certify that we have reviewed the dissertation manuscript and approve it in partial fulfillment of the requirements of the degree of Doctor of Philosophy in Microsystems Engineering.

---

Dr. Seth M. Hubbard — Date
Professor, Physics

---

Dr. Sean Rommel — Date
Professor, Microsystems Engineering

---

Dr. Michael Pierce — Date
Associate Professor, Physics

---

Dr. Parsian K. Mohseni, — Date
Assistant Professor, Microsystems Engineering

## Certified by:

---

Dr. Bruce Smith — Date
Director, Department of Microsystems Engineering

# ABSTRACT

Kate Gleason College of Engineering

Rochester Institute of Technology

**Degree**: Doctor of Philosophy **Program**: Microsystems Engineering

**Author's Name**: George Thomas Nelson IV

**Advisor's Name**: Dr. Seth M. Hubbard

**Dissertation Title**: Native and Radiation-Induced Defects in III-V Solar Cells and Photodiodes

Photodiodes made of III-V materials are ubiquitous with applications for telecommunications, photonics, consumer electronics, and spectroscopy. The III-V solar cell, specifically, is a large-area photodiode that is used by the satellite industry for power conversion due to its unrivaled efficiency and wide range of available materials. As a device driven by its minority carrier diffusion length (MCDL), the performance of a photodiode is sensitive to crystallographic defects that create states in the forbidden energy gap. Defects commonly arise during growth of the crystal and during device fabrication, and they accumulate slowly over time when deployed into the damaging environment of space. Defect-assisted carrier recombination leads to lower MCDL, higher dark current, reduced sensitivity and signal-to-noise ratio, and, in the case of solar cells, reduced power conversion efficiency. Consequently, the development of photodiode technology requires techniques for detection, characterization, and mitigation of defects and the inter-bandgap states they create. In this work, III-V material defects are addressed across a variety of materials and devices.

The first half of the work makes use of deep-level transient spectroscopy (DLTS) to deduce the energy level, cross-section, and density of traps the InAlAs, InAlAsSb, and InGaAs lattice-matched to InP. An *in situ* DLTS system that can monitor defects immediately after irradiation was developed and applied to InGaAs photodiodes irradiated by protons. Evidence of trap annealing was found to occur as low as 150 K. The second half begins with development of GaSb solar cells grown by molecular beam epitaxy on GaAs substrate intended for use in lower-cost monolithic multi-junction cells. Defect analysis by microscopy, dark lock-in thermography, and dark current measurement, among others, was performed. The best GaSb-on-GaAs cell achieved state-of-the-art 4.5% efficiency under concentrated solar spectrum. Finally, light management in III-V photodiodes was explored as a possible route for defect mitigation. Textures, diffraction gratings, metallic mirrors, and Bragg reflectors were simulated by finite difference time domain for single- and multi-junction GaAs-based cells with the aim of reducing the amount of absorber material required and to simultaneously reduce MCDL requirements by generating carriers closer to the junction. The results were inputted into a device simulator to predict efficiency. A backside reflective pyramidal-textured grating was simulated to allow a GaAs cell to be thinned by a factor of >30 compared to a conventional cell.

# Dedication

*For my wife, Katherine, and my parents & family.*

## Acknowledgments

Firstly I thank my advisor, Dr. Seth Hubbard, for his investment in me and without whom this work would not be possible. Also, my committee members, Dr. Sean Rommel, Dr. Michael Pierce, Dr. Parsian Mohseni, and Dr. Edwin Hach for their assistance, guidance, teachings, and insights.

Thank you to the present and former staff and students of NanoPower Research Labs for their support over the years. This includes Dr. David Forbes, Elaine Lewis, James Smith, Dr. Stephen Polly, Dr. Yushuai Dai, Dr. Hyun Kum, Dr. Alessandro Giussani, Elisabeth McClure, Emily Kessler, Mitsul Kacharia, Anastasiia Fedorenko, Julia D'Rozario, Gildas Ouin, and Salwan Omar. Thanks to Dr. Michael Slocum for advice and writing assistance, Dr. Zachary Bittner for training in the lab and cleanroom, Wyatt Strong for teaching me DLTS, Dr. Staffan Hellstrom for the lessons in device simulation, and Dr. Brittany Smith for assistance in the cleanroom.

Thank you to the staff of the SMFL, especially Patricia Meller and Sean O'Brien for countless occasions of assistance with many (most?) of the tools. The quality of the SEM images were improved with the help of Dr. Richard Hailstone. Thanks to Lisa Zimmerman of the Microsystems Department for all the administrative help and for all the times I forgot my student ID number.

Collaboration with other individuals or groups led to much of the work in this thesis. Specifically, the dark lock-in thermography was performed by Dr. Steve Johnston of NREL after we discussed the idea at a conference. *In situ* DLTS would not have gone smoothly without the help of the team at SUNY Albany, including Dr. William Lanford, Arthur Haberl, and Kevin Wynne. The Huffaker group at UCLA, especially Ramesh Laghumavarapu and Bor-Chau Juang, grew the GaSb samples and laid the foundation for much of that effort.

The MFIA-based DLTS system would not have been possible without the funding of Robert Lowell of Dynamic Radiation Solutions. The development of the system was assisted by Dr. Timothy Ashworth of Zurich Instruments, who provided useful guidance to using the MFIA.

Dr. Ramon Schifano of the Institute of Physics PAS had many insights that helped troubleshoot the system in its early stages.

Microlink Devices and Navy Research Labs are among other collaborators I wish to thank. Thank you to AFRL, NASA, NSF, and BAPVC for funding this work.

Finally, thanks to Rusty, the terror of Richmond Street.

# Contents

# List of Tables

# List of Figures

# Glossary

$G$ generation rate. 15, 33, 134, 137, 138, 162

***uid*** unintentionally doped. 43, 49–52, 58, 59, 61

**1-J** single-junction. 2, 3, 10, 11, 94, 96, 124

**3-J** triple-junction. 10, 11, 35, 36, 39, 93, 94, 113, 115, 117, 119, 147, 148, 151, 156, 167

**AFM** atomic force microscopy. 145

**ALD** atomic layer deposition. 99, 106

**AM0** air-mass 0. 22, 36, 138, 151, 153, 165

**AM1.5D** air-mass 1.5 direct. 38, 109, 111, 115

**AM1.5G** air-mass 1.5 global. 22, 37, 94, 97, 107, 109–112, 114–116, 130

**ARC** anti-reflective coating. 99, 110, 111, 120, 121, 132, 142, 153

**$AsH_3$** arsine. 41, 53, 70

**BEP** beam equivalent pressure. 53, 98

**BOL** beginning-of-life. 130, 131, 148, 153–156

**BSR** back surface reflector. 119, 121, 124, 127–129, 135–140, 142–145, 155, 164, 165

**BTE** Boltzmann transport equation. 32, 33, 35, 132, 159–161

**C-V** capacitance vs. voltage. 38, 46, 50, 51, 59, 61, 71, 73

**DBR** distributed Bragg reflector. 131, 132, 147–157

**DFT** density functional theory. 25

**DLIT** dark lock-in thermography. 11, 103, 104, 116

**DLTS** deep-level transient spectroscopy. 5, 6, 8, 10, 11, 27, 28, 30–32, 38, 43, 46–53, 55–57, 59–62, 64–67, 69, 71, 73–78, 80–88, 90–93, 112, 117

**ELO** epitaxial lift-off. 40, 164

**EOL** end-of-life. 119, 126, 131, 132, 147, 153–156

**EPD** etch pit density. 24, 101

**EQE** external quantum efficiency. 16, 97, 107, 108, 110, 115, 128, 132, 135, 150, 167

**FDTD** finite difference time domain. 132–135, 141, 143, 145, 147, 164

**FF** fill factor. 18–20, 96, 109–111, 114, 116, 151, 154

**FTIR** frustrated total internal reflection. 142, 143

**IBSC** intermediate band solar cell. 126, 127

**IMF** interfacial misfit. 11, 93–99, 101, 107–117

**IMM** inverted metamorphic. 36, 37, 93, 94, 96, 98, 112, 130, 131, 151–153, 167

$J_{Ph}$ photo-generated current density. 15–17

$J_{01}$ recombination current density in quasi-neutral regions. 18–20, 22, 44, 45, 50, 54

$J_{02}$ recombination current density in depletion region. 18–21, 44, 45, 54, 106, 107

$J_{MPP}$ current density at the MPP. 19, 20

$J_{SC}$ short-circuit current density. 16, 18, 19, 32, 96, 97, 107, 109–112, 149–155, 165

**J-V** current density vs. voltage. 17, 18, 20, 38, 43, 44, 48, 50, 53, 55, 56, 71–75, 77, 80–82, 89, 90, 92, 103, 106–109, 114, 115, 135, 151, 158

**MBE** molecular beam epitaxy. 10, 40, 44, 45, 52–58, 60, 61, 93, 96–98, 104, 110, 115–117

**MCDL** minority carrier diffusion length. 16, 25, 41, 108, 111, 129

**MOCVD** metalorganic chemical vapor deposition. 10, 38, 41, 43, 45, 51–55, 57–61, 70, 90, 96, 97, 116, 117, 136

**MPP** maximum power point. 18, 19

**NREL** National Renewable Energy Laboratory. 2

**$PH_3$** phosphine. 70

**PL** photoluminescence. 40, 60

**QD** quantum dot. 1, 5, 69, 119, 126–128, 135–141, 143, 145, 155

**QNR** quasi-neutral region. 19, 111

**QW** quantum well. 1, 126–128

**$R_{Sh}$** shunt resistance. 18–20, 44, 45, 54, 96, 103, 106, 107

**$R_S$** series resistance. 16, 18–20, 45, 50, 54, 88, 89, 91

**SEM** scanning electron microscopy. 100, 101, 104, 136

**SIMS** secondary ion mass spectrometry. 23, 42, 43, 46, 58, 60, 61

**SNR** signal-to-noise ratio. 5, 23, 64

**SR** spectral responsivity. 4, 16, 22, 71, 107, 109

**SRH** Shockley-Read-Hall. 6, 19, 20, 23, 26, 41, 45, 78, 83, 108, 113, 123, 130, 154, 165

**TAT** trap-assisted tunneling. 44, 72

**TBAs** tertiarybutylarsine. 41, 43

**TDD** threading dislocation density. 37, 96, 111, 112, 116, 117

**TEM** transmission electron microscopy. 24, 96

**TIR** total internal reflection. 124, 142–144, 146–148, 151, 156

**TLM** transmission line measurement. 71

**TMAl** trimethylaluminum. 41, 49, 52–58, 60, 61, 106

**TMGa** trimethylgallium. 70

**TMIn** trimethylindium. 41, 43, 53, 70

**TMM** transfer matrix method. 35, 132–135, 142, 143, 148

**TMSb** trimethylantimony. 41, 43

**TTBAl** tritertiarybutylaluminum. 41, 43, 52–56, 58, 60, 61

**$V_{MPP}$** voltage at the MPP. 18, 20

**$V_{OC}$** open-circuit voltage. 18–20, 109–112, 114, 115, 123, 124, 129, 139, 165

**XRD** X-ray diffraction. 24, 41, 60, 70

# Chapter 1

# Introduction

## 1.1 Motivation

The III-V semiconductor photodiode is a solid-state device that converts incident electromagnetic radiation into an electric signal. As a photodetector, the photodiode will detect light within a certain wavelength range or spectral bandwidth and the output signal is useful for many purposes including imaging [14], remote sensing [15], spectroscopy [16], and optical communication [17]. As a solar cell, the photodiode will convert sunlight for power generation. For these purposes, many photodiodes operate within the wavelength range from middle ultra-violet to long-wavelength infrared, or 0.2 μm to 15 μm, as this range begins with the solar spectrum and extends to most of the spectrum for room-temperature blackbody radiation.

The III-V crystalline semiconductor is well-suited to photodiode applications because of a combination of excellent optical and electronic properties. Different group III and V elements may be combined to obtain bandgap values well-suited to the wavelength range mentioned above. Figure 1.1 is a chart of bandgap vs. lattice constant for well-developed III-V materials. As seen, the available bandgaps start at 7.3 μm for binary InSb (5.5 μm under cooled conditions [18]) and stretch to 0.55 μm for GaP. The lines connecting binary III-V's are for ternary materials, like AlGaAs, which allow for intermediate bandgaps between binary materials. Furthermore, bandgap engineering is available via nanostructures like quantum wells (QWs) or quantum dots (QDs), which allow for even longer wavelengths at a specific lattice constant. Superlattices of InAs/GaSb are at the forefront of long-wavelength infrared detection and can detect at 10 μm and beyond [18].

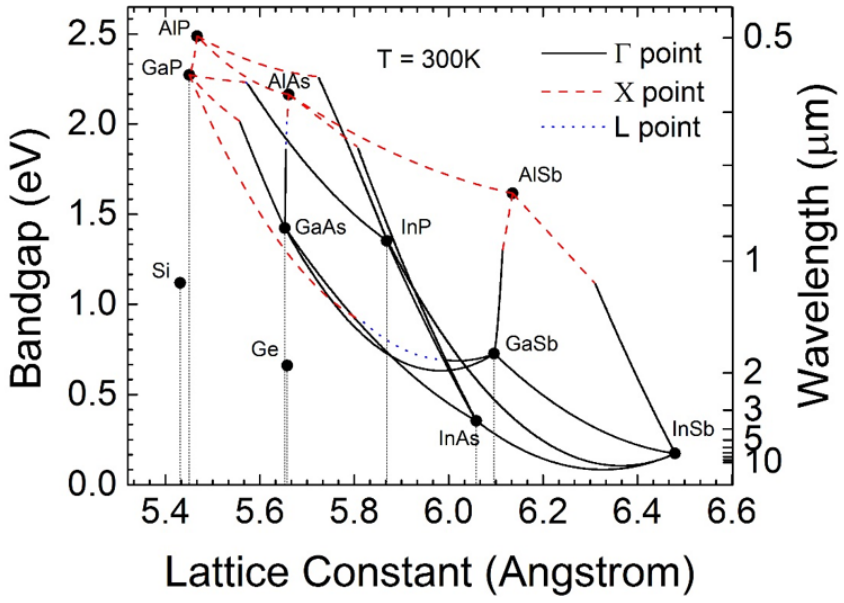


Figure 1.1: Lattice constant vs. bandgap chart with many popular group IV and III-V semiconductors. *Plot by Dr. Michael Slocum edited by the author.*

Because of the silicon complementary metal-oxide-semiconductor (CMOS) industry, it is a tempting candidate for photodiode material due to ease of integration with existing technologies. Silicon is also abundant in the Earth's crust and is low-cost compared to III-V's. However, its bandgap limits its usefulness to below 1.1 µm. Therefore there are many applications where silicon is not appropriate, such as thermal imaging or infrared optical communication in the 1.30 µm to 1.55 µm range. For these purposes, III-V InGaAs and extended InGaAs photodiodes, with respective bandgaps of 1.7 µm and 2.6 µm, have seen commercial success and can be purchased from many vendors.

III-V's have also been tremendously successful, in terms of efficiency, in the solar cell industry. According to National Renewable Energy Laboratory (NREL) (see Figure 1.2), the highest efficiency for a single-junction (1-J) terrestrial non-concentrator cell belongs to a GaAs cell by Alta Devices at 29.1% [19]. The flexibility of III-V's allows them to be easily integrated with each other to create cells with multiple junctions connected in series by tunnel junctions. The AM1.5g record for a III-V multi-junction non-concentrator cell is 39.2% by NREL [2]. The record for silicon is only 26.6% by Kaneka [20]. However, due to cost, it is silicon that dominates the terrestrial market. Figure 1.3 shows dollar-per-watt values for silicon

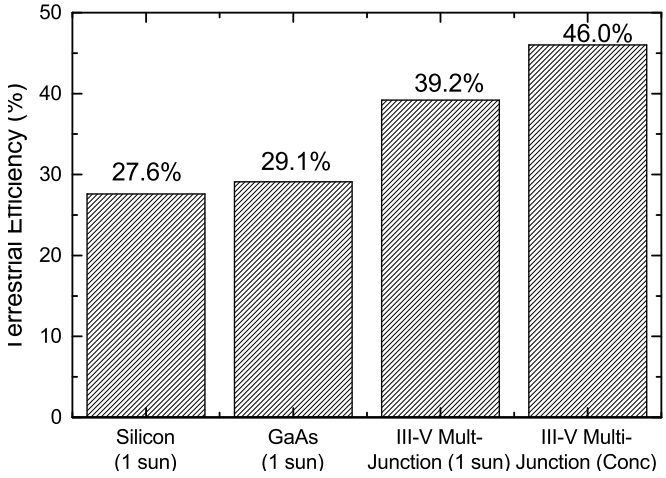


Figure 1.2: Record solar cell terrestrial efficiencies for crystalline silicon and III-V materials. *Sourced from NREL efficiency chart [2].*

cells compared to III-V technology from cost analyses assembled by Woodhouse *et al.* and Horowitz *et al.* [3, 4]. While silicon modules available today are only 17% efficient, they cost less than 0.40 USD/W, and this is a moving target as improvements to silicon modules will continue to be made. GaAs 1-J cells, III-V multi-junctions, and even III-V-on-silicon hybrid cells are all at least an order of magnitude more expensive at present. Even after extensive optimization, 1-sun III-V technology cannot be reduced below 1.00 USD/W.

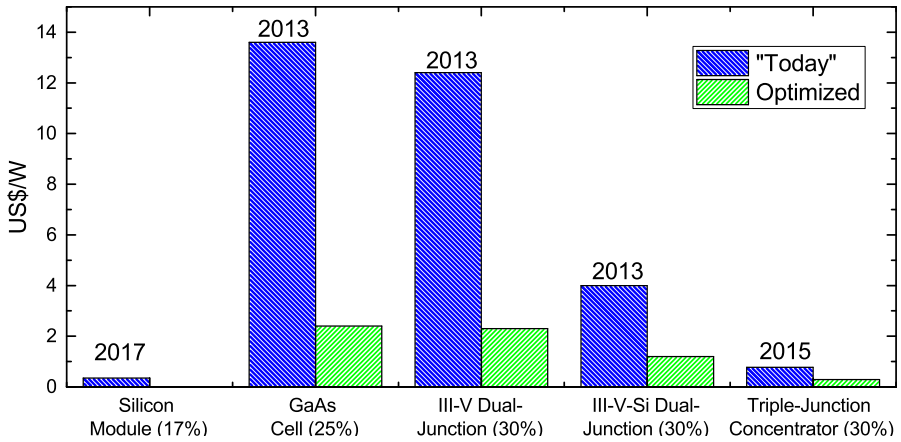


Figure 1.3: Dollar-per-watt values of silicon and III-V technologies. The value in parentheses is the efficiency used in the calculation. "Today" refers to the year above the blue bars, which was the cost at the time of the analysis. "Optimized" is the cost after presently attainable optimizations to the manufacturing process such as increased substrate re-use and improvements that come with mass-production. *Values from Woodhouse* et al. *and Horowitz* et al. *[3, 4].*

Accordingly, much of the current research in III-V solar cells is in cost reduction. Many

techniques already exist to increase the cost-competitiveness of III-V solar cells. Concentrator cells take advantage of low-expense optics to capture sunlight over a wide area and focus it onto a small but highly-efficient multi-junction III-V cell. This has an added benefit of improving the cell's efficiency over the un-concentrated case by increasing the free carrier density which leads to higher voltages. The result of concentration systems is higher efficiency cells with lower material cost because of the smaller areal coverage, a combination that greatly increases III-V marketability. Figure 1.2 shows that the absolute highest efficiency cell is a 46% concentrator multi-junction tested under 508 times the power density of the sun (508 'suns') [21]. The cost analysis from Figure 1.3 claims that concentrator technology could reduce cost 0.30 USD/W in the future, but while this is a promising result since it is competitive with silicon, the concentrator industry has thus far not has not gained significant market share [22]. Other active areas of cost-reduction research include, but are not limited to, novel materials for increased efficiency [23], reducing substrate cost through lattice-mismatched growth [24], virtual substrates [25], or substrate re-use [26], and high-speed growth [27] and light management [28] to reduce epitaxial growth expenses.

One field where high-efficiency III-V solar has already been successful is the space industry. Here, the high material and manufacturing costs are acceptable compared to the cost of launching a greater mass of lower-efficiency cells. As well, there are surface area limitations on satellites that are not a concern for terrestrial use. Returning to III-V photodetectors, these are also used on satellites, with applications for hyperspectral imaging [29], monitoring of Earth's atmosphere [30], and astronomy [31].

The excellent electronic properties of the III-V photodiode are owed to its crystalline quality. Two key metrics for photodiodes impacted by crystalline quality are the responsivity and dark current.

The responsivity is defined as the output current divided by the total incident optical power and the spectral responsivity (SR) is the responsivity as function of wavelength. High SR is desired over a spectral bandwidth determined by the application. Absorption coefficient, absorber size and thickness, and light management all affect responsivity. The spectral bandwidth and absorption coefficient are determined mostly by the material and its bandgap

(discussed above).

The dark current is the current that flows when no light shines on the device and arises due to thermal generation of carriers. In many cases it defines the noise floor of the photodetector and will limit the signal-to-noise ratio (SNR), so the lower the dark current, the better the sensitivity. For solar cells, low dark current allows for higher output voltage.

Both responsivity and dark current are ultimately limited by the material's ideal crystalline structure. However, in practice they are often limited by crystallographic defects that facilitate carrier generation, recombination, or tunneling via inter-bandgap states called deep-levels or traps.

Many of the mentioned cost-reduction techniques in III-V solar, such as novel materials (see Chapter 3) and lattice-mismatched growth (see Chapter 5), will lead to higher deep-level concentrations in the short-term as the techniques will not be mature enough to result in low-defect material. Deploying solar cells or photodetectors into the space environment will also lead to the creation of radiation-induced deep-levels, as, without Earth's protection, high-energy ionized particles bombard the material causing atomic displacement (see Chapter 4) [32, 33]. Whether defects are crystal growth-related or radiation-induced, a set of tools that can characterize both the physical and electronic properties of the defects are required because such characterization is an important step in understanding the (lack of) performance of the photodiode. The procedure of identifying defects, the inter-band states they create, and their impact on performance tie together the chapters of this work. Key tools used throughout this work are capacitance-based defect spectroscopy and dark current measurements.

Deep-level transient spectroscopy (DLTS) is a method of defect spectroscopy that measures capacitance transients in the photodiode junction capacitance as a function of temperature. The transients are related to emission of carriers from deep-levels, or traps, in the material. With this method, the location of the trap energy within the bandgap can be determined, along with the carrier capture cross-section (analogous to the capture cross-section in nuclear physics) and the trap density. DLTS is regularly used to compare the trap profiles of different III-V crystal growth techniques [34, 35] or to obtain trap profiles caused by irradiation of the material by high-energy ions [5]. DLTS spectra for an electron-irradiated GaAs photodiode

with InAs QDs is shown in Figure 1.4, where each set of peaks represents a detected carrier trap. The trap characteristics found by DLTS can be used to predict the dark current of the photodiode [36] by using the Shockley-Read-Hall (SRH) recombination model [37], where, as-mentioned, the dark current is a critical aspect of photodiode performance.

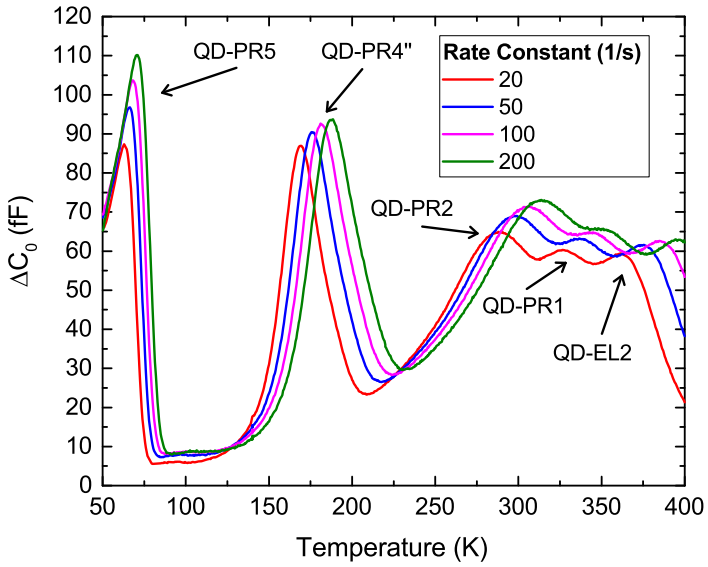


Figure 1.4: DLTS spectra obtained from a GaAs photodiode irradiated with 1 MeV electrons. The data was obtained with the MFIA-based system developed specifically for this dissertation work. This was the same sample as used by Sato *et al.* [5], though the data here is unique. Defect peaks are labeled according to Sato *et al.*. The rate constants are explained in Chapter 2.

The final section of this work examines integrated light management as a path to reduce the impact of deep-levels on device performance. In has been shown that light management can be used to improve radiation tolerance of III-V photodiodes, leading to extended mission lifetime in space applications [38, 39]. To achieve this, light management is used to maintain or improve the responsivity of the device while simultaneously reducing the thickness of the active region. Thinner photodiodes are defect-tolerant for reasons that are explained in Chapter 6. A model was created using numerical optical and electronic solvers to predict device performance single- and multi-junction III-V solar cells for different cell thicknesses and light management structures.

## 1.2 Approach

The general theme of this dissertation was to study the relationship between defects and device performance for a variety of III-V photodiodes. These defects may have been growth- or processing-related, as was the case for the novel approaches to the III-V solar cell in Chapters 3 and 5, or radiation-induced, which occurred for InGaAs photodetectors in Chapter 4. Figure 1.5 is a flow chart of the dissertation, explaining for each topic the motivation, the cause of the defects, and the techniques used to measure the defects and their impact on the device. The final topic describes how light management and thinning the device can be used to improve the performance of a photodiode.

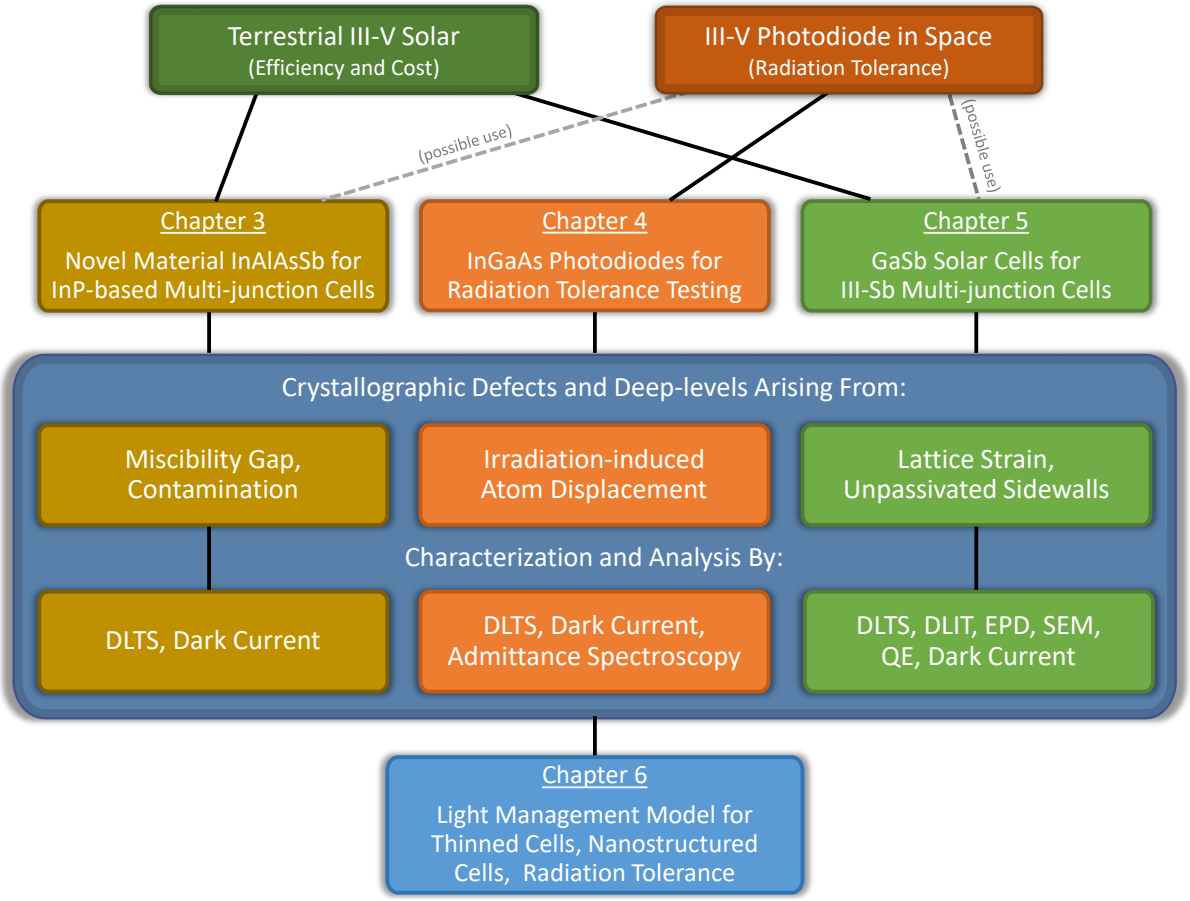


Figure 1.5: Flow chart of the dissertation. The chapters cover III-V photodiodes used for terrestrial or space applications. For the chapters covering experimental work, the source of defects is identified and the techniques used to characterize the defects or their impacts on device performance are listed. A final chapter covers a light management model that could be applied to any of the other projects to and was focused on thinning absorbing layers to mitigate the impact of defects or reduce cost.

The first half of the work focuses mostly on DLTS and dark current measurements. These were applied to detect as-grown trap levels in InAlAsSb, a novel solar cell material useful as the top-junction of an InP-based triple-junction cell (Chapter 3). Growth of the material had to overcome a mascilibility gap which favors the creation of InSb [40]. By creating a profile of traps in the novel material, a more-optimized growth condition could be developed. For instance, traps levels can be detected as a function of growth temperature, III-V ratio, and precursor species as part of a growth optimization campaign.

Following that is an *in situ* DLTS method that is able to better measure the effect of the defect-inducing space environment on devices than what is conventionally practiced (Chapter 4). Sample irradiation and the following testing are both typically performed at room temperature or above. If they are irradiated at low temperature, they are typically exposed to room temperature before DLTS is performed. It is known that, at this temperature, many defects are not stable as the displaced atoms can diffuse back into their vacancies [8]. By controlling the irradiation temperature and performing *in situ* testing, two outcomes can be achieved. One is that the device can be irradiated and tested at the temperature it is expected to operate under to better reflect deployed conditions. Two is that the sample can be irradiated and tested at very low temperatures to ensure the stability of defects in order to gain a better understanding of the principle of defect creation in that particular material. The material tested here was $In_{0.54}Ga_{0.46}As$ lattice-matched on InP, which has a number of applications as a photodetector in space including infrared astronomy [31], infrared phenomonology and remote sensing [41], and hyperspectral imaging [42].

The next chapter covers development, fabrication, and defect analysis of highly lattice-mismatched GaSb solar cells (Chapter 5). This work was meant to establish a platform leading to a variety of inexpensive, monolithically-grown, III-Sb multi-junction cells. When growing lattice-mismatched, the key concern for solar cell performance is the lattice strain leading to creation of threading dislocations which lower efficiency via increased trap-assisted recombination. Cycles of growth, fabrication, and testing led to the conclusion that a variety of defects were leading to poor performance, including voids, sidewall states, and threading dislocations. Testing driven by dark current analysis was able to quantify the performance

loss due to each type of defect, information that will help direct the next generation of experiments.

Finally, light management structures that enhance the efficiency of and mitigate the deleterious effects of trap levels in nanostructured cells and space cells were explored (Chapter 6). A variety of models predict that the addition of a textured mirror to the backside of a III-V cell can lead to high efficiencies, however, the field has struggled to replicate this in experiment, achieving less than 20% efficiency in textured GaAs 1-J cells. A precise model was developed to examine why this is the case. Many of the published models do not implement arbitrary structures and instead relied on thermodynamic arguments or pre-determined reflection parameters of the backside mirror. The model developed here was able to calculate path length or absorption enhancement for arbitrary cell structures, and many structures that may be realistically fabricated were simulated. The path length is a ray-optics concept of how many 'passes' light makes through the cell, and with higher path lengths the absorbers could be thinned. It is known that thinner cells are defect-tolerant and therefore radiation tolerant [38, 39]. With this in mind, the model was then applied to multi-junction space cells to develop light management specifically for radiation tolerance.

## 1.3 Objectives

The objectives of this work and some of the original contributions are listed below:

- Fabricated $In_{0.19}Al_{0.81}As_{0.72}Sb_{0.28}$ Schottky diodes for defect spectroscopy
- Created trap profiles for $In_{0.52}Al_{0.48}As$ and InAlAsSb
- Developed unique deep-level transient spectroscopy system with all-custom software that can be used with *in situ* irradiation experiments
- Performed *in situ* defect spectroscopy and dark current analysis on InGaAs didoes
- Created fabrication process for GaSb solar cells and photodiodes
- Fabricated GaSb-on-GaSb and GaSb-on-GaAs solar cells with state-of-the-art metrics

- Created GaSb-on-GaAs triple-junction (3-J) solar cell model in Sentaurus by fitting own GaSb-on-GaAs data
- Developed code to integrate Synopsys RSoft with Sentaurus for combined numerical optical and electronic simulation ability
- Developed 1-J GaAs light management model to optimize the rear mirror
- Developed 3-J space cell model to increase radiation tolerance of middle subcell

## 1.4 Organization of Dissertation

Chapter 1 motivates the research by highlighting the advantage of III-V solar cells in terms of efficiency and the need to reduce III-V cell cost. The motivation to improve the radiation tolerance of III-V photodiodes is also covered. The effect of defects on photodiode performance and how defects are characterized is briefly introduced.

Chapter 2 provides background on general photodiode and solar cell physics. As well, many of the important concepts and experimental techniques necessary to understand the work in later chapters are explained. These include dark current analysis, how dark current is affected by crystallographic defects through trap states, and defect spectroscopy via DLTS. Because of frequent use of the device simulator Synopsys Sentaurus, a section on the principles behind modern device simulators is included. Modern III-V solar cell technologies are introduced to give context to the contributions of this work discussed in the later chapters.

Chapter 3 presents a trap state analysis of two materials: $In_{0.52}Al_{0.48}As$ and the rare $In_{0.19}Al_{0.81}As_{0.72}Sb_{0.28}$. Diodes were fabricated from these materials for dark current measurements and DLTS. Several traps of moderate concentration were detected in the novel InAlAsSb diodes and the dark current was high. Growth of many control InAlAs samples allowed for a study of InAlAs traps comparing different methods of epitaxy and different chemical precursors. InAlAs solar cells of all varieties were found to have low trap concentration with low dark current, with cells grown by molecular beam epitaxy (MBE) containing the highest trap density when compared to growth by metalorganic chemical vapor deposition (MOCVD).

Chapter 4 describes a system built to perform *in situ* DLTS and dark current measurements on samples irradiated at low temperature. The application in this instance was $In_{0.54}Ga_{0.46}As$ on InP substrates irradiated by 2.0 MeV and 3.5 MeV protons. The InGaAs diodes were designed and fabricated specifically for this purpose. To perform faster temperature scans, a custom DLTS system was created with an unconventional capacitance meter and driven by software written by the author. After irradiation at 100 K, annealing of the dominant radiation-induced trap in InGaAs began around 150 K. Defect annealing experiments were also performed to connect dark current to certain traps. The shallow traps of the cell and their effect on the junction capacitance were examined using admittance spectroscopy.

Chapter 5 evaluated a lattice mis-matched growth technique for growing GaSb directly on GaAs that could potentially lead to a new cost-effective multi-junction solar cell technology. GaSb 1-J cells were grown on GaSb substrates natively and on GaAs substrates using the interfacial misfit (IMF) array growth technique. A fabrication process was developed that led to state-of-the-art GaSb-on-GaSb cells. Evidence of sidewall recombination and shunt-causing voids were found in the GaSb-on-GaSb cells by dark current analysis and dark lock-in thermography (DLIT), indicating that even the native solar cell was prone to performance-limiting defects. The GaSb-on-GaAs cell was concluded to be limited mostly by threading dislocations due to failure to form the ideal IMF array during growth. DLTS was performed on these samples, and more traps were found in the GaSb-on-GaAs sample. A 3-J model of InGaP/GaAs/GaSb was developed based on the GaSb-on-GaAs results.

Chapter 6 discusses numerical light management modeling used to develop new light management designs for single- and multi-junction cells. The models used Synopsys RSoft for optical simulation and Synopsys Sentaurus for device simulation with python code for integration. A model was applied to thin GaAs and nanostructured GaAs 1-J cells to optimize the rearside optical reflector, including the reflector texture. The best rear reflector lead to path lengths >30 that could be achievable with standard wet etching and deposition. Another model was developed to radiation-harden 3-J space cells. The results indicated that an interstitial structure could be used to thin the middle subcell for excellent radiation tolerance at the cost of slightly reduced efficiency at beginning of life.

Conclusions and future work for each topic are discussed at the end of their respective chapters.

# Chapter 2

# Background

## 2.1 Solar Cell General Principles

According to Nelson, a solar cell must meet three requirements to generate usable work from sunlight [43]. Those requirements are charge generation, charge transport, and charge separation. Charge generation is the ability of materials to absorb photons of sufficient energy to excite electrons from one orbital, or energy level, to a higher energy state. The key to useful charge generation is for the material to have available occupied and unoccupied electron states with a difference in energy comparable to the photon energies output by the sun. Next, for charge transport to occur, there needs to be a way for the excited electron to move around within the material in order to be collected by the device terminals. In addition to this, the transport must be done in a way that preserves electric potential of the excited electron. Finally, charge separation demands that the material have an asymmetry such that the excited electrons are preferentially collected at one terminal and not the other. The resulting potential difference between the terminals can be used to force current flow through an external load.

A crystalline semiconductor material is able to perform all three of these prerequisites. The range of forbidden energy levels in a crystalline semiconductor, known as the bandgap of the material, is both large enough to prevent immediate relaxation of excited charge carriers from conduction band to valence band (due to a lack of phonon states with this energy), and yet small enough to be within the useful range of photon energies output by the sun (ie. visible light). The current rectifying behavior of a p-n junction diode provides a low resistance path for electrons (holes) to the n-type (p-type) terminal, thus providing charge separation through

a spatial asymmetry. Figure 2.1 shows that when a p-n junction generates an electron-hole pair from absorbed light, the built-in junction and carrier-selective contacts provide the means to separate the charges, which can then be driven through the external load.

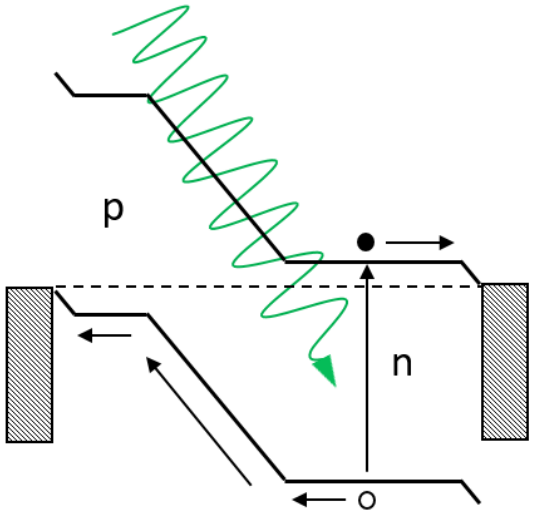


Figure 2.1: Band diagram of p-n junction with absorbed photon generating an electron-hole pair which then separate and travel to opposite contacts.

The Beer-Lambert law describes how a material with a uniform absorption coefficient, such as a crystalline semiconductor, absorbs photons and thus attenuates the intensity of a normally incident beam of light of wavelength $\lambda$ [43]. The intensity at a given depth $x$, *I(x)*, is defined by,

$$I(x) = I_0 \exp(-\alpha x) = I_0 \exp\left(\frac{-4\pi k x}{\lambda}\right), \tag{2.1}$$

where $I_0$ is the intensity just inside the surface of the material, $\alpha$ is the absorption coefficient, and $k$ is the imaginary part of the refractive index, also called the extinction or attenuation coefficient. Figure 2.2 contains a plot of absorption coefficient values for relevant photon wavelengths for semiconductor materials covered in this dissertation. The slower increase in $\alpha$ starting from the bandgap for Si and Ge compared to the III-V semiconductors is a consequence of the indirect bandgap of Si and Ge versus the direct band gap of the III-V materials. Absorption in an indirect bandgap material is a two step process that involves a photon to promote the carrier's energy and a phonon to supply the necessary momentum. As such,

absorption becomes dependent on the product of the probability distributions of both photon and phonon absorption. In a direct bandgap material, like GaAs, only photon absorption is needed.

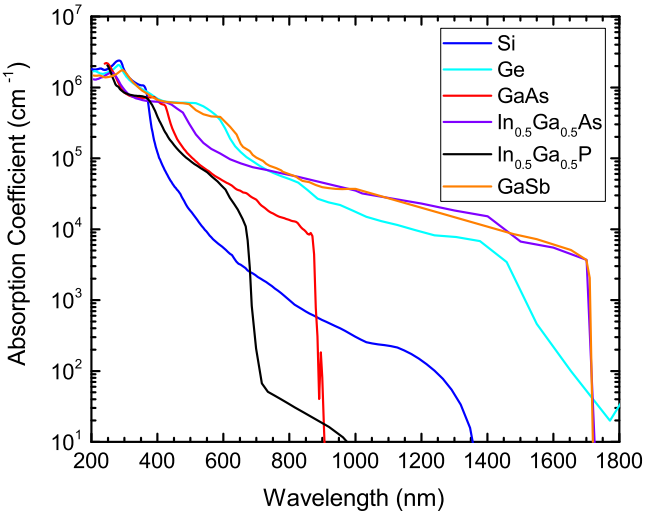


Figure 2.2: Absorption coefficient versus wavelength for semiconductor materials mentioned in this work. *GaAs and InGaP data measured by ellipsometry, all others obtain from TFCalc or Sentaurus software database.*

The absorption properties of a material have a critical impact on the cell's design. The low absorption of photons near the bandgap of Si means that cells made from this material are commonly in the 100's of $\mu$m thick in order to absorb most of the solar spectrum, an entire two orders of magnitude thicker than a typical GaAs cell. This can be affirmed by using the values found in Figure 2.2 in conjunction with Equation 2.1.

From the absorption, the photo-generated current density ($J_{Ph}$) can be obtained for a simple absorber. The carrier generation rate ($G$) is required, which is defined as,

$$G(\lambda, x) = \alpha N_0 \exp(-\alpha x), \tag{2.2}$$

where $N_0$ is the photon flux just inside the absorber surface for that wavelength. Assuming perfect collection efficiency (all carriers reach the junction), the current generated from that wavelength can then be calculated,

$$J_{Ph} = q \int_0^{x_f} G_{net}(x) dx, \tag{2.3}$$

where $x_f$ is the thickness of the absorber layer. For more than one discrete wavelength, the generation rates for each wavelengths can be summed to obtain the net generation rate and the total $J_{Ph}$. For a continuous spectrum, the photon flux density must be replaced with spectral flux density and the right-hand side of Equation 2.2 will be integrated with respect to wavelength, keeping in mind that absorption coefficient is also wavelength-dependent.

In reality, perfect collection is not obtained. To determine the current, the SR is found experimentally and the external quantum efficiency (EQE) is calculated. As mentioned, SR is the current obtained from the cell for a given amount of incident optical power density. EQE is the ratio of carriers collected to incident photons on the device, and is calculated from SR by,

$$EQE(\lambda) = \frac{hc}{q\lambda} SR(\lambda), \tag{2.4}$$

where $h$ is Planck's constant and $c$ is the speed of light. To determine the short-circuit current density ($J_{SC}$), which is the current of the cell at zero bias, the following can be used,

$$J_{SC} = \int SR(\lambda)\phi_{Spectrum}(\lambda)d\lambda \tag{2.5}$$

where $\phi_{Spectrum}$ is the desired incident spectrum. $J_{Ph}$ is the same as the measured $J_{SC}$ in most cases, and only diverges when the series resistance ($R_S$) is abnormally large. To obtain high SR or EQE, carriers must be generated within the depletion region or else within a minority carrier diffusion length (MCDL) of the edge of the depletion region. The MCDL is statistically the distance that a carrier will travel before recombining. It depends on the carrier lifetime and the mobility (discussed later). An EQE plot can be found in Chapter 5.

Charge transport through a crystalline semiconductor depends heavily on the resistance encountered in each layer and interface of the device. High doping values (>$10^{17}$) are used to ensure low sheet resistance so that carriers may travel to the contacts either vertically or laterally without loss of voltage. High doping will also increase the junction's built-in voltage, which drives the output voltage. However, there is a trade off between doping and MCDL because more dopant atoms in the lattice increase the amount of electron scattering

and decrease the carrier drift velocity and mobility. For this reason, one half of a conventional solar cell's junction will be highly doped, yet thin layer (the emitter), while the other half will be lightly doped and account for the large majority of the cell's thickness (the base). The thick layer is almost always needed in order to fully attenuate the incoming light (this is the concept of 'optically thick', see Equation 2.1). The asymmetrical p-n junction thus allows for high voltage, low resistance, and full absorption with good collection efficiency.

Carrier collection and output voltage are related and this relationship is determine by measuring the current density vs. voltage (J-V) response of the cell. This is performed by holding the terminals at specified voltages and measuring the resulting current, and can be done in either the absence of light (dark J-V) or under illumination from a desired spectrum. To understand or model the relationship between the applied voltage and the measured current through a p-n junction diode, the Poisson equation, the current transport equations, and the continuity equations must be understood and solved as a self-consistent system. A detailed derivation of p-n junction current transport is given in Appendix B. The Poisson equation models the electrical potential across the junction as a result of the fixed charge (dopant atoms, applied bias) and the mobile charge (free carriers). The current transport equations explain that transport is driven by free carrier response to electric fields (drift current) and concentration gradients (diffusion current). The continuity equations ensure charge preservation. With some assumptions, a closed form solution to these equations is the ideal diode equation. The ordinary ideal diode equation can be modified to make it a more robust model for a wider variety of solar cells, called the double diode equation with parasitic resistances [43–45],

$$J(V) = J_{\mathrm{Ph}} - J_{01}\left(\exp\left[\frac{q(V - JR_{\mathrm{S}})}{n_1 k_{\mathrm{B}} T} - 1\right]\right) - J_{02}\left(\exp\left[\frac{q(V - JR_{\mathrm{S}})}{n_2 k_{\mathrm{B}} T} - 1\right]\right) - \frac{V - JR_{\mathrm{S}}}{R_{\mathrm{Sh}}} \quad (2.6)$$

where $q$ is the elementary charge, $k_{\mathrm{B}}$ is Boltzmann's constant, $T$ is the cell temperature, and $V$ is the potential difference between the two cell terminals. Note that $\mathrm{J_{Ph}}$ only depends on the incident photon flux density and is independent of the cell bias, $V$, using what is known as the superposition assumption. It is common practice to quantify a solar cell's performance

using many of the terms in (2.6). These terms are the recombination current density in quasi-neutral regions ($J_{01}$), the recombination current density in depletion region ($J_{02}$), the ideality factors $n_1$ and $n_2$, the series resistance $R_S$, and the shunt resistance ($R_{Sh}$). Other important parameters that describe the J-V curve but are missing from (2.6) are the open-circuit voltage, the short-circuit current, the fill-factor, the maximum power point, and the cell conversion efficiency.

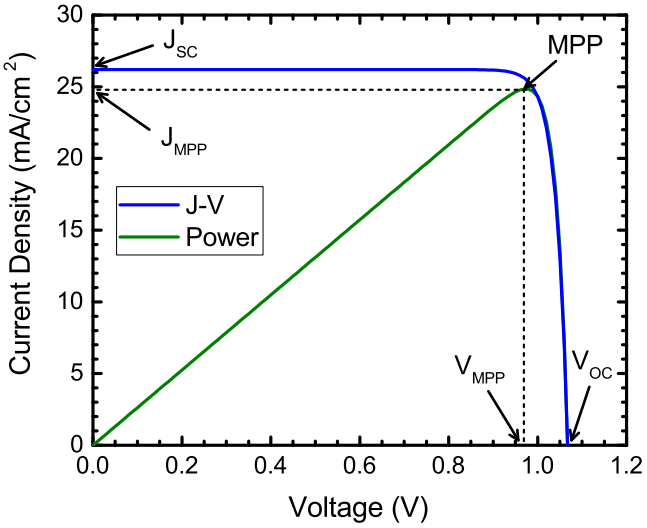


Figure 2.3: An example of a J-V curve. There is also power vs. voltage to show the MPP.

The voltage of the cell under open-circuit conditions, or open-circuit voltage ($V_{OC}$), is the voltage across the cell terminals under illumination when the cell is attached to an infinite load resistance [43]. Under this condition, no current flows through the device, so excess charge carriers ($\Delta n$, $\Delta p$) accumulate until they recombine in the cell. It is a useful metric as it represents an upper limit of carrier potential. Similarly, the $J_{SC}$ is the current output by the cell if the terminals are attached to one another with no load resistance. This represents the upper limit achievable by the cell's photo-generated current. As power is voltage multiplied by current, to better relate $V_{OC}$ and $J_{SC}$ to actual cell output and efficiency, the fill factor (FF), is used,

$$FF = \frac{V_{\mathrm{MPP}} J_{\mathrm{MPP}}}{V_{\mathrm{OC}} J_{\mathrm{SC}}} \tag{2.7}$$

where the maximum power point (MPP) is the cell's operating point where the voltage at the

MPP ($V_{MPP}$) and the current density at the MPP ($J_{MPP}$) are defined. The FF is a ratio of the usable power to the upper limit of power defined by $V_{OC}$ and $J_{SC}$. The MPP can be found by plotting $JV$ versus $V$ and finding the voltage that gives the highest power, as seen in Figure 2.3. Besides recombination currents, which can be minimized but not avoided, other factors that reduce FF are the parasitic resistances, $R_S$ and $R_{Sh}$ [44]. Series resistance is resistance to any current flow within the device and becomes more problematic as current increases. A common method to improve a cell is to reduce $R_S$. Typical sources of $R_S$ besides the sheet resistances of the device layers include the contact point with the grid fingers and resistance in the grid fingers themselves. A shunt in the cell is a path from one terminal to the other that avoids the junction, such as a short-circuit about the perimeter of the cell. A high $R_{Sh}$ prevents this from occurring, and therefore a good cell will have as high a $R_{Sh}$ as possible.

The recombination currents $J_{01}$ and $J_{02}$ and ideality factors $n_1$ and $n_2$ describe the degree and type of recombination that occurs in the cell. Recombination, the reverse process of charge carrier generation, is when an electron in the conduction band loses energy as it combines with a hole in the valence band. The three relevant types of recombination are radiative, defect- or trap-assisted, and Auger recombination. Radiative recombination is the opposite of photo-generation and occurs when the mobile electron meets a mobile hole (electron vacancy) in the lattice and results in the emission of a photon near the bandgap energy. Thermodynamically speaking, some amount of radiative recombination is unavoidable and is one of many reasons why a conventional cell's conversion efficiency cannot be 100%. As in photo-generation, radiative recombination in an indirect semiconductor is a two-step process and is usually not the dominant recombination mechanism. However, in direct semiconductors, radiative recombination is considerably more prominent and can lead to a voltage increase through the phenomenon known as photon recycling (discussed in Chapter 6). In indirect semiconductors, the dominant process is usually trap-assisted or Auger recombination. Trap-assisted recombination, also called SRH recombination, can occur anywhere in the cell and may be separated into categories: quasi-neutral region (QNR), depletion region, and surface or interface defect. The last category refers to the edges of a crystal where atoms will have missing neighbors, leading to the "dangling bond" phenomena. Dangling bonds

are recombination centers with very high concentration. If these defects are not passivated, charge carriers generated within a diffusion length of the surface have a very high chance of recombining. SRH recombination in general is avoidable through higher quality crystal growth in combination with effective interface passivation. Auger recombination is band-to-band recombination not unlike radiative, except the energy is not give off as a photon but instead is given to another electron in the conduction band. It is typically only influential under high-injection conditions, especially for direct semiconductors.

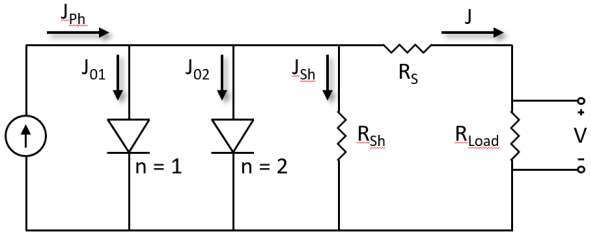


Figure 2.4: A circuit model representing a solar cell with a two diodes and parasitic resistances.

To return to the two diode model, the equivalent circuit of the model is shown in Figure 2.4. Each of the circuit components has already been described at this point. The effect of each on the J-V curve, in both the light and in the dark, is shown in Figure 2.5. In parts a and b of the figure, the different between an $J_{01}$- and $J_{02}$-dominant diode are shown for a hypothetical GaAs solar cell. The $J_{02}$ diode reduces the $V_{OC}$ and, even more so, reduces the FF. The parasitic resistances shown in parts c through f also mostly affect the FF, though a low $R_{Sh}$ mostly affects the $J_{MPP}$ while high $R_S$ primarily lowers $V_{MPP}$.

The recombination currents $J_{01}$ and $J_{02}$ and the ideality factors $n_1$ and $n_2$ describe the degree and type of recombination as previously stated. The reason for two diodes (in parallel) is that the depletion region recombination usually dominates at lower voltages while at higher bias the bulk effects take over. According to Equation 2.6, $J_{01}$ is a pre-exponential factor for a voltage-dependent generation-recombination, or diffusion, current that arises from an $n_1$ type of recombination. For an abrupt $p^+n$ junction under low injection, it is,

$$J_{01} = \frac{qD_p p_{n0}}{L_p}. \tag{2.8}$$

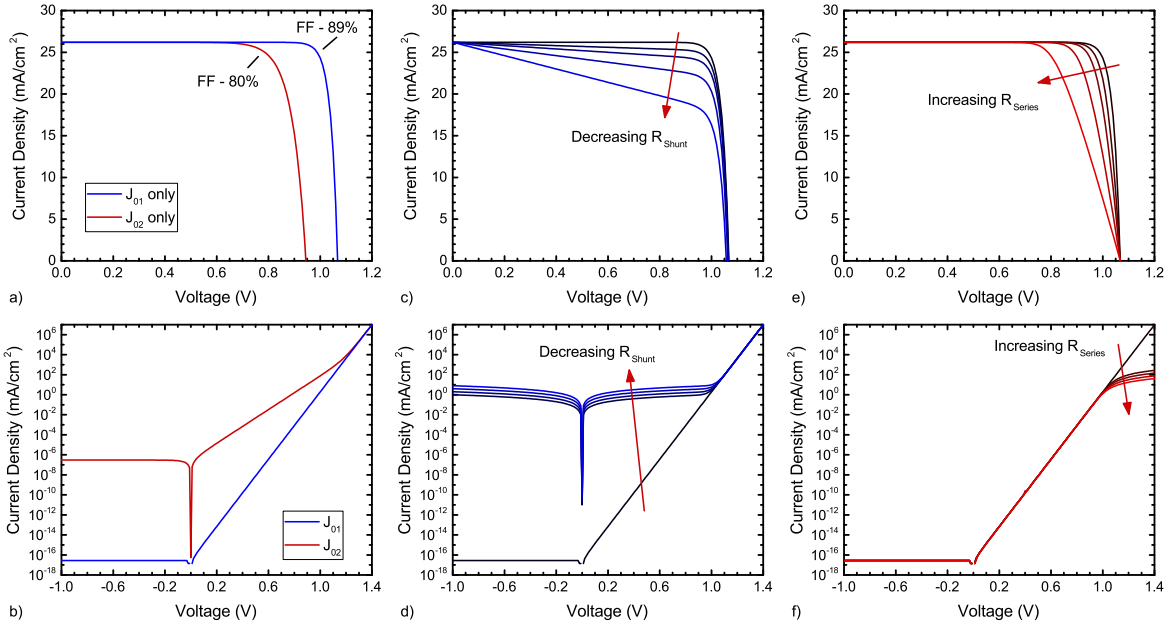


Figure 2.5: Example J-V curves of a hypothetical GaAs cell demonstrating the effect of each of the components in the double-diode model. a) J-V for $J_{01}$ and $J_{02}$ diodes under illumination and b) in the dark ($J_{Ph}$ = 0). c) The effect of $R_{Sh}$ on the illuminated and d) dark J-V. e) $R_S$ effect on J-V in the light and f) in the dark.

This recombination type is corresponds to an ideality of $n_1$=1 due to a dependence in the derivation upon only the minority carrier concentration and can be considered to be recombination that removes a single useful carrier. This occurs in the bulk regions of the emitter and base.

$J_{02}$ is the pre-exponential for recombination that removes $n_2$=2 useful carriers, which occurs in the depletion regions where the free hole and electron concentrations are on the same order. Assuming a mid-gap trap, it can be approximated to be,

$$J_{02} \approx \frac{qW_D}{2}\sigma v_{th} N_t n_i, \tag{2.9}$$

where $W_D$ is the depletion region width, $\sigma$ is the defect capture cross-section, $v_{th}$ is the carrier thermal velocity, $N_t$ is the trap density and $n_i$ is the intrinsic carrier concentration.

The dark current of a Schottky diode is similar to a p-n junction but with different pre-exponential. $J_{01}$ becomes $J_{0S}$,

$$J_{0S} = A^{**}T^2 \exp\left(\frac{q\Phi_B}{k_B T}\right)\frac{qW_D}{2}\sigma v_{th} N_t n_i, \tag{2.10}$$

where $A^{**}$ is the Richardson constant and $\Phi_B$ is the Schottky barrier height. Once carriers thermally emit over the Schottky barrier, there is no need for recombination rates or diffusion lengths like for the p-n diode case because the other side is a metal. Instead, the current is more dependent on barrier height, density of states, and majority carrier effective mass.

Finally, the conversion efficiency of the cell is defined as,

$$\eta = \frac{V_{\mathrm{MPP}} J_{\mathrm{MPP}}}{P_{\mathrm{S}}}, \tag{2.11}$$

where $P_S$ is the incident light power density and is defined by the solar spectrum. The standard spectra used are the air-mass 0 (AM0) spectrum for space, which has a power density of 136 mW/cm$^2$, and the air-mass 1.5 global (AM1.5G) terrestrial spectrum, which is 100 mW/cm$^2$ [46].

## 2.2 Photodetector Metrics

A photodiode-based photodetector is a similar device to a solar cell and the physics describing a p-n junction from the previous section will also apply to other photodiodes. In the language of the field, a photodetector can be judged using three criteria, those being responsivity, dark current, and response time [47].

The responsivity is defined by the output current divided by the total incident power and the SR is the responsivity as function of wavelength. High SR is desired for a spectral bandwidth appropriate for the application. Absorption coefficient, absorber size and thickness, and light management all affect responsivity. The spectral bandwidth and absorption coefficient is determined mostly by the material and its bandgap.

Dark current is the current that flows when no light shines on the device and arises due to thermal generation of carriers. In many cases it defines the noise floor of the photodiode

and will limit the SNR, so the lower the dark current, the better the sensitivity. Dark current is ultimately limited by the material's band structure. Dark current of a photodiode was was described in the previous section.

Unlike a solar cell, a photodetector does not need to produce power and can instead be a device powered from a separate power source. Therefore the photodiode detector does not need to be operated under forward bias like a solar cell does, and are instead operated under zero-bias or reverse bias. Recall from the previous section that, to collect a carrier, that carrier must be within a MCDL of the edge of the depletion region. One way to increase the volume over which carriers can be collected, then, is to increase the depletion region by increasing the reverse bias. This allows greater collection probability over a larger absorber volume and will increase the responsivity, especially for weakly-absorbed light. There is a trade-off, however, as increasing the reverse bias may also increase the dark current for a diode with SRH recombination-generation centers or a diode prone to tunneling.

Increasing the depletion region is also taken into account during the design of the device layers. Unlike a solar cell, which requires high doping in the base to produce high voltage, a photodiode detector can use an undoped absorber layer to maximize the depletion across it as current, not voltage, is the important part of the output signal.

Finally, the response time of a photodetector is related to the rise time or signal bandwidth of the device, and is determined mostly by the carrier transit time and the junction capacitance. Short transit-times and small junction capacitance allows for the high-speed operation required for modern fiber-optic communications and favors small devices.

## 2.3 Crystallographic Defects and Trap States

Imperfections in the crystal structure of solids are known as crystallographic defects. Such a defect may have an impact upon the electronic properties of a semiconductor, such as reduced carrier mobility by impurity scattering. When a defect introduces an electronic state in the forbidden energy region of the bandgap, that state may be considered a trap state. Doping is the well-known process of purposely introducing shallow-level traps that change

the Fermi-level of the solid and can lead to the creation of n-type and p-type semiconductors. Deep-level traps lie closer in energy to mid-gap and are often undesirable as they lead to reduced conductivity and/or high rates of SRH recombination. The relationship between crystallographic defects, electronic trap states, and solid-state device performance are often complex and difficult to predict [48].

Crystalline defects can be categorized by their dimensionality. In increasing order, those categories are point, line, planar, and bulk defects [49].

Point defects include vacancies, anti-sites, intrinsic and extrinsic interstitials, and substitutions by impurities. These are difficult to detect physically due to their size, but they are always present and in sufficient concentration they may have a substantial effect upon the electronic properties of a semiconductor. Doping is an example of a substitution defect where a host atom is replaced by an impurity. Impurity concentration (substitutions, extrinsic interstitials) can be physically detected by secondary ion mass spectrometry (SIMS), however, this measurement cannot detect intrinsic point defects (vacancies, anti-sites, intrinsic interstitials), where all atoms involved are part of the host crystal. To find these defects, electronic testing such as Hall effect or depletion-capacitance defect spectroscopy are typically used, as shown in Chapters 3 and 4. Another point-defect measurement of note is Fourier-transform infrared spectroscopy, where a sample is exposed to infrared radiation and chemical bonds absorb light at certain frequencies.

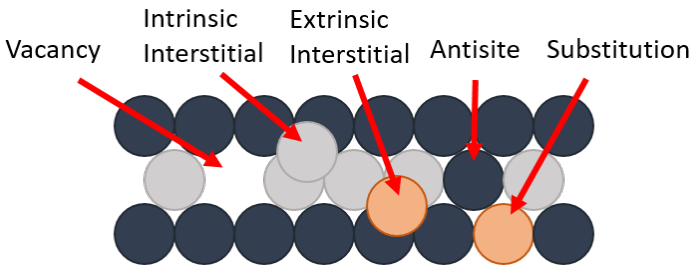


Figure 2.6: Simple depiction of crystallographic point defects.

Line defects include edge dislocations, screw dislocations, and dislocation loops. In III-V epitaxy, threading dislocations are of particular interest as their formation is due to strain relaxation when lattice-mismatched materials are grown, discussed in see Chapter 5. For

defects of this size and larger, transmission electron microscopy (TEM) is frequently used to observe or count the defects [50]. Etch pit density (EPD) tests are also used to determine the cross-sectional density of threading dislocations [51].

Planar defects include anti-phase boundaries, grain boundaries, twins, and stacking faults. Boundaries between different phases of the material can result in dangling bonds and these defects may have been responsible for effects observed in InAlAsSb diodes in Chapter 3.

Bulk or macroscopic defects include cracks, voids, and inclusions. Just a single of these types of defects can degrade solid-state device performance, as seen in Chapter 5.

The effect of a point defect upon the electronic properties of a semiconductor depend on many factor besides its concentration. Not all impurities will have an apparent electronic impact, even in high concentration. In Czochralski-grown silicon wafers, it is well known that oxygen atoms contaminate the lattice upwards of $10^{18}$ atoms/cm$^3$ [52]. Some of these incorporate in the lattice as substitutions, which can be measured by an increase in the lattice constant using X-ray diffraction (XRD). However, interstitial oxygen, measured by FTIR, is also present and has shown to be electrically inert or inactive. Annealing the wafer activates these interstitials and results in midgap states, where different states form at different annealing temperatures. Determining the exact physical reason behind phenomena such as this, or, in other words, the link between the atomic configuration and resulting electronic effects, is a difficult and complex problem to solve. The most proven approach is density functional theory (DFT) with psuedopotentials [53, 54].

DFT is a quantum mechanical modeling technique where different defect configurations are modeled until one is found that best replicates the results from experiments such as defect spectroscopy. There a number of compounding complications which cannot be measured with accuracy, such as interaction of the defect with other surrounding defects or the defect charge state and its interaction with localized electric fields [48]. The DFT model combined with defect spectroscopy, therefore, is a potentially powerful tool and was used to understand the behavior of interstitial oxygen in silicon mentioned above [53]. DFT modeling is not covered in this work but awareness of it is important context to the study of defects in III-V crystals.

Higher dimensional defects may create defect bands in the bandgap and tend to efficiently

facilitate nonradiative recombination for carriers less than a diffusion length away. These defect may also lead to shunting. There are techniques to mitigate or passivate them, such as hydrogen passivation of dangling bonds in silicon [55]. The sidewalls of mesa-isolated devices represent a boundary defect which can dominate performance for devices with area in the 1 $mm^2$ range. There are a plethora of techniques developed to mitigate this boundary for a wide range of materials and device types, and sidewall passivation is an active area of research (see Chapter 5).

The effect of trap-assisted recombination on III-V solar cell performance is decreased carrier lifetimes and an increase in the dark current. This reduces both the current and voltage. Current is lost if the MCDL of a generated carrier is lower than the distance the carrier must travel to the junction. The MCDL is related to the carrier lifetime by,

$$MCDL = \sqrt{D\tau}, \tag{2.12}$$

where $D$ and $\tau$ are the minority carrier diffusion constant and the lifetime, respectively. The diffusion constant can be modeled using the Einstein relationship to be,

$$D = \mu \frac{k_B T}{q}, \tag{2.13}$$

where $\mu$ is the carrier mobility.

The inverse of the carrier lifetime in Equation 2.12 can be represented in terms of the various recombination mechanisms as,

$$\frac{1}{\tau} = \frac{1}{\tau_{SRH}} + \frac{1}{\tau_{rad}} + \frac{1}{\tau_{Auger}} \approx A + BN + CN^2, \tag{2.14}$$

where $\tau_{SRH}$, $\tau_{rad}$, and $\tau_{Auger}$ are the SRH, radiative, and Auger carrier lifetimes, respectively, and $A$, $B$, and $C$ are the SRH, radiative, and Auger recombination coefficients, respectively. From the right of Equation 2.14, it is seen that to the SRH lifetime normally does not depend on the majority carrier concentration, largely because the SRH lifetime is determined by the mid-gap trap density, $N_t$. The recombination coefficients $B$ and $C$ are material dependent, as they depend on the band structure, and can be found in databases. The SRH recombination

rate or lifetime can be inferred from device performance by using the above equations when it is known that the carrier lifetimes are SRH-limited, and assuming low-injection and mid-gap traps is equal to,

$$\tau_{SRH} = \frac{1}{A} = \frac{1}{\sigma v_{th} N_t}. \tag{2.15}$$

The basic SRH-driven dark current under forward bias was explained previously in Equation 2.9, and is related to $\tau_{SRH}$ by,

$$J_{02} \approx \frac{qW_D n_i}{2\tau_{SRH}}. \tag{2.16}$$

The cell's voltage depends on the dark current, which from Equation 2.16 is roughly inversely proportional to the SRH lifetime assuming an abrupt junction, low-level injection, and a mid-gap trap.

## 2.4 Deep-level Transient Spectroscopy

DLTS is a form of defect spectroscopy that is widely used to identify and characterize electrically active defects in a semiconductor. It was pioneered in 1974 by D. V. Lang at Bell Labs [56] and has since been used to electronically identify and characterize the common deep-levels or 'traps' caused by lattice defects in Si, GaAs, and many other semiconductor crystals. It is often used for point defects, but has been applied to boundary and threading defects, as well [57, 58]. Among some of the defects it has characterized are the gold donor and acceptor states in silicon [59], and the defect-donor (Dx) recombination center in AlGaAs [60].

Generally, DLTS has the following requirements material requirements: 1. Sufficient material quality and fabrication ability to create a Schottky or p-n junction diode. 2. The diode depletion region is well-behaved and understood and its width can be modulated by a change in magnitude of the reverse bias. 3. The particular defect concentration is high enough to cause a measurable change in the diode capacitance, typically $10^{-5}$ times the doping concentration is the minimum [48].

The experimental procedure of DLTS begins with fabrication of a p-n or Schottky diode.

DLTS is a measurement of capacitance transients, and the capacitance that is measured is the junction capacitance. The is the capacitance formed across the junction depletion region as a result of dipole formation across the junction from the ionized dopant atoms. The drift field that forms depletes the region of carriers leading to dielectric-like conductance. The steady-state junction capacitance can be modeled as a parallel plate capacitor,

$$C = \frac{\varepsilon A}{W_d}, \tag{2.17}$$

where $C$ is the junction capacitance, $\varepsilon$ is the semiconductor permittivity, and $W_d$ is the depletion width, which for a p-n junction is,

$$W_d = \sqrt{\frac{2\varepsilon}{q}\left(\frac{1}{N_a}+\frac{1}{N_d}\right)(V_{bi}-V_a)}. \tag{2.18}$$

In Equation 2.18, $q$ is the elementary charge, $N_a$ is the acceptor density in the p-type semiconductor, $N_d$ is the donor density in the n-type semiconductor, $V_bi$ is the built-in voltage of the junction, and $V_a$ is the applied bias.

From Equations 2.17 and 2.18, it is apparent that the junction capacitance is a function of the applied bias. A change in the applied bias leads to a change in the voltage drop across the junction and a change in the depth of the drift field into the semiconductor on either side of the junction. In DLTS, the junction capacitance is perturbed from steady-state by applying a bias pulse. By switching between one applied bias to another the depletion region will expand or contract. However, the change in depletion width is not instantaneous because the carriers in the region require a finite amount of time to react to the applied potential. While free carriers react too quickly (picoseconds or less) to measure, thermal emission of carriers from deep-level trap states in the depletion region is a much slower process. This slow emission from traps in the depletion region leads to the capacitance transient that is measured by DLTS (see Figure 2.7).

A general DLTS procedure begins with a Schottky diode or a one-sided p-n diode from the material to be tested. The 'steady-state' reverse bias, $V_r$, is applied corresponding to the first diagram in Figure 2.7. Next, the voltage pulse is applied such that $V_p > V_r$. The width of the

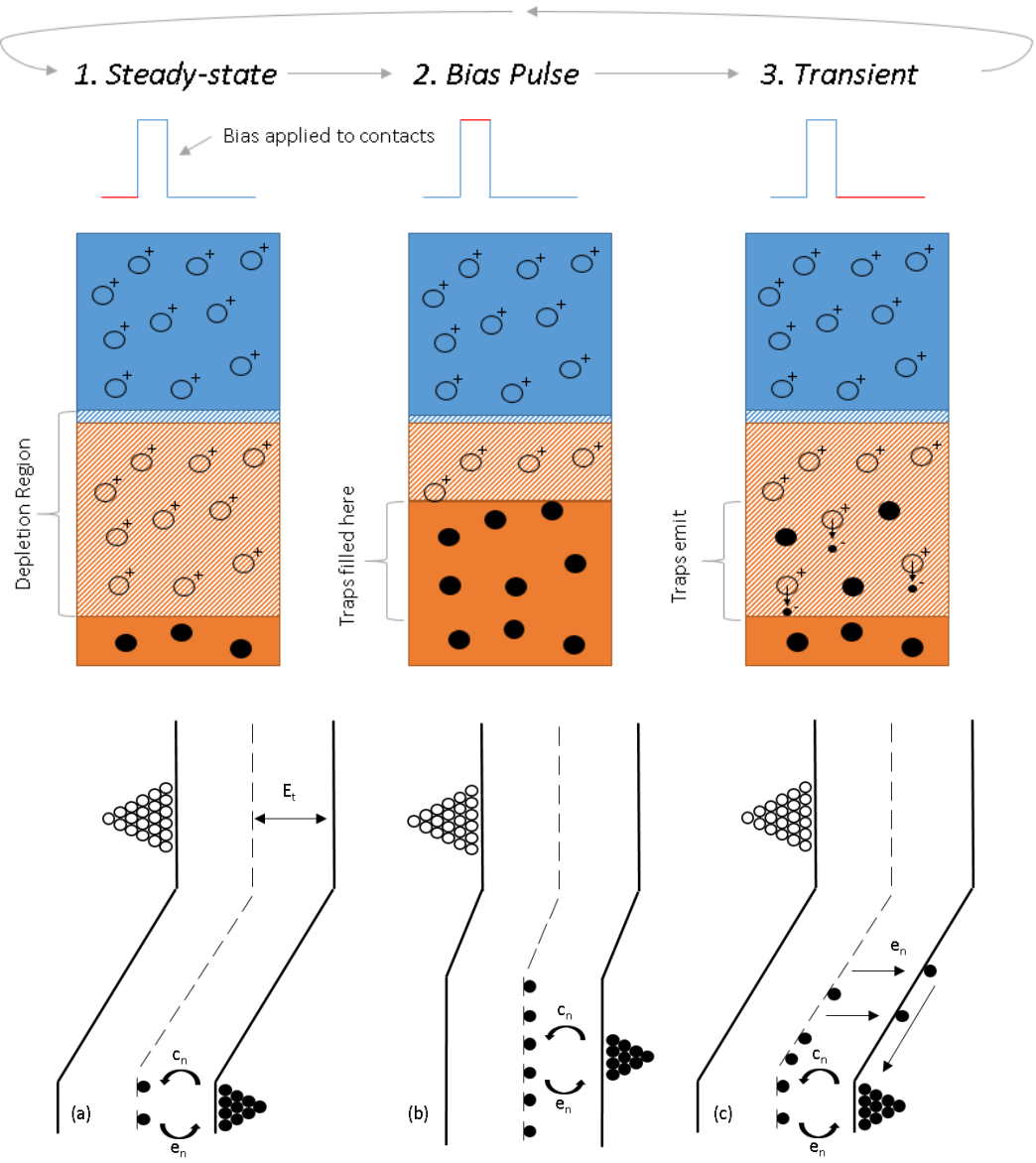


Figure 2.7: The three stages of the applied bias and the trap filling/emission behavior during each stage. From left to right: a) Behavior under steady-state reverse bias. b) Voltage pulse allows traps to be filled. c) Pulse ends and filled traps thermally emit carriers causing capacitance transient. From top to bottom: Shape of the voltage pulse applied to the contacts, spatial diagrams of the depletion region and trap behavior, and band diagram representation of the same depletion region and trap behavior.

voltage pulse must be long enough in time to allow the deep-levels to trap carriers that have diffused into the previously-depleted region (second diagram of Figure 2.7). Once the traps are filled with carriers, the steady-state reverse bias is restored (the pulse ends) and carriers will emit from the traps and the drift field will remove them from the depletion region, leading to the measurable transient (third diagram of Figure 2.7). In conventional DLTS, this process

is repeated and the capacitance transient is processed as a function of temperature in order to extract the trap parameters of activation energy, capture cross-section, and trap density.

A simple capacitance transient from a single trap level can be modeled using exponential decay,

$$C(t) = C_\infty + \Delta C_0 \exp(-e_n t), \tag{2.19}$$

where $C_\infty$ is the steady-state capacitance and $\Delta C_0$ is the amplitude of the transient. The exponential decay rate here is the carrier emission rate, which for electrons ($e_n$) and holes ($e_p$) are,

$$e_n = \sigma_n v_{n,th} N_c \exp -\frac{E_c - E_t}{k_B T}, \tag{2.20a}$$

$$e_p = \sigma_p v_{p,th} N_v \exp -\frac{E_t - E_v}{k_B T}, \tag{2.20b}$$

where $N_c$ and $N_v$ are the density of states in the conduction and valence bands, respectively.

The emission rates in Equation 2.20b can be derived from Fermi statistics for trap occupancy as a function of temperature and the principle of detailed balance. They indicate that emission rate is a function of temperature, and this relationship is taken advantage of in conventional DLTS to extract trap parameters. Rearranging leads to $\ln(T^2/e_n)$ as a linear function of $1000/T$ with activation energy and cross-section determinable from slope and and intercept, respectively,

$$\log\left(\frac{T^2}{e_n}\right) = \frac{E_c - E_t}{1000 K_B}\left(\frac{1000}{T}\right) + \log\left(\frac{1}{\gamma_n \sigma_n}\right), \tag{2.21a}$$

$$\log\left(\frac{T^2}{e_p}\right) = \frac{E_t - E_v}{1000 K_B}\left(\frac{1000}{T}\right) + \log\left(\frac{1}{\gamma_p \sigma_p}\right), \tag{2.21b}$$

where $\gamma$ is a collection of constants that depend on the effective mass of the carrier and properties of the bandgap. To obtain the slope and intercept, the emission rate at a number of temperatures must be determined. The capacitance meter will output time-series data that should roughly follow the form of Equation 2.19 for a given temperature. This data can be fitted to the model using standard curve fitting, however, if more than one defect is present the model will fail to represent the data accurately. A Laplace transform of the data is a more

effective approach, but this is numerically a difficult problem and requires very high signal-to-noise (SNR) ratio. The proven technique, definitive of conventional DLTS, is to use a filter with a weighting function, $W$,

$$S_{out} = \frac{1}{t_c}\int_{t_d}^{t_d+t_c} W(t,e_n)S_{in}(t)dt \tag{2.22}$$

where $t_d$ is the starting time of the filter and $t_c$ is the duration. Typically, $t_c \approx 2/e_n$ with a fixed ratio of $t_d/t_c \approx 0.05$, though the optimal values change depending on the choice of weighting function [61].

Many DLTS weighting functions have been developed but the one used most in this work is the shifted exponential,

$$W(t,e_n) = \exp\left(\frac{2[t-t_d]}{t_c}\right) + [\exp(-2)-1]/2, \tag{2.23}$$

where $W$ is a function of $e_n$ through the choice of $t_c$. The main point is that the weighting function in Equation 2.23 is chosen by the experimentalist to have a pre-determined, semi-arbitrary emission rate. This exponential with a known emission rate constant (sometimes 'rate window' is used) is then multiplied by the measured transient data and integrated, as in Equation 2.22, and a maximum $S_{out}$ occurs when the emission rate of the data matches the emission rate constant of the weighting function. To find this maximum, the temperature of the sample is swept to alter the thermal emission rate of the measured data. The DLTS spectra itself is $S_{out}$ as a function of temperature, where the peaks indicate a known emission rate at a known temperature, and these values are used to create a single data point in the Arrhenius plot of Equation 2.21b. To find more data points to create a line, the same measured data is filtered by more weighting functions of different pre-determined emission rate constants.

Equations in 2.21b assume that there is no temperature-dependence of the capture cross-section, when often this dependence will exist. If the cross-section changes with temperature, the capture cross-section should be determined by other methods, and the extracted activation energy will be a sum of the capture cross section activation energy, $\Delta E_\sigma$, and the trap activation energy. Nevertheless, the sum is still valid for trap identification and this is the

value that is typically reported, even if it may not represent the true trap energy level.

The final trap parameter, $N_t$, is not found by the Arrhenius plot but by the height of the peaks on the spectrum,

$$\frac{\Delta C_0}{C(\infty)} \approx \frac{N_t}{2N_d}. \tag{2.24}$$

The trap density can be found from the doping, the steady-state capacitance, and the total amplitude of the transient. An assumption made in the derivation of Equation 2.24 was that all traps in the depletion region are filled at $t = 0$ and emit their carriers to become empty at $t = \infty$. This is only valid for a large reverse bias where the depletion width is much larger than the transition region, $\lambda$. This region is due to the interaction between $E_t$, $E_F$, and band bending. During the bias pulse, there is still some band bending and the traps near the depletion edge are never filled. The never-filled traps are within $x_1 = x_0 - \lambda$ of the junction where $x_0$ is the depletion width during the pulse. After the pulse is over, the traps near the edge of the depletion layer remain filled as $E_t < E_F$ over the $\lambda$ region. If $W_d$ is the steady-state depletion width, then traps only emit carriers if they are within $x_2 = W_d - \lambda$ of the junction. Therefore, the trap density must be corrected to be a density over $x_1 < x < x_2$ rather than over $W_d$.

The corrected trap concentration can be found by introducing a position-dependent charge density to the derivation of Equation 2.24, resulting in,

$$\frac{\Delta C_0}{C(\infty)} = \frac{1}{2}\frac{x_1^2 - x_2^2}{W_d^2}\frac{N_t}{N_d}. \tag{2.25}$$

In summary, DLTS is a technique to detect the electronic properties of small yet numerous point-like defects in a semi-conductor crystal lattice. It requires fabrication of a diode and material quality sufficient to pulse a reverse bias without excessive dark current. The technique is capable of identifying or characterizing majority and minority deep-level states by their activation energy, carrier cross-section, and density.

## 2.5 Device Simulation Principles

There are two common approaches to solar cell device modeling. One is by self-consistently solving the Boltzmann transport equation (BTE) and Poisson's equation, while the other uses

the thermodynamic principle of detailed balance. This work makes use of the former. The detailed balance model is popular, however, the thermodynamic approach has some inherent disadvantages and overestimates the efficiency of real devices as a result. For example, the model by Miller *et al.* [62] had no concept of diffusion length, and thus the thickness of the cell could be increased without losing collection efficiency. The effect of this can be seen in the $J_{SC}$ and efficiency data, which increase for all cells with cell thickness even up to 100 µm. This is an unrealistic diffusion length for direct-bandgap material.

The BTE-based device simulator Synopsys Sentaurus is used throughout this dissertation to model III-V diodes. The model begins with the BTE (in one dimension for simplicity) [63–65],

$$\frac{\delta f}{\delta t} + v\frac{\delta f}{\delta x} + \frac{qE}{m^*}\frac{\delta f}{\delta p} = -\frac{f - f_0}{\tau}, \tag{2.26}$$

where $f$ is the distribution function defining the probability of finding a particle within the small distance $dx$ and within the small momentum-space $dp_x$ at time $t$. The second term in Equation 2.26 includes the effect of diffusion, while the third is the effect of an external electric field, $E$. The right hand side is from carrier colliding and indicates that during some time after a collision, $\tau$, the distribution is compelled to move back towards the equilibrium distribution, $f_0$.

The method of moments can be applied to the BTE to obtain conservation rules in carrier count (0th moment), carrier momentum (1st moment), and carrier energy (2nd moment). The carrier conservation rule becomes the continuity equations,

$$\frac{\delta n}{\delta t} + \frac{\delta (nv)}{\delta x} = G_n - R_n, \tag{2.27}$$

$$\frac{\delta p}{\delta t} - \frac{\delta (pv)}{\delta x} = G_p - R_p, \tag{2.28}$$

where $G$ and $R$ are the generation and recombination rates, respectively.

The second moment results in the drift-diffusion equations, or more generally the current transport equations. The full current density equations (in three dimensions) used by

Sentaurus are [66],

$$\mathbf{J_n} = \mu_n \left( n\nabla E + kT_n \nabla n + f_n^{\text{td}} kn\nabla T_n - [3/2]nkT_n \nabla \ln m_n \right), \tag{2.29}$$

$$\mathbf{J_p} = \mu_p \left( p\nabla E + kT_p \nabla p + f_p^{\text{td}} kp\nabla T_p - [3/2]pkT_p \nabla \ln m_p \right), \tag{2.30}$$

where $f_{n:p}$ are the carrier thermal diffusion coefficients. The first term on the right is the drift contribution, the second is from diffusion, the third is from carrier thermal gradients, and the fourth is due to spatial difference in the effective mass.

Another set of flux equations for carrier energy is used by Sentaurus but are not shown here due to their complexity. These fluxes keep track of energy destroyed and created by carrier generation and recombination and also account for any hot carrier effects. A more rigorous solution for the BTE and an example of the energy density equations are given in Appendix B.

Besides the above, another equation is required to solve the device model. This is Poisson's equation, which is used to calculate the external field, $E$, used in all the other equations. Maxwell's equations are the fundamental equations of classical electromagnetism. In differential form for external sources in a vacuum [67], they are,

$$\nabla \cdot \varepsilon \mathbf{E} = \rho, \tag{2.31}$$

$$\nabla \cdot \mathbf{B} = 0, \tag{2.32}$$

$$\nabla \times \mathbf{E} + \frac{\delta \mathbf{B}}{\delta t} = 0, \tag{2.33}$$

$$\nabla \times \mathbf{B} - \frac{\delta \mathbf{E}}{c^2 \delta t} = \mu_0 \mathbf{J}, \tag{2.34}$$

where $\mathbf{B}$ is the magnetic field, $\rho$ is the charge density, and $\varepsilon$ is the permittivity.

The electrostatic potential, $V$, is defined by,

$$\mathbf{E} = -\nabla V. \tag{2.35}$$

In a semiconductor, the charge density, $\rho$, can be expressed as a sum of the free carriers and

ionized lattice sites,

$$\rho = q(p - n + N_a - N_d). \tag{2.36}$$

The equations above can be combined to give Poisson's equation for a semiconductor,

$$\nabla^2 V = \frac{q}{\varepsilon}\left(n - p + N_A^- - N_D^+\right). \tag{2.37}$$

The continuity equations (B.13), the current equations (2.29), the energy equations (not shown), and Poisson's equation (2.37) represent a set of equations that must be solved by the simulator self-consistently. A cursory solution is as follows. Begin by discretizing the continuity equations (containing the current and energy flux equations) by a method such as finite differences on a fine mesh with spacing below the Debye length [68]. Then, Poisson's equation is solved for each mesh point using initial guesses for the carrier densities (typically the given doping concentration). The resulting potentials are inputted into the continuity equation to solve for the currents, energies and new, more accurate, carrier densities on each grid point. In an iterative scheme such as Grummel's method, the new carrier densities are used to re-compute Poisson's equation and the new potentials are again used to recompute the currents, energies and carrier densities, and so on. This is repeated until the residuals are reduced below a set tolerance defined by the convergence condition. The convergence condition sets the desired accuracy, where greater accuracy requires more computational power. For current-voltage data, an applied voltage term can be added to Poisson's equation.

Carrier generation and recombination rates are incorporated into the simulation via the continuity equation, *i.e.* the right side of Equation 2.27. Carrier generation can occur via thermal generation, electrical injection via the contacts, or optical injection. Optical injection, which is due to absorption of a photon above the bandgap, is clearly a critical aspect of simulating solar cells. To calculate the optical generation rate at each mesh an additional electromagnetic simulation is required and this will be referred to as the the optical simulation step of the solar cell model. The typical optical model available to Sentaurus is the transfer matrix method (TMM), which uses an analytical solution for Maxwell's equations across a series of material interfaces and is derived similarly to the Fresnel Equations.

The BTE is a classical formulation, but quantum mechanical transport models are available in Sentaurus. These are used in tunneling simulations but are not critical to this work and are not covered in detail [69].

## 2.6 State-of-the-art III-V Multi-junction Solar Cells

Currently, the space industry is powered by all-lattice-matched 3-J $In_{0.48}Ga_{0.52}P$/GaAs/Ge cells, where the Ge junction is created via thermal diffusion of dopants into a Ge substrate prior to epitaxial growth of GaAs and InGaP subcells. This combination of materials has come to the forefront of solar power in space despite not having the highest possible efficiency because it is currently the easiest to grow and fabricate within the tier of highest efficiency cells. The specific choice of materials for this cell - Ge, GaAs, and InGaP - can be explained by a limited availability of substrate types, a limited number of well-developed III-V materials that can be grown epitaxially on said substrates, and the requirement that the chosen materials have a bandgap combination that is well-suited to the solar spectrum. The InGaP/GaAs/Ge cell is grown on a Ge substrate (which itself is a subcell), the InGaP and GaAs subcells are lattice-matched to Ge (thus they can be grown strain-free), and the bandgap combination (1.84 eV, 1.44 eV, 0.73 eV) has been proven to be capable of high efficiency (over 30% AM0 in full production by Spectrolab [70]).

However, it is well-understood that the InGaP/GaAs/Ge bandgap combination does not result in the highest possible efficiency for a triple-junction cell [6]. The Ge subcell is not current-matched to the top cells (the bandgap is too low) so there is some voltage and therefore efficiency to be gained with other material combinations. Furthermore, it is clear that a multi-junction cell with four or more junctions could also outperform the Ge-based triple-junction. Why, then, are these materials used? The answer can be found in the lattice constant vs. bandgap chart in Figure 1.1. This chart visualizes the three considerations outlined in the previous paragraph. Some available substrates are Si, Ge, GaAs, InP, and GaSb. The materials available to be grown on each substrate without introducing strain can be found by matching the lattice constant to the substrate. As seen, a substrate with well-developed material that spans the desired direct bandgap range (roughly 0.65 eV to 2.1 eV) does not currently exist.

Faced with this realization, the Ge-based cell was a straightforward decision despite not having any material options between 0.70 eV and 1.44 eV. Chapter 3 explores the possibility of a lattice-matched 3-J cell using InP as the substrate.

Other approaches exist beyond standard lattice-matched epitaxial growth that attempt to make better bandgap combinations possible. The first challenge with other approaches is to make the theoretical efficiency boost a realistic possibility, and this is done by somehow combining lattice-mismatched material without introducing efficiency-limiting defects. The second challenge is to make the efficiency boost worth the extra cost caused by the increased manufacturing complexity. The most promising next-generation technology is the inverted metamorphic (IMM) cell, where lattice-mismatched subcells with bandgaps better-matched to the solar spectrum are grown through the use of compositionally graded buffer layers [71–73]. Growth of a typical 3-J IMM starts with a GaAs (lattice constant 5.66 Å) substrate and lattice-matched GaInP and GaAs top and middle cells, and, because a well-developed lattice-matched bottom cell is not available, a several micron-thick transparent metamorphic buffer is grown to grade the lattice constant to 1.0 eV $In_{0.3}Ga_{0.7}As$ (5.77 Å) [71, 72]. The buffer is a stepped sequence of $Ga_xIn_{1-x}P$, where each step is grown with conditions that cause partial relaxation of the compressive stress and with the intention of reducing the threading dislocation density (TDD) after the grade [71, 74]. However, not all threading dislocations can be eliminated and reduction of the TDD is an active area of research [75, 76]. The ability to grow lattice-mismatched material increases and the bandgap parameter-space and this has allowed the IMM to achieve record efficiencies. In 2013, Sharp Corporation reported an efficiency of 37.7% under 1-sun AM1.5g and 43.5% under 306.3-sun AM1.5G illumination with the triple junction IMM approach [72]. Recently, the focus of IMM technology has shifted to a four-junction (4-J) design with InGaP/GaAs/InGaAs(1.0 eV)/InGaAs(0.7 eV), with a second metamorphic grade from 1.0-eV InGaAs to 0.7-eV InGaAs (5.88 Å) [73, 76, 77]. The 4-J IMM design has achieved efficiencies as high as 43.8% under concentration [73]. Chapter 5 is an investigation into an alternate lattice-mismatched growth technique that would give a potential multi-junction cell buffer-free access to both the GaAs and GaSb lattice constants.

# Chapter 3

# Native Traps in InAlAs and InAlAsSb

## 3.1 Summary

A novel material for solar cells, InAlAsSb, would enable a high-efficiency and all-lattice-matched triple-junction solar cells to be grown on InP substrates. Diodes made of InAlAsSb and lattice-matched ternary InAlAs were grown by MOCVD, fabricated, and tested. Dark current and capacitance testing, including DLTS, were performed to examine the trap profile of the new material.

This chapter is organized into two main parts. First, the InAlAsSb samples are addressed with InAlAs results included as a basis for comparison. Second, a section dedicated InAlAs alone, comparing different epitaxial growth methods and different MOCVD growth precursors. There are five main topics:

1. InAlAs and InAlAsSb sample growth and fabrication.
2. InAlAsSb J-V and capacitance vs. voltage (C-V) results.
3. InAlAsSb DLTS results.
4. InAlAs Schottky diodes dark current and DLTS.
5. InAlAs solar cell dark current and DLTS.

## 3.2 Motivation & Background

### 3.2.1 Motivation

The InP material system gained interest as a pathway to high efficiency multi-junction solar cells at competitive costs [6, 7, 78]. Simulations by Gonzalez *et al.*indicated that, for air-mass

1.5 direct (AM1.5D) conditions, a 3-J cell could achieve record conversion efficiencies with a top sub-cell at 1.74 eV, a middle subcell of 1.17 eV, and a bottom subcell with bandgap 0.70 eV (Figure 3.1) [6]. This is possible with an all-lattice-matched cell grown on InP substrates. As shown in Figure 3.2, realization of this cell would require the quaternary material InAlAsSb as the top subcell. Lattice-matched InGaAlAs or InGaAsP would be used for the middle subcell material, while the 0.70 eV bottom subcell could be obtained with strain-balanced InGaAs quantum well layers [7].

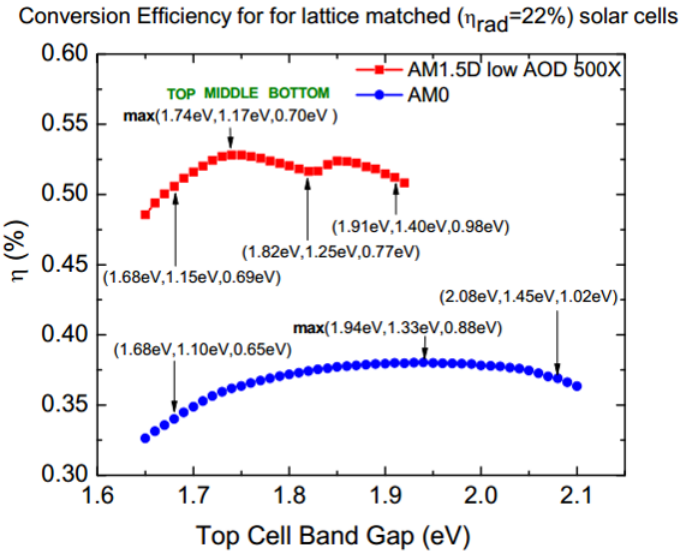


Figure 3.1: Highest triple-junction efficiencies for both AM0 and concentrated AM1.5D as a function of topcell bandgap. The other two bandgaps were allowed to float to get the maximum efficiency for each topcell bandgap. *Reprinted with permission from* [6].

Previous works with InP-based cells have used the developed and lattice-matched $In_{0.52}Al_{0.48}As$ as the top-junction, but this material has a bandgap (1.45 eV) that is too far below that of the ideal top subcell. As there is no familiar material that has the ideal 1.74 eV bandgap and is also lattice-matched to InP, the novel quaternary $In_{0.22}Al_{0.78}As_{0.74}Sb_{0.26}$ (bandgap 1.8 eV) had to be developed to fulfill this role [6]. This chapter focuses on the fabrication and testing of devices using InAlAsSb, the stoichiometry of which was near this stated target.

If the material could be grown into successful solar cells, then an all-lattice-matched InP-based 3-J could achieve higher efficiencies than conventional III-V 3-Js and without the need

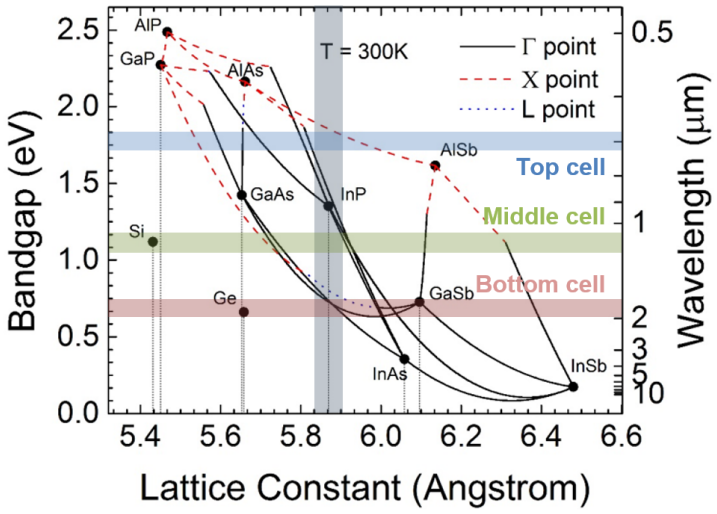


Figure 3.2: A chart of lattice constant vs. bandgap with highlighted ideal bandgap ranges for top, middle, and bottom subcells [7]. The grey vertical line corresponds to the InP lattice constant.

for a growth-intensive and expensive graded buffer. The cost of the InP substrate could be mitigated by using an epitaxial lift-off (ELO) process and re-using substrates.

### 3.2.2 Background

A consequence of the novelty of InAlAsSb on InP is the relatively unknown parameter space and a lack of widely-validated growth procedures. A few research groups have studied the growth of lattice-matched material by MBE. Lumb *et al.* attempted to make photovoltaic devices from $In_{0.42}Al_{0.58}As_{0.91}Sb_{0.09}$ grown at 450 ℃, and settled for Schottky diodes created with Ti and Pt Schottky contacts. From ellipsometry, they found that the bandgap was 1.5 eV, however, the material radiatively emitted photons at considerably lower energies, and l long defect tail was found in the absorption spectrum [79]. Annealing the material raised the emission energy from 1.33 eV to 1.42 eV, but did not eliminate the Urbach tail completely [80]. A photoluminescence (PL) study of other lattice-matched compositions of InAlAsSb found similarly low peak energy, but lowering the growth temperature and increasing excitation laser power density was able to raise the emission closer to the expected value [81]. The suspected cause was compositional variations, and atomic probe topography found In- and Sb-rich nanometer-scale volumes that may have been acting as radiative recombination centers with lower bandgap than the nominal material [40].

As for MOCVD, Yokoyama *et al.*performed what they believed to be the first study of growth rates of InAlAsSb on InP [82]. They discovered that, when injecting the group III and V precursors simultaneously, the growth rates decreased as trimethylantimony (TMSb) flow increased. From this, they hypothesized that this was due to Sb atoms on the surface stabilizing the aluminum precursor, trimethylaluminum (TMAl), in its alkyl form.

Attempts to create a successful epitaxial growth of InAlAsSb on InP have thus far seen significant hurdles, such as those found by Yokoyama *et al.*, due increased complexity of growing a relatively unknown quaternary alloy. Among the many concerns are phase segregation (see Section 2.3) caused by a miscibility gap that favors formation of InSb [40], which may lead to increased SRH recombination and poor MCDL. The material quality of the InAlAsSb top subcell is essential because poor quality present in just a single junction will have a limiting effect on the conversion efficiency of the entire cell [83]. In order to create a competitive multi-junction cell, the ideal growth condition leading to low trap densities must be found.

## 3.3 InAlAsSb Sample Growth and Diode Fabrication

Growth of $In_{0.22}Al_{0.78}As_{0.74}Sb_{0.26}$ by MOCVD proved to be a challenge [84, 85]. Initial attempts began with $In_{0.52}Al_{0.48}As$, grown with trimethylindium (TMIn), TMAl, and arsine ($AsH_3$), as a template but could not incorporate Sb effectively using TMSb. A gas-phase reaction was suspected to be depleting Sb before it could reach the substrate. To avoid this, the Al and As precursors were substituted with the alternate precursors tritertiarybutylaluminum (TTBAl) and tertiarybutylarsine (TBAs), respectively, and the growth temperature was lowered. Rather than begin with the lower bandgap lattice-matched ternary InAlAs and attempting to incorporate Sb, the growth template was switched to the alternate lattice-matched ternary, $AlAs_{0.46}Sb_{0.54}$, and addition of In was attempted via TMIn. Incorporation of In was possible by increasing the V/III ratio from 1-2 used to grow AlAsSb to 5.2. Figure 3.3 illustrates the difficulty with Sb incorporation with the combination of TMAl/$AsH_3$ precursors and that this problem was resolved by switching to TTBAl/TBAs and lower growth temperatures.

As XRD was only able to determine the lattice constant, and there exists a wide range of

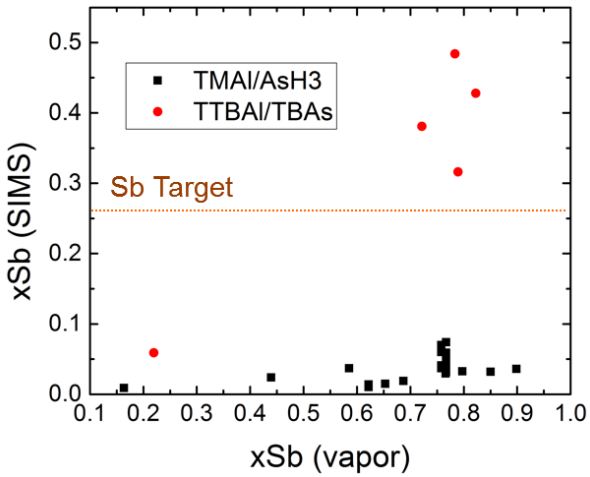


Figure 3.3: Incorporation of Sb for various InAlAsSb growths. The line represents the target composition to achieve the desired bandgap and lattice constant (matched with InP). *Figure by Dr. Michael Slocum*

InAlAsSb that is lattice-matched to InP, other methods were required to determine the stoichiometry of the epitaxial growth. SIMS was turned to as the primary technique for finding material composition. An example of the SIMS results can be seen in Figure 3.4. To make more effective use of and better comparisons from SIMS, several epitaxial layers of InAlAsSb, separated by InGaAs, were grown on the same substrate but with different growth conditions.

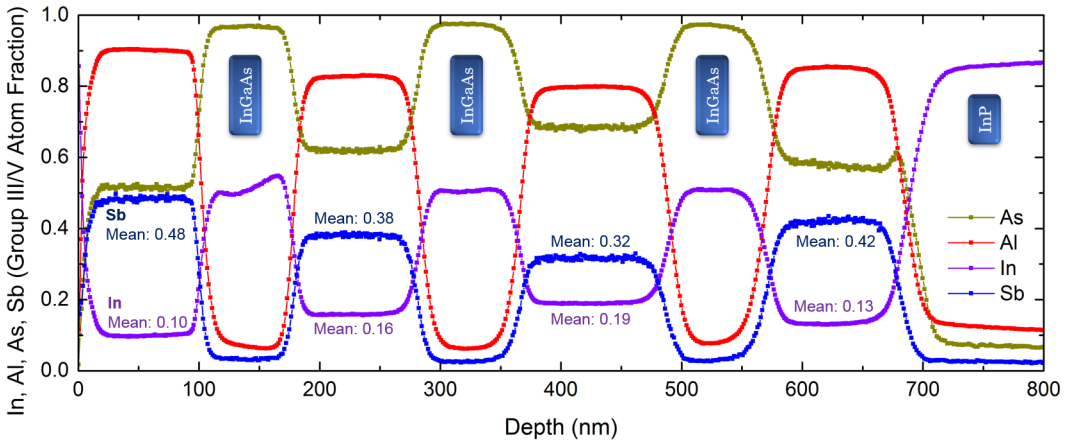


Figure 3.4: SIMS results of an InAlAsSb composition-calibration sample showing the stoichiometry as a function of sample depth. This sample had 4 InAlAsSb layers with different stoichiometry, separated by 3 InGaAs buffer layers and grown on an InP substrate. The In and Sb compositions of the 4 layers are labeled.

Of the many InAlAsSb growths, the most promising sample with composition closest to

the target was made into Schottky diodes for DLTS and other electronic testing. This sample was grown with conditions confirmed by SIMS to produce $In_{0.19}Al_{0.81}As_{0.72}Sb_{0.28}$ using TMIn/TTBAl/TBAs/TMSb precursors. This material was slightly strained as it was not perfectly lattice-matched to InP. In addition, a control sample consisting of a lightly n-doped InAlAs layer was grown for fabrication of Schottky diodes. All samples were grown epitaxially using a 3x2" Veeco D125LDM multi-wafer MOCVD reactor. Precursors used for doping n-type and p-type materials were disilane ($Si_2H_6$) and diethylzinc (DEZn), respectively. Samples were grown on 350 µm thick S-doped InP substrates. The growth temperatures and V/III ratios of the samples are shown in Table 3.1, and other growth information is available in Slocum *et al.* [84].

Table 3.1: Select growth parameters for the Schottky diode samples used in the InAlAsSb DLTS experiment.

| Material | Growth Temperature ($T_g$) | V/III Ratio |
|---|---|---|
| InAlAs | 610° C | 100 |
| InAlAsSb | 520° C | 5.24 |

The fabricated sample structures are shown in Figure 3.5. The InAlAs Schottky diode sample consisted of a 1500 nm-thick lightly Si-doped n-type InAlAs grown on top of a thin InP buffer layer [86]. The InAlAsSb was another Schottky diode device with a 750 nm-thick unintentionally doped (*uid*) InAlAsSb layer on an undoped buffer layer. For both samples, an alloyed back contact of Ge/Au/Ni/Au was deposited and then annealed at 390° C for 90 s. Schottky contacts were created from Pd/Au and Pt/Au (30/300 nm) the InAlAs and InAlAsSb samples, respectively.

## 3.4 InAlAsSb Diode Testing and Analysis

Electrical characterization was performed using an Agilent B1500A Semiconductor Analyzer. Dark J-V curves for the InAlAs and InAlAsSb diodes are shown in Figure 3.6. Most apparent was that the InAlAsSb diode had poorer rectification ratio than the InAlAs. To quantitatively compare the two diodes, the dark J-V data were fitted using the diode equation using nonlinear least-squares fitting (Equation 2.6, see Appendix A for fitting software). Generally, only

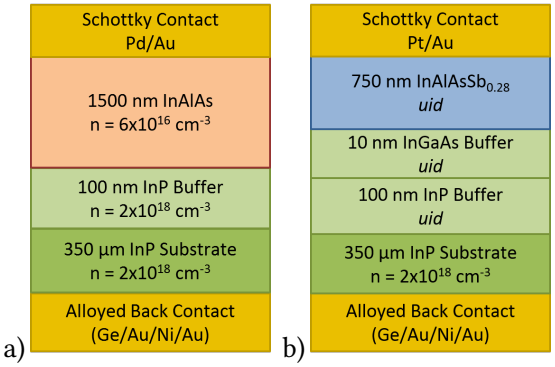


Figure 3.5: Layer structure for the fabricated a) InAlAs Schottky diode and b) the InAlAsSb Schottky diode.

the forward bias data could be fit to the model as the reverse bias behavior of the diodes, the InAlAsSb especially, demonstrated carrier transport outside of the typical drift or diffusion mechanisms derived in the ideal diode equation. The mechanisms could have been trap-assisted tunneling (TAT), as this depends on electric field which increases under reverse bias [87]. The procedure followed for fitting was to first examine if there was ohmic behavior near the zero-bias point. If there was, $R_{Sh}$ was used as a fit parameter. If no ohmic behavior was present, the shunt part of the model was omitted. Next, the ideality factor $n_1$ was set to 1, while $n_2$ was allowed to float as a fit parameter. If an $n = 1$ region could not be fit, then a single-diode model with $J_{02}$ was used instead. Excellent fits were obtained for both diodes this way.

The dark J-V fit results are shown in Table 3.2. The InAlAsSb sample did not have a $J_{01}$ region (diffusion current over the Schottky barrier), but was limited by $J_{02}$ (trap-assisted recombination in the depletion region) with an ideality factor of 1.6. The relatively high $J_{02}$ was indicative of higher trap concentration in the novel material (see Equation 2.9). This diode also exhibited low $R_{Sh}$. As for the InAlAs Schottky diode, it turned on faster and at a later bias than the InAlAsSb diode despite its bandgap disadvantage. This was because as it was mostly $J_{01}$-limited and it was not shunted. It could be fit with two diodes but both ideality factors were close to 1. Thus the control diode was well-behaved for a Schottky diode, which is a device that is expected to have higher dark current due to the reduced effectiveness of the Schottky barrier to carrier diffusion compared to a p-n junction.

Listed in Table 3.2 are dark current fit parameters for an MBE-grown InAlAsSb Schottky diode from Lumb *et al.*[79], where the dark current was three orders of magnitude lower than the MOCVD-grown diode and had ideality of 1.29 and much better rectification ratio. The composition of the MBE diode had a lower target bandgap (1.5 eV) than the MOCVD diode, so the comparison is not completely fair. However, the MBE diode had lower dark current than InAlAs, which was expected due to its higher bandgap, while the MOCVD-grown InAlAsSb dark current was higher. Both InAlAsSb diodes used Pt as the Schottky metal. The exact cause behind the poor rectification ratio, the ideality of 1.6, and the low shunt resistance in the MOCVD InAlAsSb are not known. Possible candidates besides SRH recombination are Schottky barrier tunneling, trap-assisted tunneling, surface states, or combinations of these. The MBE-grown InAlAsSb was found to have compositional variations due to a miscibility gap, with nanometer-scale InSb-rich regions, and the material's deficiencies were attributed to this problem [40]. The presence of these variations in the MOCVD-grown InAlAsSb is a potential explanation for the aforementioned problems seen in the MOCVD device.

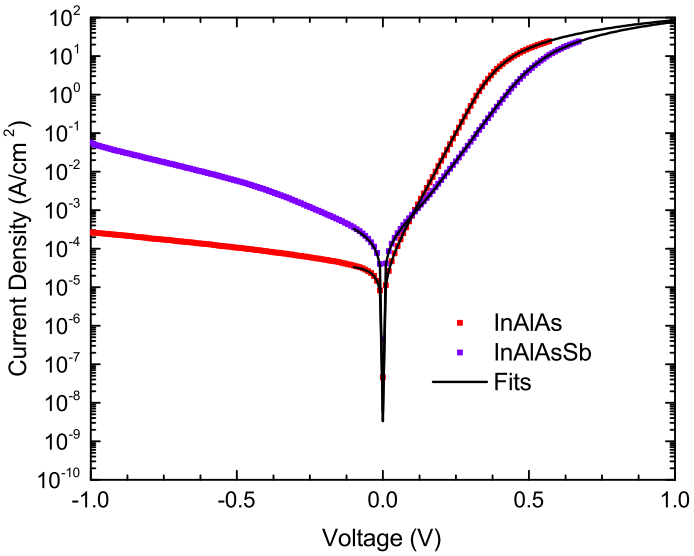


Figure 3.6: Dark J-V plots of InAlAsSb and InAlAs Schottky diode.

Table 3.2: InAlAsSb and InAlAs diode equation fit parameters.

| Diode | $J_{01}$ (A/cm$^2$) | $n_1$ | $J_{02}$ (A/cm$^2$) | $n_2$ | $R_S$ ($\Omega$·cm$^2$) | $R_{Sh}$ (M$\Omega$·cm$^2$) |
|---|---|---|---|---|---|---|
| InAlAs | $1.36\times10^{-6}$ | 1.00 | $2.65\times10^{-5}$ | 1.20 | 6.5 | >15 |
| InAlAsSb | N/A | N/A | $4.29\times10^{-5}$ | 1.60 | 5.2 | 0.35 |
| MBE $In_{0.42}Al_{0.58}As_{0.91}Sb_{0.09}$ [79] | N/A | N/A | $1.83\times10^{-8}$ | 1.29 | N/A | N/A |

C-V measurements were taken for both diodes from 0.0 V to -2.0 V in order to characterize diode quality and to extract doping concentrations. Figure 3.7 shows doping concentration vs. depletion width obtained from C-V measurements for the all samples. The average extracted doping concentrations were $5 \times 10^{16}$ cm$^{-3}$ for the InAlAs diode and $4 \times 10^{17}$ cm$^{-3}$ for the InAlAsSb diode. The InAlAs value was in good agreement with the target doping calibrated from Hall measurement. However, the InAlAsSb Schottky, which was not intentionally doped, had a higher-than-expected doping of $4-6\times10^{17}$ cm$^{-3}$. This is indicative of a high degree of anti-sites or substitutions by contaminants that act as unintentional donors [88]. High oxygen and carbon contamination in InAlAsSb was found by SIMS and this may have been the source of the doping [85]. The doping level may be compensated, as well, meaning that the total defects concentration could have been much higher than the doping concentration. The InAlAs doping value was roughly constant so that the doping concentrations was uniform within the depletion ranges chosen for DLTS. The InAlAsSb samples were not constant, which could be because the doping was not uniform or that the diode capacitance model used to calculate the capacitance did not apply well to these devices.

## 3.5 InAlAsSb DLTS Results

Conventional DLTS was performed on the InAlAsSb samples. Spectra were measured inside of a Janis ST-500-1-(3TX) cryostat using a SULA Technologies Deep Level Transient Spectrometer for sample temperatures in the range of 80-340 K [89]. The samples were reverse biased with the strategy of maximizing the depleted volume so that more traps could contribute to the signal. Samples were exposed to a filling pulse for 1 ms which ensured that all trap levels had sufficient time to capture carriers. To find the dependence of the emission

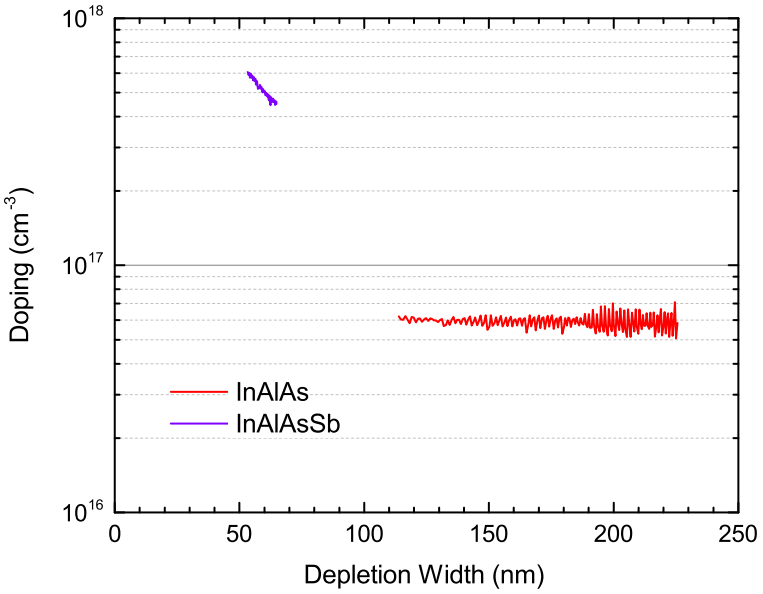


Figure 3.7: Doping concentration vs. depletion width for the InAlAs and InAlAsSb Schottky samples.

rates on temperature, capacitance transients were measured in 1 K steps using six different filters with exponential weighting functions of rate windows ranging from 4.3 ms to 215 ms. For each rate window, the temperature maxima and their corresponding ΔC values were recorded. An Arrhenius plot was created for 1000/T vs. $\ln(\tau T^2)$, where T was the temperature that corresponded to the maximum change in capacitance along the ΔC curve for a particular rate window. DLTS parameters were extracted from the Arrhenius fit line.

Figure 3.8a contains DLTS spectra found for a single rate window for InAlAs with a reverse bias of -2.0 V and a filling pulse to 0.0 V. The inset shows the Arrhenius plot of $\ln(T^2/e_n)$ vs. 1000/T with excellent fits. A majority carrier trap was found as indicated by the negative amplitude in the spectra and the observation that the Schottky diode is a majority carrier device. As a majority carrier trap in n-type material, the trap was concluded to be an electron trap. For InAlAs, a single peak was observed at ∼295 K. A summary of the extracted trap energies (referenced to the conduction band edge), the cross-section, trap density and the reported cause of the defects are shown in Table 3.3. A defect level at 0.57 eV below the conduction band was observed. A large trap cross-section indicates that this trap was an attractive trap for electrons, possibly with +1 charge state.

Three InAlAsSb traps were found from two different devices on the sample. The DLTS

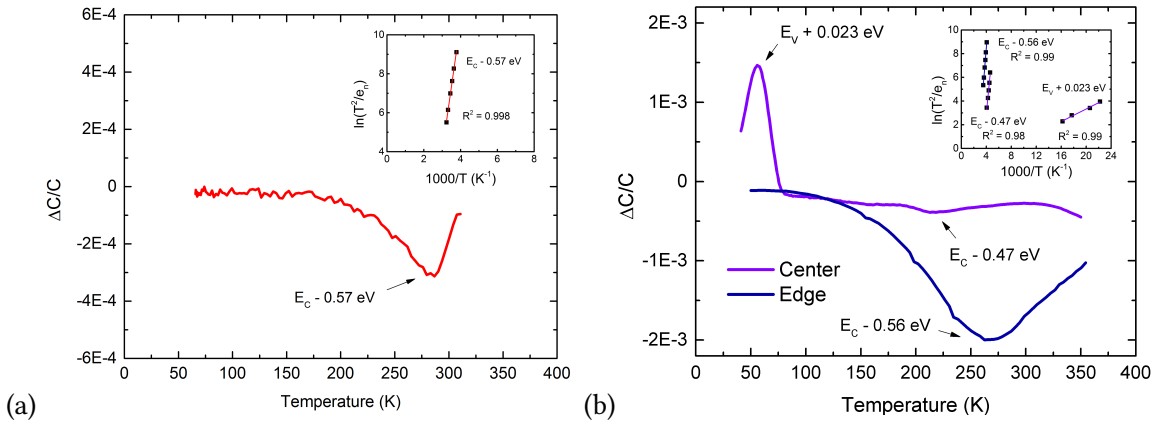


Figure 3.8: DLTS spectra for the (a) InAlAs and (b) InAlAsSb diodes. The Arrhenius plots for the detected traps are shown in the insets.

Table 3.3: DLTS results for the InAlAs and InAlAsSb samples.

| Label | $E_A$ (eV) | $\sigma$ (cm$^2$) | $N_T$ (cm$^{-3}$) | Type |
|---|---|---|---|---|
| InAlAs1 | $E_C - 0.57$ | $6 \times 10^{-14}$ | $5 \times 10^{13}$ | Electron |
| InAlAsSb1 | $E_V + 0.023$ | $5 \times 10^{-20}$ | $7 \times 10^{15}$ | Hole |
| InAlAsSb2 | $E_C - 0.47$ | $1 \times 10^{-14}$ | $6 \times 10^{15}$ | Electron |
| InAlAsSb3 | $E_C - 0.56$ | $3 \times 10^{-13}$ | $1 \times 10^{16}$ | Electron |

spectra are in Figure 3.8b. Different traps for different devices indicated that the growth was non-uniform across the sample. The device taken from the edge of the wafer had a minority carrier (hole) trap at 0.023 eV (repulsive cross-section) above the valence band and a majority carrier (electron) trap 0.47 eV (neutral cross-section) below the conduction band. Finding a minority carrier trap with conventional DLTS is rare for a Schottky diode (a majority carrier device), however, this behavior was observed in Schottky diodes for other materials and tends to only occur for very shallow traps [90, 91]. Near the center of the wafer, a different majority carrier trap was all that was found, which was at $E_C$ - 0.56 eV (attractive cross-section). The parameters are listed in Table 3.3. At around $1 \times 10^{16}$ cm$^{-3}$, trap concentrations were over two orders of magnitude higher in InAlAsSb than in InAlAs, which implied much lower carrier lifetimes according to Equation 2.15. These traps may have been responsible for the higher dark current and ideality factor seen in Figure 3.6 (see Equation 2.16).

The trap density for InAlAs was $5 \times 10^{13}$ cm$^{-3}$ for a deep electron trap 0.57 eV below the conduction band. According to Buchali *et al.*, oxygen-related traps of 0.52 eV and 0.75 eV in

InAlAs do not, in general, affect device performance [92]. This was confirmed by the mostly ideality-of-one behavior seen in the dark J-V result.

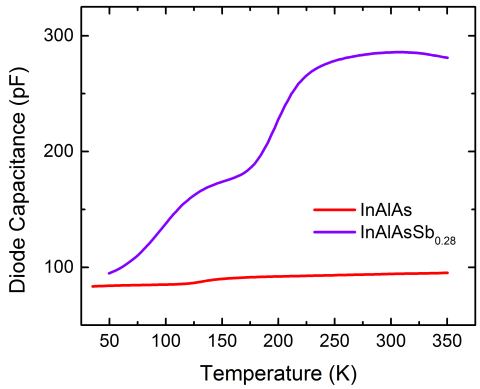


Figure 3.9: Steady-state capacitance as a function of temperature for the InAlAs and InAlAsSb Schottky diodes.

Steady-state junction capacitance vs temperature data was collected during DLTS scans and is shown in Figure 3.9 for the InAlAs and InAlAsSb Schottky diodes. The InAlAs diode capacitance was relatively well-behaved for DLTS, with a weak dependence on temperature except for one small section of sharper slope in the range of 125-150 K. The InAlAsSb diode, however, had two large increases in capacitance, first from 50-150 K, then again from 150-250 K. Increases in capacitance with temperature like this will occur when traps respond to the AC frequency used to probe the junction capacitance [48]. There are likely two traps of high concentration with 300 mV or less in activation energy. Admittance spectroscopy could be used to find and characterize these traps, as was done in Chapter 4.

## 3.6 InAlAs Schottky Diodes - Dark Current and DLTS

InAlAs has a bandgap similar to GaAs and is a potential subcell for an InP-based multi-junction solar cell [93]. Smith *et al.* published a 17.9% AM1.5G efficient cell in 2017 and predicted as high as 21.4% was possible with a few improvements [94]. For reference, the best on-substrate GaAs cell reported was 26.1% AM1.5G efficient [95], but InAlAs has not been developed nearly as much as GaAs. Here, an extensive study of InAlAs photodiode dark current and trap states was possible since many InAlAs samples were grown as a comparison to quaternary InAlAsSb.

The first two InAlAs samples were Schottky diodes grown with TMAl as the aluminum precursor (see following section for precursor information) and fabricated specifically for DLTS. One sample was *uid* and one n-type, and both were on n-InP substrates. The layer structure of the fabricated devices are depicted in Figure 3.10. The *uid* InAlAs sample had a *uid* InP cap and *uid* InP buffer layer grown on top and below the InAlAs layer of interest, respectively. The undoped buffer and cap layers were not expected to affect the DLTS results, however, they resulted in high $R_S$ in the devices. For the later-grown n-type Schottky sample, the cap was removed and the buffer layer was doped to remove any potential issues. This latter sample is the same sample as the InAlAs control from previous sections but a different diode on the sample was used.

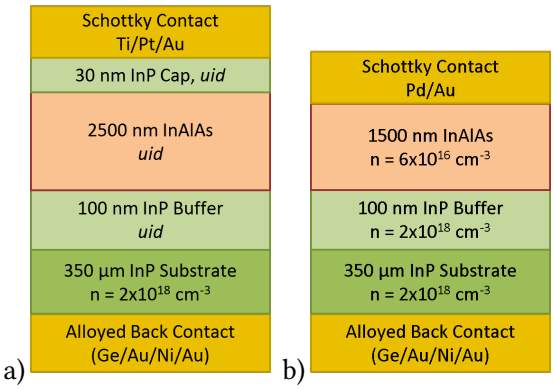


Figure 3.10: Schottky diode layer structure for the *uid* a) and n-type b) InAlAs samples.

Samples were fabricated and tested in a similar fashion to those from the previous sections. Figure 3.11 contains the J-V results of the two InAlAs Schottky diodes. Qualitative assessment of the J-V data revealed that the *uid* diode had a significantly higher reverse saturation current, $J_{01}$, compared to the n-type sample. This was expected as the location of the Fermi level in the *uid* sample should lead to less band banding and therefore the *uid* diode would have a lower barrier for diffusion currents. The consequence of higher saturation current for DLTS is a lower range of reverse bias available for pulsing before breakdown of the device under reverse bias. The series resistance of the *uid* sample was also noticeably higher due to the previously-mentioned *uid* InP buffer, but it was not enough resistance to affect the DLTS results.

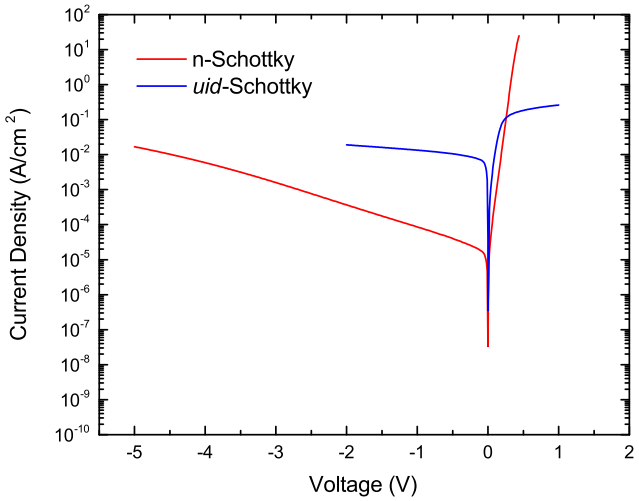


Figure 3.11: J-V of two InAlAs Schottky diodes, one doped n-type and one unintentionally doped.

C-V results, in the form of doping concentration vs. depletion width, for the two Schottky diodes are shown in Figure 3.12. The n-type sample was depleted ~150 nm to 450 nm, according to the parallel plate capacitor model, with an average doping of $4\times10^{16}$ cm$^{-3}$. This was close to the design target of $6\times10^{16}$ cm$^{-3}$. The *uid* diode had a much higher depleted width, as expected, since the unintentional doping was in the range of $2\times10^{14}$ cm$^{-3}$. The relatively high depletion width was responsible for a lower capacitance value (see Equation 2.17). C-V is unable to determine the majority carrier type, but MOCVD-grown *uid* InAlAs was determined to be n-type from Hall measurements on a similar sample. The doping value was used in conjunction with the DLTS results to determine the trap density.

The DLTS spectra of the two InAlAs Schottky diodes are shown in Figure 3.13. Both diodes exhibited an electron trap (majority carrier) with emission peak near 325 K. Most InAlAs samples showed a trap peak at this temperature, though the trap characteristics differed. Often the activation energies were near 0.50 eV or 0.90 eV. For these specific samples, the defect energies were $E_C$ - 0.60 eV for the n-type diode and $E_C$ - 0.97 eV for the *uid* diode with respective trap densities of $1\times10^{14}$ cm$^{-3}$ and $8\times10^{12}$ cm$^{-3}$ (see Table 3.5. The nature of the traps and their effect on dark current are discussed in the following sections.

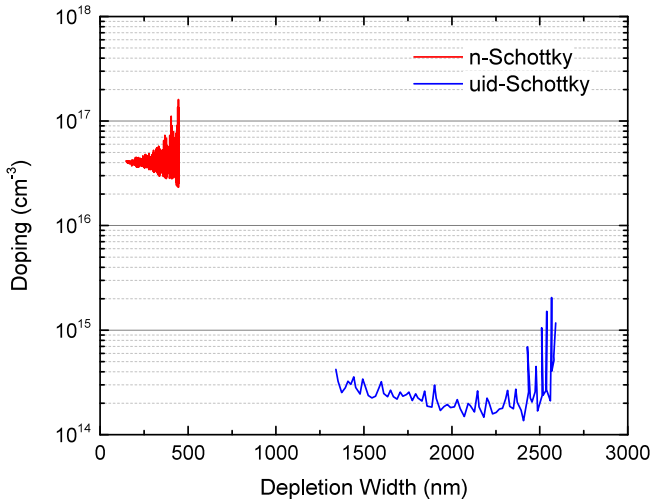


Figure 3.12: Doping concentration vs. depletion width for the two Schottky diodes.

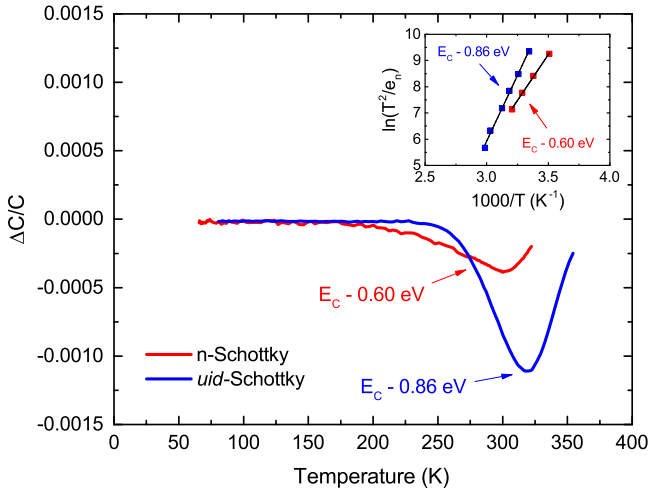


Figure 3.13: DLTS spectra for the two InAlAs Schottky samples.

## 3.7 InAlAs Solar Cells - Dark Current and DLTS

Availability of MBE-grown InAlAs solar cells allowed for a comparison between MOCVD-grown and MBE-grown $In_{0.52}Al_{0.48}As$ material. In addition, InAlAs solar cells were grown by MOCVD with different Al precursors - TMAl and TTBAl. Detailed information about the MBE InAlAs cell were given by Bittner [96], while information on the MOCVD cells can be found in work by Smith [85] and Smith *et al.* [94]. With these samples there was a unique opportunity to compare DLTS results on growths with different MOCVD precursors as well as different methods of epitaxy.

While TMAl is the industry standard, use of TTBAl has previously resulted in lower carbon and oxygen contamination in AlGaAs samples with growth temperatures below 800 ℃ [97]. In addition, TTBAl decomposes at a lower temperature (435 ℃) than TMAl [98], which is required to incorporate Sb into the lattice for growth of InAlAlSb, the subject of the previous section. Thus, use of TTBAl could also allow growth of both InAlAsSb and InAlAs in the same monolithic multi-junction cell, should a TTBAl InAlAs cell be viable. The TTBAl cell design and fabrication was identical to the TMAl MOCVD Cell (Figure 3.14a).

The three InAlAs solar cell samples were fabricated into devices compatible with DLTS. The MOCVD TMAl cell growth details were as follows: the In and As precursors were TMIn and $AsH_3$, respectively, and the n- and p-type dopants were Si (disilane) and Zn (diethylzinc), respectively. The growth temperature was 580 ℃ (610 ℃ for emitter), and the V/III ratio was 100. The TTBAl cell used similar conditions but with higher aluminum to indium molar ratio. The MBE cell was grown at lower growth temperature (<500 ℃) and high V/III beam equivalent pressure (BEP) typical of MBE growth of InAlAs [99]. Devices were isolated with 1:1:38 $H_3PO_4$:$H_2O_2$:$H_2O$ mesa wet chemistry, and p-type InP and n-type InGaAs Ohmic contacts were Au/Zn/Au and Ge/Au/Ni/Au, respectively. The device processing steps and additional growth details were reported by Smith [85] and Bittner [96]. The fabricated cell structures are shown in Figure 3.14. The tested photodiodes were all circular with 500 µm diameter.

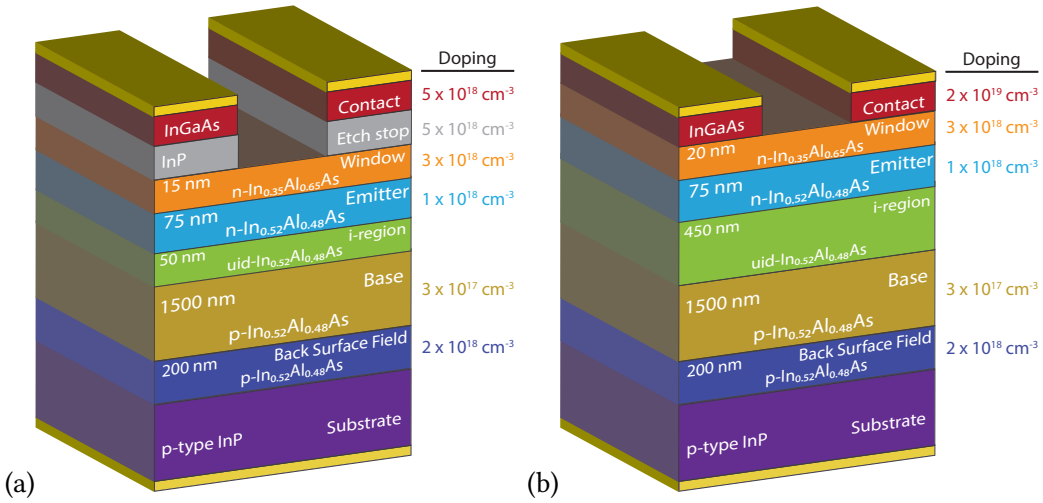


Figure 3.14: Layer stucture of the MOCVD (a) and MBE (b) InAlAs solar cells.

J-V data is shown in Figure 3.15 for the three photodiodes. At first glance, all photodiode

J-V was similar under forward bias, but the MBE photodiode had significantly higher current under reverse bias. At -5 V, the MBE photodiode current was >2 orders of magnitude higher than the MOCVD TMAl photodiode. Is it probable that the higher reverse bias current was caused by trap states, though whether they were bulk states or sidewall was not determined. To find this, different device sizes would have to be tested as done in Chapter 5, or large-area diodes would have to be tested so that perimeter effects are negligible. The MBE and MOCVD cells were fabricated similarly, except that the MBE contact layer was etched with a citric acid-based etch instead of acetic acid. Another significant difference was the 450 nm i-region in the MBE cell vs. 50 nm in MOCVD cells, and the larger depletion region may have affected depletion region carrier transport.

The forward bias of the three samples was compared in detail by fitting the double-diode equation (Equation 2.6). The fit procedure was the same as used in the previous section. The results of the fits, which were all excellent, are in Table 3.4. All three photodiode types had similar $J_{01}$ values, near 1-2$\times10^{-18}$ mA/cm$^2$. The $J_{02}$ values were similar to one another, as well, at $\sim5\times10^{-10}$ A/cm$^2$ for the MOCVD photodiodes with $n_2$=$\sim$1.95, while the MBE photodiode had slightly different recombination current at $1.4\times10^{-10}$ A/cm$^2$ with $n_2$=1.77, perhaps caused by the larger depletion width mentioned earlier. At a device size of 0.2 mm$^2$, there is always a concern that sidewall states are contributing to the dark current, however, Smith *et al.* published similar values to those above for both $J_{01}$ and $J_{02}$ for MOCVD TMAl solar cells (from the same growth as in this work) with area of 1 cm$^2$, so the dark currents in Table 3.4 were not perimeter-dominant. The photodiodes all had very high $R_{Sh}$, $\geq 10$ M$\Omega$·cm$^2$. All of these parameters are nearly as good as reported for GaAs junctions [100, 101], which has $J_{01}$ of $\sim10^{-19}$ A/cm$^2$ and $J_{02}$ of $\sim10^{-12}$ A/cm$^2$. Given the success of the more-developed GaAs, InAlAs grown by MOCVD or MBE is a promising material for photovoltaics.

Table 3.4: Double diode fit parameters for the MBE and MOCVD InAlAs diodes.

| Diode | $J_{01}$ (A/cm$^2$) | $n_1$ | $J_{02}$ (A/cm$^2$) | $n_2$ | $R_S$ (m$\Omega$·cm$^2$) | $R_{Sh}$ (M$\Omega$·cm$^2$) |
|---|---|---|---|---|---|---|
| MOCVD TMAl | $9.5\times10^{-19}$ | 1.00 | $5.2\times10^{-10}$ | 1.95 | 6.5 | 10 |
| MOCVD TTBAl | $1.5\times10^{-18}$ | 1.00 | $4.5\times10^{-10}$ | 1.94 | 8.9 | 80 |
| MBE | $2.0\times10^{-18}$ | 1.00 | $1.4\times10^{-10}$ | 1.77 | 11 | 10 |
| GaAs [102] | $3.0\times10^{-20}$ | 1.00 | $2.3\times10^{-11}$ | 2.00 | 6.0 | 0.12 |

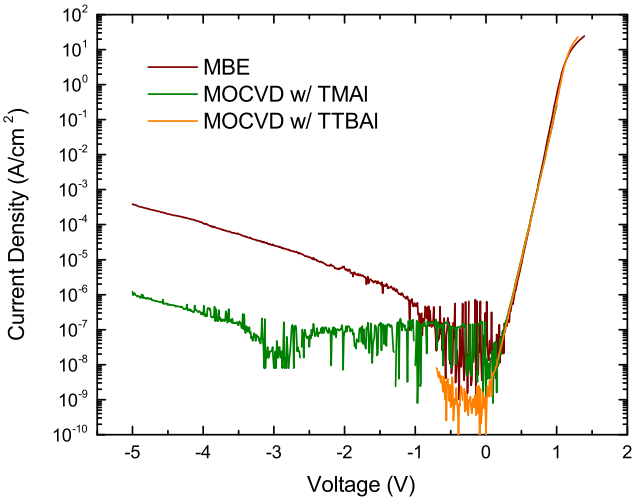


Figure 3.15: J-V results for the MBE photodiode and the two MOCVD photodiodes with different Al precursors - TMAl and TTBAl. The current near zero bias was below the noise floor of the measurement equipment.

The doping concentration as a function of depletion width for all photodiodes are shown in Figure 3.16. The doping value was near the designed value of $3\times10^{17}$ cm$^{-3}$ for all photodiodes. The MOCVD TMAl diode had a consistent value with low noise, indicative of excellent diode quality. At a depletion width near 225 nm, the MOCVD doping value began to drop unexpectedly, which could indicate that the depletion region from the junction began to overlap the depletion width from the winder/emitter interface, or perhaps some other interface. The TTBAl diode had similar behavior but was not consistent, oscillating around $2\times10^{17}$ cm$^{-3}$. For the MBE diode, at the lowest depletion width (390 nm) the doping was $8\times10^{16}$ cm$^{-3}$. The doping did not approach the expected value of $3\times10^{17}$ cm$^{-3}$ until $\sim$420 nm. This width was close to the thickness of the i-region in the MBE InAlAs solar cell design (450 nm), and it indicated that the i-region was not fully depleted under open-circuit conditions. Thus, an applied reverse bias was required to begin to deplete into the base. The thickness of the i-region presented an issue when interpreting DLTS results, which assumes depletion into a uniformly doped material, but this was accounted for by choosing appropriate biases.

Figure 3.17 contains the DLTS spectra for the MOCVD photodiodes with the different Al precursors. The TMAl diode had a minority carrier trap in the p-type base (electron trap) at 0.61 eV below the conduction band. This is likely the same trap as found before in the

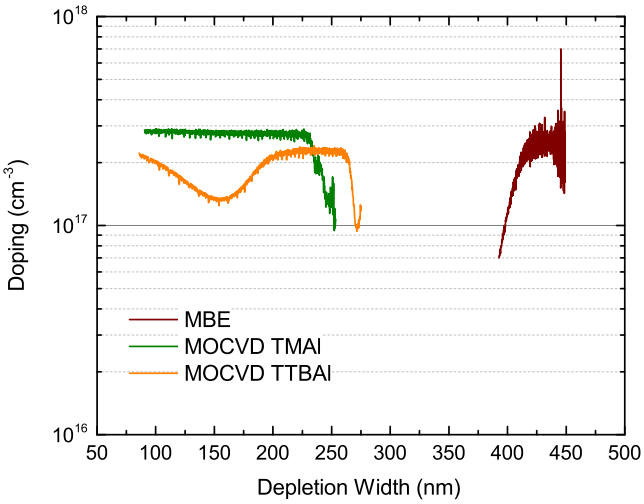


Figure 3.16: Doping concentration vs depletion with for the MBE photodiode and the two MOCVD photodiodes with different Al precursors.

Schottky samples, which were also grown using TMAl. The defect density was relatively low (see Table 3.5), which confirms the excellent diode performance seen in Figure 3.15. Judging from the near-identical J-V results, the TTBAl sample might be expected to have the same defect profile as TMAl. However, the trap densities were higher for the two traps found in the TTBAl diode, which were an electron trap at 0.37 eV below the conduction band and a hole trap 0.39 eV above the valence band. The close energy levels for different carrier types is questionable, and perhaps there was something unexpected occuring during the experiment. However, it was clear that there was at least one trap in the TTBAl photodiode that emitted near the same temperature as the TMAl trap and that the effect on the J-V was identical, regardless of the higher trap density.

The MBE InAlAs photodiode DLTS spectra is shown in Figure 3.18. For this sample, DLTS was taken on three devices from different locations on the wafer. As seen, there was nonuniformity in the defect signatures. The 'Edge 2' portion of the sample had the characteristic '325 K' trap, which was an electron trap based on the sign of the peak, however, the device failed due to thermal cycling before enough data could be taken to find the trap parameters. The same issue prevent the lower temperature electron trap on 'Edge 2' from being characterized. The device from the center of the wafer had two hole traps unlike any other seen in InAlAs samples. These were 0.27 eV and 0.54 eV above the valence band and at slightly higher density

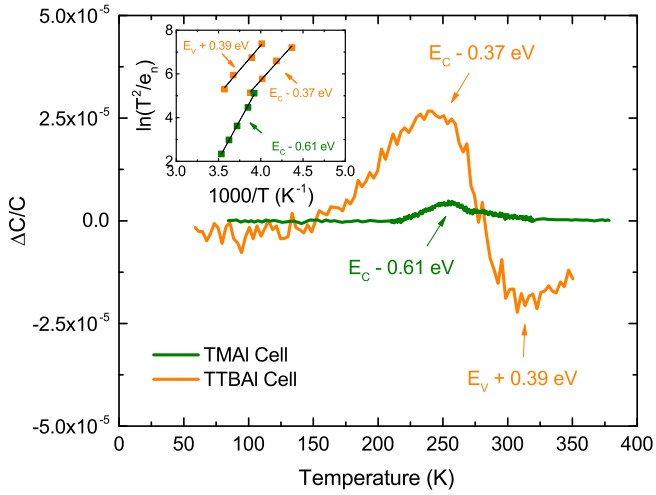


Figure 3.17: DLTS spectra for the MOCVD InAlAs solar cells.

than traps in in the baseline TMAl photodiode. Another edge device, 'Edge 1', was found to have two electron traps at 0.29 eV and 0.47 eV below the conduction band. These traps had lower densities than the center traps. Evidence for a higher temperature 'Edge 1' trap was found, but not enough data was collected to find the trap parameters. The variety of traps found with comparable-to-higher trap densities in the MBE diode is some evidence for why the current under reverse bias was significantly higher than the TMAl MOCVD diode (Figure 3.15).

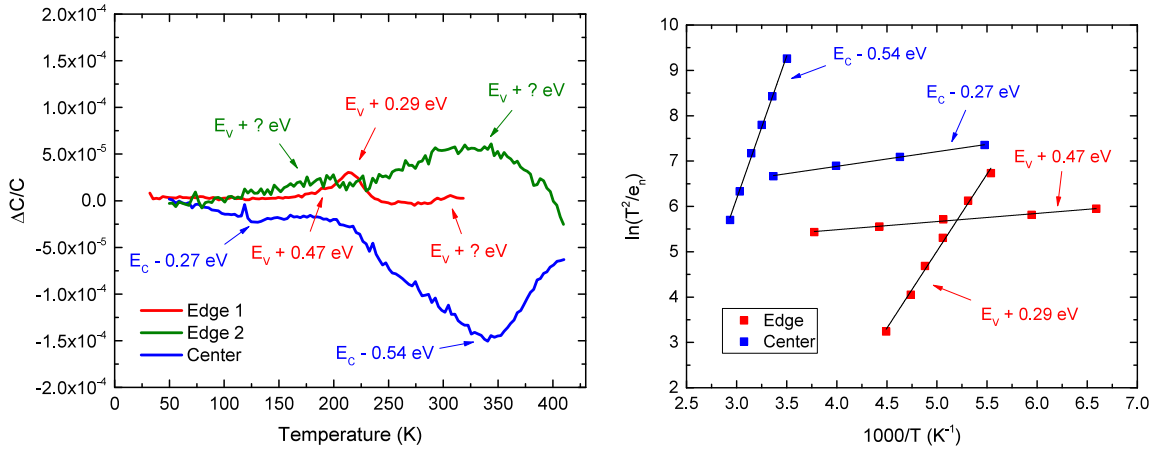


Figure 3.18: DLTS spectra for the MBE InAlAs solar cell.

DLTS results on these diodes revealed trap densities at $2 \times 10^{14}$ cm$^{-3}$ or less. The MBE cell had different traps on diodes from different parts of the wafer. The TMAl cell had overall

the lowest trap density, with just one trap at $3 \times 10^{13}$ cm$^{-3}$. The physical origin of these traps was investigated by literature search. A deep-level ∼0.6 eV below the conduction band has been typically observed in InAlAs [103–105]. There is evidence that this defect is caused by oxygen contamination. Naritsuka *et al.*found that there was a high correlation between the amount of oxygen detectable via NMR spectroscopy in the aluminum source and the trap concentration for deep-levels found at 0.5 eV and 0.7 eV [103]. Bouzgarrou *et al.*used SIMS results to demonstrate that the oxygen concentration found in their samples affected the trap densities for traps with energies of 0.55 eV and 0.61 eV, however, this group found that the defect was most likely a repulsive defect, which does not correlate to the large cross-section observed for the sample tested here [104]. Furthermore, Goto *et al.*found that the trap concentrations they observed for 0.45 eV had no correlation with oxygen contamination [105]. Instead, the researchers found that increasing the growth temperature of their samples was the key to lowering the trap density, a process which they hypothesized prevented the formation of aluminum anti-sites. As for evidence that the TMAl trap was oxygen related, SIMS results from Smith on TMAl MOCVD layers found higher oxygen contamination ($7\times10^{15}$ cm$^{-3}$) than was found in TTBAl layers ($<6\times10^{15}$ cm$^{-3}$) [85].

Table 3.5: DLTS results for all the InAlAs diodes.

| Label | $E_A$ (eV) | $\sigma$ (cm$^2$) | $N_T$ (cm$^{-3}$) | Type |
|---|---|---|---|---|
| MOCVD n-Schottky | $E_C - 0.60$ | $3 \times 10^{-14}$ | $1 \times 10^{14}$ | Electron |
| MOCVD *uid*-Schottky | $E_C - 0.87$ | $2 \times 10^{-10}$ | $8 \times 10^{12}$ | Electron |
| MOCVD TMAl Cell | $E_C - 0.61$ | $5 \times 10^{-11}$ | $3 \times 10^{13}$ | Electron |
| MOCVD TTBAl Cell | $E_C - 0.37$ | $5 \times 10^{-16}$ | $2 \times 10^{14}$ | Electron |
| MOCVD TTBAl Cell | $E_V + 0.39$ | $3 \times 10^{-16}$ | $6 \times 10^{13}$ | Hole |
| MBE Cell Center | $E_V + 0.27$ | $2 \times 10^{-13}$ | $1 \times 10^{14}$ | Hole |
| MBE Cell Center | $E_V + 0.54$ | $3 \times 10^{-15}$ | $2 \times 10^{14}$ | Hole |
| MBE Cell Edge | $E_C - 0.29$ | $1 \times 10^{-15}$ | $3 \times 10^{13}$ | Electron |
| MBE Cell Edge | $E_C - 0.47$ | $2 \times 10^{-9}$ | $7 \times 10^{13}$ | Electron |

## 3.8 Conclusions & Future Work

### 3.8.1 InAlAsSb

InAlAs and InAlAsSb samples were grown by MOCVD on InP substrates and fabricated into Schottky diodes. The InAlAsSb was a novel material with a theoretical bandgap of 1.8 eV to be used as the top subcell of a multi-junction solar cell lattice-matched to InP. The InAlAs (bangap 1.47 eV) diodes were grown as a basis for comparison as this material is more well-known.

Dark current analysis revealed that the InAlAs diode had dominant ideality factor of $\sim$1 while the InAlAsSb diodes had ideality of 1.6. This was the first sign of trap states in InAlAsSb that affected the device performance. The InAlAsSb dark current magnitude was also similar to the InAlAs diode, which should not be the case as the dark current in general decreases with increased bandgap. Both devices were Schottky diodes with metals of similar work function, and with a higher barrier height the InAlAsSb would have lower dark current and better rectification ratio. A high concentration of growth-related bulk traps would explain the dark current issues with InAlAsSb. These were likely related to the miscibility gap [40] and the failure of the MOCVD system to prevent thermodymically-favorable InSb segregation.

C-V results for these diodes revealed the doping and depletion widths which would be used in the DLTS experiments. The InAlAs diode results indicated doping close to the design target. The InAlAsSb diode, which was not intentionally doped, had a doping concentration of 5-6 $\times 10^{17}$ cm$^{-3}$. Quality *uid* material is typically <$10^{17}$ cm$^{-3}$. The high doping was evidence that the crystal was doped by excess carbon or oxygen incorporation in the lattice or other point defects behaving as donors [88]. Steady-state capacitance vs. temperature revealed good behavior from the InAlAs diodes with weak temperature dependence, but the InAlAsSb had two activations that almost tripled the capacitance, believed to be caused by high densities of shallow traps.

DLTS experiments on the quaternary alloys resulted in higher trap densities than ternary InAlAs. InAlAs had one electron trap, which was close to midgap at 0.57 eV below the conduction band with a moderate cross-section of $6 \times 10^{-14}$ cm$^{-2}$ and low density of $5 \times 10^{15}$

$cm^{-3}$. The material of interest, InAlAsSb, had more traps and with the higher densities. Two deep electrons traps were detected at 0.47 eV and 0.56 eV below the conduction band. The former had a larger cross-section of $1 \times 10^{-14}$ $cm^{-2}$ with concentration $6 \times 10^{15}$ $cm^{-3}$, and the latter had a large cross-section of $3 \times 10^{-13}$ $cm^{-2}$ but with the highest density at $1 \times 10^{16}$ $cm^{-3}$. A shallow hole trap was also found with $7 \times 10^{15}$ $cm^{-3}$ concentration. The lower growth temperature and different precursors could explain the high trap density in the target-composition InAlAsSb, although the physical nature of these traps are unknown at this time. These DLTS results are in agreement with the dark current and steady-state capacitance vs. temperature results, in that InAlAsSb diode had higher dark current and sharp rises in capacitance with temperature.

It is clear that MOCVD growth optimization must be performed to obtain material capable of low, ideality-of-one diode dark current. DLTS and dark current measurement of simple Schottky diodes can be used as feedback along with usual techniques of analyzing surface morphology, PL, and XRD. If a consistent DLTS spectra can be obtained for MOCVD-grown InAlAsSb, efforts could be made to determine the source of the traps. Trap density could be correlated with oxygen contamination in SIMS, for example, or compared to MBE growth which has less contamination of hydrocarbon elements. This could then be used to guide growth decisions. If a diode with low dark current can be grown, the next step for DLTS experiments is irradiation of the material by protons or electrons to determine if it is radiation-tolerant enough for use in space.

### 3.8.2 InAlAs

Growth of InAlAsSb required an exploration of different MOCVD precursors. As a consequence, TMAl and TTBAl InAlAs control samples were grown. These samples created an opportunity to detect traps that occur in InAlAs originating from use of these precursors. In addition, MBE-grown TMAl InAlAs samples were available to compare the different epitaxial growth methods.

Five different InAlAs diodes were tested. Two were TMAl MOCVD Schottky diodes. The other three were photodiodes from InAlAs solar cell samples, two grown by MOCVD but

with the different aluminum precursors TMAl and TTBAl, and the last grown by MBE. The photodiodes had well-behaved dark currents that were nearly as low as GaAs solar cells. By curve fitting, it was determined that all three of the p-n junction diodes had similar dark currents under forward bias. The MBE cell had higher reverse-bias current, however, which could have been trap-related.

The *uid*-InAlAs was found to have a doping of low $10^{14}$ cm$^{14}$, which is competitive with undoped MOCVD-grown GaAs and indicative of good material with low concentration of contaminants. All other InAlAs doping profiles obtained from C-V data were in good agreement with the target doping from the device designs.

DLTS results on these diodes indicated relatively low trap densities at $2 \times 10^{14}$ cm$^{-3}$ or less. Compared to InAlAsSb, this was low and did not cause $n = 2$ behavior in the InAlAs Schottky diodes. The MBE sample had different traps on diodes from different parts of the wafer. The TMAl cell had overall the lowest trap density, with just one trap at $3 \times 10^{13}$ cm$^{-3}$. Electron traps $\sim$0.5 eV to $\sim$0.7 eV below the conduction band have been typically observed in InAlAs. There are conflicting reports in that these defects can be caused by oxygen contimination [103, 104], or by aluminum anti-sites [105]. Whether the traps here were caused by oxygen contamination was not known for certain but the trap density of samples grown with TMAl were correlated with higher oxygen contamination found via SIMS. Oxygen could not be detected in samples grown with TTBAl and these samples exhibited a different trap profile. Some traps were not consistent with literature and it would require more DLTS work to be done to find a consistent trap profile for each material type before investigating the physical source of the defects.

The material could nearly be used as-is in a multi-junction space cell. Lumb *et al.* has simulated that a four-junction InP-based device with two InAlAs top subcells rivals the InGaP/GaAs/Ge cell currently used for space solar [93]. Whether or not the InAlAs-based cell is a superior technology depends upon its radiation tolerance. InAlAs could be exposed to protons or electrons, similar to what was done in the following chapter for InGaAs, to determine how it would react to damaging radiation in space. It would have to be more tolerant than GaAs, which is the weak point of the conventional space cell.

# Chapter 4

# *In Situ* Trap Characterization of Irradiated InGaAs Photodiodes

## 4.1 Summary

This chapter is a thorough study of dark current measurements and DLTS for proton-irradiated $In_{0.54}Ga_{0.46}As$ diodes. The primary contribution of this work was irradiation of diodes at low temperature and with DLTS performed as the samples were slowly heated to room temperature. This was called *in situ* DLTS and was used to find traps that were only stable at low temperature; traps that are not possible to find in a typical irradiation which exposes the samples to room temperature before DLTS. The technique could be used on any DLTS-compatible material and took considerable development including a custom DLTS system and custom beamline setup. Other testing and analysis performed was *in situ* dark current measurement, trap annealing, angle-of-incidence DLTS, and admittance spectroscopy.

This chapter contains eight main topics.

1. Development of MFIA-Based DLTS System.
2. Design, Growth, and Fabrication of InGaAs Diodes.
3. Pre-irradiation Characterization.
4. Irradiation Procedure.
5. *In Situ* DLTS and Dark Current.
6. Trap Annealing.

7. Trap Dependence on Angle of Incidence.

8. Capacitance vs. Frequency and Admittance Spectroscopy.

## 4.2 Motivation & Background

### 4.2.1 Motivation

Discovered early in the space age were the trapped particle radiation belts, or Van Allen belts. These belts are created when particles from solar winds become trapped in the Earth's magnetic field, where they may remain for years. The belts extend outward from the planet along the equatorial plane to an altitude of 58,000 km. Figure 4.1 is a depiction of the belts. Of the two belts, the inner has a stronger field and captures mostly protons (0.5 - 100 MeV), while the outer mostly electrons (0.1 - 10 MeV) [106].

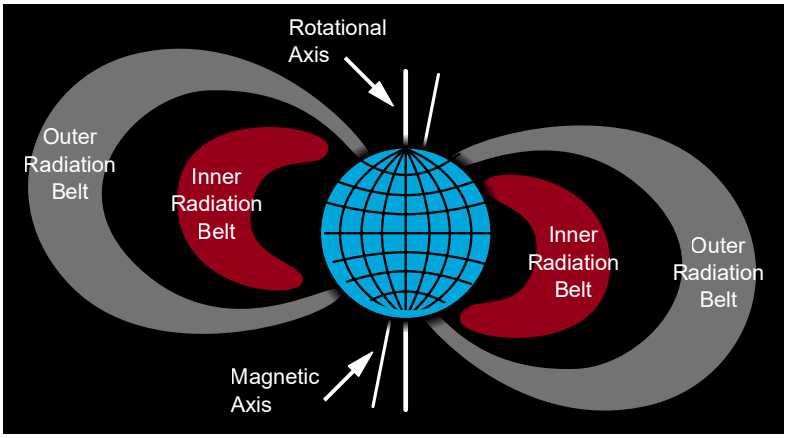


Figure 4.1: The Van Allen belts around Earth. The inner belt ranges from 1,000 km to 6,000 km altitude and mostly captures protons. The outer belt ranges 13,000 km to 58,000 km and traps mostly electrons. *Image by NASA is in the public domain.*

Due to damaging effects of radiation in the space environment, III-V optoelectronic devices deployed on satellites experience degradation and even failure during the course of a mission. Exposure to high-energy electrons, protons, neutrons, or heavier ions causes displacement damage to the crystal structure, where atoms are displaced in the lattice due to collisions. This leads to vacancy-interstitial pairs or Frenkel defects, which will accumulate over the mission time. If these defects cause a mid-band state suitable for carrier recombination, minority carrier lifetimes and diffusion lengths suffer (see Section 2.3). Besides a loss in

detection sensitivity, this causes higher dark current which leads to reduced SNR. It is important to know how a material or device will respond to the space environment so that missions relying on these devices can be properly planned or so that devices can be radiation-hardened.

To determine the radiation fluences that a satellite will encounter during its mission, a program like SPENVIS can be used [107]. The satellite orbit can be inputted into the program and it will output the mission fluence. To give an example, a 'Molniya' orbit was inputted into SPENVIS and it was calculated that, for a solar cell with 12 mils of coverglass, the annual 1 MeV electron equivalent fluence was $\sim 1 \times 10^{15}$ cm$^{-2}$.

Reliability testing can be performed on the ground by replicating the space environment in the laboratory. However, the full range of conditions are difficult to reproduce. Specifically, irradiation is often performed at room temperature and with significant time delay between exposure and testing. It was proposed that crystal defects that rapidly anneal at room temperature could be stable at the nominal device operating temperature of some satellite-deployed devices such as infrared detectors [8]. This hypothesis has been addressed in this work by performing *in situ* dark current and DLTS using a cryostat equipped with electrical leads and attached to the beamline of a particle accelerator.

### 4.2.2 Background

The material chosen for this study was $In_{0.54}Ga_{0.46}As$ (referred to as InGaAs), which is lattice-matched to InP and with a bandgap of 0.75 eV is suitable for wavelengths from 950 nm to 1650 nm. It is widely available, well-understood, and irradiation results have been previously reported (see below). An InGaAs FPA will consist of a 1D or 2D array of InGaAs photodiodes bonded to a silicon readout integrated circuit [108]. The photodiode layer structure can be of the mesa type, where the junction is formed during epitaxial growth, or planar type, which is a diffused-junction design [109, 110]. InGaAs photodectors and FPAs can have space applications including infrared astronomy [31], infrared phenomonology and remote sensing [41], and hyperspectral imaging [42].

Table 4.1: DLTS results for the irradiated InGaAs from literature.

| Source and Species | $E_A$ (eV) | $\sigma$ ($cm^2$) |
|---|---|---|
| Shaw [111] 1 MeV electrons | $E_C - 0.10$ | $6.5 \times 10^{-17}$ |
| | $E_C - 0.29$ | $2.7 \times 10^{-15}$ |
| Ohyama [112] 1 MeV neutrons | $E_C - 0.37$ | N/A |
| | $E_C - 0.45$ | N/A |
| Marshall [113] 63 MeV protons | $E_C - 0.31$ | $2.9 \times 10^{-16}$ |

In this work, InGaAs p-on-n photodiodes were irradiated with 2.0 MeV and 3.5 MeV protons with fluences of $10^{10}$ $cm^{-2}$ to $10^{13}$ $cm^{-2}$. The diodes were exposed both at room temperature and at 100 K, with the former representing the more common testing method with a delay time between exposure and testing, while the latter is the novel *in situ* method that can better replicate the space environment. In the past, InGaAs photodiodes were exposed to electrons [111, 114], protons [113], fast neutrons [112], alpha particles [115], and carbon ions [116]. A trend in DLTS results was difficult to find between many of the mentioned exposures. It has been shown in irradiated GaAs DLTS experiments that electron, protons, and alpha particles all produce similar trap profiles according to DLTS [117]. There is a difference in the number of displacements per particles, as the heavier ions have more momentum and create more knock-ons, the but the displacements themselves (and the traps created) are similar from particle to particle. Given that, the results by Shaw *et al.* for 1 MeV electrons and Ohyama *et al.* for 1 MeV neutrons produced similar DLTS peaks near 150-200 K range, though the energies were different. Marshall *et al.* found a similar energy to Shaw *et al.* for 63 MeV protons, however, the peak occurred at temperature higher than 250 K. The trap characteristics by these three studies are given for reference in Table 4.1.

As for background on the testing method itself, *in situ* DLTS was performed on n-type germanium samples with Schottky contacts by Mesli *et al.* in 2008 [8]. They irradiated the sample at 22 K with 1 MeV electrons at a fluence of $5 \times 10^{14} cm^{-2}$, and then immediately began a temperature ramp and DLTS scan to 90 K. At 90 K, they reversed the ramp but continued to collect DLTS data down to 40 or 50 K. During the first ramp, a shallow trap they hypothesized to be a germanium vacancy-interstital pair (labeled FP) was detected, but this trap was missing during the ramp down. The trap disappeared due to annihilation or annealing starting at 65

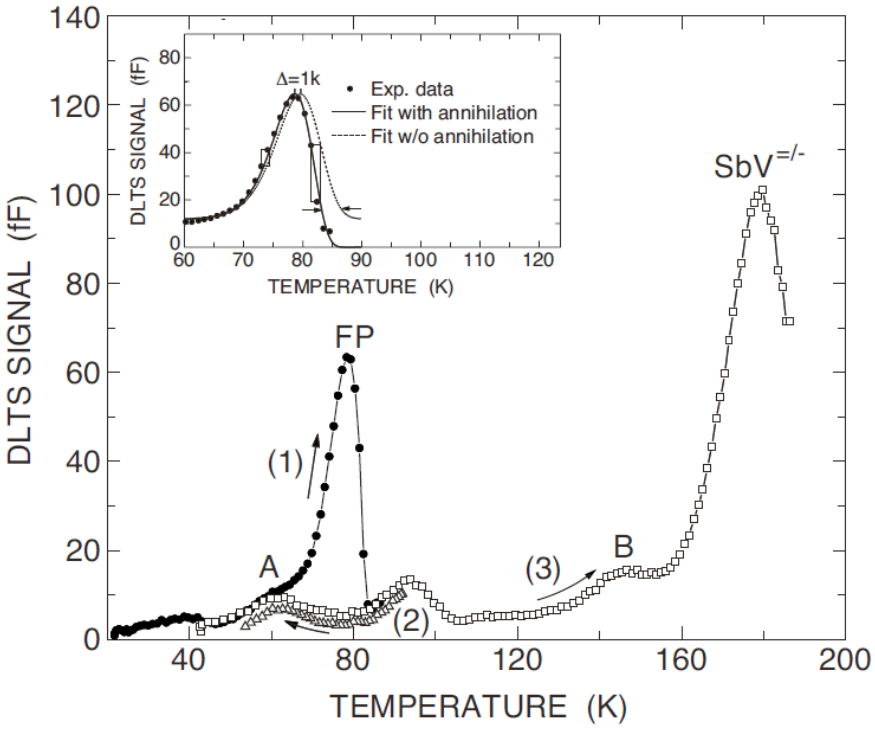


Figure 4.2: *In situ* DLTS spectra obtained by Meslia *et al.* on n-type germanium Schottky diodes. (1) The initial temperature ramp, which found a Frenkel pair defect labeled FP. (2) The temperature scan was reversed and the FP peak disappeared, indicating that the defect underwent annihilation via annealing during the ramp up. (3) A second upward ramp confirmed that the FP peak was gone. The inset shows a model of the defect peak if there had been no annihilation via annealing. *Reprinted with permission from* [8].

K, and by 90 K the trap had completely annealed out. This work demonstrated the usefulness of *in situ* DLTS by detecting a trap that would be impossible to find with any exposure to room temperature.

## 4.3 Development of MFIA-Based DLTS System and *In Situ* DLTS

The system used in the previous chapter was an analog conventional DLTS system that was deemed inadequate for the experimental loads planned for this chapter. As an analog spectrometer, the legacy equipment could not digitize the direct capacitance vs. time transients (see Equation 2.19). To obtain spectra, the spectrometer processed transients in analog hardware with dedicated filtering circuits used to implement Equation 2.22. This is the same approach as Lang in the seminal DLTS paper [56]. The old system was equipped with only two

of these filtering circuits, so only two emission rate constants could be measured for each sampled transient. To get enough points to fit a line on Arrhenius plot therefore required multiple temperature scans. Each temperature scan typically takes one to several hours, and these required repeat scans are not acceptable when performing *in situ* DLTS as the multiple-scan method can only work well when temperature cycling does not affect the behavior of the sample. The main point of *in situ* DLTS is to find effects that would be hidden by temperature cycling.

A custom DLTS system was developed to overcome these hurdles. The new implementation was designed to digitally capture the capacitance transients. Then, Equation 2.22 could be implemented in software, allowing for an arbitrary number of filters and freedom to design custom filters. This system would also allow other ways of processing the transients in software, such as performing a numerical Laplace transform. It was built around the Zurich Instruments MFIA, a dual-phase digital lock-in amplifier and LCR meter, and driven by software written in MathWorks MATLAB (available in Appendix A). The cryostat was an M22 model from Cryo Industries of America, capable of a temperature range of 10 K to over 400 K with cooling from a closed-loop helium recirculator. The system was designed to have have minimal physical switches so that scans could be started, monitored, and altered remotely via remote desktop. A similar system driven by LabVIEW was developed and described in work by Schifano *et al.* [118].

The MFIA lock-in unit has greater capabilities and flexibility when compared to common DLTS capacitance meters such as the popular Boonton models. While the Boontons and similar may only use 1 MHz, the MFIA can modulate a DC bias with frequencies from DC to 5 Mhz in order to measure sample capacitance. The amplitude of the AC wave can also be set arbitrarily on the MFIA versus the limited settings available on most meters. The MFIA can apply DC biases from -10 V to 10 V, which is adequate for DLTS measurements, and can apply the square wave DLTS pulse on its own without an external pulse generator. It can transfer digital samples via ethernet at 107 kHz continuously or higher in bursts, which is more than adequate for good SNR when processing spectra and does not require a separate analog-to-digital converter for data acquisition. Figure 4.3 is a block diagram of all the components in the

DLTS setup, with the MFIA combining the three components: Pulse generator, capacitance meter, and data acquisition system.

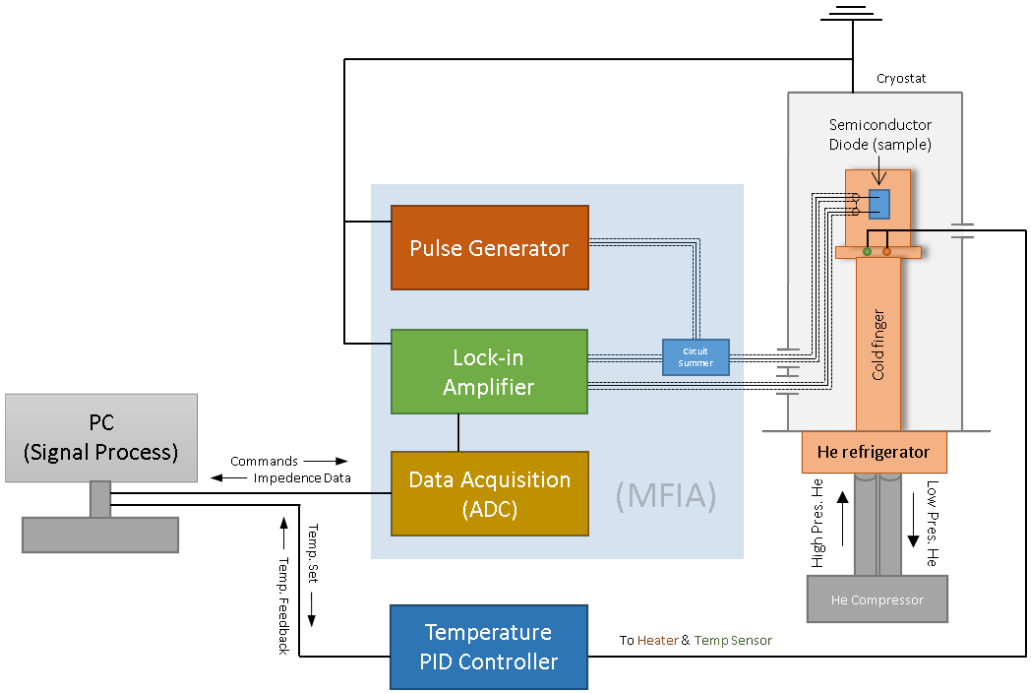


Figure 4.3: Block diagram of DLTS system. The use of MFIA simplified the setup without sacrificing features.

The sample capacitance can be measured by using a dual-phase lock-in amplifier to analyze the complex current response to a reference sinusoidal AC voltage. The sensible circuit representation for the depletion-region capacitor is a resistor in parallel with a capacitor as in Figure 4.4. The complex impedance of a parallel RC circuit is $1/Z = 1/R_p + j2\pi f_{ref} C_p$ and $I = V/Z$, thus,

$$C_p(t) = \frac{I_{\phi=\pi/2}(t)}{2\pi V_{ref} f_{ref}}, \tag{4.1}$$

where $I_{\phi=\pi/2}$ is the component of the current that is 90° out-of-phase with the applied reference AC voltage, and $V_{ref}$ and $f_{ref}$ are the amplitude and frequency of the reference voltage, respectively.

The lock-in can extract the 90°component of the current as it effectively multiplies the measured current signal by a cosine function over some time constant, $T$, which is at least as

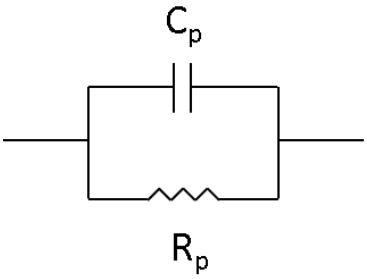


Figure 4.4: Parallel RC circuit diagram representative of a diode junction capacitance.

large as one period of the reference frequency,

$$I_{out,\phi=\pi/2}(t) = \frac{1}{T}\int_{t-T}^{t} \cos 2\pi f_{ref} s I_{in}(s) ds. \tag{4.2}$$

The principle of the lock-in amplifier is that, because sinusoidal functions are orthogonal, the only component that can be extracted from the filter in Equation 4.2 is the part of $I_{in}$ that has the same frequency and is in-phase with the cosine function, which is 90° out-of-phase with the reference voltage.

The MFIA time constant found to have the best signal extraction without taking too long compared to the transient itself was 2.6 usec with a filter order of 8. The period of a 1 MHz AC signal is 1 usec and the fastest emission rate in DLTS is usually 5 kHz, which is 200 usec.

To test and calibrate the MFIA-based system, DLTS was performed on an irradiated QD GaAs sample. Results for this sample were previously published by collaborators [5], however, the prior results were obtained with a Bio-rad DL8000, which is a commercial DLTS unit. A comparison of the results obtained from the custom MFIA system and the DL8000 are shown in Table 4.2. The DLTS spectra were already shown in Figure 1.4. The two DLTS systems were in close agreement for activation energy the cross-section for the two traps listed in the table, indicating that the MFIA-based system was operating as expected. Note that cross-section was found by y-intercept of a log plot and therefore same order of magnitude is an acceptable match.

Table 4.2: DLTS results for the irradiated QD GaAs calibration diode.

| Defect Label | DLTS System | $E_A$ (eV) | $\sigma$ ($cm^2$) |
|---|---|---|---|
| QD-PR4" | Bio-Rad DL8000 | $E_C - 0.30$ | $4 \times 10^{-15}$ |
| | Custom MFIA-based | $E_C - 0.31$ | $8 \times 10^{-15}$ |
| QD-PR2 | Bio-Rad DL8000 | $E_C - 0.67$ | $5 \times 10^{-13}$ |
| | Custom MFIA-based | $E_C - 0.68$ | $7 \times 10^{-13}$ |

## 4.4 Design, Growth, and Fabrication of InGaAs Diodes

The $In_{0.54}Ga_{0.46}As$ photodiodes were grown by MOCVD using an Aixtron 3x2" reactor. All diodes were grown lattice matched to InP on 2" (100) oriented substrates with vicinal offcut of 0.2° toward <110>. Standard precursors of trimethylgallium (TMGa), TMIn, $AsH_3$ and phosphine ($PH_3$) were used as well as disilane and diethyzinc for n- and p-type dopants, respectively. Growth temperatures varied from 600 ℃ to 630 ℃ depending on material and doping level, while the V/III ratio was maintained at 70 for $In_{0.54}Ga_{0.46}As$ growth. Reactor pressure was maintained at 100 mbar throughout growth. Material thicknesses, composition, and doping was confirmed by *in situ* optical characterization and *ex situ* by XRD, and Hall effect. The targets of material composition, doping level, and thicknesses of the grown diodes are shown in the design diagram in Figure 4.5a.

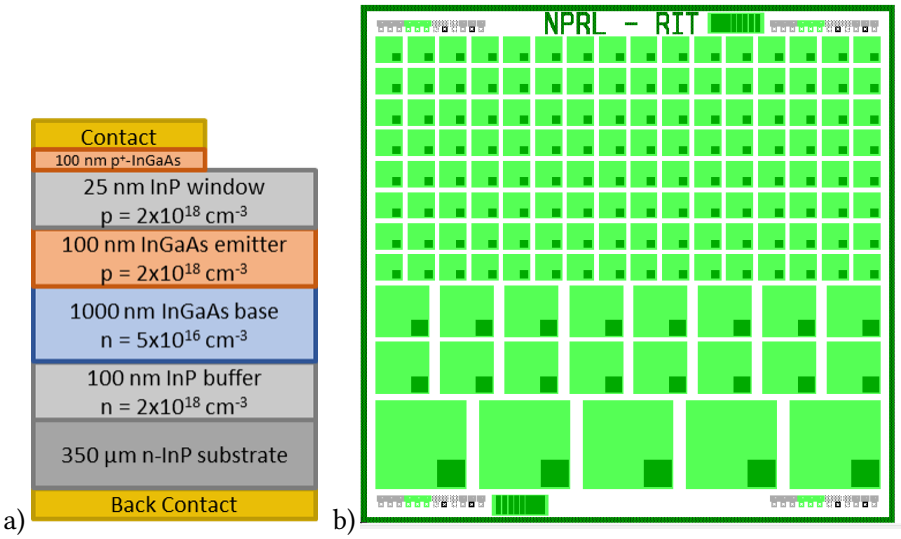


Figure 4.5: a) InGaAs mesa photodiode layer structure. b) Mask layout for the DLTS photodiode array (1 cm by 1 cm). Light green indicates the device mesas and dark green is the metal coverage.

The photodiode layer structure was of the mesa-type, not planar with diffused-junction. The front a backside windows materials were InP, while the emitter and base of the one-sided step-junction were $In_{0.54}Ga_{0.46}As$. Polarity of p-on-n was chosen to match the InGaAs photodiode products available on the market. Doping limits in p- and n-type InP and InGaAs were found using Hall effect measurement on calibration samples with an Accent/Nanometrics HL5500. Doping level for both windows as well as the emitter was chosen to be $2 \times 10^{18}$ $cm^{-3}$. A model was used to determine the base doping such that the junction capacitance was in the range of 30-50 $nF/cm^2$. Since this corresponded to a depletion width of roughly 100 nm to 500 nm in the base, the base thickness was set to 1.0 µm. Frontside window thickness and emitter thickness were kept low, 25 nm and 100 nm, respectively, to maximize SR over concerns of sheet resistance. A 100-nm InGaAs contact layer was doped as high as possible for p-type doping, roughly $2 \times 10^{18}$ $cm^{-3}$.

The samples were designed as InGaAs DLTS test diodes primarily but there was significant freedom to also mimic a photodiode array. The layout of a single 1 cm by 1 cm chip was made to mimic a photodiode array and is shown in Figure 4.5b. Three different device sizes allowed for measurement of perimeter effects. The device sizes from smallest to largest were 0.5 mm by 0.5 mm, 1.0 mm by 1.0 mm, and 1.7 mm by 1.7 mm. The metal contacts were made large enough to easily probe but did not cover the entire diode to allow optical measurements if desired. Each 2" wafer contained 12 chips.

The diodes were fabricated by etching the original stack of material and depositing front and rear metal contact. Standard lithography and evaporation processes were used to accomplish this. The sample was first cleaned, covered in photoresist using spin coating, and then exposed with the mesa isolation pattern. The mesa etch was a three-step wet chemical etching process to remove the InGaAs contact, InP window, and then InGaAs absorber layers. The frontside ohmic contacts were placed using a liftoff process with thermal evaporation of Au/Zn/Au at respective 20/20/500 nm thicknesses. Finally, a backside ohmic contact was deposited using thermal evaporation consisting of Ni/Ge/Au with thicknesses of 20/50/500 nm. The contacts were not annealed as this led to unpredictable effect on the dark current, though a 400 ℃ for 4 minutes was found to reduce contact resistance.

## 4.5 Pre-irradiation Characterization

Pre-irradiation transmission line measurement (TLM), dark J-V, and C-V measurements were taken before irradiation with an Agilent B1500 semiconductor analyzer. The contact resistances were characterized by TLM method and were measured to be $5.0 \times 10^{-3} \Omega \cdot \text{cm}^{-3}$ for contact to p-type (unannealed) InGaAs and $5.4 \times 10^{-7} \Omega \cdot \text{cm}^{-2}$ for contact to n-type InP. With the contact layer on, the p-type sheet resistance was 4.1 kΩ/sq. Because of this high value, it was debated whether the contact layer should remain instead of being etched away in areas not covered by metal. The decision to keep the contact layer was made after measuring J-V of test diodes with and without the contact layer etched. From Figure 4.6, one can see that the contact-etched diode had lower dark current at small bias, however, the reverse bias behavior of this diode overall was much worse than the diode with intact contact layer. The dark J-V is ideally not affected by the presence or absence of the contact layer as this layer is removed only to reduce parasitic absorption during optical experiments. Clearly that was not the case here, and it was hypothesized that the cause of the dark J-V change was due to the contact etch chemistry altering the sidewall properties, leading to a new current transport mechanism like TAT [119].

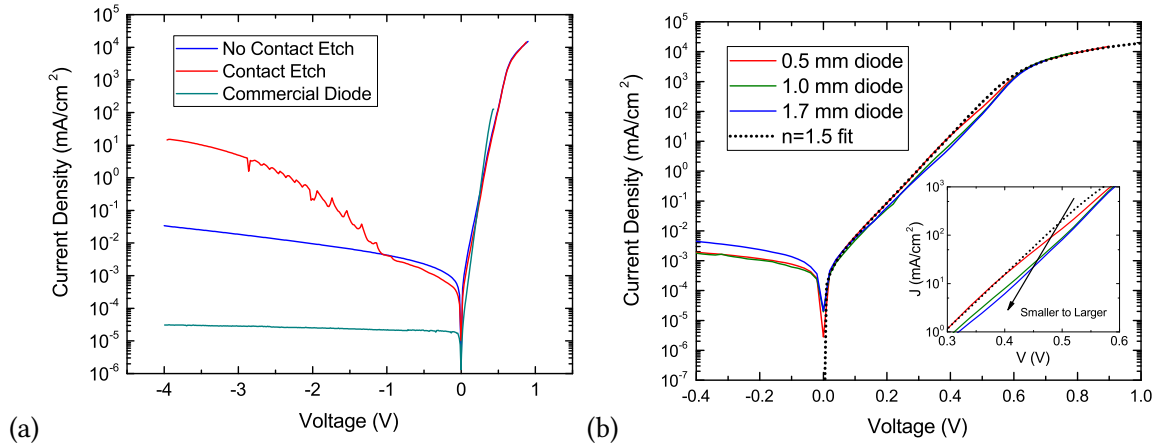


Figure 4.6: (a) Comparison of dark J-V of a representative diode that did not have the contact layer etched with a diode that was contact-etched. Also shown is a commercial Hamamatsu InGaAs photodiode for reference. (b) Forward bias behavior of representative 0.5 mm, 1.0 mm, and 1.7 mm diodes, with a fit of the small diode to a n=1.5 single diode model. The inset focuses on the perimeter-related divergence of the dark currents.

To isolate the effect of the sidewall, dark J-V was collected for each of the device sizes and data from representative diodes are in Figure 4.6. The small diode data was fit using the double diode model. The best fit was with a single diode with ideality factor of 1.5. The physical origin of this abnormal ideality factor was not clear, but it was likely tied to the device sidewall. Evidence for this is seen in the figure's inset. The larger devices showed a deviation from the $n = 1.5$ model at lower forward bias. This could be due to state-filling or saturation occurring more quickly in the sidewalls of larger devices compared to smaller ones. As the device size is increased, the perimeter effects are reduced when compared to those in the bulk (perimeter scales as $x$, area as $x^2$). Also in the figure are J-V results for a commercial Hamamatsu InGaAs photodiode (model G11193-10R) for reference. This diode did not have the sidewall problems and had ideal dark current values for InGaAs with ideality factor of 1.0. However, the structure was unknown and so was not appropriate for the experiment.

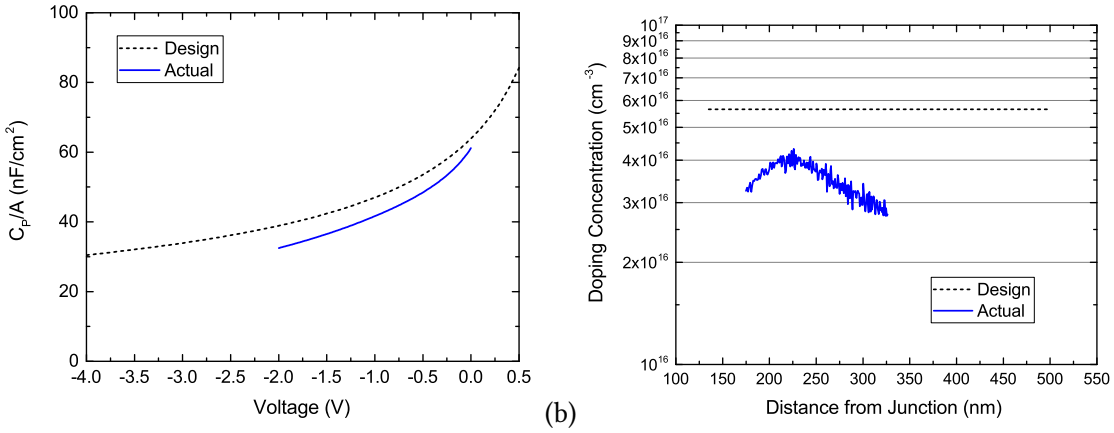


Figure 4.7: (a) Normalized capacitance vs. voltage data for a representative 0.5 mm diode as well as results from the model used to design the diode structure. (b) Doping concentration as a function of distance from the junction, extracted from the C-V data.

Pre-irradiation C-V results are shown in Figure 4.7. The normalized capacitance values were a good match to the model used to design the diode structure. From the C-V data, the doping was extracted as a function of depletion depth. The base doping in the region of 200-300 nm was 3-4 $\times$ $10^{16}$ cm$^{-3}$, which was close to the target value of 5 $\times$ $10^{16}$ cm$^{-3}$. The variation was likely an artifact of the measurement as SIMS data from calibration samples showed constant doping.

## 4.6 Irradiation

Samples were irradiated at SUNY Albany using the Dynamitron particle accelerator. A block diagram of the experimental setup is shown in Figure 4.8. As mentioned, a unique feature of this setup was the ability to connect the sample cryostat and DLTS system directly to the Dynamitron beamline. This allowed *in situ* measurements of both J-V and DLTS. The beam was rastered over an area marginally larger than the 1 $cm^2$ size of a sample chip. The beam could be aligned to the sample mounting position with the use of four Faraday cups that were located along the 45°, 135°, 225°, and 315° angles to the sample, just outside the sample area and equidistant to the sample mounting point center. A gate valve located just above the sample could be closed to allow for beam alignment and calibration, then opened when ready for exposure. Low beam currents of 1 nA at low fluence to 3 nA at high fluence were used to prevent sample heating.

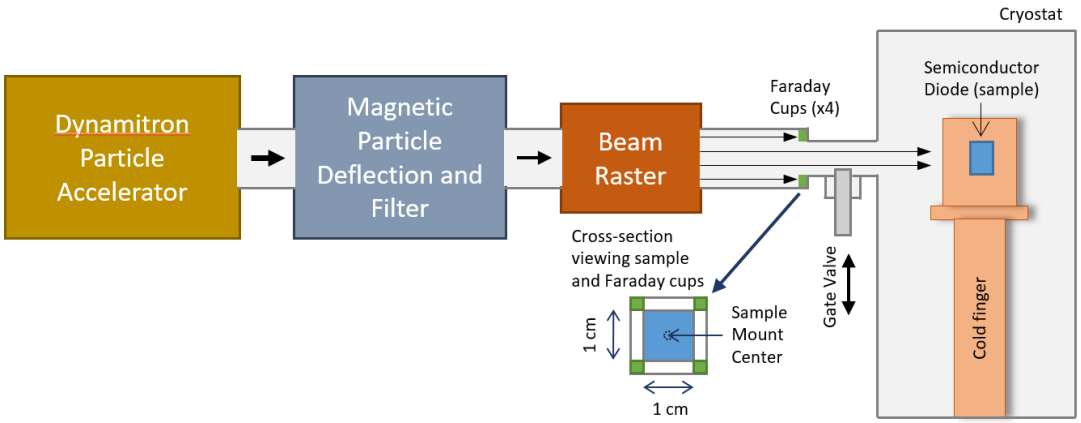


Figure 4.8: Beamline diagram illustrating the path of ions from the Dynamitron to the rasterizer and ending at the Faraday cups and the sample in the cryostat.

Table 4.3 contains a list of all samples that were irradiated. The table indicates the energy, fluence, irradiation temperature and angle, and intended experiments of each sample. For the *in situ* testing, two diodes on separate chips were used. One was dosed with 2.0 MeV protons and the other with 3.5 MeV protons to compare response of devices to proton energy. For each energy, fluences of $1.1\times10^{10}$ $cm^{-2}$, $1.0\times10^{11}$ $cm^{-2}$, $1.0\times10^{12}$ $cm^{-2}$, and $1.0\times10^{13}$ $cm^{-2}$ were tested. These were done incrementally so that the same device could be used for each fluence. These irradiations were done with the sample held at 100 K and 0° incidence

angle. Another sample set was designed to test the effect of angle of incidence. These three diodes were exposed to $1.0 \times 10^{12}$ cm$^{-2}$ of 2.0 MeV protons at room temperature without the cryostat system. The angle was changed with the use of machined sample-holders that attached to the gate valve with surfaces for 0°, 60°, and 80° angles.

The *in situ* exposures and testing was performed using the following procedure. The cryostat sample was first taken to 100 K for exposure. Exposure of the lowest fluence was then done. Immediately after, dark J-V data was taken, then DLTS began. During the DLTS temperature ramp, the scan was paused every 50 K to take dark J-V data. When the 300 K data was taken, then sample was returned to 100 K. The next irradiation was then done with enough fluence such that this next fluence plus the previously administered fluence would sum to the target fluence. For example, since the sample had already seen $1.1\times10^{10}$ cm$^{-2}$ on the first dose, the next dose was $8.9\times10^{10}$ cm$^{-2}$ so that the target fluence of $1.0\times10^{11}$ cm$^{-2}$ was reached. This process was continued until the final fluence was achieved and measurements completed.

Table 4.3: List of Dynamitron sample exposures including the energy and fluence and the purpose of the exposure.

| **Proton Energy (MeV)** | **Fluence (cm$^{-2}$)** | **Irradiation Temp. (K)** | **Irradiation Angle (°)** | **Experiment Type** | **Purpose** |
|---|---|---|---|---|---|
| 2.0 | $1.1\times10^{10}$ | 100 | 0 | *in situ* DLTS and J-V, then annealing and C-f | Determine if defect peaks change with energy or angle |
| | $1.0\times10^{11}$ | | | | |
| | $1.0\times10^{12}$ | | | | |
| | $1.0\times10^{13}$ | | | | |
| 3.5 | $1.1\times10^{10}$ | 100 | 0 | *in situ* DLTS and J-V | Determine if defect peaks change with energy or angle |
| | $1.0\times10^{11}$ | | | | |
| | $1.0\times10^{12}$ | | | | |
| | $1.0\times10^{13}$ | | | | |
| 2.0 | $1.0\times10^{12}$ | 295 | 0 | DLTS | Determine if defect peaks change with energy or angle |
| | | | 60 | | |
| | | | 80 | | |

## 4.7 *In Situ* DLTS and Dark Current

At the beamline facility, dark J-V was measured using a Kiethley 2400 Source Measure Unit. DLTS was performed with the MFIA-based DLTS system. All samples were held at -1.5 V steady-state bias, with DLTS pulse to -0.3 V. These biases probed enough of the base region (200 nm to 300 nm from junction) but were small enough in magnitude to avoid excess dark current for heavily-irradiated devices. The pulse width was 10 ms, which was long enough for all traps to capture carriers. The AC frequency used was 250 kHz rather than typical 1 MHz, because higher than 250 kHz led to problems with series resistance (see Section 4.10). The measured transients were 150 ms long and averaged for 1 K temperature steps such that an entire scan from 100K to 300K took roughly 2 hours.

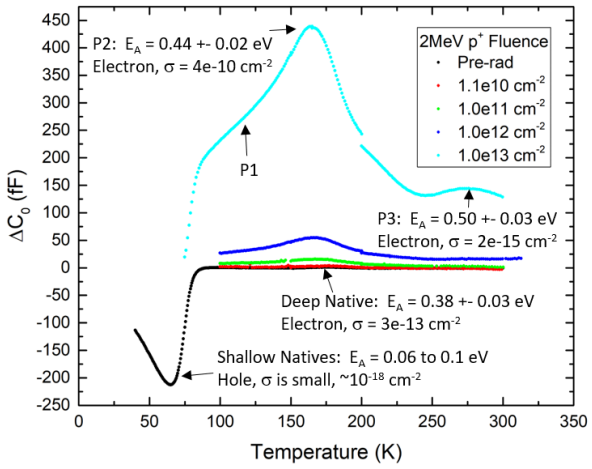


Figure 4.9: Linear plot of the *in situ* DLTS spectra for the 2.0 MeV fluences with traps indicated by label.

The measured DLTS spectra are shown in Figure 4.9 and Figure 4.10. Figure 4.9 is a linear plot of the processed DLTS signal with all discovered traps labeled, while Figure 4.10 is plotted with a rough calculation of the trap density on log-scale to better show the effect of increasing fluence. Two traps were found in most samples before irradiation (pre-rad), one shallow hole-trap near 75 K labeled N/F1 and one mid-gap electron-trap near 175 K labeled N/F2. These have been attributed to defects arising from either the epitaxial growth or the fabrication process and are not related to irradiation. The mid-gap electron trap has a very low density

(near $10^{12}$ cm$^{-3}$) and would likely not affect minority carrier lifetime significantly. This mid-gap trap may be related to similar mid-gap traps in GaAs (e.g. the vacancy trap EL2), but would require further study to make this determination. The shallow trap, N/F1, was likely related to lack of passivation and sidewall recombination. The N/F1 trap deviated from the thermal emission model of Equation 2.20b and could not be fit a straight line on the Arrhenius plot.

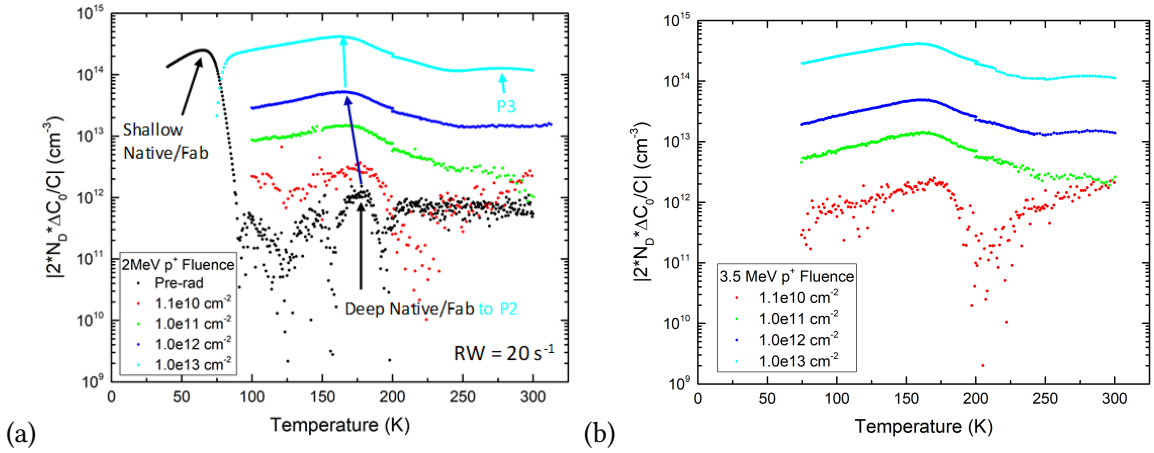


Figure 4.10: Semilogarithmic plot of the *in situ* DLTS spectra for both 2.0 MeV and 3.5 MeV fluences. The 3.5 MeV sample did not have pre-irradiation data.

Trap peaks form and increase with increased fluence due to the non-ionizing energy loss (NIEL). Protons are fully penetrating at 2 and 3.5 MeV, so the NIEL is expected to be constant across the active region of the device. Two clear traps were detectable after continued irradiation, with a possible third trap occurring as a shoulder peak left of the strong peak found near 150 K to 200 K. All appear to be majority carrier electron traps. These three proton irradiation induced electron-traps have been labeled P1, P2, and P3. Table 4.4 contains the extracted DLTS parameters from the spectra. The table includes activation energy, capture cross-section, trap density, and carrier type for each of the discovered traps. The electron trap labeled P2 was the dominant trap, located at roughly mid-gap and with a large cross-section, indicated the trap is either complex or has a positive charge state. The P2 was detected at all fluence levels, although energy and cross-section could not be extracted reliably at the lowest fluence due to higher noise floor at the accelerator test facility. This trap has similar behavior to the E2 trap from Shaw *et al.* [111], appearing at roughly the same temperature, though

the parameters are not the same as this trap was discovered at 0.44 eV below the conduction band compared to 0.29 eV for E2. This discrepancy could be due to measurement error and is examined in more detail in Section 4.10.

Table 4.4: All extracted DLTS parameters for traps detected during the *in situ* experiments.

| Energy | Fluence ($cm^{-2}$) | Label | $E_A$ (eV) | $\sigma$ ($cm^2$) | $N_t$ ($cm^{-3}$) | Type |
|---|---|---|---|---|---|---|
| Pre-rad | 0 | N/F1 | $0.09 \pm 0.03$ | N/A | $1.8 \times 10^{14}$ | Hole |
| | | N/F2 | $0.38 \pm 0.03$ | $3 \times 10^{-13}$ | $1.7 \times 10^{12}$ | Electron |
| 2.0 MeV | $1.1 \times 10^{10}$ | P2 | N/A | N/A | $6.5 \times 10^{12}$ | Electron |
| | $1.0 \times 10^{11}$ | P2 | $0.38 \pm 0.03$ | $1 \times 10^{-12}$ | $3.1 \times 10^{13}$ | Electron |
| | $1.0 \times 10^{12}$ | P2 | $0.47 \pm 0.02$ | $8 \times 10^{-10}$ | $1.1 \times 10^{14}$ | Electron |
| | $1.0 \times 10^{13}$ | P2 | $0.44 \pm 0.02$ | $4 \times 10^{-10}$ | $9.3 \times 10^{14}$ | Electron |
| | | P3 | $0.50 \pm 0.03$ | $2 \times 10^{-15}$ | $2.6 \times 10^{14}$ | Electron |
| 3.5 MeV | $1.1 \times 10^{10}$ | P2 | N/A | N/A | $5.1 \times 10^{12}$ | Electron |
| | $1.0 \times 10^{11}$ | P2 | $0.41 \pm 0.03$ | $2 \times 10^{-11}$ | $2.8 \times 10^{13}$ | Electron |
| | $1.0 \times 10^{12}$ | P2 | $0.43 \pm 0.02$ | $1 \times 10^{-10}$ | $1.0 \times 10^{14}$ | Electron |
| | $1.0 \times 10^{13}$ | P2 | $0.43 \pm 0.02$ | $1 \times 10^{-10}$ | $9.2 \times 10^{14}$ | Electron |
| | | P3 | $0.49 \pm 0.03$ | $1 \times 10^{-15}$ | $2.7 \times 10^{14}$ | Electron |

Two traps observed in this work but not by Shaw *et al.* were identified as P1 and P3. P1 appeared as a shoulder to P2 at temperatures around 125K. The trap was only apparent at higher fluences. It was not possible to resolve parameters for this peak with conventional DLTS due to its proximity to P2. P3 was a trap near 275K, and like P1 it was only visible at the higher fluences. P3 had a relatively small cross-section and trap energy nearer the valance band. The small cross-section may indicate this trap either was a neutral point defect or had a slight negative (repulsive) charge state.

The *in situ* dark J-V for the 2.0-MeV diode is shown in Figure 4.11. The 3.0 MeV diode data was similar. To simplify the data, dark current densities at -200 mV bias for both the 2.0 MeV- and 3.5 MeV-irradiated sample are shown in Figure 4.12. The on-site testing performed with the Kiethley unit was not able to measure below 20 nA/$cm^2$, affecting low-irradiation and low-bias measurements between 100 K and 200 K. The pre-rad data was not limited by noise as it was taken with an Agilent B1500 semiconductor analyzer beforehand, but it was limited by blackbody photo-current caused by the room-temperature cryostat chassis, which was about 3 nA/$cm^2$. The data was most straight-forward at 250 K and 300 K, but regardless there existed a clear trend of higher dark current with increased fluence. The dark current

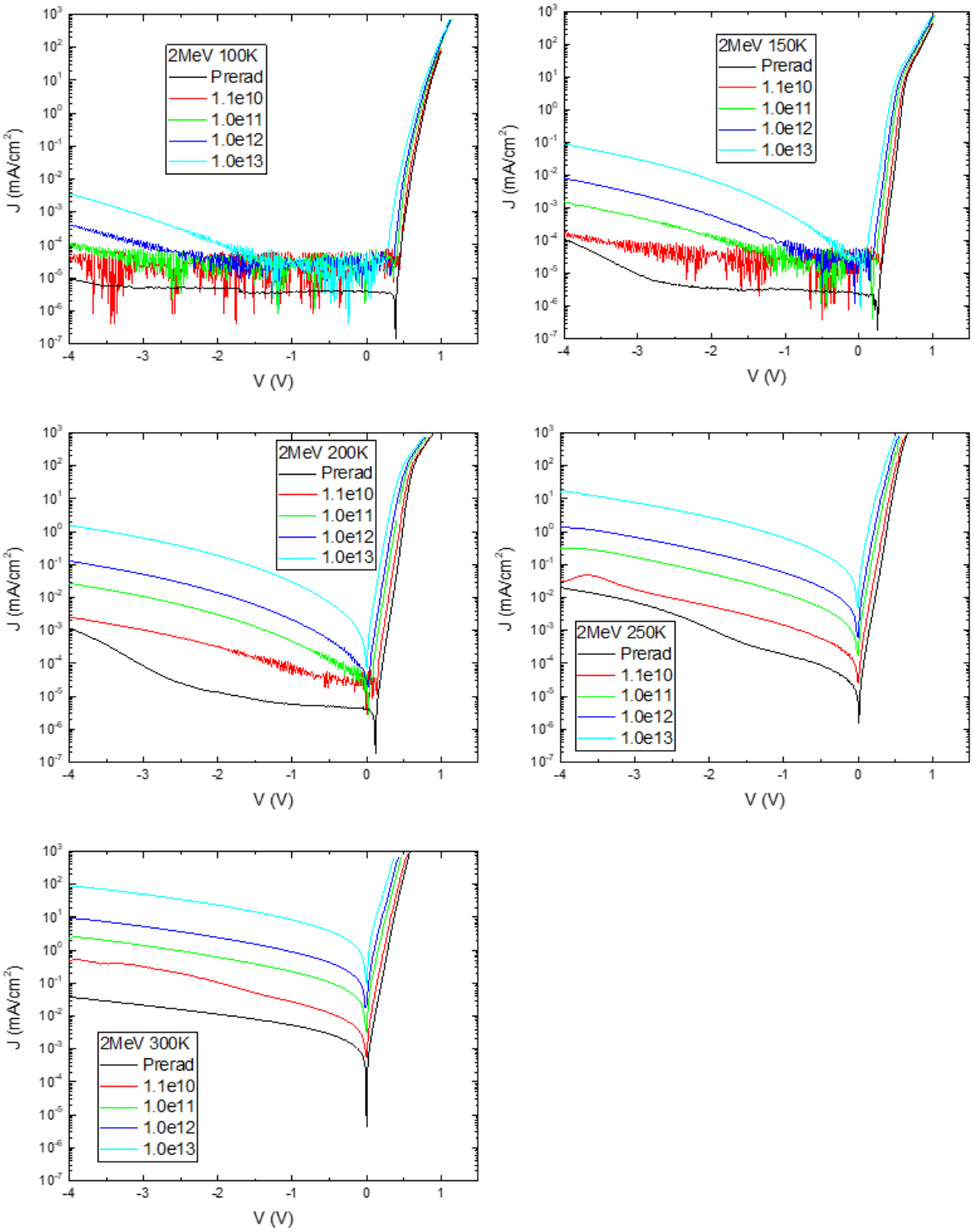


Figure 4.11: All *in situ* J-V data collected for the 2.0 MeV diode. The noise floor was about 20 nA/cm$^2$, except for the pre-irradiation data for the 2.0 MeV diode.

roughly increased linearly with fluence in this regime. Both the 2.0 MeV and 3.5 MeV sample dark current densities followed the same trends. There was no pre-irradiation data taken at RIT for the 3.5 MeV, so the only pre-rad data that existed for this diode were taken on site at 300 K and 100 K.

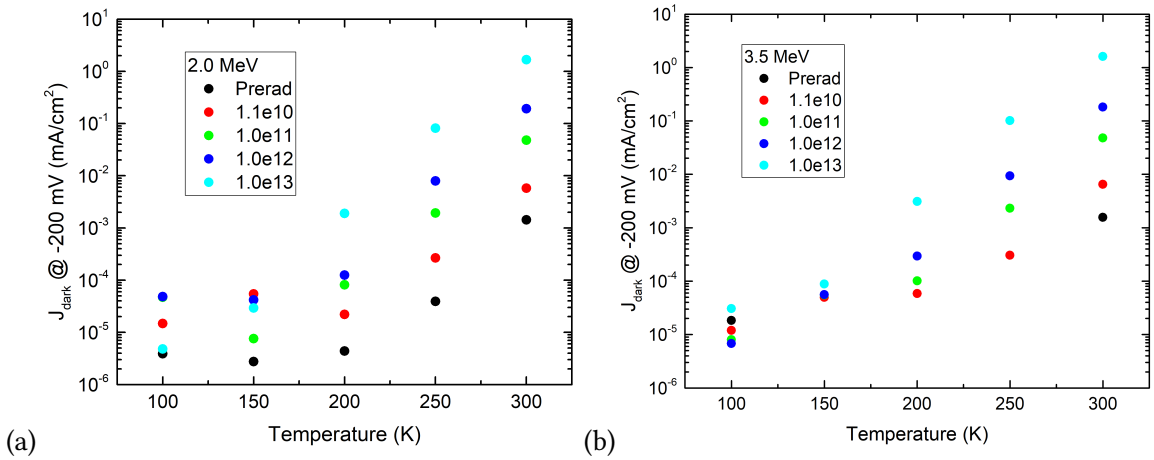


Figure 4.12: Dark current at -200 mV bias for all *in situ*J-V temperatures and fluences for (a) 2.0 MeV and (b) 3.5 MeV. The pre-irradiation 3.5 MeV current density was not available for most temperatures.

Figure 4.13 shows the mid-gap trap density data from DLTS plotted on log-log scale against the dark current density measured at -200 mV bias and 250 K. There is an excellent linear fit between the trap density and the dark current for both the 2.0 MeV and 3.5 MeV proton samples. The 3.5 MeV device had higher dark current for the same trap density, possibly originating from device-to-device variability.

A linear relationship was found between the fluence, the trap density, and the dark current. This was in agreement with the SRH-driven reverse-bias generation current model, which is simply $J = J_{02}$ from Equation 2.9 for a mid-gap trap. It was expected from this result that the mid-gap trap P2 detected from DLTS is responsible for the dark current. That the N/F2 trap, which is mid-gap, also lies close to the fit line supports this hypothesis. More evidence can be gathered by annealing, where the dark current and the mid-gap trap density should both anneal at the same rate.

Figure 4.14 is a comparison of *in situ* and *ex situ* DLTS spectra for two neighboring diodes that had similar pre-irradiation dark J-V. Both samples were irradiated at 100 K, but the *ex situ* DLTS was taken after that diode had been exposed to room temperature for 2 hours.

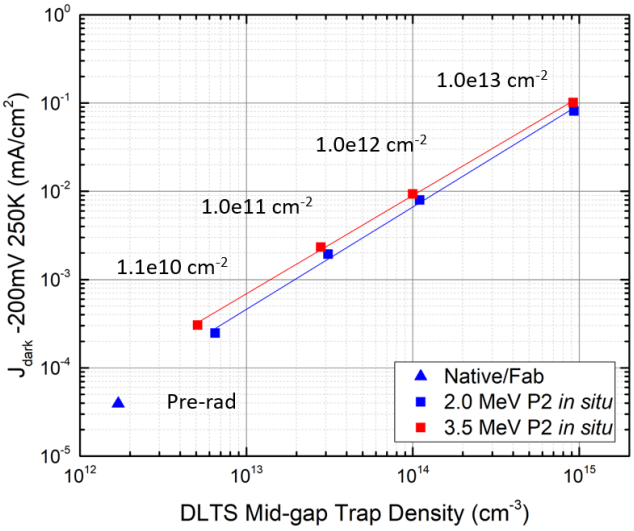


Figure 4.13: Dark current at -200 mV bias for all *in situ* J-V temperatures and fluences for (a) 2.0 MeV and (b) 3.5 MeV. The pre-irradiation 3.5 MeV current density was not available for most temperatures.

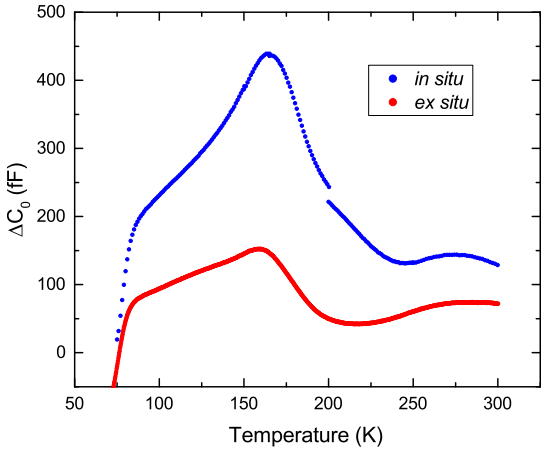


Figure 4.14: *In situ* and *ex situ* DLTS spectra for $1\times10^{13}$ fluence of 2 MeV protons. The rate constant was 20 Hz.

The diode tested *ex situ* exhibited the same peaks as the one tested *in situ*, however, the peak amplitudes were reduced by a factor of 3, indicating that annealing occurred at or below room temperature. The gap in the data taken *in situ* at 200 K was due to a 10 minute pause in the DLTS scan during which dark J-V data was taken. This gap indicated that annealing of P2 began below 200 K. A small gap was also present at 150 K (another temperature with dark J-V pause), but this gap was almost negligible compared to the gap at 200 K. Nevertheless, the onset of annealing must have began somewhere around 150 K. Annealing at such a low temperature could be evidence that the P2 trap is an indium vacancy, as this defect is known

to have low migration energy in the InP system with possibility of annealing at 150 K [120]. Ga- and As-related defects in the GaAs system have higher migration energies and do not anneal at room temperature [121]. Trap annealing is examined more in the following section.

## 4.8 Trap Annealing

Irradiation-induced traps are likely vacancy-interstitial pairs of displaced lattice atoms, also known as Frenkel defects. In this case, thermal energy in the lattice could cause an interstitial to diffuse and recombine with the vacancy, annihilating the defect. Annealing experiments were therefore performed after irradiation for two purposes. If the majority of the defects could be removed via annealing, then this could be a potential route to 'healing' deployed devices if the annealing temperature and rates were found to be reasonable. Additionally, the annealing temperature and rates could be used to better understand the connection between the DLTS traps, the dark current, and the possible physical defects created by irradiation.

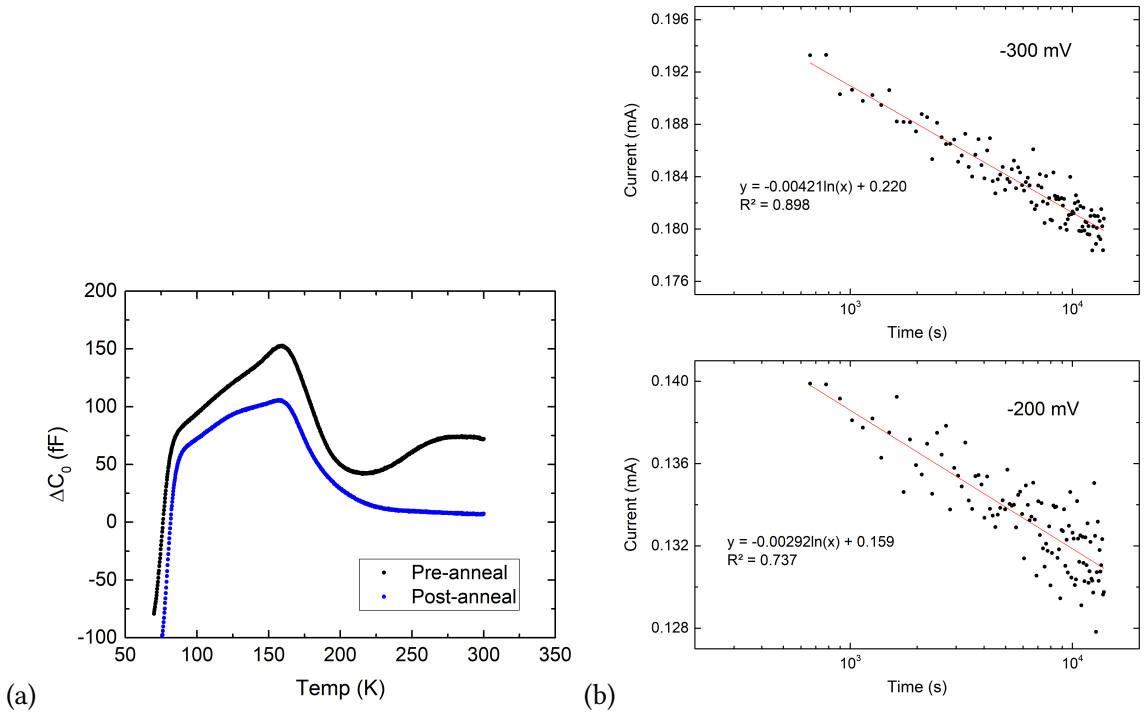


Figure 4.15: (a) DLTS spectra taken before and after the 3 hour 400 K anneal. (b) Top - Dark current at -300 mV (top) and -200 mV (bottom) bias vs. time.

A single device was irradiated at 100 K by 2.0 MeV protons at a fluence of $1 \times 10^{13}$ cm$^{-2}$. It

was brought to room temperature and then immediately stored in liquid nitrogen to prevent as much annealing as possible. It was removed from the liquid nitrogen and DLTS data were gathered, shown as 'pre-anneal' in Figure 4.15a. It was then heated 400 K for about 3 hours, during which time dark J-V measurements were performed every 2 minutes. After annealing, another DLTS spectrum was collected, shown as 'post-anneal' in Figure 4.15a.

Table 4.5: List of metrics for J-V and DLTS from before and after the annealing experiment.

| Metric | Before Anneal | After Anneal | Remaining Factor |
|---|---|---|---|
| Dark Current -300 mV, 300 K | 4.51 μA | 3.20 μA | 0.76 |
| Dark Current -200 mV, 300 K | 3.20 μA | 2.44 μA | 0.76 |
| P1 Peak (128 K) | 123.2 fF | 95.3 fF | 0.77 |
| P2 Peak (158 K) | 152.3 fF | 105.5 fF | 0.69 |
| P3 Peak (280 K) | 74.0 fF | N/A | N/A |

Dark current data was taken at 300 K before and after annealing so that it could be compared to the pre- and post-anneal DLTS peaks. Table 4.5 contains the data, as well as the calculated remaining factor, which is a ratio of the post-anneal value to the pre-anneal value. The remaining factors for the DLTS peaks were also calculated using the temperatures 128 K, 158 K, and 280 K for P1, P2, and P3 traps, respectively. After annealing, the P3 trap density was below the detection limit. The P2 peak clearly annealed at a faster rate than P1, with P2 annealing considerably faster than the dark current itself. The dark current and P1 annealed at the most mutually consistent rate. This contradicts the implied result from Figure 4.13, where P2 was implied to be responsible, although it could be the case that both P1 and P2 scale linearly with fluence and it was P1 that was responsible for the dark current. It may also be the case that dark current is driven by some combination of P1 and P2, or that P1 and P2 are related in some way.

The dark current data is in Figure 4.15b for two biases, -200 mV and -300 mV, chosen because low bias mostly avoided trap assisted tunneling in favor of SRH generation. The data followed a logarithmic decay trend, similar to what was observed by Shaw *et al.* [122]. Data was fit to the equation,

$$J(t) = B - A \log \frac{t}{t_0}, \tag{4.3}$$

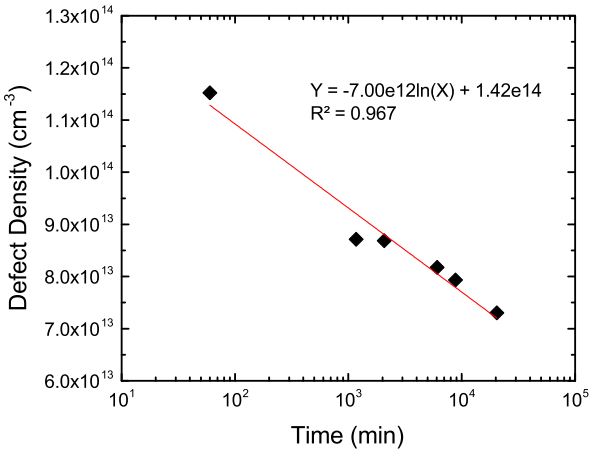


Figure 4.16: The P2 defect density, determined from DLTS scans, over ∼14 days of annealing at 300 K.

where $A$ and $B$ were fit parameters and $t_0$ is 1 second in this case. The quantity $A/B$ is the logarithmic decay rate, which was 0.018 for -200 mV and 0.019 for -300 mV. It is believed that the logarithmic decay rate is evidence of a range of similar defects that present as a single peak in the DLTS but are physically not identical defects, possibly due to lattice disorder of the ternary material [122]. The decay rate of ∼0.019 was a slower rate than the one reported by Shaw *et al.* for their mid-gap trap, which was 0.039-0.047, even though a higher rate was expected for higher temperature. Another DLTS annealing experiment was performed at 300 K to more closely match the approach in Shaw *et al.*, and the result for 14 days of annealing are in Figure 4.16. The sample was mostly kept at 300 K except for during DLTS scans when the temperature was cycled down to 100 K and back. Annealing was considered to be 'paused' during the DLTS cycle. The DLTS decay rate at 300 K was 0.049, which was in good agreement with Shaw *et al.* The reason for the slower rate at 400 K was likely due to the fit term $B$, which represents the unannealed dark current. It is the author's view that this is the dark current in the absence of any defect annihilation, where annihilation of P2 was already established to occur as low as 150 K. Because of finite temperature ramp time, it is impossible to measure the 400 K dark current pre-anneal, and it can only be modeled from the low-temperature *in situ* data. Using the data from Figure 4.12a, the value of $B$ at 400 K was found as 4.1 mA using a simple exponential relationship with temperature. However, the $B$ found from the fit was only 0.16 mA, which was the result of assuming a ten minute delay for the temperature ramp

from 300 K to 400 K. The difference was too large, meaning that the exponential model must have failed to accurately describe the dark current above 300 K. However, the 4.1 mA value set an upper limit on the logarithmic decay rate, that being 0.10, thus the true anneal rate at 400 K was somewhere between 0.02 and 0.10. Apparently, fitting a decay rate to Equation 4.3 reliably across multiple temperatures will require a different approach than done here.

## 4.9 Trap Dependence on Angle of Incidence

A standard irradiation test will irradiate the sample at normal incidence. It is well-known from ion implantation that implanting directly along a crystal direction, such as <110>, will cause nonlinear channeling effects. However, outside of this effect, the angle is not predicted to cause any nonlinear effects within the forward scattering regime of the radiation (*i.e.* avoiding end of range effects). The angle might change the path length of the radiation in the material, but this can be accounted for with simple trigonometry. To confirm this hypothesis, custom sample mounting blocks were made to enable exposure at specific angles. Three samples were exposed at room temperature with $1 \times 10^{12}$ cm$^{-2}$ fluence of 2.0 MeV protons, but with increasing angle of incidence from normal to 60° to 80°. Channeling was not desired and channeling angles were avoided. The 0° and 80° samples were exposed to room temperature for 2 hours before DLTS was performed, while the 60° was exposed to room temperature for 4 hours.

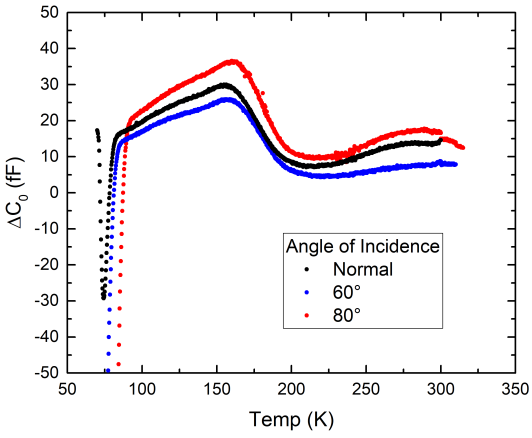


Figure 4.17: DLTS spectra for three diodes, each exposed to $1 \times 10^{12}$ cm$^{-2}$ 2.0 MeV protons at room temperature but with different angles of incidence.

The resulting spectra are in Figure 4.17. The change in angle did not produce any new peaks, but the peak heights were different. The P2 peak height was 30 fF for 0°, 26 fF for 60°, and 36 fF for 80°. Experimental error was perhaps 10% and could account for this difference. The 60° sample was exposed to room temperature for longer which would explain the reduced peaks for that sample. One hypothesis is that the path length of a proton through the device increases by a factor of $\sec\theta$, causing more damage and thus increasing the peak heights. However, in this test, the total number of protons that strike the device is reduced by a $\cos\theta$ factor due to smaller apparent cross-section, leading to a simultaneous reduction in damage. The result here indicated that the longer path length does lead to increased damage, likely by a factor of $\sec\theta$, which compensated for the reduction in total number of protons incident on the device.

## 4.10 Capacitance vs. Frequency and Admittance Spectroscopy

Multiple attempts were made to separate the P1 and P2 peaks by manipulating testing parameters. One parameter that was changed was the AC frequency used to probe the junction capacitance. As mentioned, all previous results were obtained with 250 kHz as it was the highest frequency that could best avoid the effects of series resistance. However, by changing the frequency, a previously-unseen relationship between P1 and P2 was found. In Figure 4.18 are DLTS spectra collected as a function of frequency from 150 kHz to 1.5 MHz. The effect of series resistance was observed as the sign of N/F1 changed and P1 and P2 peak magnitudes decreased with increasing frequency. This effect will be discussed later. Most importantly, it was apparent from the figure that the position and temperature onset of P2 was frequency dependent, whereas the P1 location was relatively resistant to changes in frequency.

It was also noticed that the onset of the P2 peak was closely correlated to behavior observed in the steady-state junction capacitance. Figure 4.19 shows the capacitance behavior at -1.5 V applied bias as a function of frequency and temperature. There are three clear regimes observed. At low temperature, the traps emit slowly compared to the AC frequency ($e_n \ll 2\pi f_{ref}$) and cannot respond. The capacitance measured here was the high-frequency capacitance and corresponds to the depletion width from Equation 2.18, where only the shallow

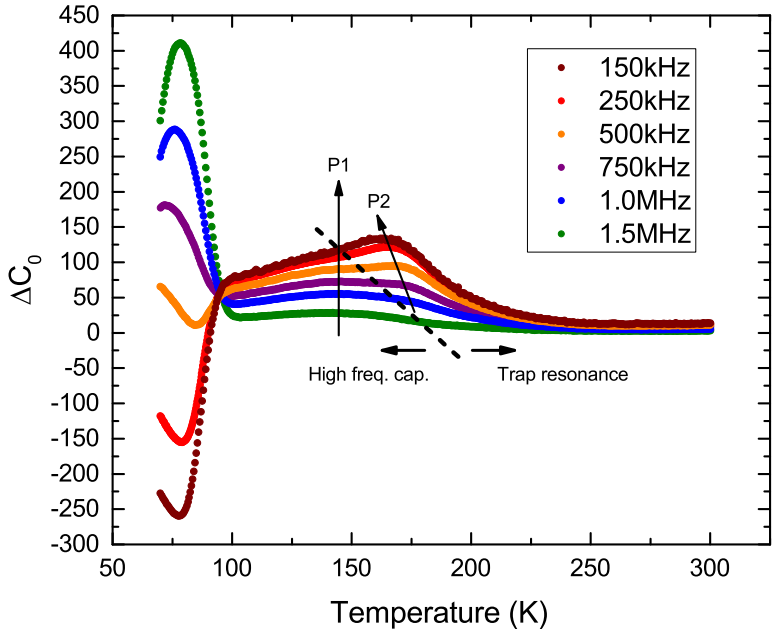


Figure 4.18: DLTS spectra for different AC frequencies. The line indicates the change in capacitance regimes for each frequency. The hypothesized trend of the P1 and P2 peaks with frequency are shown.

donors and acceptors contribute. In contrast, at high temperature was the low-frequency capacitance ($e_n \gg 2\pi f_{ref}$), where traps responded nearly instantaneously to the changing field, causing the depletion width to deviate from Equation 2.18 increasing the measured capacitance. The intermediate regime is caused by trap resonance ($e_n \approx 2\pi f_{ref}$), where traps respond to the AC frequency slowly so that a lag is introduced to the phase between current and voltage, leading to a change in the conductance. This conductance change had some effect on the capacitance transients collected in this regime. It could be that the carriers from traps that capture and emit during an AC period then go on to interact with the traps that emit after the DLTS pulse, leading to some cross-talk or hysteresis.

The conductance change described above is the principle behind defect characterization via admittance spectroscopy. To determine which trap state was causing the capacitance behavior seen in Figure 4.19, steady-state capacitance and conductance vs. frequency were measured as a function of temperature. From the capacitance vs. angular frequency ($\omega$) data, shown in Figure 4.20, a few observations were made. There is a cut-off frequency, around 300 kHz, due to high series resistance that caused all data to attenuate and converge at higher frequency. At temperatures below 160 K, the different frequency regimes seen in Figure 4.19

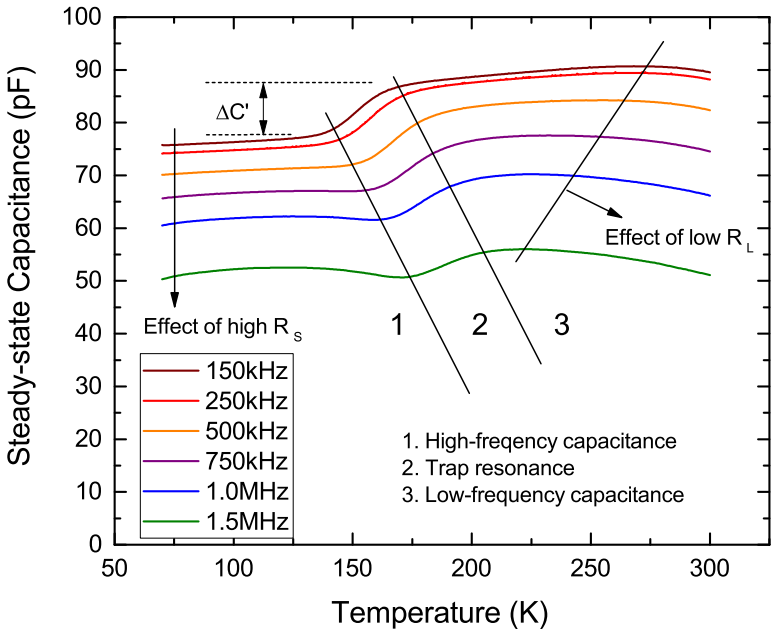


Figure 4.19: Steady-state junction capacitance vs. absolute temperature for different AC frequencies. Taken during the DLTS scan.

are apparent. Conductance/frequency vs frequency (Figure 4.21) showed peaks for the temperatures and frequencies where the trap resonance was observed.

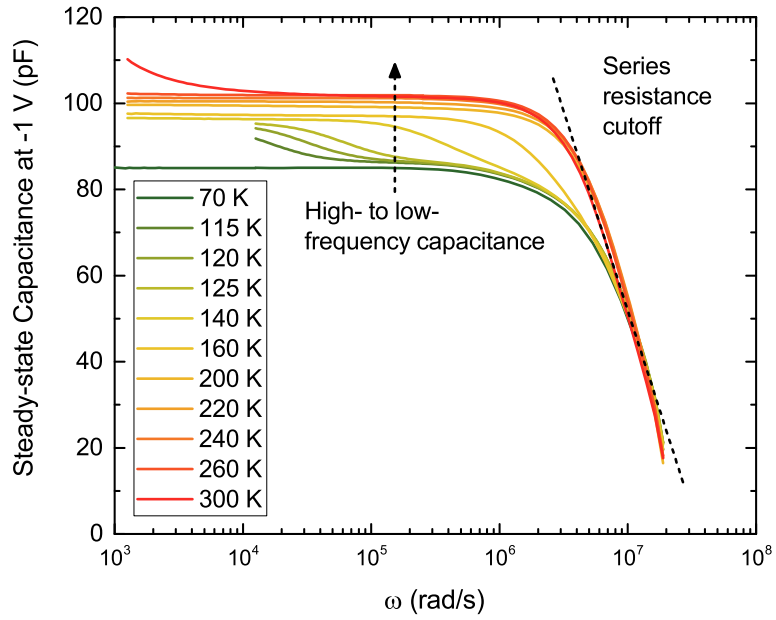


Figure 4.20: Capacitance vs. angular frequency for different temperatures.

The peaks from Figure 4.21 were used to make an Arrhenius plot similar to the one for

DLTS. The emission rate for a trap responding to a sinusoidal AC frequency is simply twice the angular AC frequency ($e_n = 2\omega_{ref}$). The extracted activation energy was 0.16 eV, and the cross-section was $9 \times 10^{-16}$ cm$^{-2}$. It is likely that this trap was caused by sidewall defects, as the steady-state capacitance change from Figure 4.19 was seen in both irradiated and unirradiated diodes. Diodes with sidewall passivation do not exhibit this capacitance behavior. Because this shallow trap alters the capacitance of the diode in unpredictable ways, the validity of the values for traps P1 and P2 must be questioned. It could be that P1 is the only 'real' trap caused by irradiation and P2 is an artifact generated from a combined capacitance effect from of N/F1 and P1.

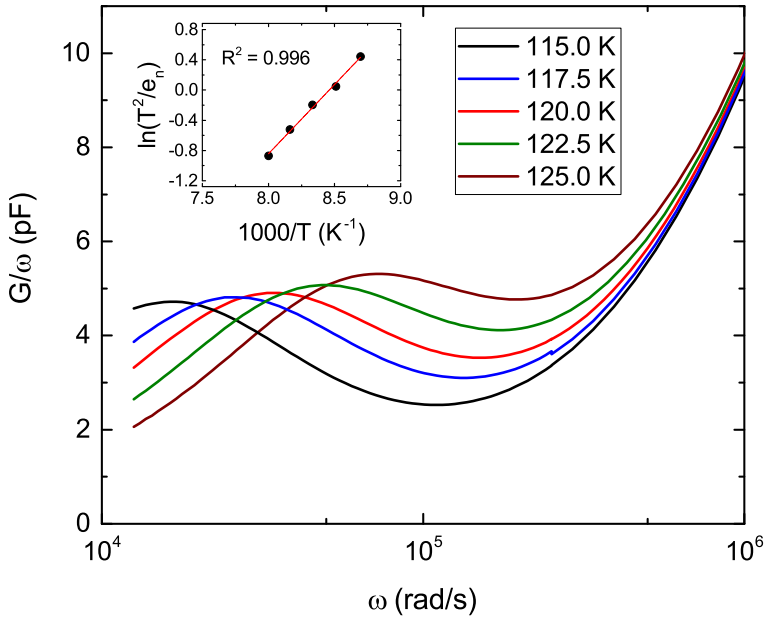


Figure 4.21: Conductance divided by angular frequency vs. angular frequency data for 5 different temperatures, zoomed in to the defect peaks. (b) Arrhenius plot constructed from the defect peaks.

Series resistance behaves as a low-pass filter for a series RC circuit. The cut-off frequency caused by $R_S$ can be seen in Figure 4.20, where attenuation occurred for angular frequencies higher than 1 MHz. By applying a series RC circuit model to the measured impedance, value of 1000 Ω was obtained for $R_S$. This amount of resistance was not seen in the DC J-V measurements, where 10 Ω was obtained for $R_S$. The reason for the large discrepancy was not determined but may have to do with with measuring $R_S$ under reverse bias for AC and forward bias for DC. A typical GaAs diode has an $R_S$ between 10-20 Ω from the AC impedance

measurement, two orders of magnitude less than the diodes measured here. The reason for this is the high sheet resistance of the p-type layers combined with the lack of full metal grid coverage. The problem was worse on the larger 1.0 mm and 1.7 mm diodes than the 0.5 mm.

## 4.11 Conclusion & Future Work

The key result found was that no additional traps could be detected by the *in situ* measurements compared to *ex situ* ones for the parameter-space explored here. What was found was significant annealing that occurred quickly at room temperature, which was prevented by performing the measurement *in situ*. Comparing the *in situ* and *ex situ* results in Figure 4.14, one can see that initially the P2 peak height was 450 fF, but after room temperature exposure for 2 hours, this same peak height was only 150 fF. More evidence of fast room-temperature annealing was the gap seen in the *in situ* DLTS signal at 200 K during a pause in the DLTS scan for dark J-V collection. Even with just a 10 minute pause at 200 K the DLTS signal was reduced by 25 fF. From this observation, a reduction of 100's of fF of the peak height at room temperature is not a surprise. Overall, the *in situ* measurements were successfully performed and low-temperature annealing behavior in InGaAs was observed for the first time. While no extra *in situ*-exclusive traps were found in $In_{0.54}Ga_{0.46}As$, it has been shown that *in situ* trap peaks do occur in other materials [8] and a test system such as used here has the best chance of finding them.

The InGaAs traps discovered were most closely reminiscent of those found by Shaw *et al.* [111], Ohyama *et al.* [112], and Marshall *et al.* [113] (see Table 4.1). Shaw *et al.*irradiated with electrons, but different radiation species often create similar traps for a given material as seen in GaAs where electrons, protons, and alpha particles all lead to similar DLTS results [117]. What was different between the electron result and the present proton result is that the electron-induced E1 trap was shallow and observed between 50 K and 100 K, while P1 was a much deeper trap consistently found in the range of 100 K to 150 K. Ohyama *et al.* irradiated InGaAs with 1 MeV neutrons and Marshall *et al.* with 63 MeV protons. The trap found by Ohyama *et al.* around 150-200 K with energy $E_C - 0.37$ eV was similar to P2 found in this work. For Marshall *et al.*, who also used protons, the energy of 0.31 eV was

similar to P2 but the spectra look very different compared to most of the other reported data, including the data presented here. It could be that the spectra change when the particle energy is much higher. Reported here was virtually no difference in the result from 2.0 MeV and 3.5 MeV protons. Another possible difference in the spectra could be from the different epitaxy techniques used to grow the crystals. The Shaw *et al.* diodes were grown via vapor phase epitaxy (VPE), and a different radiation-induced trap profile between VPE- and MOCVD-grown crystals has been observed before for InP [123]. The mechanism for this is that the growth methods change the contaminants which then interact with the radiation-induced defects.

The annealing results at 400 K indicated that the P3 trap anneals the fastest, P1 the slowest, and P2 somewhere in between. The remaining factors indicated that, at least after significant annealing has occurred, the trap driving the dark current was P1 and not P2. The P3 trap was annealed below the detection limit in 3 hours or less.

Exposing three samples at room temperature but with different angles of incidence did not lead to an observation of new traps. Increasing angle increased the damage done by each proton as the proton path length in the active region increased, likely by a factor of $\sec\theta$ or greater. At the same time, the total number of protons seen by a device as it was angled was decreased by the same factor due to smaller apparent area. The difference in the spectra did not follow a trend and was within experimental error.

Admittance spectroscopy of an irradiated diode discovered a single trap and provided insight into the relationship between the traps P1, P2, and N/F1. The trap had an activation energy of 0.17 eV and cross-section of $9 \times 10^{-16}$ cm$^{-2}$ and had to have been a native fab-related trap as the capacitance shift that caused it was found in the pre-irradiation diodes, as well. It is reasonable to believe that this trap is the same as N/F1, as DLTS itself could not resolve N/F1 reliably due to deviation of the transients from the thermal emission model of Equation 2.20b. This trap was suspected to originate from the device sidewall. Coincidentally, the capacitance shift of this trap occurred at a frequency and temperature that overlapped the DLTS peak of P1 and P2. A change in the capacitance-probing AC frequency led to a shift in P2 peaks where no such shift was expected. It was difficult to determine if P1 also shifted but,

if it did, it appeared to shift less than P2. It may be that both P1 and P2 were the same trap or that P2 is an artifact of P1 due to interference of N/F1.

It is known that an $R_S$ of high magnitude, such as found here, can reduce DLTS peaks and even invert them [124]. This is a reasonable explanation for the N/F1 peak behavior seen in Figure 4.18. As $R_S$ is reduced with decreased frequency, the true peak would be most like the 150 kHz data. On the other hand, this would make the peak a minority carrier peak when minority carriers were not supposed to have been injected. These conflicting observations, along with the previously mentioned deviation from the standard thermal emission model, made it difficult to determine the nature of N/F1. The resistance could be lowered by covering the entire diode with metal, eliminating any spreading resistance problem (see Figure 4.5b). As well, the emission equation can be modified to take include the Poole-Frenkel effect or phonon-assisted tunneling from traps and these effects could more accurately model the N/F1 trap [48]. Qualitatively, both the sidewall behavior in J-V and the N/F1 trap behavior in DLTS were unstable, unpredictable, and appeared to be related to tunneling.

The effect of sidewalls can be eliminated with proper passivation. The industry standard for InGaAs on InP is to use a diffused, rather than epitaxial, emitter [109]. This allows the sidewall of the diode to be physically separated from the InGaAs junction and thus the depletion region, which is the DLTS test region, does not include any sidewall states in the low-bandgap InGaAs.

# Chapter 5

# GaSb-GaAs Multijunction Solar Cells with Interfacial Misfit Arrays

## 5.1 Summary

A growth technique to grow lattice-mismatched GaSb on GaAs substrates could lead to record efficiencies due to a wide array of bandgaps available to both GaSb and and GaAs lattice constants. It could do this at lower cost than the IMM as there is no need for the thick graded buffer. GaSb single-junction solar cells were grown on both GaSb and GaAs substrates to evaluate the growth technique, but the lattice-mismatched growth clearly suffered from higher threading dislocation density. Nevertheless, the material as-is was shown, by simulation, to be useful as the bottom junction of an InGaP/GaAs/GaSb 3-J concentrator cell, beating the InGaP/GaAs 2-J cell by 2.5% absolute at 40 suns.

This chapter has seven main topics:

1. GaSb Solar Cell Design, Growth, and Fabrication.
2. GaSb Wet Etching.
3. MBE GaSb Defects.
4. Sidewall Leakage and Sidewall Passivation.
5. GaSb Cell Results.
6. IMF GaSb DLTS.
7. IMF Triple Junction Simulation.

## 5.2 Motivation & Background

### 5.2.1 Motivation

An alternative to the high efficiency IMM multi-junction cell is the III-Sb multi-junction with interfacial misfit (IMF) arrays. The IMF growth technique enables growth of III-Sb materials directly on GaAs or Si without the need for a step graded buffer [125, 126]. When compared to the IMM cell, the III-Sb IMF multi-junction cell has two significant advantages. One is, as mentioned, the foregoing of the growth-intensive and costly metamorphic grade in favor of an IMF monolayer. In 2013, Woodhouse *et al.* found that the metamorphic buffer of a dual junction Si/GaAsP IMM cell accounted for ∼29% of the capital expenditure of the cell [3], and this cost would be similar for other IMM designs. A summary of IMM costs is depicted in Figure 5.1. The second advantage is the wide range of well-developed direct bandgap materials that are lattice-matched to GaSb. This bandgap range begins at 0.3 eV with InAsSb and extends up to 1.3 eV with AlGaAsSb. With the GaAs and GaSb lattice constants, therefore, the combined direct bandgap range available is roughly 0.3 eV to 1.9 eV [127]. This presents a straightforward path to cells with 4, 5, or more junctions with only a single IMF layer required. The IMM multi-junction cell, in contrast, will require one or more additional graded buffers for additional junctions, adding to its cost.

As a long-term goal, Lumb *et al.* modeled that a 7-J series-connected cell can achieve 54.6% efficiency under 1000-sun concentration, where the lower bandgaps, down to 0.5 eV, can be achieved with GaSb-based material [127, 128]. Medium-term, an inverted InGaP/GaAs/$Al_{0.3}Ga_{0.7}Sb$(1.0 eV [129]) IMF 3-J solar cell could be a less-expensive substitute for the 3-J IMM InGaP/GaAs/InGaAs(1.0 eV) cell. A Sentaurus TCAD simulation of this cell is shown in Figure 5.2, and, since this cell has the same bandgap combinations as the 3-J IMM cell, the simulated efficiency of 38.7% (AM1.5G) is comparable to the 3-J IMM record [72]. From a growth and fabrication point of view, however, the simplest goal in the short-term is an IMF GaSb 1-J cell to evaluate the impact of the IMF growth on device properties. And although the GaSb bottom cell bandgap is not ideal for a triple junction cell (1.0 eV AlGaSb will current match and contribute higher voltage), a GaSb subcell could still be used in a cell

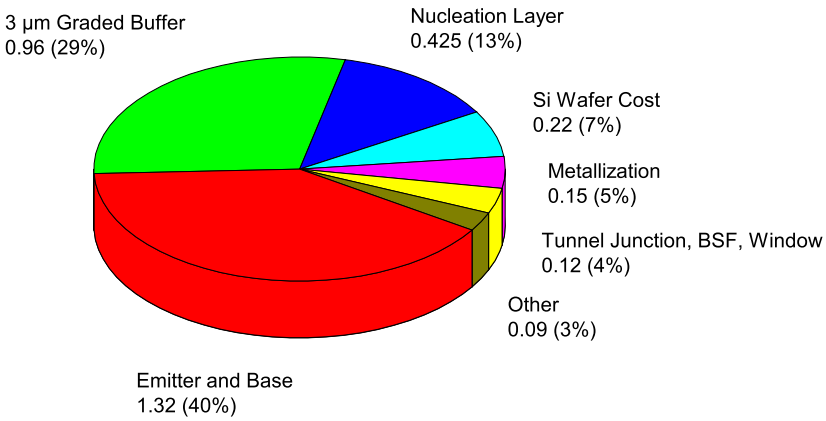


Figure 5.1: Capital expenditure analysis of a modern dual-junction solar cell by NREL [3]. The values are USD per watt.

of 4 or more junctions.

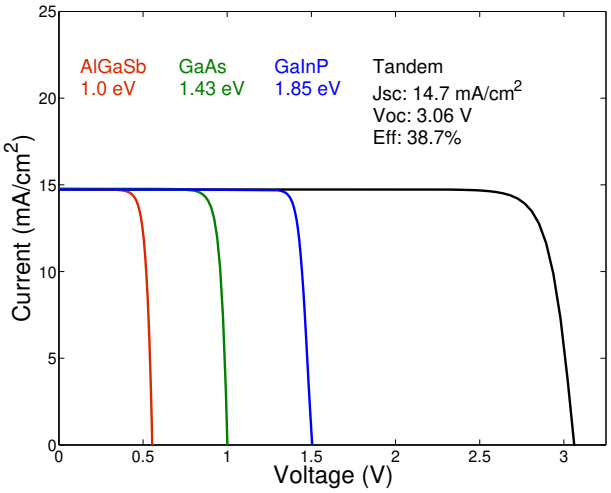


Figure 5.2: Simulated 1-sun AM1.5G J-V of a current-matched GaInP/GaAs/AlGaSb(1.0 eV) cell. *Data and plot by Dr. Staffan Haelstrom*

### 5.2.2 Background

IMF technology has been used in the past successfully for InGaAsSb photodetectors grown on GaAs [130], and has recently seen interest for applications to photovoltaics [9]. Without

the IMF technique, the high degree of strain (7.8%) caused by growth of a III-Sb material such as GaSb on GaAs results in strain relief in the form of misfit dislocations that cause 60° threading dislocations to propagate through the active region of the device. However, with an IMF array, nearly all strain (98.7% for GaSb-on-GaAs) is strategically relieved by a sequence of 90° Lomer dislocations [131]. The technique takes advantage of the alignment of a period of 13 GaSb lattice (13 × 0.609/1.414 nm = 5.599 nm) sites with that of 14 GaAs sites (14 × 0.565/1.414 nm = 5.594 nm). This is demonstrated by the diagram and TEM image in Figure 5.3. To keep the dislocations confied to the interface, the growth conditions are carefully controlled. In previous work, an IMF GaSb layer grown on GaAs was found via transmission electron microscopy to have a dislocation density of only $5 \times 10^5$ cm$^{-2}$, an order of magnitude lower than published 2% grade IMM [132].

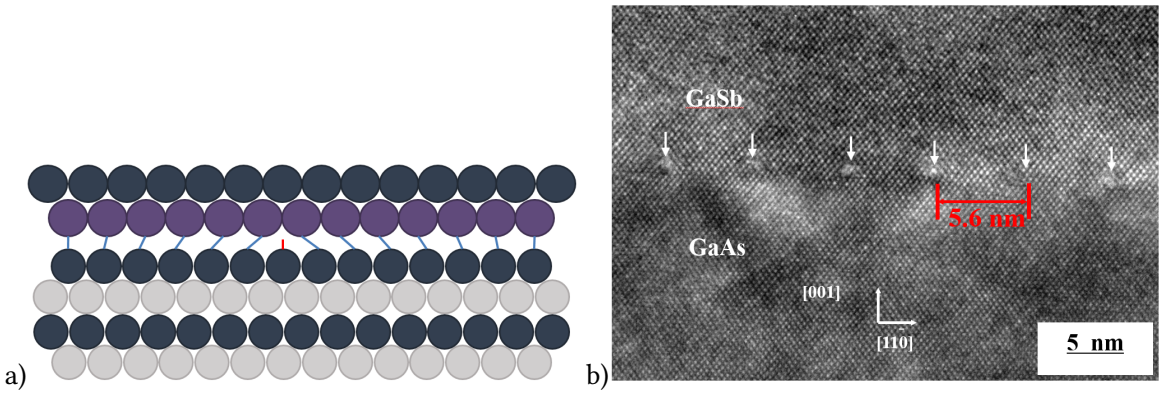


Figure 5.3: a) Crystal structure diagram of IMF interface for one period of GaSb/GaAs, seen from (110) direction, with missing bond responsible for misfit dislocation indicated by red dangling bond. b) TEM image of the GaSb/GaAs IMF interface with in-plane dislocations visible with period of 5.6 nm. No threading dislocations were seen in the GaSb epilayer. *TEM image courtesy of Huffaker group at UCLA.*

The highest efficiency IMF cells thus far by the author's research group has been a 1.0% efficient MBE-grown GaSb 1-J cell [133] and a 2.2% efficient (2 µm buffer) MOCVD-grown GaSb cell [84, 134], both at <1 mm$^2$ in size. These cells compare favorably to other reported IMF GaSb cells from Tufts [135], University of New Mexico [136] and from the collaborators at UCLA [9]. UCLA reported a 0.7% efficient cell with a size of 0.1 mm$^2$. However, despite the lower efficiency, the UCLA cell had the highest FF due to higher $R_{Sh}$ and lower dark current, perhaps caused by the thicker post-IMF buffer layer which lowers TDD. The most notable deficiency in the UCLA cell was lower photo-generated current. $J_{SC}$ in the UCLA cell was

likely low due to the thickness of the emitter, which was 450 nm compared to 125 nm in the RIT cells. This emitter thickness is too high compared to the IMF diffusion length, and since most of the current is absorbed in the top of the cell the loss could be substantial. The UCLA $J_{SC}$ was 15.5 mA/cm$^2$ compared to the RIT 1.0% cell which had 29.9 mA/cm$^2$. Figure 5.4 depicts the EQE of the UCLA cell and the RIT cell (before deposition of an anti-reflective coating), where there is a notable difference in the shape. At 800 nm, which is mostly absorbed in the emitter, the RIT cell had ∼55% EQE whereas the UCLA only had 30%. At longer wavelengths the two IMF cells converge to ∼25%, limited by diffusion lengths in the base, as will be seen.

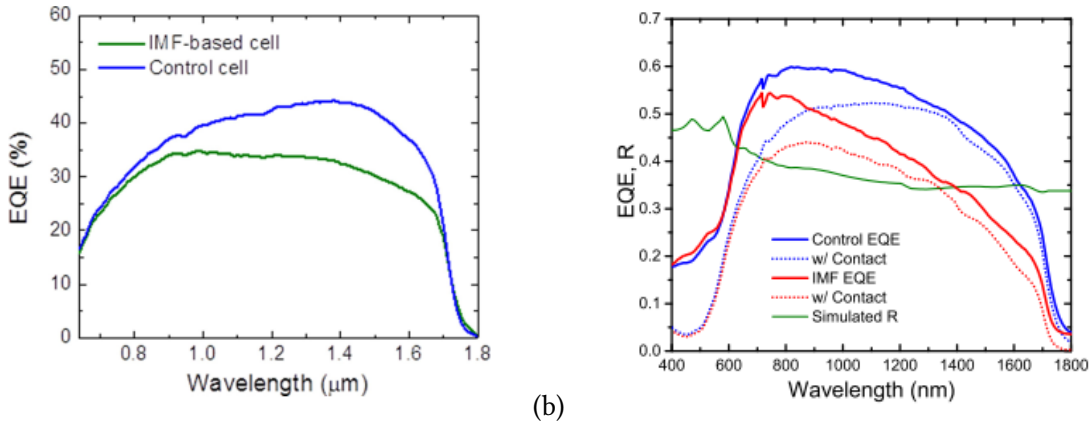


(a) (b)

Figure 5.4: EQE of the MBE-grown cells with UCLA design (a) [9] and RIT design (b). The UCLA cells appear to match the RIT cells before the RIT cells were contact etched. The RIT contact layer is a 'dead' layer causing parasitic absorption, and the similarity to the UCLA data may be because the too-thick emitter was also behaving as a 'dead' layer.

If one is to grow and fabricate an efficient IMF solar cell, it is a virtual requirement that one must first be able to grow and fabricate an efficient homoepitaxial GaSb cell. For many years, the best GaSb cells were formed from a GaSb substrate with a diffused junction [137]. No epitaxy was required for these cells. In 2006, an MOCVD-grown epitaxial junction GaSb cell was reported to be 10% efficient under 1-sun AM1.5G with a size of 1.5 cm$^2$ [138]. MBE-grown cells have lagged behind, with 5.9% reached in 2018 at 0.25 cm$^2$ [139], following the author's 5.5% in 2017 [133].

## 5.3 GaSb Solar Cell Growth, Design, and Fabrication

Cells were grown on p-type 2“ GaSb (001) and GaAs (001) substrates via MBE using a Veeco Gen 930 solid-source reactor. Control cells were grown homoepitaxially on GaSb substrates, while the IMF cells were grown on GaAs substrates with the IMF growth technique, the details of which are discussed in previous work [132]. To summarize, IMF growth began with a GaAs buffer layer grown at 580° C followed by growth pause leading to As desorbtion at the surface. This surface behavior was detected by the switch from a (2x4) As-rich reflection high-energy electron (RHEED) pattern to a (4x2) Ga-rich pattern. Flux of $Sb_2$ was then applied until the RHEED pattern changed to (2x8) to indicate an Sb-rich surface. Finally, the the substrate was cooled to the GaSb growth temperature before commencing with GaSb growth. Epitaxial GaSb layers were grown at a growth temperature of 500 ℃ and a V/III BEP of 6. The p- and n-type dopants were Be and Te, respectively.

The fabricated IMF cell structure in Figure 5.5 depicts layers grown along with thickness and doping values. The control cell was grown identical to the IMF device, but on a GaSb substrate and without the GaAs buffer and IMF procedure. Strained $Al_{0.3}Ga_{0.7}Sb$ (1.0 eV) was grown as the front window material, but a back window was eschewed in favor of a GaSb back surface field (BSF) layer to prevent strain in the base and emitter. InAs was chosen for the contact layer as it could be highly doped and a selective wet etch against (Al)GaSb was available. A thin i-region was added to prevent inter-diffusion between dopants at the junction by dopant diffusion. The p-type base and n-type emitter were grown 1000 nm and 125 nm thick with doping $1\times10^{17}$ $cm^{-3}$ and $1\times10^{18}$ $cm^{-3}$, respectively. These thicknesses were chosen based on diffusion lengths obtain from the IMF cell results by Juang *et al.* [9]. While the homoepitaxial cell was expected to have diffusion lengths than the IMF cell and could presumably take advantage of an optically thick, $\sim$3 μm, absorber, both cells were matched in thickness to maintain a straightforward comparison. The n-i-p polarity was chosen because this would match a standard IMM polarity and high mobility of majority electrons in the emitter reduces series resistance which is important for high concentration.

Figure 5.6 is a process flow of GaSb cell fabrication. Fabrication procedure was identical

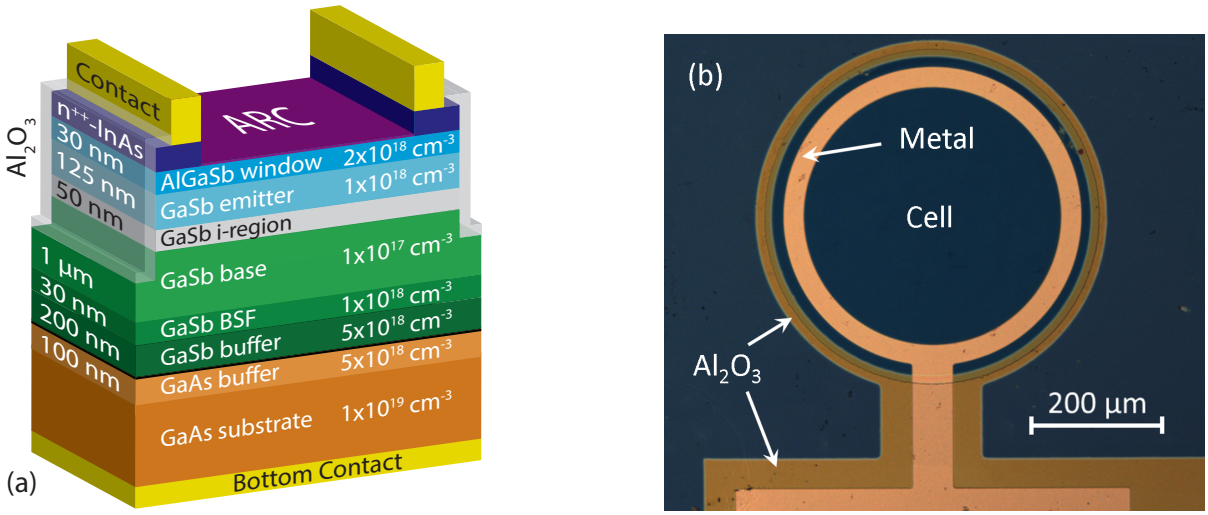


Figure 5.5: (a) Layer structure of the IMF cell and (b) microscope image of sidewall-passivated GaSb cells.

on IMF and homoepitaxial cells. A citric acid/HF/$H_2O_2$ solution was used to etch device mesas. A sidewall passivation scheme known to work for GaSb-based infrared detectors was adapted to replace the sidewall oxide with $Al_2O_3$ [140]. The mesa etch and passivation are discussed in more detail in Sections 5.4 and 5.6, respectively. Before passivation, the native oxide was removed using 1:1 HCl:$H_20$ [141] and transferred to a 2nd generation Cambridge Nanotech Savannah atomic layer deposition (ALD) reactor. A 100-nm-thick layer of $Al_2O_3$ was deposited on the entire sample at 150 ℃. The passivation layer was then patterned with photoresist and etched in 50:1 $H_2O$:HF solution to leave $Al_2O_3$ only on the sidewalls. An evaporated metal stack of Pt/Ti/Au was used for the back contact while Ti/Au formed the front-metal grid. The 50 nm InAs contact layer was etched using a citric acid and peroxide mixture (1:1) for 50 sec, which was selective over AlGaSb by a factor somewhere between 130 to 3000 [142]. Finally, a two-layer anti-reflective coating (ARC) of $MgF_2$ and ZnS was deposited. The $MgF_2$ thickness was 136 nm, the ZnS was 72 nm, and these thicknesses were determined via minimization algorithm that reduced average reflection over the wavelength range of 500 nm to 1200 nm (see reflection in Figure 5.15).

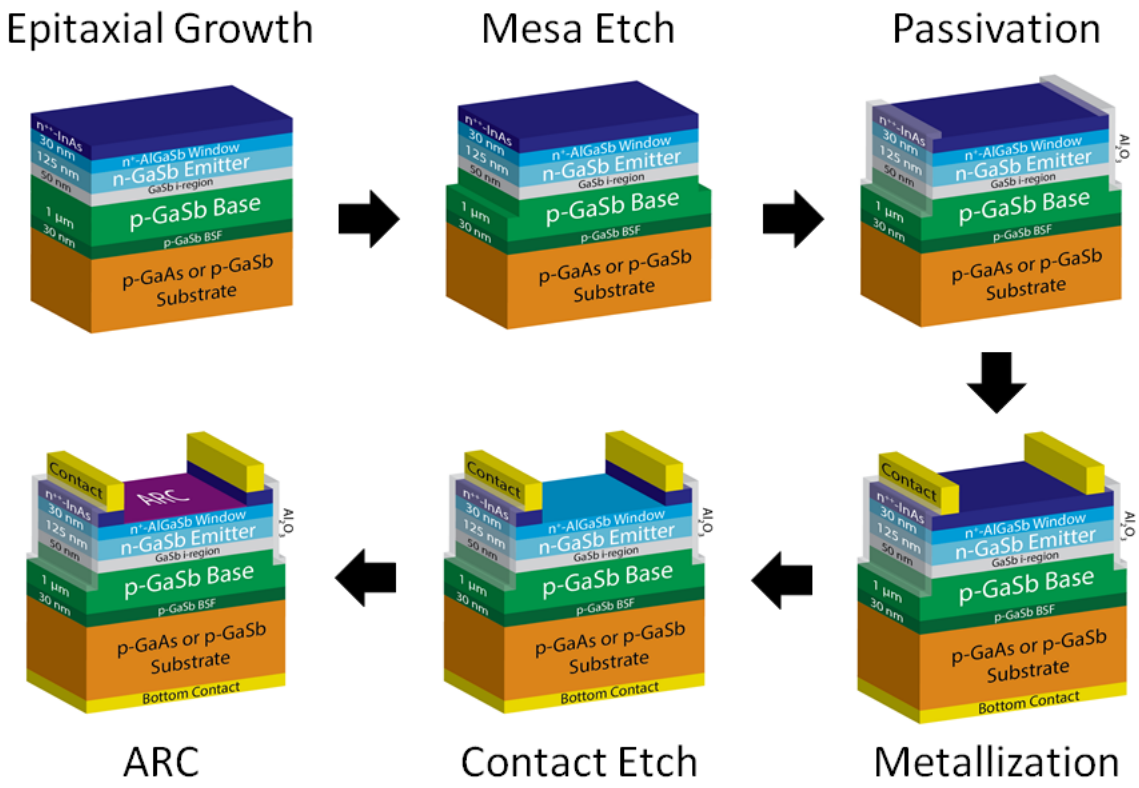


Figure 5.6: Fabrication flow for small-area sidewall-passivated solar cells.

## 5.4 GaSb Wet Etching

Without convenient access to a dry etch tool, several wet etches were developed and tested to isolate the GaSb device mesas. Previous work utilized a dry etch chemistry, $BCl_3$/Ar [9]. The dry etch profile was imaged by scanning electron microscopy (SEM) (Figure 5.7 (a)) and it proved to be anisotropic, as expected. Replicating the well-behaved dry-etched sidewall surface was the initial goal of the wet etch experiments. It should be noted that the dry etch procedure by Juang *et al.* ended with a short wet etch in HCl:$H_2O_2$:$H_2O$ (1:1:100 volumetric ratio) to clean the surface of damage caused by the dry etch, so this etch may be considered a dry and wet etch hybrid.

Several rounds of etch tests were required to attain the desired wet etch results. The etch process of III-V material typically is a two-step chemical process, where an oxidizer is needed to oxidize the semiconductor atoms at the exposed surface and an acid is used to dissolve the surface oxides [143]. A common oxidizer used in many well-known wet etch chemistries is

hydrogen peroxide, $H_2O_2$. Initial tests with diluted solutions of HCl and $H_2O_2$ resulted in a black (rough) surface and shallow etch termination. Continued etching had no effect. This was likely due to the formation of $Sb_3O_6$, which is insoluble in any known acidic or alkali solution and forms when GaSb is exposed to a strong oxidizer such as $H_2O_2$ [144]. Therefore, the use of $H_2O_2$ can result in the a build up of $Sb_3O_6$ at the surface, which cannot be etched by HCl or HF and causes the etch to halt.

With this in mind, etch solutions without a strong oxidizer were tested. Unlike GaAs, GaSb can be etched by weak bases alone via a mechanism that is not fully clear [145]. Both ammonium hydroxide ($NH_4OH$,) 30% and tetramethylammonium hydroxide (TMAH) 5% were tested. Without agitation, both solutions etched very slowly and with poor uniformity, though the TMAH solution had a clear advantage in these aspects. With constant stirring, however, the rate of the TMAH solution improved to a more reliable 25 nm/min. It is likely that the $NH_4OH$ solution would have also benefited from stirring, however this was not tested. The TMAH, with stirring, was used to etch AlGaSb and GaSb in the preliminary devices and the resulting etch profile of an IMF sample was imaged by SEM (Figure 5.7 (b)). As seen, the etch resulted in roughness on the sidewall and and pitted marks on the etched surface. This might have been caused by the etch chemistry by itself in some way, or it may be that these features were the result of a reaction of the chemistry with defects, such as threading dislocations, in the IMF test piece. If the latter was the case, then the EPD of the IMF in this sample was $\sim 5 \times 10^7$ cm$^{-2}$. A TMAH-etched homoepitaxial device was not imaged.

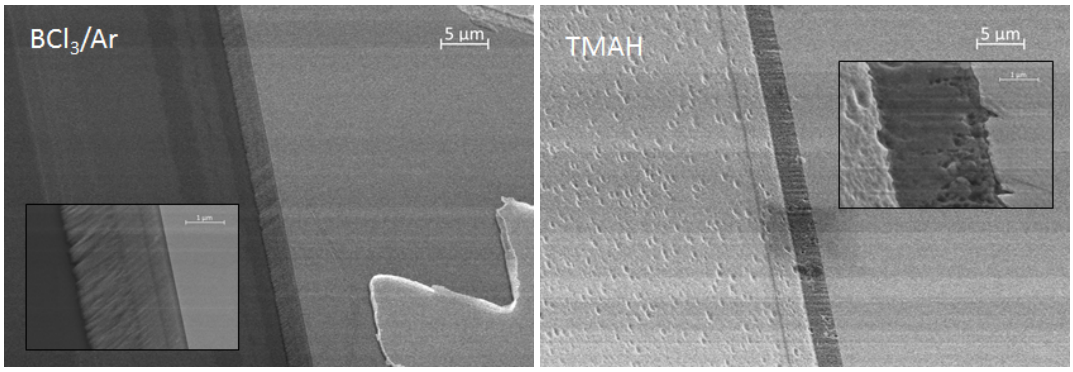


Figure 5.7: SEM etch profiles for the dry and TMAH etches.

After the preliminary devices were fabricated, the TMAH-based mesa etch was abandoned and a new wet etch chemistry was sought for two reasons. Firstly, the device results indicated that sidewall conduction and recombination were limiting the performance of smaller devices (discussed below), and the roughness seen in the TMAH-etched sidewall was a concern as it exposed more surface area. Secondly, TMAH is a positive photoresist developer which posed a significant risk to the photoresist used as the etch mask. The lengthy etch time and agitation meant that even unexposed photoresist could develop, leading to partial etching of the devices.

The strategy for the replacement of the TMAH etch was to return to a more traditional acid and oxidizer mixture, but with the addition of an organic acid such as citric or tartaric acid. Research has shown that the organic acid in the presence of a strong base prevents the formation of the insoluble Sb oxide species [144, 146]. The two candidates tested were a solution of KNa-$C_4H_4O_6$-4$H_2O$/HCl/$H_2O_2$/$H_2O$ (tartaric solution) and $C_6H_8O_7$/HF/$H_2O_2$/$H_2O$ (citric solution). After some iterations, the optimized relative concentrations were found to be 12 g:33 mL:9 mL:500 mL for the tartaric solution and 40 g:40 uL:10 mL:40 mL for the citric. Preparation of citric solution started by fully dissolving the solid citric acid in the water. Then the HF was added, then the $H_2O_2$, and the solution was allowed to mix for 15 minutes. The tartaric solution was prepared similarly by first dissolving the solid tartrate in the $H_2O$. The addition of HCl to tartaric acid starts an exothermal reaction, so after mixing in HCl the solution was allowed to cool to room temperature before adding the $H_2O_2$ and mixing another 15 minutes before etching. Both of these etches were performed without agitation. It was observed that interaction between the citric acid and SC1827 positive photoresist led to highly scalloped sidewalls post-etch. To prevent this, the S1827 photoresist was cured at 130 ℃ after development and the results improved. Post-development curing was not needed for AZ5214 resist. The tartaric acid solution did not etch or develop any of the used resists (SC1827,SC1813,AZ5214).

The citric and tartaric solutions GaSb etch profiles are shown in Figure 5.8. The citric acid solution etched GaSb anisotropically at a rate of 120 nm/min, while the tartaric etched crystallographically along the (110) plane at a rate of 130 nm/min. Both etched samples exhibited

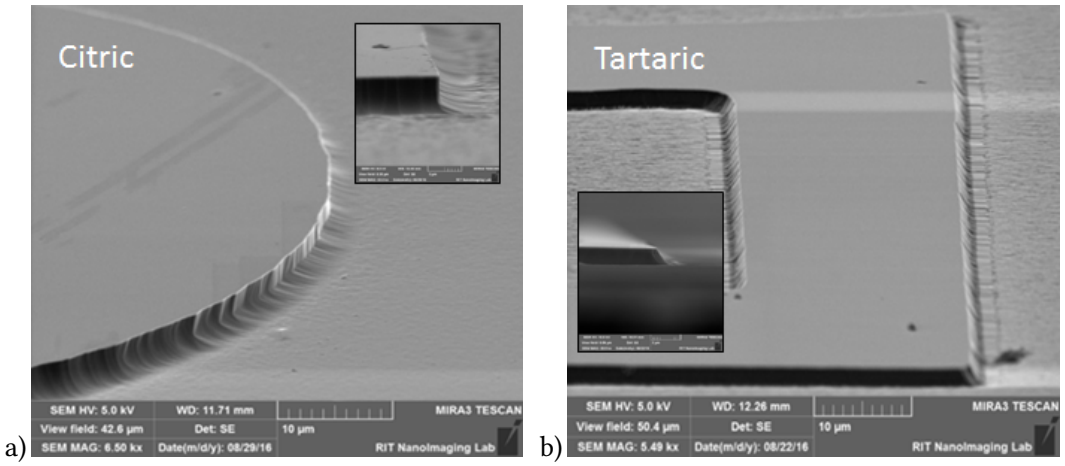


Figure 5.8: SEM etch profiles of the a) citric- and b) tartaric-based etch chemistries. The etch profiles are displayed in the insets.

smooth sidewalls similar to the dry etch.

## 5.5 MBE GaSb Defects

Fabrication of large area cells (1 $cm^2$ range) repeatedly resulted in very low yield due to unpredictable shunting of devices. Figure 5.9 contains dark J-V curves of many small-area diodes taken from a single sample, and it was clear that many diodes were shunted. The $R_{Sh}$ of each of these curves was approximated by taking the slope at zero bias, and the resulting values were binned in a histogram (Figure 5.10). The diodes with $R_{Sh}$ above 100 $\Omega$-$cm^2$ were considered 'unshunted', and for small-area devices (1 $mm^2$ range) the yield was near 50%, which was unsatisfactory.

DLIT was used to determine the cause of the shunt seen in the defective devices that led to low yield, the experimental setup for which is detailed elsewhere [147]. The principle of the technique is that a localized shunt path will heat up as current flows through it and this can be imaged with an infrared camera.

Dark lock-in thermograms (Figure 5.11) correlated well with dark J-V results for shunted and unshunted homoepitaxial cells. The cell in (a) of the figure was known to be shunted as demonstrated by the black dotted dark J-V curve in (d). The current under reverse bias flowed nearly exclusively through a small area in the bottom right part of the image (bright spot

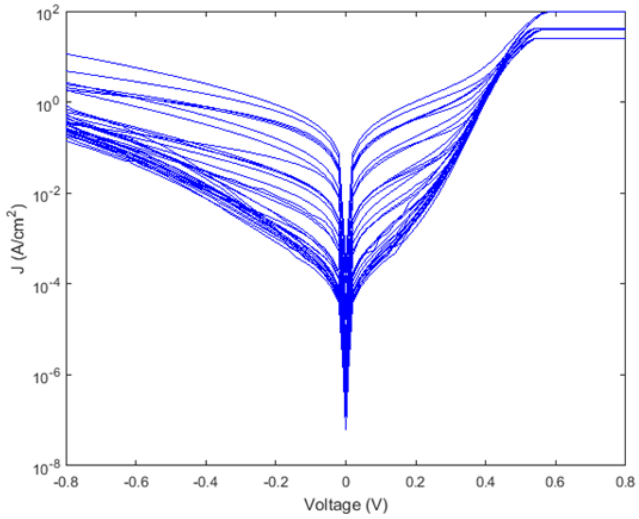


Figure 5.9: Dark J-V uniformity check. The unshunted diodes are clustered at the bottom.

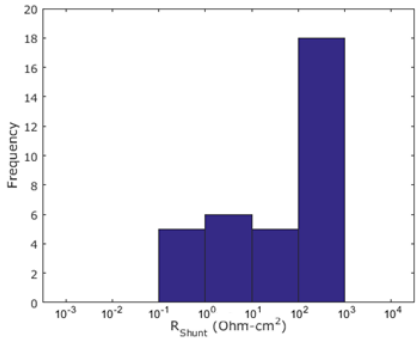


Figure 5.10: Logarithmically-binned histogram of the many diode $R_{Sh}$.

in thermogram). The unshunted cell in (b) of the figure had uniform illumination indicative of normal diode leakage under reverse bias. The trend from these cells and thermograms of other shunted cells indicated that the shunt was related to the front grid metal.

SEM images of surface defects suspected to be responsible for the shunt are shown in Figure 5.12. These defects are similar to the surface defects to those found by Romero *et al.* [148] caused by Ga spitting from the MBE solid source, and the DLIT results above are further evidence for the hypothesis that a shunt is formed when a surface defect void is filled with metal. It is known that using a dual-zone Ga cell in an MBE reactor will reduce the amount of Ga spitting [149]. It may be possible to anneal the samples to remove the voids before metal deposition, as well.

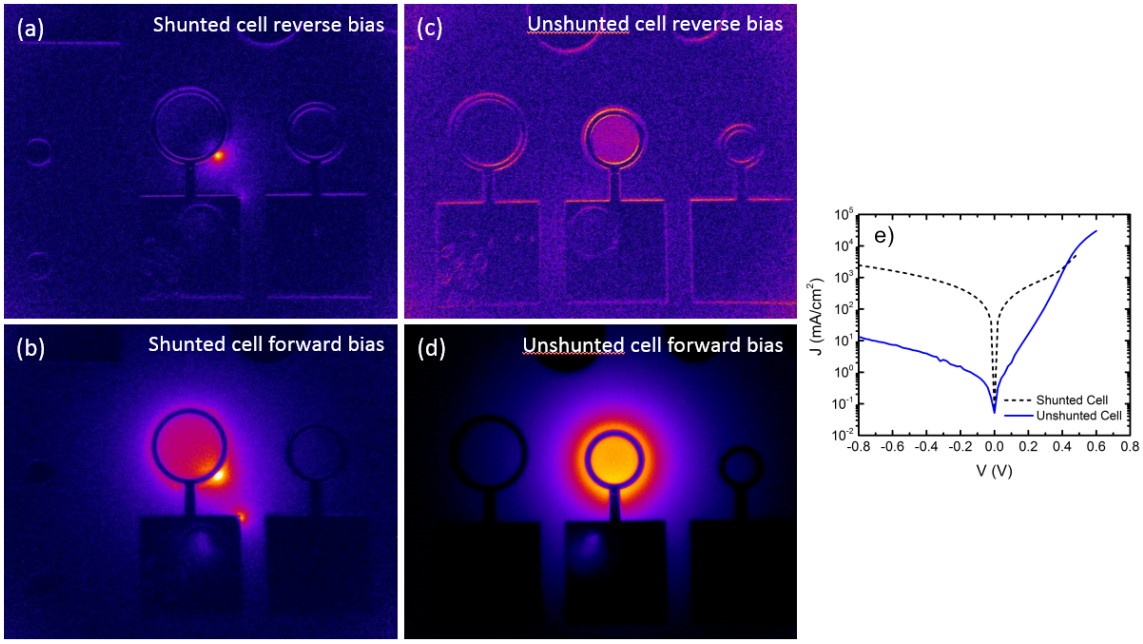


Figure 5.11: Reverse bias thermograms of two cells, a shunted cell (a) and an unshunted cell (b). In (c) is an SEM image of a Ga-rich GaSb surface defect believed to be the cause of the shunt. In the dark J-V results for these cells (d), the dotted line is the cell in (a) and the blue line is the cell in (b).

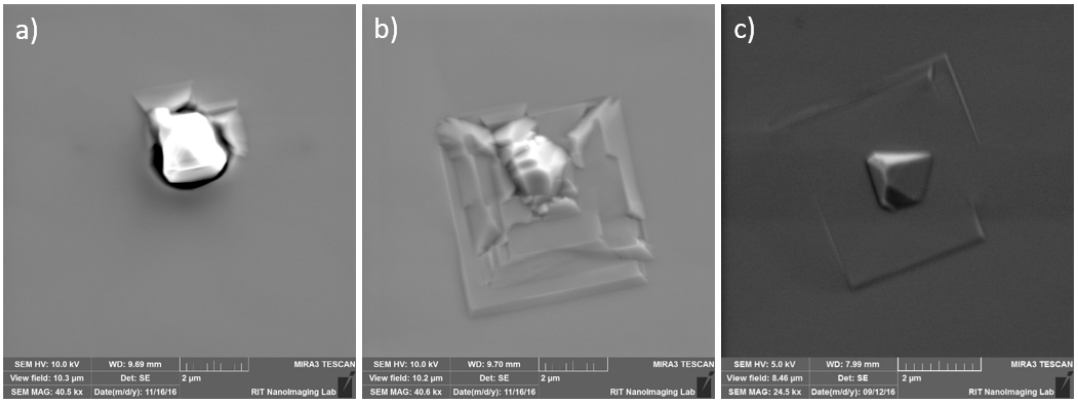


Figure 5.12: SEM images of Ga-rich GaSb surface defects and possible evolution of the defect during growth from a to b to c.

## 5.6 Sidewall Leakage and Sidewall Passivation

The need for sidewall passivation was observed in earlier work by Juang *et al.* [9], and it was confirmed that the homoepitaxial cells of the size used here (circular with 400 µm and 500 µm diameter) were sidewall-limited at 1-sun currents. Rather than use a wet passivation like Juang *et al.*, the procedure from Salihoglu *et al.* for infrared detectors was followed to replace the sidewall native oxide with 100 nm of $Al_2O_3$ deposited by atomic layer deposition using

a 2nd generation Cambridge Nanotech Savannah [140]. Before passivation, the native oxide was removed using 1:1 HCl:$H_20$ [141] and quickly transferred to the ALD reactor. Roughly 100 nm of $Al_2O_3$ was deposited using TMAl and water precursors at 150 ℃ with 5 sec wait time between precursor pulses. The passivation layer was patterned with photoresist and etched in 50:1 $H_2O$:HF solution to leave $Al_2O_3$ only on the device sidewalls (see Figure 5.5).

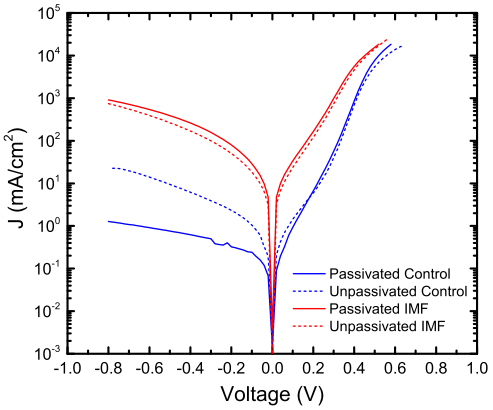


Figure 5.13: Dark J-V for unpassivated (dotted) and passivated (solid) homoepitaxial (control) and IMF cells.

To evaluate sidewall passivation, dark J-V measurements were taken of devices with and without the $Al_2O_3$ layer (see Figure 5.13). Diode parameters of ideality-of-two dark current, $J_{02}$, and shunt resistance, $R_{Sh}$, were fit to the double-diode equation (Equation 2.6) for devices of different radius [9]. Figure 5.14 is a plot of the fitted $J_{02}$ and inverse $R_{Sh}$ as a function of reciprocal device radius for homoepitaxial cells. $Al_2O_3$ coated homoepitaxial devices had, on average, a factor of 5 higher $R_{Sh}$ than unpassivated devices, though this was at the cost of roughly double the dark current. The sidewall-dependence of $J_{02}$ can be determined by,

$$J_{02} = J_{02,bulk} + J_{02,surface} = J_{02,bulk} + \frac{qn_iSW}{r/2}, \tag{5.1}$$

where $n_i$ is the intrinsic carrier concentration, $S$ and $W$ are the sidewall surface recombination velocity and depletion width, respectively, and $r$ is the mesa-defined crystallite radius [150, 151]. Equation 5.1 predicts that the y-intercept in Figure 5.14 represents the bulk-limited $J_{02}$, which was about 25 μA/cm$^2$. The $R_{Sh}$ sidewall-dependence can be found using a similar treatment described elsewhere [152]. From the intercept of Figure 5.14, the bulk-limited $R_{Sh}$

is expected to be up to 1.6 kΩcm$^2$. A larger cell will therefore perform better, however, the difficulties with large-area GaSb device yield were discussed above.

For the IMF cells, $R_{Sh}$ and $J_{02}$ did not show any trend with perimeter and the IMF devices were already bulk-limited. The best IMF $J_{02}$ and $R_{Sh}$ were 2.4 mA/cm$^2$ and 6 Ωcm$^2$, respectively. DeMeo *et al.* attributed the low $R_{Sh}$ of their IMF devices to possible shunt paths along threading dislocations. [135]

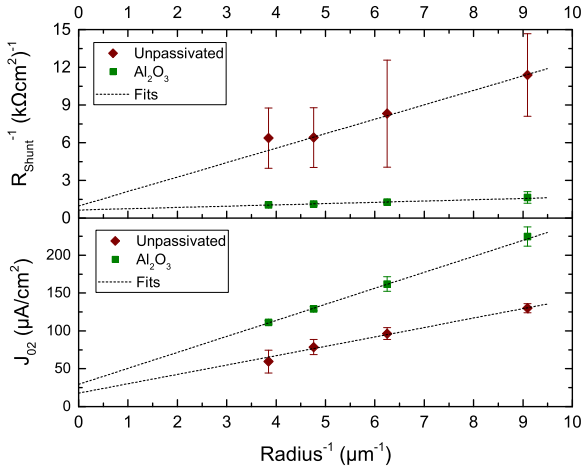


Figure 5.14: Dark J-V parameters as a functions of device radius for $Al_2O_3$ sidewall-passivated cells and baseline cells without sidewall passivation.

## 5.7 GaSb Cell Results

SR was measured with a Newport IQE-200 Quantum Efficiency Measurement System. Due to small cell size, only relative SR could be taken by overfilling the cells. The lamp was calibrated using Si and Ge reference cells which received a portion of the light via a dichroic beamsplitter. The absolute SR was determined by scaling until the AM1.5G integrated current was equal to the calibrated $J_{SC}$ (see J-V results below). The EQE (external quantum efficiency) of homoepitaxial and IMF cells are shown in Figure 5.15). Qualitatively, both cells had good collection in the emitter and but showed losses in the base. The loss for the homoepitaxial cell base was transmission loss as the absorber was less than half as thick as needed to absorb all light below the bandgap. The IMF cell had 10% to 20% (absolute) lower EQE for wavelengths above 800 nm. Since it had the same design as the homoepitaxial cell, the IMF cell

must have been limited by recombination. The EQE of both cells was fit with Sentaurus to extract SRH lifetimes ($\tau_{SRH}$) and MCDL. The SRH lifetimes were assumed to be independent of doping [153], but MCDLs followed a doping dependence through the radiative component. The radiative recombination coefficient and other GaSb simulation parameters (Table 5.1) were sourced from literature [153, 154], except for mobilities, which were based on Hall effect measurements of calibration samples. To improve the fit accuracy, especially for the control cell which had diffusion lengths longer than the cell thickness, the MCDL values were recursively fit against the J-V results discussed below. The fit MCDL of holes in the control cell emitter was 1 µm, while the MCDL of electrons in the base was 3 µm. For comparison, parameters from Sulima *et al.* predict MCDL of holes at the doping level of the emitter to be 4 µm and MCDL in the base to be 12 µm [154]. The fitted control MCDLs represent minimums rather than exact values as sidewall recombination (discussed later) was not explicitly accounted for in the simulation and thus the true 'bulk' diffusion lengths were longer. For the IMF, a good fit was achieved with MCDL of 0.2 µm and 0.6 µm for emitter and base, respectively. The reduced MCDLs in the IMF compared to the homoepitaxial cell correlated with lack of photoluminescence from IMF samples and was indicative of carrier loss from non-radiative recombination due to defects related to the IMF growth.

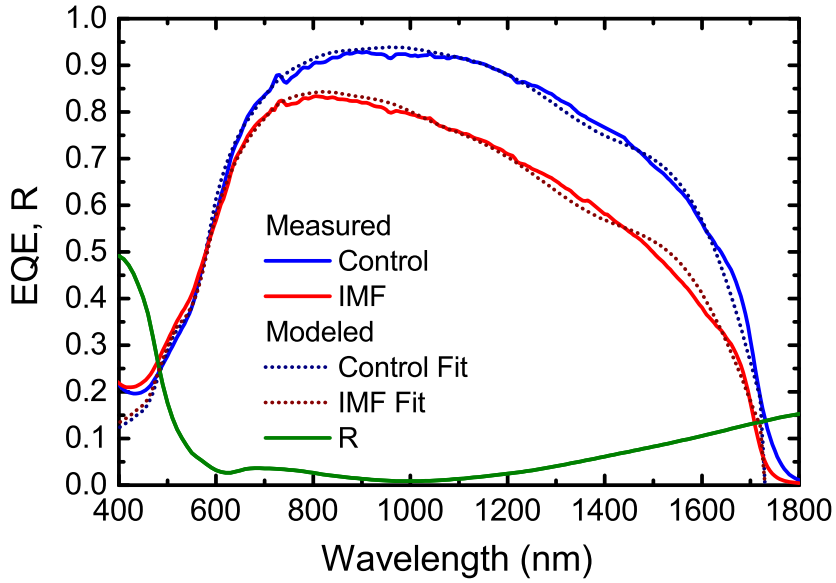


Figure 5.15: Measured EQE of homoepitaxial (control) and IMF cells (solid lines). Simulated EQE (dotted) and reflectance (R) of the control and IMF with fitted lifetimes.

Table 5.1: Parameters used for the GaSb 1-J simulations.

| Parameter | Value |
|---|---|
| Bandgap, $E_G$ (300 K) | 0.73 eV |
| Electron mobility, $\mu_e$ ($N$ = $10^{17}$ cm$^{-3}$) | 3500 cm$^2$/V·s |
| Electron mobility, $\mu_e$ ($N$ = $10^{18}$ cm$^{-3}$) | 1500 cm$^2$/V·s |
| Hole mobility, $\mu_h$ ($N$ = $10^{17}$ cm$^{-3}$) | 500 cm$^2$/V·s |
| Hole mobility, $\mu_h$ ($N$ = $10^{18}$ cm$^{-3}$) | 230 cm$^2$/V·s |
| $\tau_{e,SRH}$ Control fit | 0.90 ns |
| $\tau_{h,SRH}$ Control fit | 2.5 ns |
| $\tau_{e,SRH}$ IMF fit | 0.040 ns |
| $\tau_{h,SRH}$ IMF fit | 0.070 ns |
| Radiative recombination coeff., $B_{opt}$ | $8.5\times10^{-11}$ cm$^3$/s |
| Auger coefficient, $C_{Auger}$ | $5\times10^{-30}$ cm$^6$/s |
| GaSb/AlGaSb interface recomb. vel. | 200 cm/s |
| Series resistance, $R_S$ | 10 mΩ·cm$^2$ |

A Kiethley Source Meter 2440-C was used to measure J-V of devices. Illuminated J-V data were taken with a TSS Space Systems two-zone solar simulator calibrated to the AM1.5G spectrum using GaInP and Ge reference cells. The simulator was equipped with an AM1.5 filter and concentrating optics capable of increasing the power density to 50 suns of air mass 1.5 direct (AM1.5D). A liquid-cooled, temperature-controlled brass stage was used to hold the samples at 23℃. For concentration measurements, the number of suns, $X$, was determined by dividing the $X$-sun short-circuit current ($J_{SC}$) by the AM1.5D 1-sun $J_{SC}$. The AM1.5D 1-sun $J_{SC}$ was itself calculated from the SR and the AM1.5G $J_{SC}$. The concentrating optics consisted of an acrylic fresnel lens and a fused-silica condensing lens and care was taken to not re-image the light sources. The concentrated spectrum was not measured but the acrylic lens was expected to absorb only a minor amount of infrared light. As well, grid shading was over 18% and this was not factored out of current densities. Optimizing the grid shading is a straightforward route to increased current in future cells.

J-V results are shown in Figure 5.16(a) and tabulated cell metrics are in Table 5.2. Under AM1.5G, the GaSb control cell was 5.5% efficient, with a FF of 59%, an open-circuit voltage ($V_{OC}$) of 280 mV, and a short-circuit current ($J_{SC}$) of 33.9 mA/cm$^2$. The metrics improved to 8.9% efficiency, 68% FF, and 386 mV $V_{OC}$ under 44-sun direct spectrum. The simulated J-V

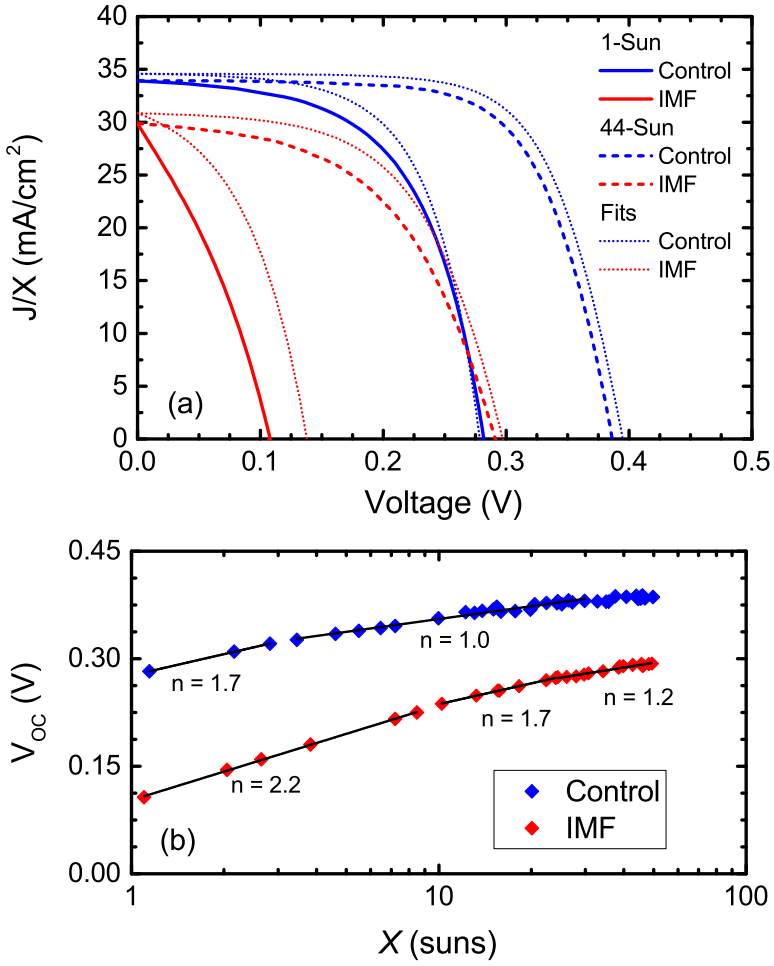


Figure 5.16: (a) AM1.5 illuminated J-V results at 1 sun (global) and 44 suns (direct, normalized to 1-sun global) for measured and simulated cells with the same lifetimes used in the EQE fit. (b) Measured open-circuit voltages under increasing concentration from 1 to 50 suns for the homoepitaxial and IMF cells with fit lines labeled by ideality factor.

data for the control device, produced by the same two-dimensional Sentaurus model as the EQE simulations, was in satisfactory agreement with the measured data. While the simulation tended to overestimate $J_{SC}$ and FF it matched well with $V_{OC}$. The experimental results compare favorably to reported MBE-grown homoepitaxial GaSb photovoltaic cells because of improvements to sidewall shunt resistance (discussed below) and higher current collection due to the ARC. [9, 135, 136]

The IMF cell under AM1.5G was 1.0% efficient, with a FF of 33%, $V_{OC}$ of 108 mV, and a $J_{SC}$ of 29.9 mA/cm$^2$. Under concentration, the IMF cell had better relative recovery than the control. At 44 suns direct, the IMF cell efficiency improved to 4.5%, the FF to 52%, and the $V_{OC}$ to 291

Table 5.2: Homoepitaxial and IMF 1-J measured solar cell metrics.

| Cell | Spectrum | $J_{SC}$ (mA/cm$^2$) | $V_{OC}$ (mV) | FF (%) | Eff (%) |
|---|---|---|---|---|---|
| Homoepitaxial | AM1.5G | 33.9 | 282 | 59 | 5.5 |
| | 44-sun AM1.5D | 1357 | 387 | 68 | 8.9 |
| IMF | AM1.5G | 29.9 | 108 | 33 | 1.0 |
| | 44-sun AM1.5D | 1196 | 291 | 52 | 4.5 |

mV. The simulated data from the IMF model at 1 sun overestimated the $V_{OC}$ and FF compared to experimental data due to the bulk shunt in the IMF, which could not be replicated easily in the model. At 44 suns direct, the effect of the shunt was reduced as the shunt path was saturated and this caused the fit accuracy to improve. The authors previously reported an IMF cell efficiency of 0.7%, surpassed here due to greater current collection likely caused by a thin emitter better suited for the shorter IMF diffusion lengths as well as addition of the ARC. [9] Despite the optimized cell thickness, the $V_{OC}$ of the IMF was low relative to the control and this was further evidence of IMF-related defects.

In Figure 5.16(b), $V_{OC}$ was measured as a function of concentration from 1-sun to 50-sun AM1.5D. Ideality factors were extracted by fitting to the double-diode equation (Equation 2.6). The ideality factor of the control changed from 1.7 (depletion region recombination) to 1.0 (QNR recombination) at $\sim$3 suns, or about 320 mV $V_{OC}$. This indicated that only a small increase in solar flux was needed to push the cell towards QNR recombination. In contrast, this transition occurred in the IMF cell at $\sim$26 suns, or $\sim$270 mV $V_{OC}$, indicating that the IMF cell had a higher number of trap states in the depletion region to fill before it became QNR-limited.

Threading dislocations were the suspected reason for the large difference in MCDL and $V_{OC}$ between control and IMF cells. A simple model by Yamaguchi *et al.* relates MCDL to TDD, [155]

$$\mathrm{TDD} = 4/\left[\pi^3(\mathrm{MCDL})^2\right], \tag{5.2}$$

where the MCDL is assumed to be dominated by TDD. Using the simulation MCDLs, the IMF cell TDD was predicted to be at least $3\times10^7$ cm$^{-2}$, indicating that formation of 90°dislocations was not uniform and the IMF array did not fully relieve lattice-mismatch strain. If the TDD

can be brought below $10^7$ cm$^{-2}$, the results will be more competitive with IMM. To reduce TDD, two approaches may be taken. One is to prevent threading dislocations from forming by further IMF array optimization. The other is to cause annihilation of threading dislocations in post-IMF array growth. Practically, a combination of the two may be required to achieve a good result. In previous work by Juang *et al.* [9], the AM1.5G $V_{OC}$ was 121 mV despite a lower $J_{SC}$ of 15.5 mA/cm$^2$. The smaller dark current and higher shunt resistance suggests lower TDD than reported here, most likely due to the thicker (500 nm vs. 200 nm) post-IMF array buffer layer. A thick buffer of 2 or 3 µm would improve performance but sacrifice the lower-cost thin buffer. However, as mentioned, the combined GaAs and GaSb lattice constants would allow for six-junction cells with a single buffer layer and thus a thick buffer approach may still be an economically viable strategy.

## 5.8 IMF GaSb DLTS

A Sula deep-level transient spectrometer (the DLTS system developed in Chapter 4 was not available for this work) was used to perform conventional DLTS in order to electrically probe and characterize traps states within the IMF and control cell bases. The rate windows ranged from 0.86 ms to 43 ms, and a long pulse width of 1 ms ensured that deep levels were fully filled. Capacitance transients were measured every 1 K in a helium-cooled cryostat capable of a temperature range from 20 K to 450 K.

Trap states were the suspected source of the low shunt resistance and higher non-radiative dark current in the IMF devices and thus DLTS was performed on both control and IMF cells to electrically characterize defects caused by the heteroepitaxial growth. The DLTS spectra and trap peak temperatures vs. trap emission rates are plotted in Figure 5.17. The control spectra used a pulse from -0.14 V to +0.10 V, while the IMF was 0 V to +0.20 V due to leakage current which made larger reverse biases unfeasible. The depleted region was assumed to be entirely in the p-type base due to higher doping in the emitter leading to a one-sided abrupt junction. The pulse to forward bias functioned as a minority carrier injection pulse, ensuring that minority carrier traps could be detected.

The DLTS characteristics of all detected traps are listed in Table 5.3. One majority trap,

GaSb1, was found in the homoepitaxial GaSb p-type base with an activation energy of 0.50 eV above the valence band and with a moderate capture cross-section size of $7\times10^{-15}$ cm$^2$ (see Figure 5.17). Due to its discovery in the homoepitaxial device, this trap cannot be attributed to the IMF interface. Its properties are similar to a trap reported by Kuramochi *et al.*, which they attributed to Te diffusion across the junction [156]. This trap was also observed in the IMF sample, though it was partly obscured by the stronger minority trap, IMF2, which was found at 0.65 eV below the conduction band. The cross-section of IMF2 was $8\times10^{-13}$ cm$^2$, and a cross-section this large (>$10^{-16}$ cm$^2$) is typically indicative of a attractive trap with possible positive charge state. The Arrhenius plot shows that the behavior of IMF2 was similar to GaSb1, even though the former was an electron trap and the latter a hole trap, but the nature of the interaction of the IMF with the GaSb1 trap is unclear at this time. The trap density of IMF2 was ∼6 times larger than that of GaSb1, and the relatively high trap density is a possible explanation for the high non-radiative dark current observed in the IMF cells.

Table 5.3: DLTS results for the control and IMF samples.

| Label | $E_A$ (eV) | $\sigma$ (cm$^2$) | $N_T$ (cm$^{-3}$) | Type |
|---|---|---|---|---|
| GaSb1 | $E_V+0.50$ | $7\times10^{-15}$ | $7\times10^{15}$ | Hole |
| IMF1 | $E_V+0.19$ | $3\times10^{-18}$ | $2\times10^{15}$ | Hole |
| IMF2 | $E_C-0.65$ | $8\times10^{-13}$ | $4\times10^{16}$ | Electron |

Another IMF trap, the hole trap labeled IMF1, was discovered at lower temperature with activation energy of 0.19 eV above the valence band and a with smaller cross-section of $3\times10^{-18}$ cm$^2$. This trap was similar to the suspected Ga vacancy reported in [156], possibly indicating that the IMF GaSb growth conditions lead to a greater concentration of native defects. While the density of IMF1 ($2\times10^{15}$ cm$^{-3}$) was low compared to IMF2, it was closer to mid-gap and thus could be a more effective SRH recombination center.

## 5.9 IMF Triple Junction Simulation

With an understanding of the current IMF material, the next step was to determine the performance of an IMF GaInP/GaAs/GaSb 3-J as it could be presently grown. A 3-J model was

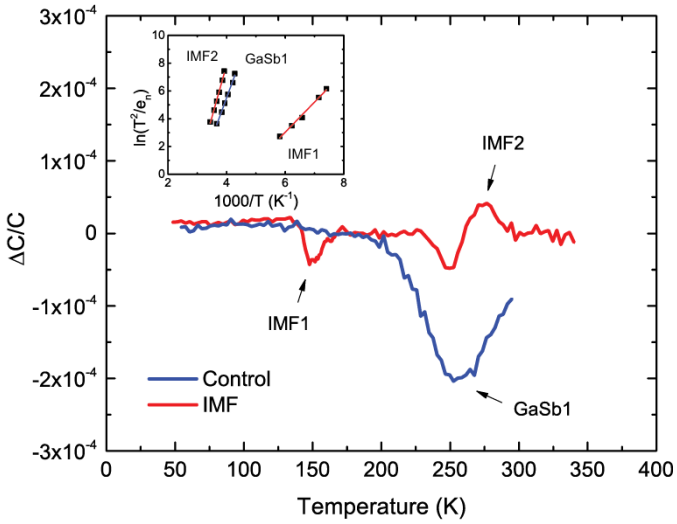


Figure 5.17: DLTS spectra of control and IMF samples using a 4.3 ms rate window and 1 ms pulse width. The inset is an Arrhenius plot of the trap peak temperatures vs emission rate for the three detected traps.

created with the IMF fit lifetimes from Table 5.1 and the AM1.5 J-V in Figure 5.18 was simulated. The GaAs subcell was simulated with typical lifetime values to achieve a 1.03 V AM1.5G $V_{OC}$. For GaInP, the AM1.5G $V_{OC}$ was 1.43 V. The GaAs and GaInP subcell designs were similar to work by Takamoto *et al.* [157] and used parameters from Algora *et al.* and Sato *et al.* [33, 158] As the inverted IMF cell must have its substrate removed, the gold contact on the back of the cell was also used as a mirror to increase the path length of interior photons. This allowed the IMF cell to be thinned to 0.6 µm which mitigated the shorter $L$ and also improved $V_{OC}$. The subcell was kept current-rich to help offset the effect the low subcell FF at 1 sun. The simulated cell was 32.0% efficient, although at 1 sun this is optimistic as it assumed no bulk shunt in the IMF GaSb. At 44-suns, efficiency improved to 37.8%. To determine the contribution of GaSb subcell, the GaInP/GaAs subcells were simulated as a two-junction (2-J) cell. The 2-J cell was 31.5% and 35.3% efficient under 1 sun and 44 suns, respectively. The addition of the GaSb subcell, therefore, led to absolute efficiency improvement of 0.5% at 1 sun and 2.5% at 44 suns, suggesting that the viability of IMF multi-junction cells could be dependent on concentration. The industry-standard bottom subcell, the diffused-junction Ge cell, contributes more to the GaInP/GaAs system at 1 sun with a reported AM1.5G $V_{OC}$ (unfiltered) of 269 mV, but the difference between it and the IMF subcell is reduced under concentration.

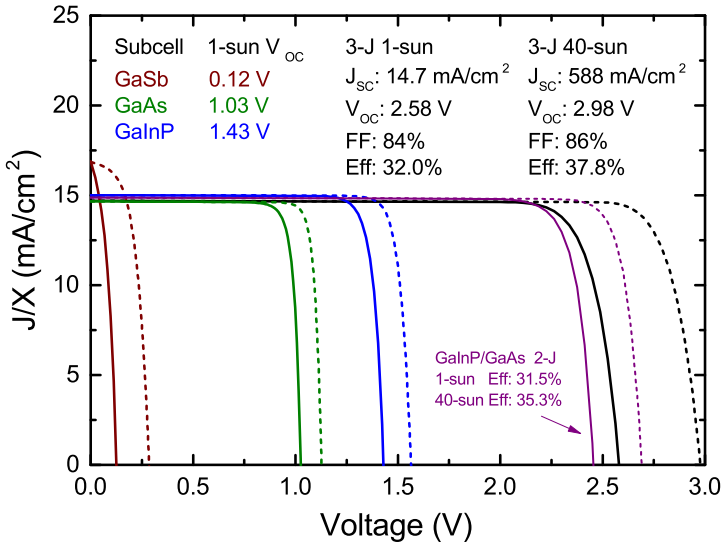


Figure 5.18: Simulated IMF 3-J GaInP/GaAs/GaSb solar cell with the fitted IMF GaSb lifetimes used for the GaSb bottom cell under 1 sun (solid) and 44 suns (dotted, normalized to 1-sun). For comparison, a 2-J GaInP/GaAs cell is also plotted.

## 5.10 Conclusions & Future Work

Homoepitaxial and IMF GaSb solar cells were grown via MBE. The passivated homoepitaxial and IMF cells achieved 5.5% and 1.0% efficiency under AM1.5G illumination, respectively. The IMF cell was able to improve to 4.5% efficiency under 44-sun AM1.5D with 291 mV $V_{OC}$, while the homoepitaxial cell achieved 8.9% efficiency under said illumination with 386 mV $V_{OC}$. A device simulator was used to fit EQE and J-V of cells and diffusion lengths were extracted. From the fit, a simulated IMF GaInP/GaAs/GaSb 3-J cell was 37.8% efficient under 44 suns, an absolute improvement of 2.5% over simulated GaInP/GaAs 2-J cells.

Two reliable wet etches were found for GaSb, the citric acid and tartaric acid-based etches. Both were found to have similar etch rates and smoothness of etched surfaces, but resulted in different etch profiles. A selective contact etch for InAs over AlGaSb using citric acid and peroxide mixture was confirmed to work well for $Al_{0.3}Ga_{0.7}Sb$. Several other etches were tested but found to give poorer results.

The 0.2 $mm^2$ homoepitaxial cells were believed to be the highest efficiency of an MBE-grown GaSb at the time they were tested, although a higher efficiency is reported now by Tournet *et al.* [139]. The cells from this work held back by three issues, which were:

1. The cells were too thin. As mentioned, the thin cell design was a result of targeting the growth for the (expected) shorter IMF diffusion lengths. The diffusion lengths of the homoepitaxial cell could have made use of a thicker cell that could absorb more light. The GaSb absorber layers in the MBE cell totaled 1.175 µm compared to 3.000 µm in the record MOCVD cell. Related to this is the use of a GaSb BSF instead of a higher bandgap window, where the BSF may leak minority carriers outside the active region due to insufficient barrier. AlAsSb could be used like Vadiee *et al.* [159], which is discussed below.

2. Unoptimized grid coverage. The MBE cell was a prototype, small-area design and the grid coverage was calculated from the mask to be 19%. The optimal coverage for 1-sun AM1.5G is 2-4% [95]. Applying a simple correction factor to the area used in the efficiency calculation, 5.5% efficiency improved to over 6%.

3. Perimeter effects. MBE-related growth complications made growing shunt-free cells on the $cm^2$-scale difficult. The solution was to fabricate smaller cells; however, these cells were limited by sidewall effects. Based on current results and modeling, a >7% GaSb solar cell should be within reach by MBE by fabricating either sidewall-passivated cells or larger ($cm^2$-scale) cells that are less-affected by perimeter effects. An attempt at passivation was made, with $Al_2O_3$-passivated homoepitaxial cells achieving a factor of 5 average improvement in $R_{Shunt}$ compared to unpassivated cells. However, sidewall recombination was still the dominant loss in the passivated cells.

Larger area cells were difficult to realize by MBE due to the shunting defects found by DLIT which led to lower device yield as area increased. Reducing the defect density in the MBE growths may be possible by switching to a dual filament Ga cell. This type of source cell has been shown to reduce 'Ga spitting' in the literature on both GaAs and GaSb [136, 149]. A possible alternative is to grow an MOCVD-based large area cell, but the best MOCVD cells are grown with modified reactors with atypical precursors [138].

The best MBE IMF cell result was 1.0% efficiency. This was far behind the 5.5% of the homoepitaxial cell. Shunting and higher non-radiative dark current were the main cause of FF and efficiency loss in IMF devices. The IMF was bulk-limited in both shunt and non-radiative recombination. Not much can be done fabrication-wise to improve the cells as the high TDD

formed during growth. Thermal cycle annealing is one possible method that has been shown to reduce TDD of lattice-mismatched growth before [160]. Growth-wise, strained-layer superlattices grown have also been shown to reduce TDD [132]. If the TDD can be reduced by these or other improvements, IMF cells would be a competitive alternative to modern multijunctions, especially at high concentration.

DLTS was performed and an IMF defect was found. This may have been a trap related to IMF growth such as a repeating trap state on a threading dislocation, but it could have been general uniformity issue or caused by fabrication. More DLTS testing should be done to confirm the results. Post-growth annealing at 400-600 ℃ has been shown by Aziz *et al.* to change the DLTS spectra (and the trap characteristics) of IMF GaSb, though not necessarily reducing trap concentration [161].

A number of future projects could come from this work, besides the already mentioned large-area cells by either MBE or MOCVD. One is growth of 1.0-eV $Al_{0.3}Ga_{0.7}Sb$ solar cell. Vadiee *et al.* published results on solar cells made of $Al_{0.15}Ga_{0.85}Sb$ (0.85 eV) and $Al_{0.5}Ga_{0.5}Sb$ (1.4 eV) on both GaSb and GaAs substrates with some success [159]. The 1.0 eV material was partially developed already for both MBE and MOCVD for use as the window layer in the GaSb cells. An even higher bandgap AlGaSb will likely need to be used for the window layer. Vadiee *et al.* used $AlAs_{0.08}Sb_{0.92}$ as a front and back window, which is lattice-matched to GaSb and has a high, indirect bandgap of 1.62 eV [159]. While the AlAsSb is a good window material, it may be difficult to grow and the high Al content means it must be protected from atmosphere [84, 162].

Another avenue of work would be to grow and fabricate a dual-junction or triple-junction IMF solar cell. This cell could use the more-well-developed IMF GaSb as a bottom junction. Growth of this type of cell would require a number of advances in fabrication capabilities. Bonding the inverted cell to a carrier wafer and subsequent substrate removal is a required technique for the 3-J IMF cell and this technology has not yet been developed by the author beyond proof-of-concept. A substrate lift-off process was already demonstrated by Renteria *et al.*, however [136]. Also, a transparent (>1.4 eV) buffer material lattice-matched to GaSb will be needed to grow the buffer between the IMF GaSb layer and the GaSb subcell. Currently,

the buffer material is also GaSb, which is adequate for an upright cell as the buffer is below the subcell but in an inverted cell a GaSb buffer would parasitically absorb most of the light meant for the GaSb subcell. A good candidate would be AlAsSb lattice-matched to GaSb, which was already discussed above.

# Chapter 6

# III-V Integrated Light Management Modeling

## 6.1 Summary

Light management is a key component of III-V cells. Unlike in silicon cells, the phenomena known as photon recycling and radiative coupling are critical for state-of-the-art terrestrial III-V cells and have thus far favored 'flat-plate', untextured cells. Textures and gratings are still useful in certain III-V cells, but these structures are somewhat underdeveloped in III-V's as a result of industry focus on flat-plate cells.

Three types of cells have been identified to benefit most from textures or gratings. These are: ultra-thin cells, nanostructured cells, and radiation-damaged space cells. A numerical model was developed to explore textures and gratings for these three categories of III-V cells.

This chapter has four main topics:

1. Numerical model of solar cell with integrated light management.
2. Light management for QD solar cell.
3. Path length simulations for GaAs with textured back surface reflectors (BSRs).
4. Light management for middle subcell of InGaP/GaAs/Ge 3-J space cell to enhance end-of-life (EOL) efficiency.

## 6.2 Motivation & Background

### 6.2.1 Motivation

Light management is a well-known and important part of modern solar cell design that is perhaps best explained within the context of historical silicon solar cell progress. In the 1960's,

the best silicon solar cells (∼14% terrestrial efficiency) were known as "blue" cells as they had poor absorption of the blue part of the visible spectrum [10, 163]. Then, in 1972, the "violet" cell was released by Comsat Laboratories and featured a new kind of ARC made of $Ta_2O_5$. This was the first cell in a decade to convincingly break the 14.5% efficiency barrier and overcame the known absorption limitation in the blue cells (caused by using $SiO_2$ as an ARC) [164]. This cell achieved 15.3% terrestrial efficiency [10].

Soon after, in 1974, Comsat Laboratories reported a 17.3% terrestrial efficiency record with its 'black' or 'textured non-reflecting' cell [10]. Instead of using a flat surface as in all previous record cells, the 1974 cell used a front-side texture to trap and scatter light at oblique angles into the cell [165, 166]. The texture was created by a chemical that etched preferentially along crystal planes, leading to tetrahedral structures [164]. Light incident on the texture was more likely to transmit into the cell, as illustrated in Figure 6.2. The texture could also scatter light internally at oblique angles, leading to longer path lengths of rays in the cell. Longer path lengths allowed poorly-absorbed wavelengths a greater chance to be absorbed and generate an electron-hole pair. In theory, a perfectly random texture could increase the path length by a factor of $4n^2$, where n is the refractive index of the material [167]. The two benefits from the texture were thus an improved anti-reflective surface, as well as improved absorption of longer wavelengths as a consequence of light scattering.

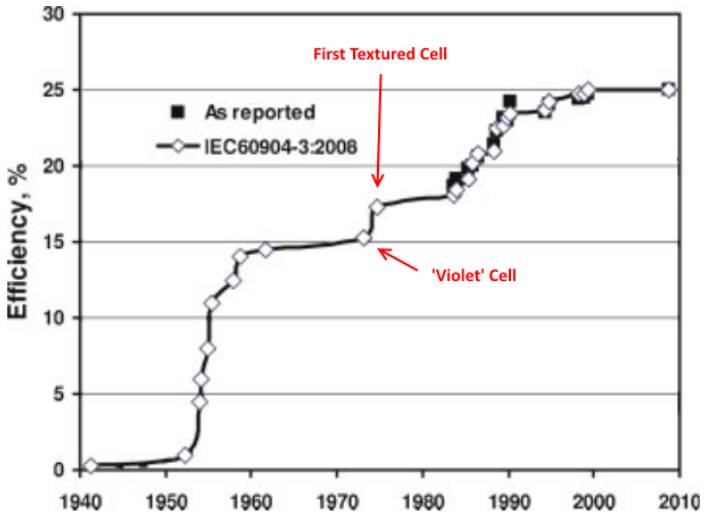


Figure 6.1: AM1.5G efficiency record progression of crystalline silicon cells. *Reprinted/adapted with permission from* [10].

Since the Comsat cell, all further world records have built upon the light management of the Comsat cells. They all include some form of non-reflective front surface and a texture in order to maximize absorption. The history of silicon solar cell efficiencies are shown in Figure 6.1. As seen, the Comsat 'black' cell represented a significant improvement in efficiency that was not overtaken until a decade later. A modern silicon cell structure is depicted in Figure 6.3, and it can be seen that the cell is textured in addition to having a silicon nitride (SiN) ARC. This cell type is known as the 'interdigitated back contact-heterojunction with intrinsic thin layer' or 'IBC-HIT' cell [168].

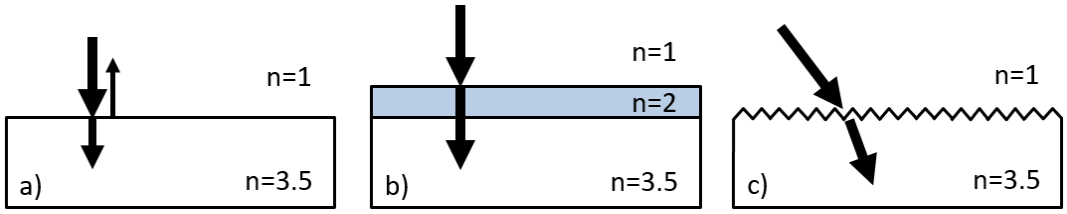


Figure 6.2: a) Cell without anti-reflective structure, the index of refraction change causes roughly 30-40% of light to be reflected. b) Cell with a conventional ARC, where the thin-film effect causes destructive interference of the reflected waves for limited range of incident angles. c) Cell with sub-wavelength frontside texture spatially grades the refractive index, allowing broadband and wide-angle anti-reflection.

Another light management technique used in silicon solar cells, such as the IBC-HIT cell, is the BSR. As the back surface of a solar cell does not face the sun, a photon-reflecting mirror can be placed there. If the rear interface of the cell is perfectly reflecting, then, intuitively, the path length of (un-absorbed) light rays in the cell are doubled. In reality, the surface will never be perfectly reflecting, but a dielectric/metal back reflector stack can achieve broadband wide-angle reflection in the high 90% (see Figure 6.17).

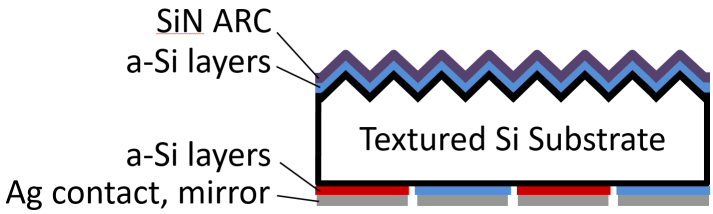


Figure 6.3: IBC-HIT cell structure with textured front surface with ARC and rear mirror.

The three successful light managing elements of a modern silicon cell are thus: An anti-reflective front surface, a back surface reflector, and a light trapping or light scattering texture. As will be seen, only the first two of these components are commonplace in high-efficiency III-V solar cells.

Light management for cells made of direct-bandgap III-V material, like GaAs, is not as well developed as it is with silicon cells. The silicon solar cell market is larger and more historic. This would not be a problem if the light management technology in silicon was easily applied to III-V materials, but often it is not. One reason is because of the much higher absorption coefficient of direct bandgap semiconductors leads to cell widths much thinner than in indirect Si. A GaAs cell's thickness is in the single-digit micron range versus hundreds of micron for the Si cell. In a silicon cell, the feature height of the texture is typically on the scale of one to five micron [169, 170], which clearly cannot be used as-is in a III-V cell that may only be a micron thick. Light scatterers on the front or back of III-V cells are often made from a deposited non-absorbing material such as dielectrics or high-bandgap transparent III-V windows. The added complexity nearly always leads to issues with parasitic absorption or excess surface recombination [171]. Another complication from the thin device is the implementation of a rear mirror. To add a mirror, the III-V cell must be bonded to a handle and then the substrate must be removed, which is a more complicated process than in silicon where dielectric and metal layers are deposited in a straightforward manner to the back of the silicon substrate.

Further complications for a III-V cell stems from the direct bandgap through a phenomenon known as photon recycling. With sufficient material quality, the primary loss mechanism in a GaAs cell will be radiative recombination or emission. An emitted photon has a chance to re-absorb elsewhere in the cell, giving a generated minority carrier another chance to contribute to useful work. This has the effect of lowering the radiative recombination rate and subsequently the dark current, providing a significant improvement to voltage. A simple explanation for this is that the open-circuit voltage is the voltage at which the recombination (diffusion) current is equal to the photo-generated (drift) current. If the recombination process is radiative and the photon is recycled back into the photo-generated

current, then higher voltage will be needed to increase the diffusion current to counter the increased drift current and maintain a net-zero current (open-circuit) condition. If the photons could be 100% recycled, then the $V_{OC}$ would be limited by Auger recombination [172]. Realistically, the photons are never 100% recycled and radiative recombination can remain the dominant loss mechanism, at least at 1 sun.

Related to photon recycling is the concept of radiative coupling. In a multi-junction cell, the photons emitted due to radiative recombination for one cell may be easily absorbed by other cells with smaller bandgap. For terrestrial cells, this has an important impact on current-matching of subcells that are connected in series. Any excess current in a cell will tend to recombine and emit a photon, which will be absorbed by the next subcell which may not have enough current. In this way, radiative coupling may balance the currents and make the cell more robust for different conditions that cause the currents to be un-matched (such as cloud cover removing current excessively from one subcell) [173].

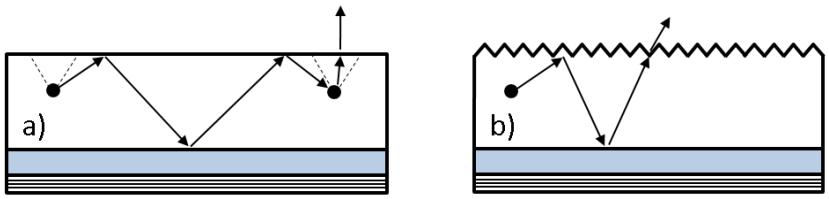


Figure 6.4: a) Flat-plate solar cell behaving as a planar waveguide. Escape cone critical angles are defined by dotted lines. b) Textured front surface prevents planar waveguide modes and widens escape cone to a hemisphere.

Photon recycling (and radiative coupling) adds an additional dimension to direct bandgap semiconductor light management. In silicon, recycling is not a concern as the ideal material is already Auger-limited. It is also not a consideration in III-V's that are limited by non-radiative recombination like SRH recombination. A cell limited by SRH recombination could arise due to presence of mid-gap traps, such as might happen after a cell is exposed to large doses of radiation in space. However, photon recycling is of critical importance for obtaining the highest efficiencies in GaAs and likely others such as InP and GaSb. According to Miller *et al.*and Steiner *et al.*, the current world record efficiency for GaAs under terrestrial spectrum (29.1%) owes its success over the previous record (26.4%) thanks to improvements to photon

recycling [62, 174]. From a previous record to the current record, the $V_{OC}$ improved from 1.03 V to 1.12 V. This increase in photon recycling was attributed to the use of a flat highly-reflective BSR which prevented loss of photons across the rear surface.

It is possible, perhaps likely, that a light management structure could excel at facilitating absorption of photons of external origin while simultaneously having a detrimental effect on the cell's ability to recycle internally emitted photons. By reciprocity, a broadband non-reflective surface would both couple external light into the cell and also couple internal light out of the cell. As an example, a front surface texture on a GaAs cell would create an excellent non-reflective surface, especially for rays that are incident at oblique angles, but this would also cause the cell to emit internal photons from the surface to a greater degree. For a 'flat-plate' cell with a flat front surface, the index of refraction change from semiconductor (high) to air (low) leads to an angular *escape cone* defined by the angle for total internal reflection (TIR), and any photon that strikes the surface outside of the escape cone, which is the majority of them, is internally reflected back into the cell where it will have a high chance to be re-absorbed. Between the flat front and rear surfaces, the cell behaves as planar waveguide for light outside the escape cone, a process illustrated in Figure 6.4a. However, with a randomly textured surface, as with Figure 6.4b, the escape cone is effectively expanded to a hemisphere, allowing internal photons to escape with any surface-pointing initial emission angle. A textured front surface will therefore not take full advantage of voltage-enhancing effect of photon recycling as it 'leaks' considerably more photons and is unable to build up a high internal photon density [172].

The effect of texturing on photon recycling in GaAs was addressed in detail by Miller *et al.* [62] and Kosten *et al.* [172]. The authors used the thermodynamic approach of detailed balance to model 1-J GaAs cells with photon recycling effects included. Miller simulated one with a frontside texture and one with only planar surfaces, where both cells had a perfectly reflecting BSR. The conclusion was that that the textured and planar cells had nearly identical efficiency potential for cells above 2 μm in thickness. At this thickness, all sunlight above the GaAs bandgap can be absorbed with near-unity quantum efficiency, and consequently light scattering is not needed to obtain full current for GaAs. Additionally, the textured cell does

not benefit from the planar waveguide modes for photon recycling and will suffer reduced voltage enhancement because of this. Kosten *et al.* explained this in their model by showing that limiting the emission angle of internally emitted photons traps them, leading to a high internal 'concentration' factor due to recycling. The authors predicted that a GaAs cell could achieve >35% efficiency with <5° emission angle, at which point it becomes Auger-limited. These observations explain why textured GaAs cells have not become popular contenders for record breaking efficiencies. Added to the absence of possible efficiency gains is the additional fabrication complexity from adding a texture to a thin-film cell. As previously explained, the thinness of the cell makes texturing it a difficult proposition. Also, the model assumed a perfectly random front surface texture, and a truly random texture is difficult to fabricate even in silicon cells.

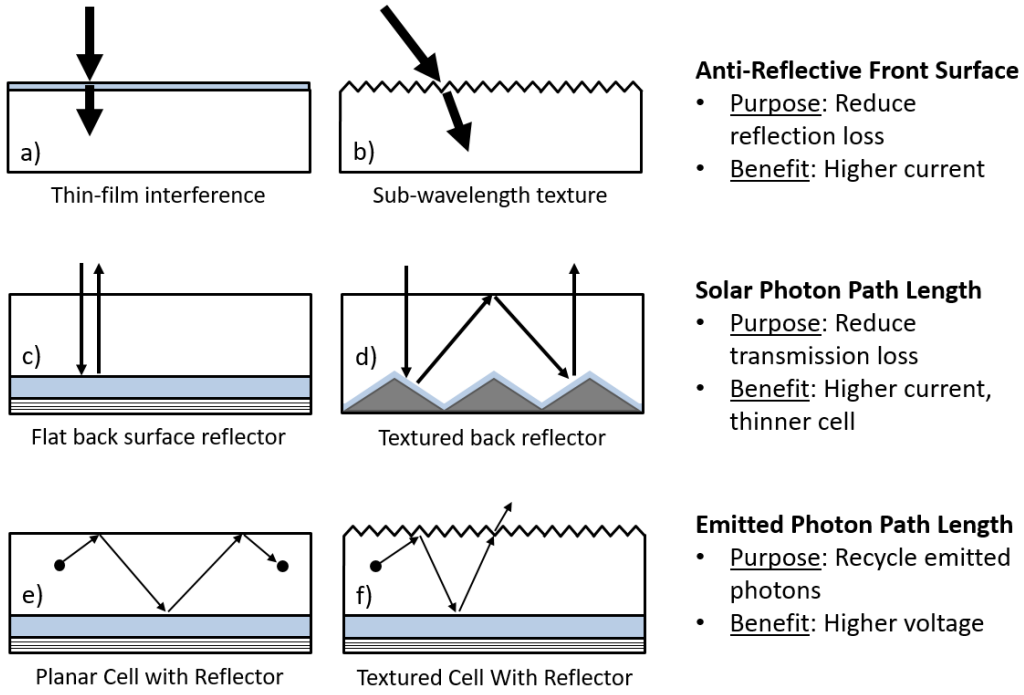


Figure 6.5: a) ARC and b) textured method of creating anti-reflective front surface. c) Rear BSR increases the path length of solar photons by two, while d) a textured BSR can increase path length considerably more. e) A planar cell maximizes the path length of internally emitted photons, while a f) textured cell collapses the waveguide modes and reduces the emitted photon path length.

In summary, there are three main concerns when designing light management for III-V cells: 1) The reflection loss of the front surface, 2) the path length of solar photons that couple into the absorber, and 3) the path length of photons emitted by the cell through radiative

recombination. These are illustrated with some common light management structures that apply to each category in Figure 6.5. The third item is only important for cells that utilize photon recycling or radiative coupling, and if this can be ignored the dynamics of the light management can change drastically. If photon recycling can be ignored, then the texture can be designed as in silicon, where is it purely used to enhance the path length of solar photons incident on the cell. There are a number of III-V solar cells where this is the case:

1. Nanostructured solar cells and the intermediate band solar cell (IBSC). Nanostructures like QWs and QDs are poorly-absorbing, and adding extra path length can increase the absorption of these structures.

2. Ultra-thin III-V cells of 500 nm thickness or less. These cells are less expensive to grow but cannot absorb all of the solar irradiance above their bandgap in a planar configuration, therefore an increase in current provided by a texture is more important to these cells than the voltage enhancement of photon-recycling.

3. Cells with traps states leading to non-radiative recombination. These cells do not radiatively emit and therefore there are no photons to recycle. The primary candidate cell here is the space multi-junction cell. Space cells are damaged by radiation to the point that non-radiative recombination dominates. The salient metric of the space cell is EOL efficiency, which is the performance of the cell at the end of its mission in space. For an EOL cell, the diffusion lengths suffer due to damage-induced traps that lead to non-radiation recombination. A texture can allow the cell to have a fair efficiency even for very thin cell thickness, and a thin cell is better able to cope with the shorter diffusion lengths at EOL as the light management ensures carriers are generated closer to the junction on average.

### 6.2.2 Background

#### Background: Nanostructured Models and Experiments

In both ultra-thin GaAs and the nanostructured (QW or QD) solar cells, limited absorption of the longer wavelengths is a critical issue. For thin GaAs, there is not enough material to

absorb wavelengths near the band edge. In the nanostructured cell, the nanostructures are weakly absorbing but adding more is not always an option as there is a limit of nanostructures that can be grown without degrading the quality of the host cell. To increase absorption in both cells, light management can be used.

Nanostructured cells have a variety of applications. One is bandgap engineering, where the nanostructured is designed to absorb light of a specific bandgap which might not be available with typical bulk materials. An example of this is the work by Inoue *et al.* discussed below. Another application of nanostructures is for the IBSC. The IBSC is a solar cell concept that increases the absorption in the cell by deliberately introducing a band of states within the bandgap of the host cell [175]. Photons below the bandgap can excite carriers into the intermediate band and then into the conductions band in a two-photon process which reduces transmission loss. The IBSC concept is commonly attempted with closely-spaced QD superlattice solar cells, where the QD states provide the intermediate band states. The detailed balance efficiency of an IBSC at 1-sun is 47%, compared to 34% for a standard single junction solar cell [176]. The ideal material for 1-sun operation would have a band gap of 2.4 eV and VB-IB gap of 0.8 eV, however, the InAs/GaAs system is studied here as its growth is well-understood. A roadblock to functional IBSC is fast thermal escape of carriers out of the QD confined states that out-paces the second optical transition. To observe the two-photon process, low-temperature measurements can be used to quench the thermal escape, or concentrated light can be used to increase the optical transition rates [177, 178]. Light management has been proposed as a method to increase photon absorption in the QD, as increasing the optical path length through the dots has a similar effect as increasing the concentration of the spectrum.

Light management targeting nanostructure absorption was studied experimentally by Inoue *et al.* [11]. Their multi-QW GaAs-based cell was designed with a planar front surface but a thick textured rear window layer with a BSR deposited directly on the texture. The textured was used to enhance absorption in their InGaAs/GaAsP multi-QWs. The confined states of the nanostructures gave the cell an effective bandgap of 1.2 eV, which is closer to the ideal bandgap for the solar spectrum, allowing it to potentially achieve higher efficiency than a

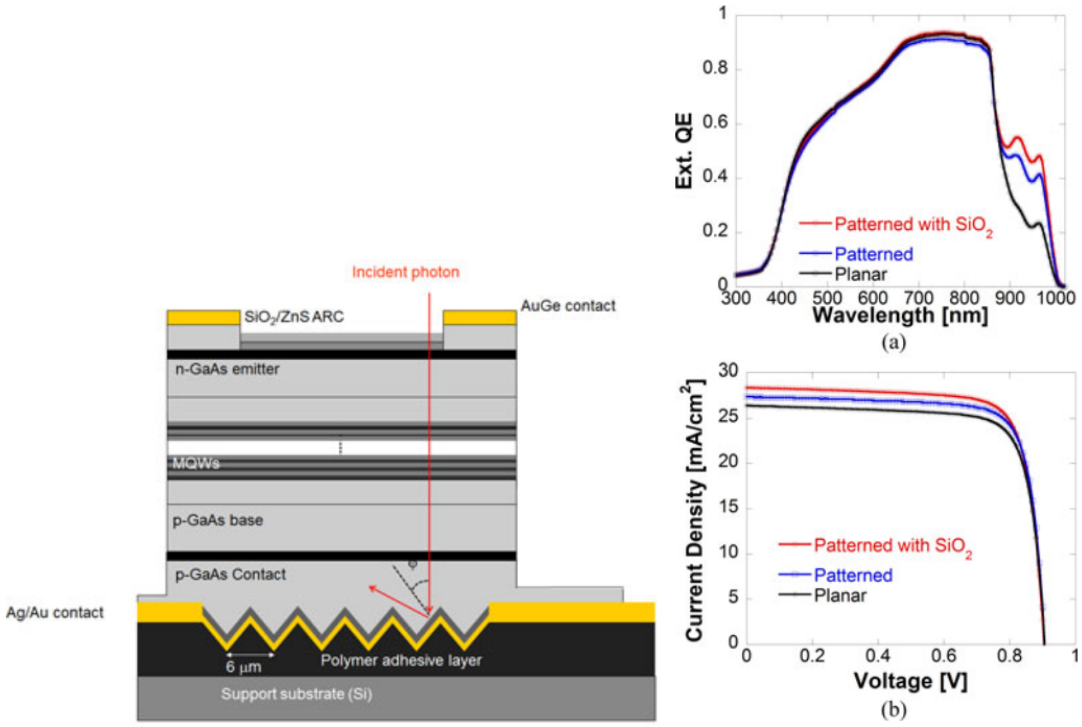


Figure 6.6: Left: QW solar cell with triangular BSR simulated by Inoue *et al.*. Right: (a) EQE and (b) J-V results showing that the textured BSR increases current generation in the QWs. *Reprinted from* [11], © 2015 IEEE.

standard GaAs cell. However, the QWs on their own did not absorb enough light beyond the GaAs bandgap, so increased QW absorption was needed. By using a selective chemical etch to etch a v-groove pattern in the AlGaAs window layer (Figure 6.6), and then depositing a layer of oxide and silver on the texture to act as a mirror or BSR, they were able to increase the absorption in the QWs by a factor of ∼5. The enhanced absorption can be seen in the EQE data in Figure 6.6b in the 900-1000 nm (sub-GaAs-bandgap region) range.

Musu *et al.* performed backside reflector simulations for QD GaAs cells [12]. They took the same v-groove pattern concept and designed a cell structure similar to Inoue *et al.*, but their simulations altered the period and aspect ratio of the etched grooves to optimize the reflector texture. They found that an aspect ratio of ∼0.35 with period of 2.0 μm or greater enhanced the QD photocurrent by a factor of 3 compared to a planar BSR, which represented an optical path length of 6 (see Figure 6.7).

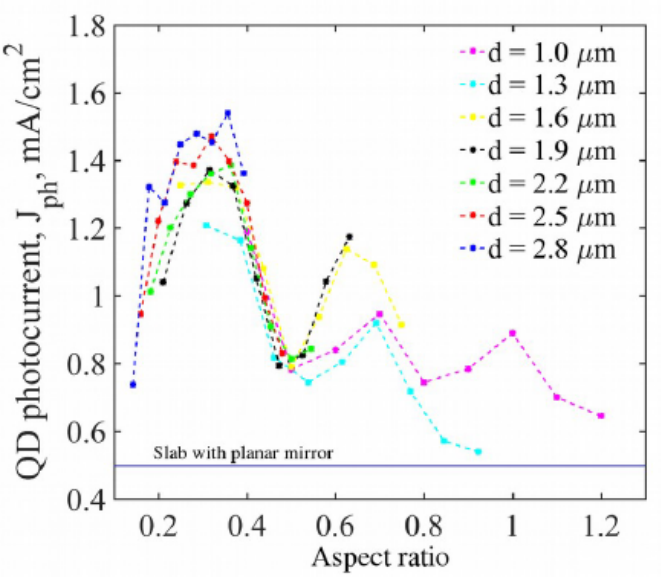


Figure 6.7: Simulated photocurrent generated by the nanostructures in a GaAs cell as a function of period and aspect ratio of the v-groove texture of the metal BSR *Reprinted with permission from* [12].

**Background: Thin GaAs Models and Experiments**

A thin GaAs model by Miller *et al.* was already discussed in Section 6.2.1. In that model, a frontside texture was found to increase absorption in thin cells, but, due to photon recycling, a 2 µm-thick flat-plate cell was predicted to have the highest efficiency. The compromise between textures and photon recycling has been studied by other groups [62]. Liu *et al.* attempted to find a better cell design than that used by Miller *et al.* by texturing the BSR instead of the front surface to maintain a small escape cone and to keep the frontside layers thin to avoid parasitic absorption of high energy photons. The back surface was textured by growing a 5 µm AlInP rear window layer with conditions that led to random surface pits or bumps. As seen in the previous section, a thick, high-bandgap rear window is now a common method for texturing in III-Vs as the rear window does not parasitically absorb like a thick frontside window might. In addition, the rear window MCDL does not typically impact the device performance, so there is no need to passivate the textured surface. Liu *et al.* found via modeling that the back side texture still diminished the photon recycling factor as it broke down the planar waveguide modes, but it allowed the active region of the cell to be thinned considerably ($\leq$500 nm) which allowed for higher $V_{OC}$. Their model predicted a better maximum

efficiency for a completely random texture (∼31%) compared to a planar cell (∼28.5%), but they failed to achieve this by experiment, reaching only 19.1%.

The model by Miller *et al.* also predicted thin cells of ≤500 nm thickness to perform well, with efficiency near AM1.5G 30% (also see Appendix C for thin cell model by author). However, experimental cells of these size have struggled to break 20%. Liang *et al.* achieved 17% with a textured frontside InGaP window [171], and Chen *et al.* used a backside grating to achieve 19.9% [28, 179]. It is agreed that >25% is achievable with thin GaAs cells, but the fabrication is difficult and a design that minimizes parasitic absorption is critical.

**Background: Space Cell Models and Experiments**

It is well-known that non-ionizing radiation present in the space environment leads to displacement damage in exposed III-V solar cells. Over time, accumulation of traps states lead to reduced SRH lifetimes (see Equation 2.15). Because of this, space cells must be carefully optimized, or radiation-hardened, so that they can remain efficient for many years despite decreased diffusion lengths. A major consideration for multi-junction cells is the dynamics of the individual subcell currents. Since the subcells are connected in series, the overall cell will be limited by the subcell with the lowest current. After some time in space, the limiting cell is most often the cell that is the most damaged. Perhaps counter-intuitively, this is not typically the top subcell, as the radiation species that damage space cells fully penetrate the thin films and, in this forward scattering regime, the damage depends most on the subcell material. An empirical relationship between material, radiation species, fluence (or dose), and minority carrier diffusion length was developed [32, 33]:

$$\frac{1}{L} = \frac{1}{L_0} + K_L \Phi \tag{6.1}$$

Where $L$ is the diffusion length after exposure, $L_0$ is the beginning-of-life (BOL) diffusion length, $K_L$ is the damage coefficient and $\Phi$ is the radiation dose or fluence. The damage coefficient is unit-less and depends on the material and type of radiation used; there's a different damage coefficient for GaAs for 1 MeV protons and 2 MeV electrons, for example.

GaAs and InGaAs are damaged more quickly than InGaP, and therefore an IMM cell (see

Section 2.6) that is current-matched at BOL will quickly become current-mismatched due to over-production of current in InGaP. This extra current in InGaP represent photons that could be better used in the degraded bottom subcells. The solution is to use Equation 6.1 to predict diffusion lengths and attempt to current-match the device at its EOL, after it has received the expected total mission radiation dose. Thinning the InGaP topcell is one way to increase photon flux in the degraded bottom cells [39].

Integrated light management is already used in IMM space cells to increase the bottom subcell EOL performance [38]. A flat back surface reflector will increase the optical path length in the InGaAs subcell, allowing it to be thinned by a factor of two while still absorbing the same amount of light as a subcell with baseline thickness. The thinner cell will, on average, generate minority carriers closer to the junction. This relaxes the diffusion length requirements for carrier collection and allows the subcell to retain more current at EOL. It has the additional benefit of improving voltage by increasing minority carrier densities and reducing total number of traps.

Middle subcells, such as the GaAs subcell in a Ge-based upright 3-J cell, can also be the target of a current enhancement through light management. The most successful concept so far is the interstitial all-semiconductor distributed Bragg reflector (DBR). The DBR reflects light for the part of the spectrum absorbed by GaAs, but allows longer wavelengths to transmit to the germanium. Emelyanov *et al.* demonstrated via analytical modeling that an all-semiconductor, AlAs/AlGaAs DBR grown between the Ge and GaAs subcells could allow a cell to maintain efficiency of $\geq$26% for 4 years with standard EOL conditions compared to 1 year for an EOL-optimized cell without a DBR [39]. Because it can be grown with the epitaxial reactor, the DBR does not add much production complexity, and the material used to grow it is offset by the reduced absorbing material required. The DBR must be doped to a high value to allow current to flow through it with minimal resistance.

Another idea proposed by Mellor *et al.* is the combined diffraction grating and DBR structure, where a diffraction grating is placed on the GaAs side of the DBR [13]. The reflective grating is designed to scatter light back into the GaAs subcell to increase path length even further. Scattered light that is not absorbed in the GaAs can totally internally reflect off the

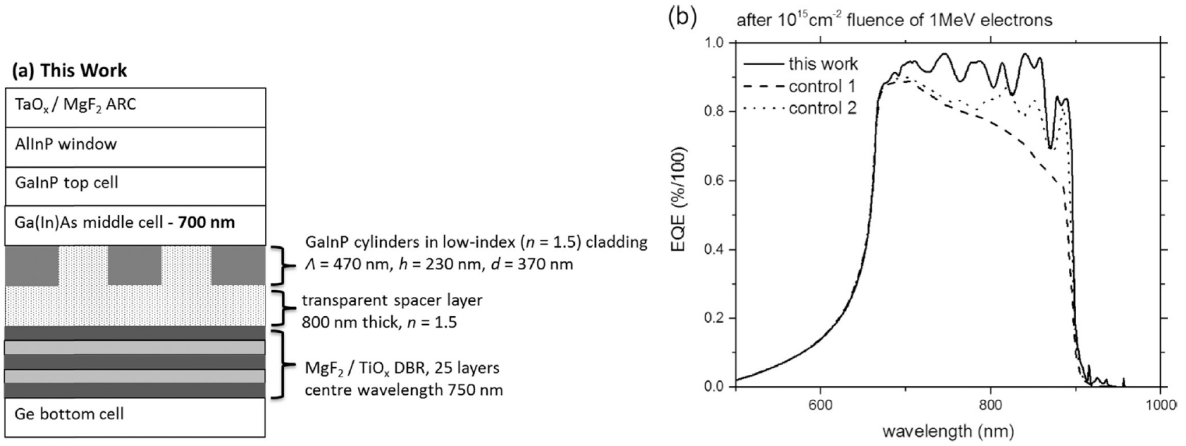


Figure 6.8: (a) Cell structure and (b) Middle subcell EOL EQE enhancement reported by Mellor *et al.*. 'This work' indicated the structure in part a, 'Control 1' was a cell with baseline thickness, and 'Control 2' had a half-thick middle subcell with a DBR. *Reprinted with permission from* [13].

the cell's top surface and make it to the GaAs cell again as InGaP is transparent to the GaAs wavelengths. Simulations by Mellor *et al.* show that this scheme greatly increases the middle cell EOL EQE (see Figure 6.8).

## 6.3 Overview and Procedure of Integrated Light Management Simulations

Electrical simulation of all devices was performed with Synopsys Sentaurus TCAD. Carrier transport through devices was modeled using Sentaurus' hydrodynamic model, which is derived from the BTE, the fundamental equation of semi-classical macroscopic transport, via inclusion of certain physical phenomena considered to be of significance for carrier transport. These phenomena include drift of carrier species due to electric fields, diffusion of carriers due to concentration gradients, localized heating effects and energy transport, band transitions, carrier collisions with lattice phonons and ionized sites, and spatial non-uniformity of the effective masses in hetero-structures [66].

Two methods were used to simulate the propagation of electromagnetic waves through the device; TMM and finite difference time domain (FDTD) [180]. For single-dimensional light management structures, such as a DBR stack or ARC, TMM was used to model wave propagation with the analytical solution for the electromagnetic fields. FDTD is a numerical technique that is suitable for arbitrary geometries and was used for 2D and 3D structures,

like gratings or textures. FDTD could be used for all situations, but discretizing Maxwell's equations in the time domain required extensive computational power and so TMM was used whenever possible.

A thorough derivation of TMM including how to calculate absorption as a function of depth, which is critical for the present use, is given by Byrnes [181]. Most importantly, the relationship between the amplitudes of the forward and reverse traveling waves, $v$ and $w$, at the $m$th boundary in a system of $N$ layers of media with complex refractive index, is given by,

$$\begin{bmatrix} v_m \\ w_m \end{bmatrix} = M_m \begin{bmatrix} v_{m+1} \\ w_{m+1} \end{bmatrix}, \tag{6.2}$$

where $M_m$ is the transfer matrix,

$$M_m \equiv \frac{1}{t_{m,m+1}} \begin{bmatrix} e^{-iL_m k_0 (n_m + i\kappa_m)} & r_{m,m+1} e^{-iL_m k_0 (n_m + i\kappa_m)} \\ r_{m,m+1} e^{iL_m k_0 (n_m + i\kappa_m)} & e^{iL_m k_0 (n_m + i\kappa_m)} \end{bmatrix}. \tag{6.3}$$

Here, $r_{m,m+1}$ and $t_{m,m+1}$ are the reflection and transmission, respectively, across boundary $m$ and $m+1$, $L_m$ is the thickness of layer $m$, $k_0$ is the wavenumber in free space, and $(n_+ i\kappa_m)$ is the $m$th layer's complex refractive index.

To compute across more than one boundary, *i.e.* $m$ to $m+2$, Equation 6.2 can be modified by to use the product of the relevant transfer matrices, *i.e.* $M_m \cdot M_{m+1}$, in place of the single matrix. To compute for the entire stack, the appropriate boundary conditions must be chosen for the wave amplitudes. That is, the incoming wave in the incident medium will be a known quantity (*i.e.* solar spectrum), and there is no reverse wave ($w_N$=0) in the exit medium. The reflection and transmission across a single boundary are the well-known equations (for normal incidence),

$$r_{m,m+1} = \frac{n_m - n_{m+1}}{n_m + n_{m+1}}, \tag{6.4a}$$

$$t_{m,m+1} = \frac{2n_m}{n_m + n_{m+1}}, \tag{6.4b}$$

which should not be confused with reflected and transmitted power (*i.e.* $R = |r|^2$).

FDTD is a numerical technique first introduced by Yee [182]. Wave propagation through

media is approximated by applying the finite difference method iteratively on a grid to the differential terms in Faraday's law and Ampere's circuital law (Equations 2.33 and 2.33). For these simulations, the initial source is a traveling plane wave of the form,

$$E_z(x,y,t) = E_0 \sin(kx - \omega t + \phi), \tag{6.5}$$

where $k$ is the wave number, $\omega$ is the angular frequency, and $\phi$ is the phase. Outside of the source region, wave propagation is simulated by calculating the **E** and **H** fields on each grid point at each time step. According the equations just mentioned, the time- and spatial-dependence of the **E** field depends on the spacial- and time-dependence of the **H** field, respectively. The finite difference method uses the relationship,

$$f'(x) \approx \frac{f(x+\Delta x) - f(x)}{\Delta x} \tag{6.6}$$

where $\Delta x$ is the grid step, to approximate the field differentials. An analogous equation holds for the time derivatives, where $\Delta t$ is the time step of the simulation. One may also use staggered or 'leap-frog' grid and time steps, where **E** and **H** are calculated on alternating grid points and time steps, to increase accuracy or speed. The key to acquiring accurate results are to minimize the error in Equation 6.6 by choosing a small enough grid step. A fraction of the wavelength is best, and the time step requirement is,

$$\sqrt{(\Delta x)^2 + (\Delta y)^2 + (\Delta z)^2} > c\Delta t, \tag{6.7}$$

where $c$ is the speed of light. The time step is incremented until the simulation reaches steady-state.

The simulation flow of the model is shown in Figure 6.9. First, the cell structure was created virtually, which was done with the included CAD tools. Then, the simulation meshes and boundary conditions were established. From the structure and materials' optical parameters, the optical simulation was performed, by either TMM or FDTD, and the spacial absorbed power density was found. The optical $G$ was then calculated for each mesh point in the device by scaling the absorbed power per wavelength against the solar spectrum. The commercial

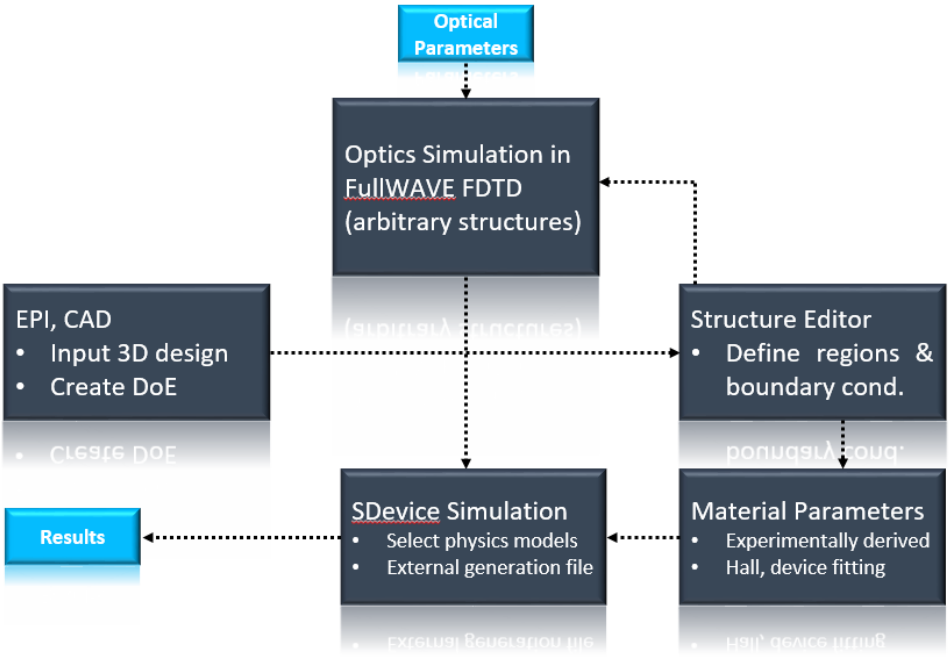


Figure 6.9: Block diagram of the optical and electrical simulation flow.

software Synopsys RSoft FullWAVE was used to perform FDTD simulations, while TMM was done in Sentaurus Device. Finally, the device simulation was executed using the optical generation and the materials' electronic parameters. The results were many useful metrics and experiments, such as band diagrams, dark or light J-V, and EQE.

## 6.4 Light Management for QD Solar Cell

Initial simulations were performed to determine the effect of a textured BSR on the path length of light through InAs QD layers of a GaAs solar cell. The goal was to replicate the result of Inoue *et al.* and to guide an experiment by Smith *et al.* [183]. RSoft FDTD and Sentaurus TCAD simulations were performed on a QD solar cells with structures as depicted in Figure 6.12. The cell absorber consisted of a 500 nm GaAs emitter, 180 nm i-region with 10 repeat QD layers, and 2.5 µm GaAs base. A 4 µm $Al_{0.1}Ga_{0.9}As$ transparent rear scattering layer was used as the transparent texture layer. For the flat BSR cell, a reflecting gold layer was placed below the un-etched AlGaAs scattering layer. The patterned-BSR cell had triangular prisms removed from the bottom of the AlGaAs layer, which were then filled in with gold (see Section 6.2.2).

This latter BSR was based on a experimental texture etched into an AlGaAs layer grown on a GaAs substrate by MOCVD. The texturing process began by developing lines of photoresist perpendicular to the major flat (for US wafer orientation) and then wet etching the exposed AlGaAs with 1:1:75 $NH_4OH$:$H_2O_2$:$H_2O$ [183]. The resulting v-groove texture had a periodicity of 6 μm, which was controlled by the photoresist spacing. An SEM image of the textured AlGaAs is in Figure 6.11. The simulated texture, however, did not include the rounded edges and other imperfections of the experimental sample and was created from simple triangular polygons. For the simulated nanostructures, a slab of QD material with absorption coefficient calculated by the 8-band **k•p** method was implemented [184]. Utilizing a uniform slab allowed more detailed studies of the light field within the QD region compared to simulations with discrete thin QD layers. The absorption coefficient of the QD slab shown in Figure 6.10. The QD peak was at 1050 nm, corresponding to the QD ground level for dots of 2 nm height, 15 nm diameter, and density of $10^10$ $cm^{-2}$. About 18 nm thickness of this material was equivalent to 1 layer of QDs, and 180 nm total was used for 10 QD repeated layers.

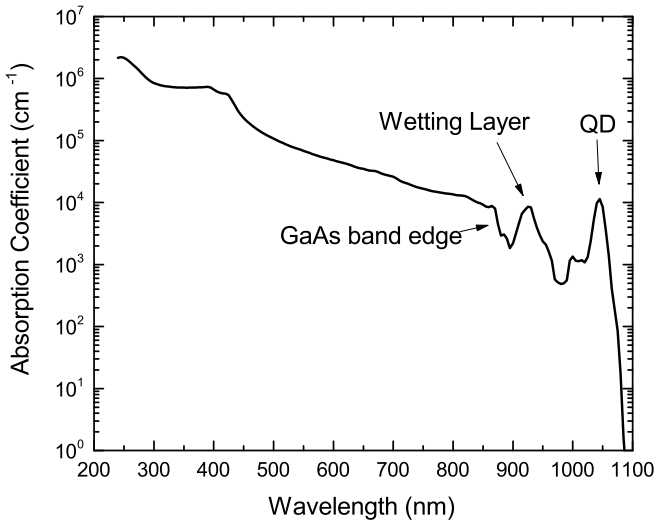


Figure 6.10: Absorption coefficient data used for the QD region in the QD solar cell simulations.

The simulations were run on a cross-sectional unit of each cell with periodic and symmetric boundary conditions. The spectrum of excitation wavelengths ranged from 300 nm to 1150 nm. A fine mesh was used with uniform spacing of 10 nm and a time step of about 0.023 fs. Electric field data were saved for each grid point and examples of these data are depicted

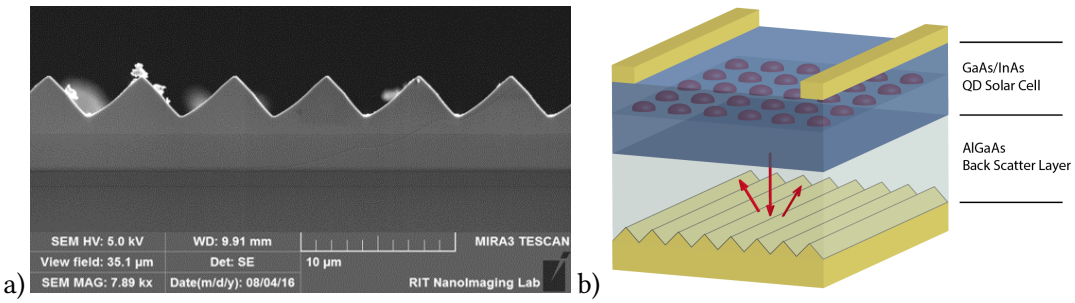


Figure 6.11: a) Cross-sectional SEM image of the triangular prism texture in an etched AlGaAs layer grown on a GaAs substrate. b) Illustration of a QD solar cell with transparent back scatter layer and textured BSR.

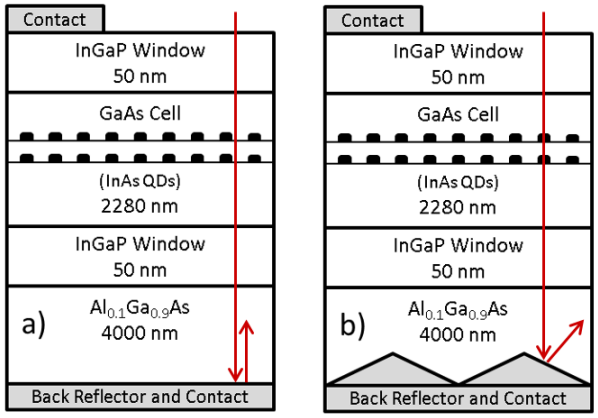


Figure 6.12: Simulated QD cell structure with a) flat BSR and b) triangular BSR.

in Figure 6.13 for a wavelength near the QD absorption peak (1047 nm). The multidimensional effect of the patterned BSR was immediately apparent versus the fundamentally 1D case of the flat BSR. The electric field pattern caused by the triangular BSR had clear nodes of interference due to the period and highly ordered BSR texture. A random BSR would create a spatially less-ordered field. The spatial-dependence of the absorbed power in the QD layer is also shown in the figure. The trends were the same as for the electric field, with clear nodes of high absorption several factors higher than the maximum absorption in the flat BSR.

The optical $G$ data plotted in Figure 6.14 is useful to quantify the contour plot data to show total QD absorption across the entire solar spectrum. The data show that the patterned BSR outperformed the flat BSR for the sum of all of the relevant QD wavelengths. Both BSRs had clear nodes of constructive and destructive interference, which could make the average $G$ a function of QD placement. The triangular BSR achieved an average $G$ of $2.98 \times 10^{21}$ $cm^{-3}s^{-1}$

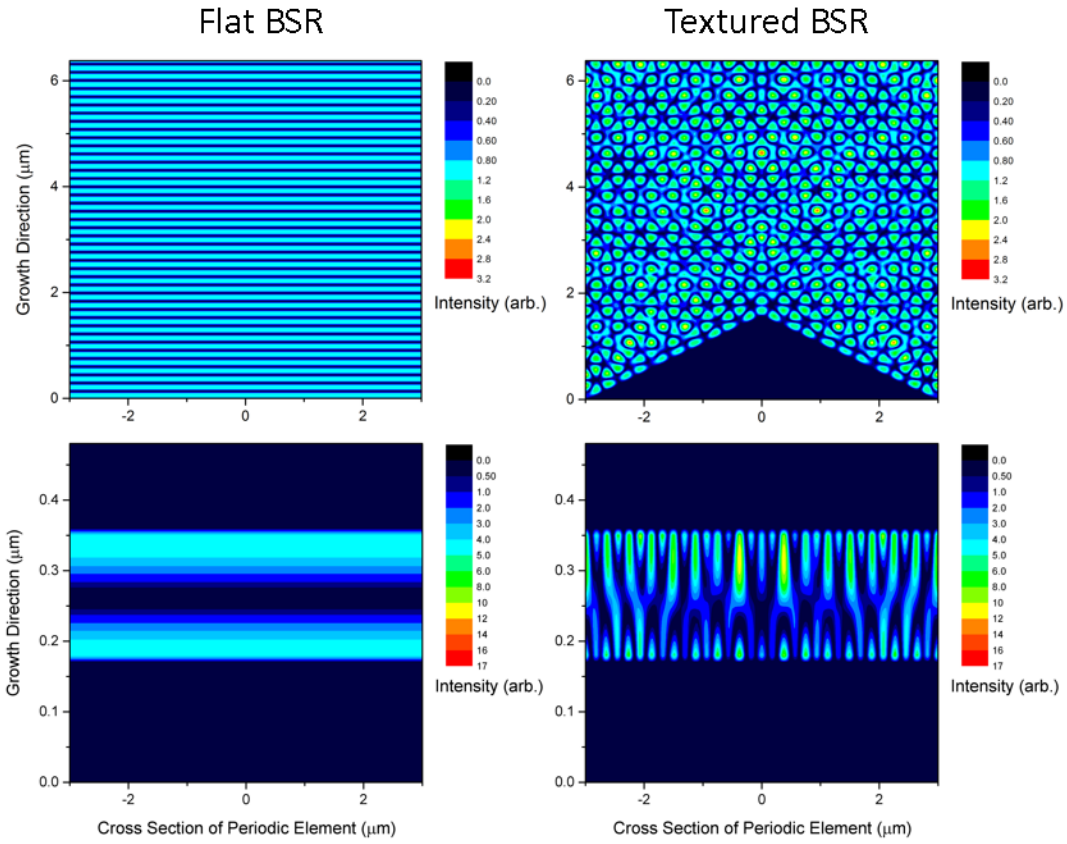


Figure 6.13: Top Row - Contour plots of the electric field intensity vs location for 2D cells with flat (left) and triangular (right) BSRs. The intensity scale is transverse electric field component normalized to input power. A monochromatic plane wave (continuous wave) with TE polarization and a wavelength of 1047 nm (near the QD absorption peak) was used as the excitation source for these simulations. Bottom Row - Contour plots of the absorbed power vs location for 2D cells with flat (left) and triangular (right) BSRs for TE-polarized 1047 nm excitation wave. The intensity scale is absorbed power normalized to input power.

in the QD region, while the flat BSR averaged $2.50 \times 10^{21}$ $cm^{-3}s^{-1}$. The contribution of wavelengths below 900 nm to each of these was $2.09 \times 10^{21}$ $cm^{-3}s^{-1}$, leading to sub-bandgap generation in the flat and textured BSRs to be $4.13 \times 10^{20}$ $cm^{-3}s^{-1}$ and $8.94 \times 10^{20}$ $cm^{-3}s^{-1}$, respectively. If it can be assumed that the flat BSR provided an optical path length of 2, then the $G$ data indicated that the triangular BSR led to a path length of 4.3.

The generation data was used in Sentaurus TCAD to simulate the AM0 illuminated I-V curves shown in Figure 6.15. The GaAs parameters were already given in Table 5.1. Since the QD region was simulated in Sentaurus as a slab of material with bandgap below GaAs, as 3D nanostructures are poorly supported in the software. Due to the wide region with

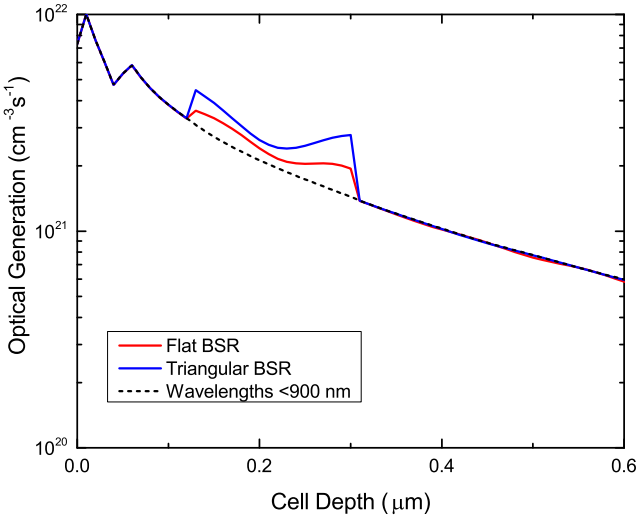


Figure 6.14: Optical generation curve assembled via integrating per-wavelength absorption data against the solar spectrum for the two cells with different BSRs. Zoomed in on the QD region (∼120 nm to 300 nm cell depth).

lower bandgap, the model predicted much lower $V_{OC}$ than what is typically observed in QD cells. This could be fixed in future simulations by fixing the bandgap but not disabling carrier generation below the bandgap. Nevertheless, superior absorption of the patterned-BSR cell allowed for a significant gain in short-circuit current with a value of 26.4 mA/cm$^2$ compared to 24.7 mA/cm$^2$ for the flat BSR cell. The simulated efficiency of the triangular- and flat-BSR cells, were, respectively, 13.2% and 12.3%.

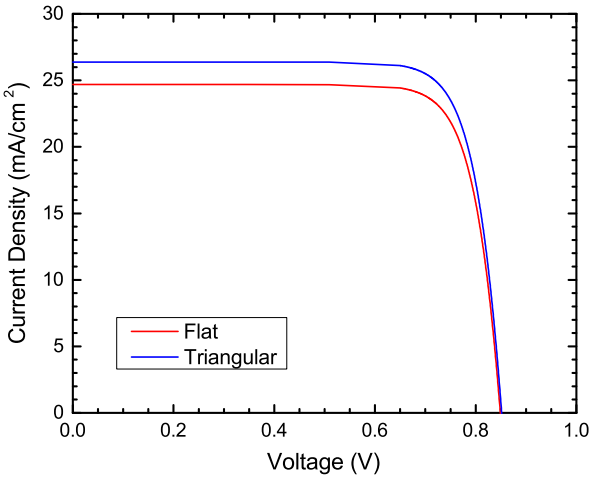


Figure 6.15: AM0 J-V results for the three QD solar cells with different BSRs.

The QD GaAs solar cell model demonstrated that the triangular BSR enhanced absorption

in the QDs by providing a path length of 4.3. The cell designs from this model were grown and fabricated by Smith *et al.* [85, 183], where a path length of 3.0 was obtained. Inoue *et al.* achieved a path length of 3.9 with a very similar triangular BSR design [11]. The reason for the higher path length of the simulation could have been from the optical constants used or idealities in the model that are difficult to obtain experimentally. The shape of the reflector may have had an impact, as the simulated cell had nominal geometry while the experimental cells had imperfect shapes such as rounded corners. These imperfections could have led to different interior angles and modes from the BSR, or could have caused greater parasitic absorption in the metal. The next section was dedicated to determining loss mechanisms in the BSR design, as well an optimizing the BSR design for higher path length.

## 6.5 Path Length Simulations for GaAs with Textured BSRs

The next set of simulations were optical only, with the goal of optimizing the textured BSR for high path length. Three different texture types were tested. First, the triangular-prism linear grating used in the previous section. Then, a pyramid-shaped 3D grating. Finally, a pseudo-random texture was tested based on an experimental texture obtained from a maskless crystallographic etch. The first two textures were optimized based on their aspect ratio and grating period. Additionally, the reflector material stack was optimized to obtain higher reflection by inserting a low-index layer between the metal and semiconductor.

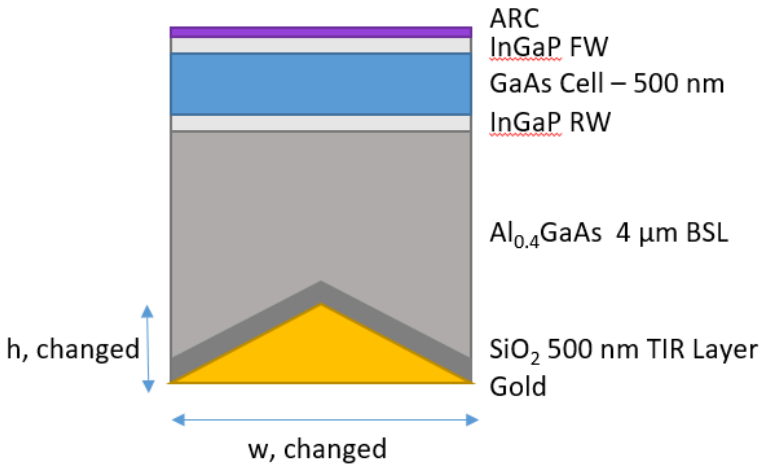


Figure 6.16: Simulated thin GaAs cell structure used to calculate the absorption enhancement.

FDTD simulations were performed with a 3D mesh with uniform spacing of 10 nm. The simulated structure is shown in Figure 6.16. To easily calculate absorption enhancement enabled by the textures, a simple thin GaAs cell of 500 nm total thickness and with 50 nm-thick front and rear InGaP windows was designed. Behind the rear InGaP window was a 4000 nm-thick $Al_{0.4}Ga_{0.6}As$ rear scatter layer, where high Al% was used to prevent parasitic absorption of shorter wavelengths that could transmit through a single pass of the thin GaAs absorber. A periodic unit was simulated with periodic boundary conditions used on the lateral boundaries, but with perfectly matched layers (PML) along the direction of the input-wave propagation, which was normal to the cell surface. Results were averaged between transverse-electric (TE) and transverse-magnetic (TM) excitation-wave polarizations. An excitation wavelength that was very weakly absorbed by GaAs, 900 nm, was chosen to ensure that high enhancement factors could be achieved before the light was significantly attenuated. This configuration should find absorption enhancement factors that are relevant to QD cells as well as certain multi-junction cells such as an InGaP/GaAs dual junction; or any cell of similar refractive index that requires higher absorption of wavelengths near 900 nm. Scattering will not have a strong wavelength dependence unless the texture features approach sub-wavelength [185].

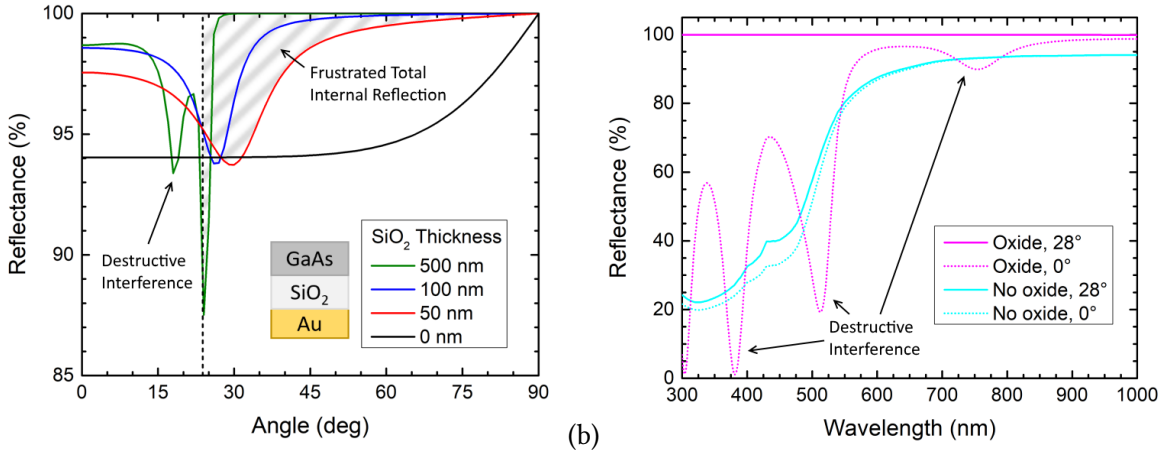


Figure 6.17: (a) TMM results for reflectance vs angle of incidence for the AlGaAs-gold interface in the BSRs using different intermediate layer widths of $SiO_2$ to improve reflection. The wavelength used here was 950 nm. (b) TMM result for fixed angles of incidence vs wavelength for incident angles on a flat BSR (normal) and for a 0.3 aspect ratio triangular BSR. The solid lines are for a metal-only BSR stack while the dotted lines include a 500 nm $SiO_2$ layer.

In the structure, a TIR layer made of $SiO_2$ was added to the BSR stack between the AlGaAs and the gold. In silicon cells, it is understood that a low-index layer between the metal and semiconductor can lead to higher reflection and lower parasitic absorption by avoiding both propagating and plasmonic modes in the absorbing metal, especially for textured reflectors [169]. To confirm this, reflection calculations were performed on oxide-based BSR structures using TMM. The effect of the dielectric layer on the reflection of the BSR is shown in Figure 6.17. Figure 6.17a is a plot of reflectance vs. angle of incidence for a fixed wavelength of 950 nm [11]. The incident medium was non-absorbing GaAs, so the reflection in the plot refers to reflection off of the BSR back up into the semiconductor, not air. Increasing the width of a $SiO_2$ layer between the GaAs and gold led to higher reflectance for most wavelengths. With $SiO_2$ thickness at 500 nm, there was 100% reflection for most angles of incidence higher than the critical angle ($\theta_C$) for TIR ( 24°). When the $SiO_2$ thickness was 100 nm or less, the phenomena of frustrated total internal reflection (FTIR) occurred, a concept similar to quantum tunneling. For angles above the critical angle ($\theta > \theta_C$), evanescent waves transmitted energy into the metal by exciting surface plasmon polaritons modes, leading to parasitic absorption in the metal and loss of reflection [169]. Even at 500 nm thickness, there was still FTIR between $\theta_C$ and ∼27°, though at this thickness the overall reflection loss was greatly reduced compared to 100 nm.

For $\theta < \theta_C$, the $SiO_2$ reduced reflection loss by suppressing propagating modes, as the metal was more reflective when the incident medium had lower index of refraction. The exception to this was when the $SiO_2$ layer behaved as an ARC. At certain angles and thicknesses, light reflected off of the semiconductor-oxide interface destructively interfered with light reflected from the metal. The destructive interference condition was when the $SiO_2$ layer was $n\lambda/2$ where $\lambda$ was the effective wavelength in the $SiO_2$ corrected for refracted angle and $n$ was any integer of 1 or greater. This was different than the traditional ARC condition, $(2n-1)\lambda/4$, due to the configuration of the refractive indices in the BSR layers. Optimizing the $SiO_2$ thickness to remove any destructive interference was not attempted, as there was always at least one condition for destructive interference for thickness above ∼300 nm, but below 300 nm led to greater loss through FTIR which was more important to avoid. An oxide

thickness of 500 nm was ultimately chosen for the remainder of the simulations as this was a good compromise between preventing FTIR, maintaining generally good reflection below $\theta_C$, and remaining practical for fabrication of experimental devices.

Figure 6.17b is a plot of reflectance vs wavelength for fixed angles of incidence. The pink curves in the figure were for metal only, and with 0° (solid) or 28° (dotted) angle of incidence the reflectance was similar. The choice of 28° here was because this was the angle of the triangular texture simulated in the previous section (Section 6.2.2). The blue curves in the plot had the 500 nm-thick $SiO_2$ TIY layer, and for 28° incidence angle the reflectance was 100% for all wavelengths as this angle was beyond $\theta_C$. For normal incidence, the reflection was improved over the bare metal for most angles beyond 550 nm. Below this wavelength, thin-film interference was observed again with modes of both constructive and destructive interference. As most wavelengths below 550 nm will be absorbed on the first pass, even in very thin cells, these effects will not be of much concern. There was one destructive interference condition above 550 nm, at ∼750 nm, which was not alarming as 750 nm was not of any particular interest. Had this interference occurred for the QD wavelength, however, this could be avoided by changing the oxide thickness to shift the interference wavelengths. Destructive interference at the wavelength for a QD absorption peak, for example, would want to be avoided in a flat BSR cell driven by normal incidence. For a textured BSR, the oxide layer was clearly superior for all wavelengths.

All of the results in Figure 6.17 were found with a 1D analytical approach using TMM. In the silicon industry where texturing is more common and well-understood, it is known that a textured metal reflector leads to parasitic plasmonic modes in the metal [186]. To examine the effect of the TIR layer on the reflection of a textured BSR more accurately, 3D FDTD simulations were performed for the structure in Figure 6.16 for a pyramid texture both with and without the TIR layer. Figure 6.18a is a 3D contour plot of absorbed power from one of these simulations. Absorption in the GaAs cell can be seen near the top, and parasitic absorption on the surface of the metal in the BSR is seen at the bottom. To better quantify the loss, the absorption was summed across cross-sections and plotted against the growth direction in Figure 6.18b for cells with and without a TIR layer. Without the TIR layer, the

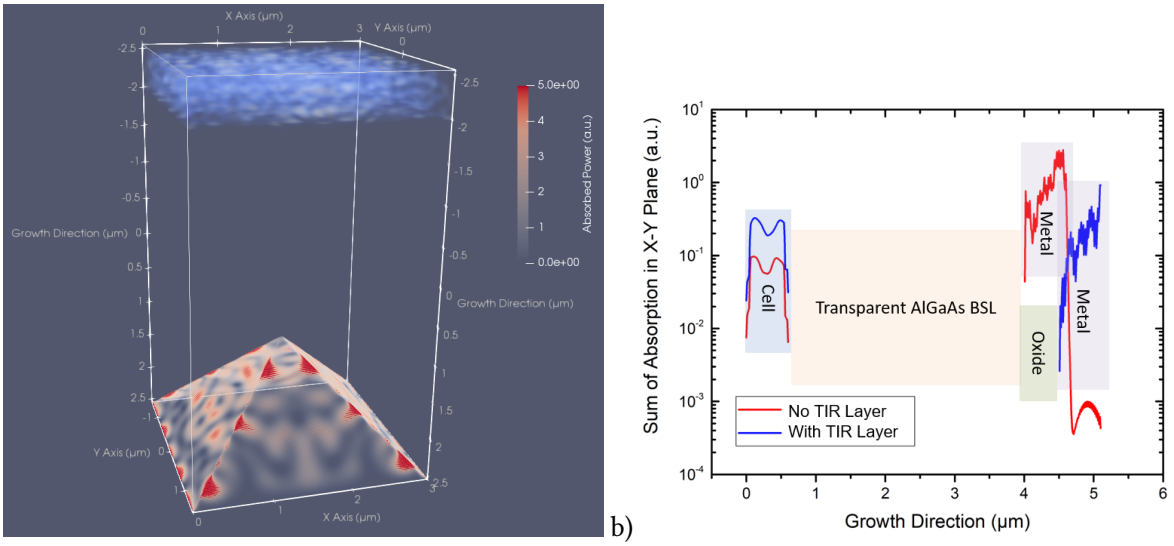


Figure 6.18: a) 3D spatial contour plot of absorbed power of 900 nm light in a single period of the thin GaAs cell with a pyramid-textured BSR. b) Total absorption in a cell plane as a function of growth direction (Z) for cells with without a TIR layer. The aspect ratio and period of the scattering structure was the same for both cells, the only difference was the presence of the TIR oxide layer between the metal and AlGaAs back scatter layer.

absorption in the metal was an order of magnitude higher than in the GaAs layer for 900 nm. When the TIR was added, parasitic loss in the metal was much reduced and instead that light was reflected and absorbed in the GaAs layer. This result confirmed that the 500 nm-thick TIR layer should be included in the BSR stack for the texture optimization study. Quantification of the improvement due to the TIR layer on the path length is discussed later.

Figure 6.19 contains absorption enhancement factors for triangle and pyramid BSRs of different aspect ratio and periods. The enhancement factor, or path length, was calculated for 900 nm light by normalizing the total absorption in the GaAs cell for the textured cell in question by the total absorption in a conventional, on-substrate GaAs cell of the same thickness. Trends were not easily identified in the results, but the triangular BSR generally enhanced absorption by a factor of 3 to 8, while the pyramids offered 9 to 23, with some outliers. All but one of the simulations in the plot used the 500 nm-thick $SiO_2$ TIR layer in the reflector stack. A metal-only stack was simulated for pyramids of aspect ratio of 0.3 and period of 2 μm ('+' symbol in figure), and the enhancement factor dropped from 33 to 10, indicating that this layer is crucial to obtaining high path lengths. The 6 μm period triangular BSR with

aspect ratios near 0.3 matched well with previously reported experimental work [11], where an enhancement factor in the QDs was reported to be 4.8. The most promising result was the pyramid BSR with period of 2 µm, which reached 33 factor for an aspect ratio that corresponds to the wet etch crystallographic angle (near 0.3). For 0.7 aspect ratio, 1 µm period approached the theoretical limit for a random texture (see Section 6.2.1), 49, indicating a strong diffraction order into a mode that allowed for very long path lengths before escaping. This result agreed well with Battaglia *et al.*, who discovered that the most resonant period for triangular structures was $\sqrt{3/2}$ times the wavelength, or $\sim$1.1 µm in this case. However, as the 0.7 aspect ratio would be difficult to achieve via wet etch, 2 µm period was the most reasonable approach and could also avoid stronger wavelength dependence of smaller features.

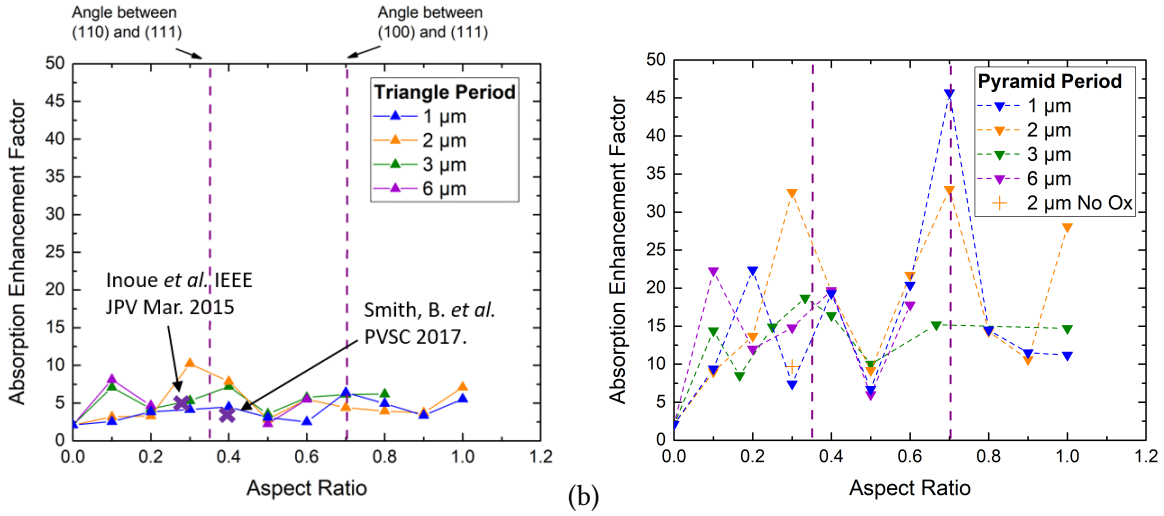


Figure 6.19: Absorption enhancement for (a) triangular and (b) pyramidal BSRs of varying periods and aspect ratios. Calculated aspect ratios resulting from anisotropic etching along crystal planes, as well as the aspect ratio estimated from SEM of the triangular texture are highlighted.

One additional BSR was tested as part of the simulated set, and this was a pseudo-random textured BSR. The texture was developed experimentally with a maskless etch [85] and then digitized for the simulation using atomic force microscopy (AFM). The 5 µm by 5 µm grid data, seen in Figure 6.20a, was imported into the FDTD software to incorporate into the 3D structure. A cross-section of the simulation structure is shown in the Figure 6.20b. The gold reflector was modeled flat in this instance, with the texture applied only to the oxide-AlGaAs interface. At the edges of the simulation, periodic boundary conditions were applied as usual.

The large area simulated (5 μm by 5 μm) was to provide a sufficiently random surface lacking any obvious repetition at the 1 μm-wavelength scale due to the boundaries. The absorption enhancement factor was 13.8, which is a favorable value compared to the triangular linear grating (3-8 factor, generally), but not so compared to the pyramid texture (9 to >20). As already state, a fully-random texture would obtain near 50 factor. However, the maskless etch was not completely random as the etched features were expected to have similar aspect ratios with some range of variation in the heights and widths.

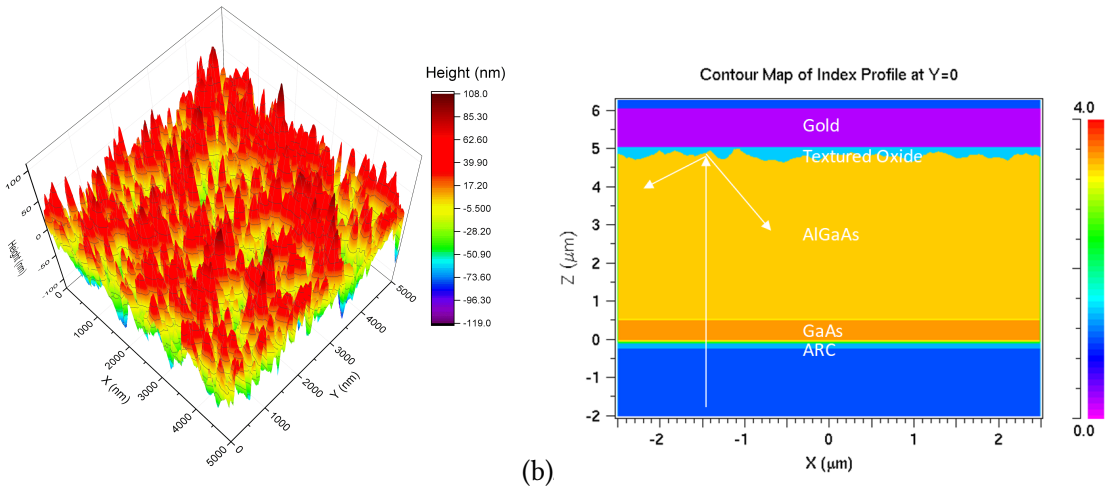


(a) (b)

Figure 6.20: (a) AFM data for a maskless etch texture. (b) Cross-section of 3D solar cell with random texture, layers colored according to refractive index.

To conclude, the optimal wet-etched texture allowed for a factor of 30 path length enhancement of light compared to an upright cell on a thick substrate. High reflectivity of the mirror was critical to achieving this result, which was achieved with a low-index dielectric to promote TIR on the backside of the cell and to prevent parasitic modes in the metal. Without this layer, the result was only a factor of 10 increase. The periodic pyramid texture had the best performance with >30 path lengths, and outperformed the maskless-etch pseudo-random texture for many periods and aspect ratios. Whether or not a periodic or random texture texture is better theoretically is a subject of debate in the silicon field, with some work indicating that periodic gratings can achieve $14.5n^2$ path length for single wavelengths [187], compared to the classic $4n^2$ for a random texture [167]. The key is that the periodic structure can be designed to avoid modes that couple into the escape cone.

## 6.6 Light Management for GaAs Subcell of InGaP/GaAs/Ge Space Cell

The goal of these simulations was to reduce the middle subcell thickness of an InGaP/GaAs/Ge-type space cell as this improves the radiation tolerance and allows for longer missions [39]. It is well-understood that the GaAs subcell in the InGaP/GaAs/Ge triple junction space solar cell is current-limiting at EOL. With a ∼1 µm-thick GaAs subcell, the 3-J cell will have improved radiation tolerance, however light management is then required for a GaAs absorber layer that is not optically thick.

To improve the GaAs subcell current, a photonic crystal has been inserted between the middle and bottom junctions in the simulation. The photonic crystal was inspired by previous simulations reported by Mellor *et al.* [13] and consists of a diffraction grating, a low-index spacer, and a DBR. The grating scatters GaAs band-edge light, the spacer internally reflects scattered light (restricting it to the top subcells) and prevents coupled modes into the DBR [188], and the DBR reflects any GaAs band-edge light that could not be scattered or reflected off the TIR layer.

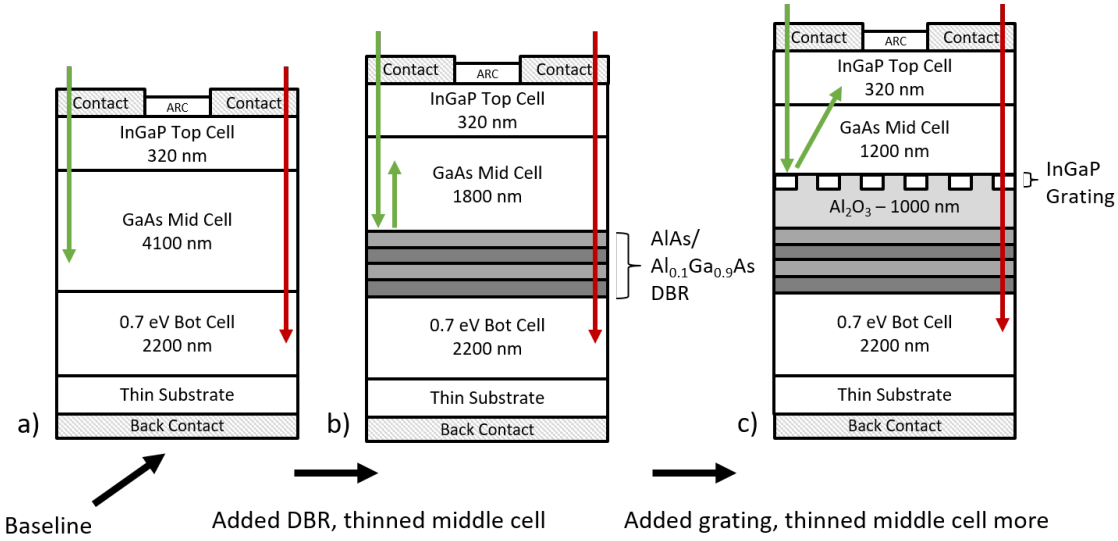


Figure 6.21: Simulated a) baseline triple-junction cell with thick 4.1 µm GaAs subcell, b) cell with thin 1.8 µm GaAs subcell and a DBR between the middle and bottom junctions, and c) cell with even thinner 1.2 µm GaAs subcell with the DBR as well as the grating and TIR layer.

Synopsys RSoft FullWAVE FDTD and Synopsys Sentaurus TCAD simulations were used to evaluate the performance of a light management structures intended to increase current

collection in the GaAs subcell of a InGaP/GaAs/Ge space cell. The material parameters for the electronic simulation began with those from Sato *et al.* [33], but with optical constants for InGaP and GaAs measured via spectroscopic ellipsometry. The parameters of diffusion length and layer thickness were refined until a satisfactory baseline match to the BOL performance of a typical ZTJ cell [1] was obtained. The thick bottom Ge cell was replaced with a much thinner 0.7 eV subcell based on GaSb in the interest of saving computational time. Several 3-J cell structures were simulated to evaluate the photonic crystal. First, a baseline cell was simulated with a GaAs subcell thickness of 4100 nm. The subcell was then thinned to 1800 nm before adding in the DBR layers. While half of the original thickness would be expected for a reflector that effectively doubles the path length, the slightly-less-than-half thickness emphasized differences in the DBR layers to more easily find the optimal DBR. Finally, the subcell was thinned to 1200 nm and a diffraction grating made of InGaP in a low-index, TIR layer made of $Al_2O_3$ was added to complete the photonic structure. The progressively thinned structures are shown in Figure 6.21.

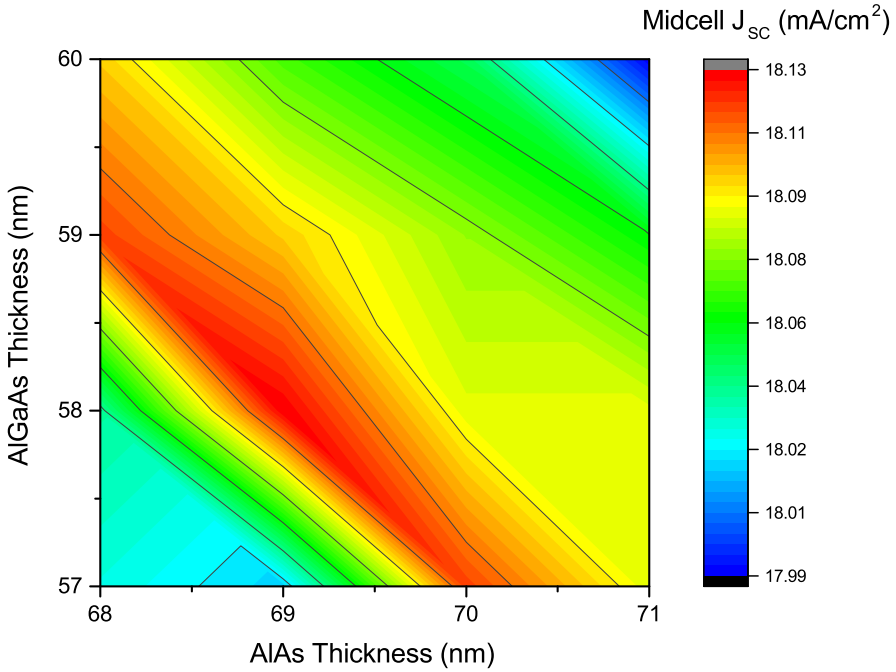


Figure 6.22: DBR layer thickness vs. middle subcell $J_{SC}$ contour plot used to optimize the AlGaAs/AlAs DBR. This DBR was 24 pairs.

TMM-based simulations were performed to optimize both the thicknesses of the

$Al_{0.1}Ga_{0.9}As$ and AlAs layers and the number of repeated pairs. The data is shown as a contour plot of $J_{SC}$ as a function of AlGaAs and AlAs layer thicknesses in Figure 6.22. At 58 nm and 69 nm for AlGaAs and AlAs, respectively, middle subcell $J_{SC}$ was maximized. For number of DBR pairs, it was found that increasing the number of pairs increased the middle subcell $J_{SC}$, but there was no benefit after about 20 pairs (see Figure 6.23a). Thinning the subcell from 4100 nm to 1800 nm caused transmission loss of 1 $mA/cm^2$, and the addition of 20 or more DBR pairs returned 80% that current. The remaining 20% could not be recovered due to insufficient bandwidth of the DBR. The refractive indices of AlGaAs and AlAs are similar, and the DBR created from them reflected only a narrow set of frequencies near the GaAs band edge. To resolve this, a second DBR was added behind the first using different thicknesses of AlGaAs and AlAs at 51 nm and 62 nm, respectively. This 2x-DBR design proved to the more effective of the two DBR types, as it returned nearly all of the lost current at 48 total DBR pairs (24 + 24).

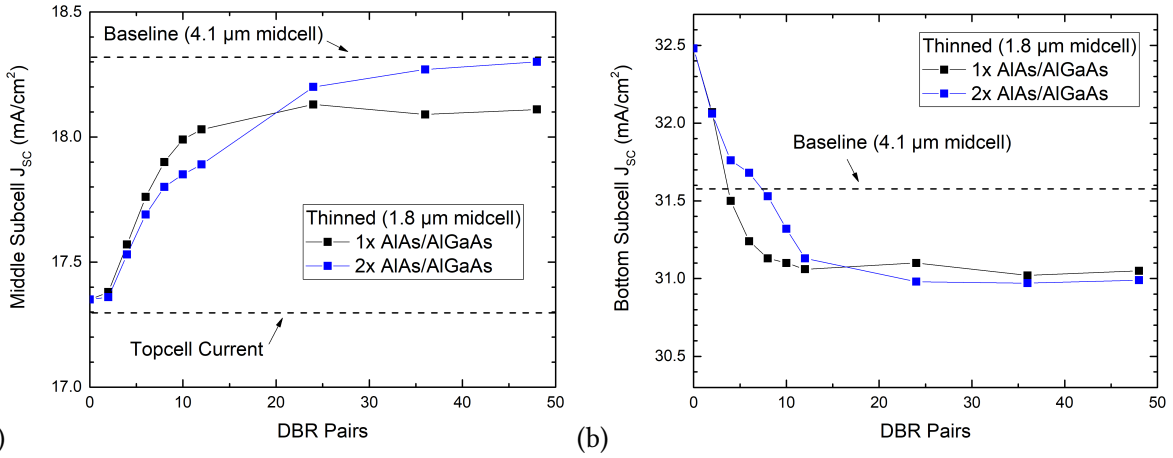


Figure 6.23: a) Middle subcell $J_{SC}$ (a), and b) bottom subcell $J_{SC}$ as a function of number of DBR pairs for the 1x- and 2x-DBR designs.

The reflection vs. wavelength of the 1x-DBR and 2x-DBR stacks are shown in Figure 6.24a. The 1x-DBR had reflection near 100% in the wavelength region of 800 nm to 900 nm for 26 pairs. The 2x-DBR structure of similar overall thickness to the single-DBR structure, with 13 pairs of 51nm/62nm thickness and another 13 pairs of the original 58nm/69nm thickness. This 2x-DBR sacrificed peak reflection for added bandwidth, starting at ∼700nm instead of 800nm. The 2x-DBR could be optimized further, as optimizing the four thicknesses involved

as well as pair ratio is more extensive and was not performed yet. Furthermore, a graded DBR might be the best design. The effect of the 1x-DBR and 2x-DBRs on the the external quantum efficiency is in Figure 6.24b. The baseline had 4100 nm-thick middle subcell while the DBR cells had 1800 nm. The EQE data indicated that, although the DBR cells displayed interference fringes in the middle subcell, the average EQE was close to that of the thick baseline. Due to its greater bandwidth, the 2x-DBR maintained baseline-like EQE for the shorter GaAs wavelengths when compared to the 1x-DBR design; the 2x-DBR cell did not have the reduction at 750 nm like the 1x-DBR cell did.

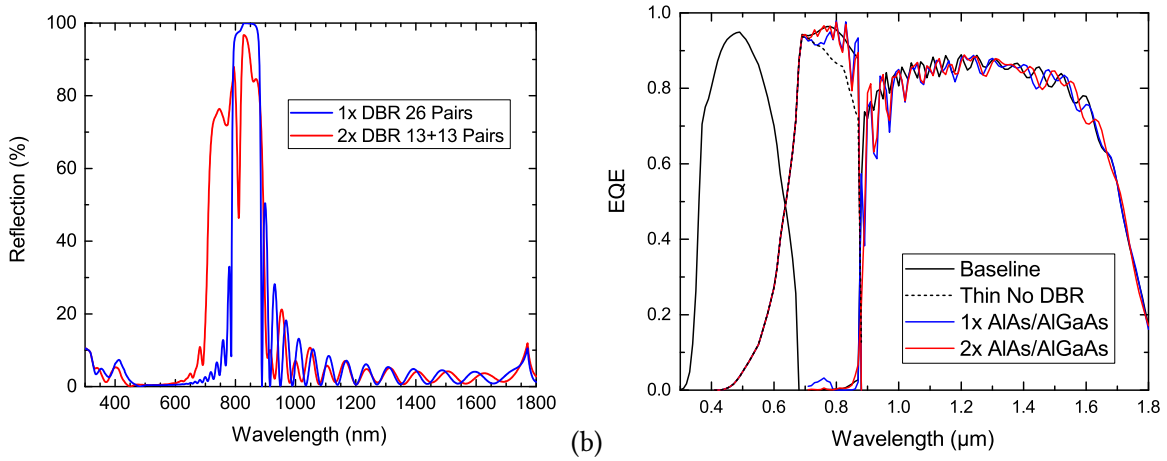


(a) (b)

Figure 6.24: a) Reflection vs. wavelength for 26 pair 1x-and 2x-AlGaAs/AlAs DBR. Absorption was disabled for the GaAs incident medium. b) EQE of the baseline cell with 4100 nm-thick GaAs subcell, and the *sans*-DBR, 1x-DBR, and 2x-DBR cells with 1800 nm-thick GaAs subcell.

Figure 6.23b is bottom subcell $J_{SC}$ vs. number of DBR pairs, used to determine the extent of the bottom subcell $J_{SC}$ reduction due to DBR interference fringes. Both DBR designs performed similarly and converged on 0.5 mA/cm$^2$ of lost current, which was a small value compared to the amount of excess subcell current (31 mA/cm$^2$ in Ge vs. 17 mA/cm$^2$ in InGaP).

Figure 6.25 is a plot of middle and bottom subcell $J_{SC}$ correlating to the process in Figure 6.21. Beginning with the baseline GaAs subcell thickness of 4100 nm, the subcell was thinned to 1800 nm and then the DBR was added. Then the middle subcell was thinned again to 1200 nm and the final piece of the photonic structure, the grating, was added. Once the middle subcell was thinned to 1800 nm from 4100 nm, the DBR (26-pair 1x-DBR) was required to restore the original ratio of currents. Thinning the subcell further to 1200 nm, the DBR-only design

had only 94.4% of the baseline GaAs subcell $J_{SC}$, which was a loss of 1 mA/cm$^2$. Addition of the grating and TIR layer brought the current back above 18 mA/cm$^2$, or 97.8% of the baseline current. However, the grating led to greater than 8 mA/cm$^2$ loss (74.5% of baseline) in the bottom subcell $J_{SC}$. Loss of this much current could lead to a bottom subcell-limiting condition at the maximum power point, which is addressed later. The grating dimensions used for these simulations were 430 nm grating period consisting of 320 nm InGaAs width in 110 nm of $Al_2O_3$ cladding, the height or thickness of the InGaP was 230 nm, and the $Al_2O_3$ TIR layer was 1000 nm thick. The grating section of the structure could be optimized to reduce the bottom subcell loss as this grating prototype was optimized to increase middle subcell current only without concern for the bottom subcell.

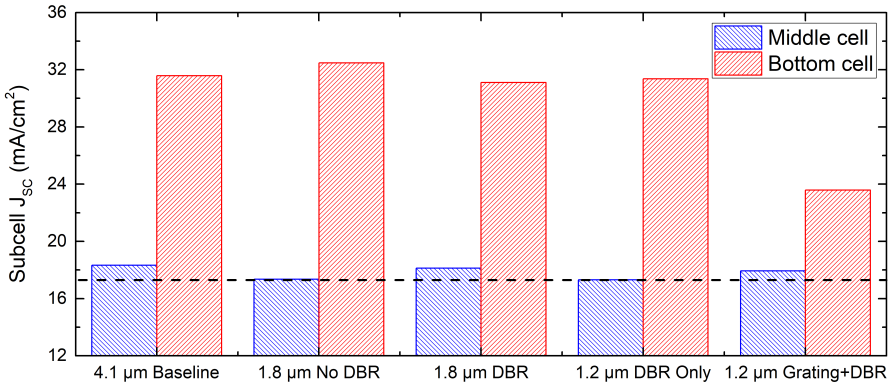


Figure 6.25: Simulated $J_{SC}$ for the middle (blue) and bottom (red) subcells of the triple-junction cells with and without light management features. The black dotted line was the InGaP top subcell $J_{SC}$. The goal was to maintain the baseline currents while making the cell as thin as possible.

Figure 6.26 contains the simulated AM0 J-V three cells of Figure 6.21. These results indicated that the performance of the three cells was nearly the same, even though the GaAs subcell thickness were different in each one. The grating cell did have some FF loss due reduced current in the Ge subcell due to the grating and TIR layer reflecting a significant portion of the Ge wavelengths as discussed above. Implementing a thinner subcell without sacrificing initial performance made the DBR-only and grating designs better suited for the radiation environment of space. However, the grating design could not be used as-is in newer designs of multi-junction space cells. The InGaP/GaAs/InGaAs IMM, for example, is much closer to current-matched than the Ge-based 3-J, meaning that the 1.0 eV InGaAs cell could not afford

to lose 8 mA/cm$^2$ of its current to the photonic crystal. The Ge subcell studied here had 31 mA/cm$^2$ of current (see Figure 6.21) before the photonic crystal was implemented, while a current-matched bottom subcell would have 20 mA/cm$^2$ or less. Losing 8 mA/cm$^2$ from the Ge subcell still keeps it well above the ~17 mA/cm$^2$ $J_{SC}$ of the InGaP subcell, however, a current-matched bottom subcell, like 1.0 eV InGaAs, would drop to 12 mA/cm$^2$ with the crystal, which would current-limit the cell and cause a large drop in efficiency. Either the bottom subcell loss would have to optimized to virtually eliminate the loss, or the IMM would have to be redesigned to account for the loss, *i.e.* by grading further to 0.9 eV InGaAs.

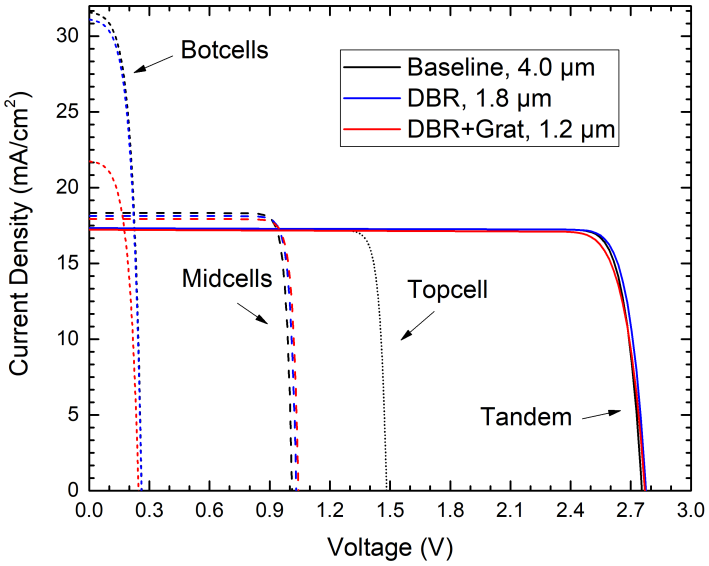


Figure 6.26: Simulated AM0-illumninated I-V the three structures.

Another issue with the photonic crystal is the increased fabrication complexity. Mellor *et al.* have preferred the approach of wafer bonding, but avoiding this would be preferable as it requires two substrates. The DBR section of the crystal can be grown monolithically in an epitaxial reactor with no extra fabrication steps as the layers are all semiconductor. The grating structure is a much more difficult growth problem, but could possibly be accomplished by halting the growth, forming the grating, then re-growing the top layers with lateral overgrowth and creating the low-index $Al_2O_3$ layer from AlAs via steam oxidation [189, 190]. One problem with this approach is the transition from high index semiconductor to low-index oxide leads to a broadband semi-reflective surface. The grating could by tapered to make it

behave as an ARC, but this may interfere with its ability to scatter and reflect the wavelengths for GaAs.

Figure 6.27 is an example of how one can optimize grating feature sizes. The 1st diffraction order is the desired order for the GaAs wavelengths, as these are the wavelengths that will be sent back up into the GaAs subcell at an angle beyond the front surface's critical angle for escape. The 0th order is wanted for the Ge-absorbing wavelengths, as the 0th order is undeflected light traveling normal to the surface that should transmit through DBR if it is outside the DBR bandwidth. This grating, the same as used for the multi-junction simulations above, was not well-optimized, as the 1st order diffraction peaked between 650-800 nm at ~50% of the photons instead of 650-890 nm to cover the entire GaAs range. Fringes for the 1st order continued out into the longer wavelengths, which led to bottom subcell losses. Optimization is possible by changing the grating features to obtain high reflection for 650-890 nm and high transmission for >890 nm.

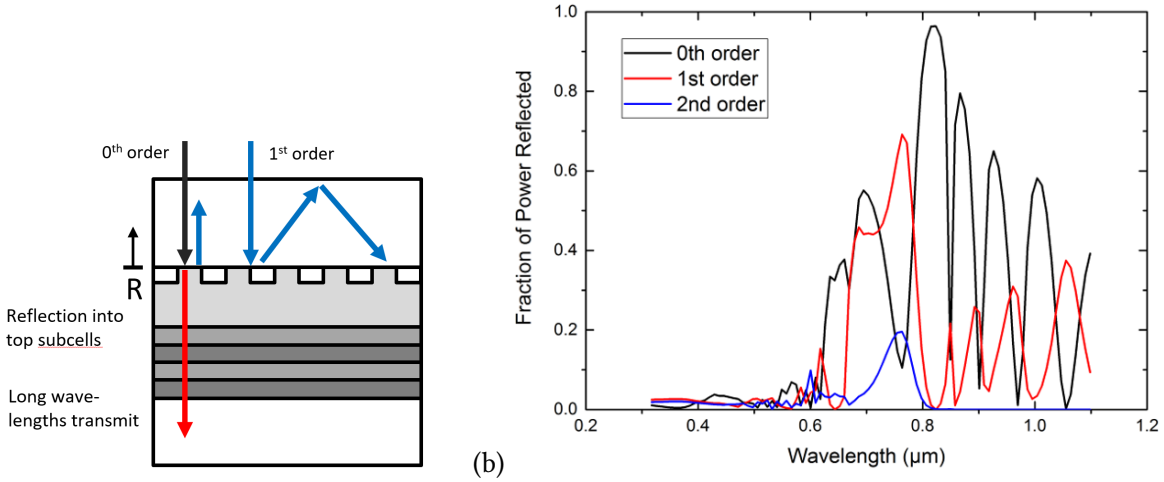


Figure 6.27: (a) Illustration of the photonic crystal and examples of the path of 0th and 1st diffraction orders. (b) A diffraction order efficiency plot for the 0th, 1st, and 2nd diffraction orders as a function of wavelength. The 1st order angle in the 800 nm range was ~28°.

With Equation 6.1 and the damage coefficients, the EOL efficiency of the multi-junction structures could be simulated. In Appendix D, damage coefficients for GaAs and InGaP were fit using data from irradiated IMM cells, and those damage coefficients were used to perform EOL simulations. Table 6.1 contains the BOL and EOL AM0 efficiency of the simulated cells as well as the middle subcell BOL and EOL $J_{SC}$. The EOL/BOL ratio is also given for these

metrics, as this is a measure of the radiation tolerance of the cell. The expected EOL/BOL is taken from the ZTJ cell datasheet [1], where the assumptions made are that the ZTJ cell is middle-subcell-limited at all fluences and that the ZTJ cell does not already contain a DBR. The baseline cell (4100 nm thick middle subcell, no DBR or grating) had higher $J_{SC}$ EOL/BOL of 0.958 compared to the expected value of 0.94. It also had lower cell efficiency ratio with 0.844 compared to the given 0.85. The exact structure of the ZTJ is not given so this is an acceptable fit, however, it may be that the simulation here over-estimated the minority carrier mobility and over-estimated the damage to the SRH lifetime.

The general trend was higher EOL/BOL ratio for both $J_{SC}$ and efficiency as the middle subcell thickness is decreased. The 1200 nm thick middle subcell with DBR and grating design was the most radiation tolerant, at 0.994 and 0.851 for both middle subcell $J_{SC}$ and cell efficiency, respectively. However, the 1800 nm with DBR design had the highest efficiency at EOL at 26.42%, compared the 24.20% for the baseline cell. The grating cell under-performed in absolute efficiency due to the FF reduction caused by bottom subcell current loss, which was explained previously. The conclusion to be drawn from Table 6.1 is that the DBR and DBR-plus-grating designs were clearly more radiation tolerant, but these cells were not optimized carefully enough for EOL. The middle subcell was still overproducing current at EOL for the 1200 nm cell with DBR-plus-grating, for example, since the top subcell was limiting the cell to 17.32 mA/cm$^2$ while the middle subcell was at 17.82 mA/cm$^2$.

Table 6.1: $J_{SC}$ and AM0 efficiency of the five simulated solar cells for BOL and EOL, along with expected EOL/BOL ratio from ZTJ datasheet [1]. The EOL condition was $1\times10^{15}$ cm$^{-}2$ fluence of 1 MeV electrons. The ZTJ thicknesses were assumed and may be incorrect.

| Metric | BOL | EOL | EOL/BOL | Expected EOL/BOL |
|---|---|---|---|---|
| 4100 nm midcell $J_{SC}$ | 18.22 mA/cm$^2$ | 17.46 mA/cm$^2$ | 0.958 | 0.94 |
| 1800 nm midcell $J_{SC}$ | 17.23 mA/cm$^2$ | 17.02 mA/cm$^2$ | 0.988 | |
| 1800 nm midcell $J_{SC}$ w/ DBR | 18.12 mA/cm$^2$ | 17.88 mA/cm$^2$ | 0.987 | |
| 1200 nm midcell $J_{SC}$ w/ DBR | 17.30 mA/cm$^2$ | 17.20 mA/cm$^2$ | 0.994 | |
| 1200 nm midcell $J_{SC}$ w/ DBR+Grating | 17.93 mA/cm$^2$ | 17.82 mA/cm$^2$ | 0.994 | |
| 4100 nm midcell 3-J eff. | 31.03% | 26.20% | 0.844 | 0.85 |
| 1800 nm midcell 3-J eff. | 30.79% | 26.04% | 0.846 | |
| 1800 nm midcell 3-J eff. w/ DBR | 31.04% | 26.42% | 0.851 | |
| 1200 nm midcell 3-J eff. w/ DBR | 30.77% | 26.08% | 0.848 | |
| 1200 nm midcell 3-J eff. w/ DBR+Grating | 30.63% | 26.07% | 0.851 | |

To summarize, the interstitial DBR allowed the middle subcell to be effectively halved in thickness while maintaining good current in the bottom subcell and without any loss in BOL cell efficiency. Adding a grating texture between the DBR and the middle subcell allowed the middle subcell to be thinned to 1200 nm, but the texture at this location led to loss of 25.5% of the bottom subcell current. EOL simulations demonstrated that both DBR and DBR-plus-grating designs were more radiation tolerant, but that these cells were not fully optimized for EOL yet. Even without optimization, the DBR design improved the thick baseline cell by 0.22% absolute efficiency at EOL.

## 6.7 Conclusions & Future Work

A numerical model for integrated light management was developed to explore textures or gratings in III-V solar cells in three areas: thin GaAs cells, QD solar cells, and space cells. All three of these cells are not dependent on photon recycling or radiative coupling, which were not included in the model.

To increase absorption in nanostructured single-junction GaAs-based cells, the GaAs substrate was removed and replaced with a textured BSR. The QD GaAs solar cell model demonstrated that the triangular-prism textured BSRs enhanced absorption in the QDs. This model was designed to replicate experiments by Smith *et al.* [85, 183] and Inoue *et al.* [11]. The model predicted that the textured BSR had an average path length of sub-bandgap wavelengths through the QDs of 4.3, while the experimental results calculated this path length to be 3.0 and 3.9. The error could have come from non-ideal conditions in the experimental cells, such as the random smoothing or variation in the texture, or from error in the optical constants used.

To optimize the rear-side BSR texture design, a series of absorption enhancement simulations were performed for three texture types: triangular linear gratings, pyramidal gratings, and a psuedo-random maskless-etch texture. In theory, these textures could be replicated in experiment via wet etching. The first two textures were explored in terms of aspect ratio and period. It was generally found that the optimal period was 2 μm for both pyramid and triangular textures. The pyramid texture could achieve path lengths of 10 to 35 depending

on aspect ratio, while the triangular texture achieved 3 to 10. The psuedo-random texture, based on data imported from an experimentally etched sample, achieved path length of 10. High reflectivity of the mirror was critical to achieving this result, which was achieved with a low-index dielectric to promote TIR on the backside of the cell and avoid parasitic absorption in the metal. Without this layer, a texture with 30 path length was reduced to 10.

The texture and mirror combination was then applied to a 3-J cell intended for use in space. The goal was to harden it against radiation by thinning the middle subcell. An AlAs/AlGaAs DBR, which could be grown monolithically, was placed between the middle and bottom subcells and designed so that it reflected the GaAs wavelengths but allowed the longer Ge wavelengths to transmit. The DBR allowed the middle subcell to be effectively halved in thickness while maintaining good current in the bottom subcell and without any loss in BOL tandem efficiency. Adding a grating texture between the DBR and the middle subcell allowed the middle subcell to be thinned to 1200 nm, but the texture at this location led to significant loss in the bottom subcell current. A more optimized grating design could reduce the bottom subcell loss. EOL simulations were performed and demonstrated that the light management structure improved the radiation tolerance, but that more careful EOL optimization had to be done to take better advantage of this aspect. The DBR cell beat the thick baseline cell at EOL by 0.22% absolute efficiency.

Future work includes experimental testing of the path length experiments. Confirmation of the the mirror quality results could be done by fabricating textured samples with and without an oxide layer. The pyramid texture may be possible to create by using the technique developed by Kicin *et al.*, where a sacrificial AlAs layer is used as a 'dwindling' etch mask [191]. A larger variety of textures could be simulated. Rather than apply the texture to semiconductor, the oxide layer-metal interface could be textured on its own. The wavelength dependence could be examined, as well as any dependence of the absorber layer thickness itself [187]. A front-side texture could also be explored.

Implementing DBRs in multi-junction space cells is not a novel concept [39], but the grating and DBR design has not been tried experimentally, yet. Whether or not this can be done monolithically needs to be carefully explored and would require epitaxial overgrowth [189]

and lateral oxidation of AlAs [190]. The structure could also be made by wafer bonding [13], but this requires two substrates and extensive processing and it may not be viable from a cost perspective.

Another avenue of work is improvement of the model. Including photon recycling or radiative coupling in the model would make it capable of predicting results for terrestrial III-V cells with low non-radiative recombination rates. In the light emitting diode (LED) industry, the ratio of the number of photons lost through the front surface to the total number of spontaneously generated photons (luminescence) in the device is referred to the extraction efficiency and is often computed numerically [192]. The numerically obtained extraction efficiency could be used as a photon recycling probability, which can be applied iteratively (as a geometric series) to extend the radiative lifetime in the device simulation [174]. The extraction efficiency could be obtained by simulating the solar cell as an LED as a separate optical simulation step.

# Appendix A

# Software

## A.1 MFIA DLTS

This program is used to capture capacitance transients using the Zurich Instruments MFIA digital lock-in amplifier. It can then process the transients into DLTS spectra. The program can also perform admittance spectroscopy. It was originally written in MATLAB.

The software and instructions for use can be found online at GitHub:
`https://github.com/nelsongt/mfiaDLTS`

## A.2 Double-diode Curve Fitting

This program is used to fit J-V data to the two-diode model (Equation 2.6). It was originally written in MATLAB.

The software and instructions for use can be found online at GitHub:
`https://github.com/nelsongt/LMDiodeFit`

# Appendix B

# Sentaurus Hydrodynamic Model

The model begins with a generalized BTE [63–65],

$$\frac{\delta f(\mathbf{r},\mathbf{p},t)}{\delta t} = \left(\frac{\delta f}{\delta t}\right)_{fields} + \left(\frac{\delta f}{\delta t}\right)_{diff} + \left(\frac{\delta f}{\delta t}\right)_{coll}, \tag{B.1}$$

where $f$ is the distribution function defining the probability of finding a particle within the tiny volume $d^3\mathbf{r}$ and within the tiny momentum-space $\mathbf{p}$ at time $t$. The time-rate of change of this distribution is equal to the sum of the changes due to externally applied fields, diffusion, and collision or scattering events.

Even under non-equilibrium conditions it is still clear that external forces and diffusion alone cannot change the total number of particles at any time (unlike collision effects such as recombination) and it can further be shown by Liouville's theorem that under these two components the total phase-space must remain constant and thus the distribution density must be conserved. It follows that the total time rate of change of the distribution function can only come from collisions,

$$\frac{df(\mathbf{r},\mathbf{p},t)}{dt} = \left(\frac{\delta f}{\delta t}\right)_{coll}. \tag{B.2}$$

Expansion of the derivative (in one dimension for simplicity) leads to,

$$\frac{df(x,p,t)}{dt} = \frac{\delta f}{\delta t} + \frac{\delta f}{\delta x}\frac{dx}{dt} + \frac{\delta f}{\delta p}\frac{dp}{dt} = \left(\frac{\delta f}{\delta t}\right)_{coll}. \tag{B.3}$$

Assuming the only external force acting on the particles is an applied electric field, the

familiar quantities $dx/dt$ and $dv/dt$ can be rewritten to obtain,

$$\frac{\delta f}{\delta t} + v\frac{\delta f}{\delta x} + \frac{qE}{m^*}\frac{\delta f}{\delta p} = \left(\frac{\delta f}{\delta t}\right)_{coll}, \tag{B.4}$$

where $q$ is the carrier's charge (negative for electrons, positive for holes), $m^*$ is the carrier effective mass, and $E$ is the magnitude of the external electric field, and $v$ is the real-space velocity. Note that the effective mass approximation has been used.

The collision term is then treated using,

$$\left(\frac{\delta f}{\delta t}\right)_{coll} = \int \left(f(x,p,t)[1-f(x,p',t)]S(p,p') - f(x,p',t)[1-f(x,p,t)]S(p',p)\right) dp', \tag{B.5}$$

where $S(p,p')$ is the rate of carrier transition from initial state to final state after a collision, and $S(p',p)$ represents the inverse process. The first term in the integral represent the probability that a collision will occur that changes a carrier from an initial state to a final state and the second term represents the reverse process. For transition to occur, the initial state must be occupied ($f(x,p,t)$) and the final state must be unoccupied ($[1-f(x,p',t)]$). To net a number of state transitions, the probability of the initial-to-final state transition must differ from its inverse process. The integral sums the net state transitions over all possible momenta.

The full BTE form in Equations B.4 and B.5 is generalized for semiconductors and may by solved numerically by Monte Carlo simulations, however, this is too complex and computationally demanding for most applications. Instead, it may be more easily solved by careful approximation. The relaxation time approximation (suitable for low-field conditions) is commonly used,

$$\left(\frac{\delta f}{\delta t}\right)_{coll} = -\frac{f-f_0}{\tau}, \tag{B.6}$$

where $f_0$ is the equilibrium distribution (Fermi distribution) and $\tau$ is a macroscopic relaxation time defined as the average time it takes for the current non-equilibrium state to relax back into the equilibrium state. Thus the rate of change of the distribution due to a collision is simply the rate at which the distribution relaxes back to equilibrium. One of the consequences

of this assumption is the carrier mobility model. Substitution leads to,

$$\frac{\delta f}{\delta t} + v\frac{\delta f}{\delta x} + \frac{qE}{m^*}\frac{\delta f}{\delta p} = -\frac{f - f_0}{\tau}. \tag{B.7}$$

Equation B.7 is still difficult to solve and, rather than directly solving for the distribution function, it is usually approximated up to a few orders by the method of moments.

By using the method of moments to solve the distribution-containing differential equation, several important and familiar relationships can be determined without directly solving for the distribution. Recall that the expectation value of a macroscopic quantity from a distribution function can be found by,

$$< \Theta >= \int \Theta f dp, \tag{B.8}$$

where $\Theta$ is the moment generating function and will be chosen to be some function of momentum as averaging the distribution over momentum leads to useful relationships in carrier momentum and energy. The functions of momentum will be in increasing powers of $p$, where $p^0$, $p^1$, and $p^2$ terms correspond to moments of the 0th, 1st, and 2nd orders. As will be shown, these moments result in conversation laws of carrier density, momentum, and energy, respectively.

The 0th order function is the simplest, $\Theta = p^0 = 1$. To obtain terms that resemble the form in Equation B.8, the BTE of Equation B.6 will have both sides multiplied by the moment generating function, $\Theta$, and integrated over momentum space,

$$\int \Theta\frac{\delta f}{\delta t}dp + \int \Theta v\frac{\delta f}{\delta x}dp + \int \Theta\frac{qE}{m^*}\frac{\delta f}{\delta p}dp = -\int \Theta\frac{f - f_0}{\tau}dp. \tag{B.9}$$

Treating the first integral in Equation B.9, and recalling that $\Theta = 1$,

$$\int \frac{\delta f}{\delta t}dp = \frac{\delta}{\delta t}\int f dp = \frac{\delta n(x,t)}{\delta t}. \tag{B.10}$$

The second part of Equation B.10 has come about because the explicit time-rate of change of $f$ will be unaffected by integrating over momentum.

The last part of Equation B.10, which includes the carrier density for carriers, $n(x,t)$, comes

from the following,

$$N = \int\int f(x,p)dxdp = \int n(x)dx, \tag{B.11}$$

$$\frac{dN}{dx} = \int f(x,p)dp = n(x), \tag{B.12}$$

where $N$ is number of particles in the phase-space volume $dxdp$, which must also be equal to the integral-over-space of the carrier density.

Similar treatment of the remaining integrals in Equation B.9 results in the carrier continuity equations,

$$\frac{\delta n}{\delta t} + \frac{\delta(nv)}{\delta x} = G - R, \tag{B.13}$$

where $G$ and $R$ are the generation and recombination rates, respectively. The quantity $nv$ in Equation B.13 is the current density contribution from electrons. An analogous equation for holes can be derived.

The 1st moment comes from $\Theta = p^1 = \hbar k$, and results in the drift-diffusion (DD) equations,

$$\frac{\delta(n < p >)}{\delta t} + qnE + \frac{\delta}{\delta x}k_B\mathbf{T}n = \frac{n < p >}{\tau}, \tag{B.14}$$

where the parabolic band approximation, $\varepsilon = hk^2/2m^*$ has been used. A non-isothermal relationship can be used here if $\mathbf{T}$ is the carrier temperature tensor.

The closure relation is $< p >= m^*v$ and the definition of carrier mobility is $\mu = q\tau/m^*$. Substitution into Equation B.14 and assuming steady-state leads to,

$$J_n = qn\mu_n E - \frac{\delta}{\delta x}\mu_n k_B T n, \tag{B.15}$$

with an analogous equation for holes.

The 2nd moment, with power of $p^2$, results in an energy conservation relation and utilizes the parabolic band approximation, $\Theta = \varepsilon = hk^2/2m^*$,

$$\frac{\delta nw}{\delta t} + \frac{\delta nvw}{\delta x} = -qnvE - \frac{\delta}{\delta x}(nk_B\mathbf{T}v) - \frac{\delta Q}{\delta x} - \frac{n}{\tau_E}w - w_0, \tag{B.16}$$

where $w$ is the average kinetic energy, $Q$ is the heat flow, and $\tau_E$ is the energy relaxation time.

The utilization of the higher moments allows Sentaurus to relax some of the assumptions that exist in the more conventional and commonly-used isothermal DD model. Non-isothermal modeling with energy transport and conservation allows for more accurate sub-micron regime modeling with high field intensity or high carrier densities that push the carrier populations away from quasi-equilibrium. Specifically, the DD model does not reproduce carrier velocity overshoot and can overestimates impact ionization rates [66]. The higher moments would be most useful in thin cells under high carrier concentrations.

# Appendix C

# Light Management for Textured Thin GaAs Cells

The goal of these simulations were to reproduce the model by Miller *et al.* [62] to establish a reliable framework. Synopsys RSoft and Synopsys Sentaurus TCAD were used to perform electromagnetic and device simulations, respectively, in order to model cell performance as a function of cell thickness for the considered light trapping schemes. Those schemes are the conventional upright cell with thick absorbing substrate, ELO cells with a flat BSR, and ELO cells with a triangular BSR pattern. To replicate experimental textures etched in AlGaAs by Smith *et al.* [183], the period of the pattern was 6 µm and the height of the triangles was 1.6 µm. For each of the BSR types, rear metal stack was simulated with $SiO_2$/Au, where the dielectric layer was used to improve the reflectivity of the BSR by totally internally reflecting beyond the critical angle. Light inside the critical angle was reflected by the metal. The optical solver used was RSoft's FDTD solver, FullWAVE.

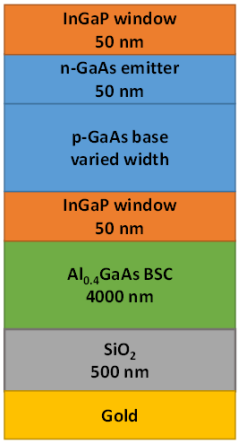


Figure C.1: Layer structure of the 'Flat BSR' cell. The upright cell has a thick absorbing substrate, while the triangle BSR cells have a triangular pattern etched into the AlGaAs layer using the same pattern as simulated in previous reports.

An example layer structure of the simulated devices is shown in Figure C.1. An n-GaAs emitter of fixed width and p-GaAs base of varied width form the GaAs single junction baseline cell, with a pair of InGaP windows on either side. The highly doped AlGaAs back surface contact (BSC) is used as both the contact layer to the back contact metal as well as a thick, non-absorbing layer in which the light trapping pattern can be etched into. The high Al% in the $Al_{0.4}Ga_{0.6}As$ was chosen to prevent parasitic absorption of shorter wavelengths as the GaAs absorber layer thickness was reduced.

Figure C.2 contains AM0 solar cell metrics vs. cell thickness for the three light trapping schemes. For the upright cell, the maximum efficiency was 27% at 2 μm and it was clear that this cell type could have benefited from an even thicker base. For the flat BSR cells, 27% efficiency was achieved at around half the the base thickness or about 1 μm, which was expected due to the roughly doubled path length. For the patterned cell, high efficiencies and currents are maintained with sub-micron cell widths, with sub-400 nm cells capable of 27% efficiency, indicating greater than a factor of 5 path length increase from the upright cell. There was no effect of the BSR on FF. The $V_{OC}$ was improved by texturing, however, this result is only valid is the carriers are lost due to SRH recombination. If radiative recombination is dominant, photon recycling will increase the voltage and favor the planar cell, as already discussed.

The $J_{SC}$ trends for all three cell types were in agreement with Miller *et al.*, which was the goal of these simulations and established a framework to move on to more predictive results.

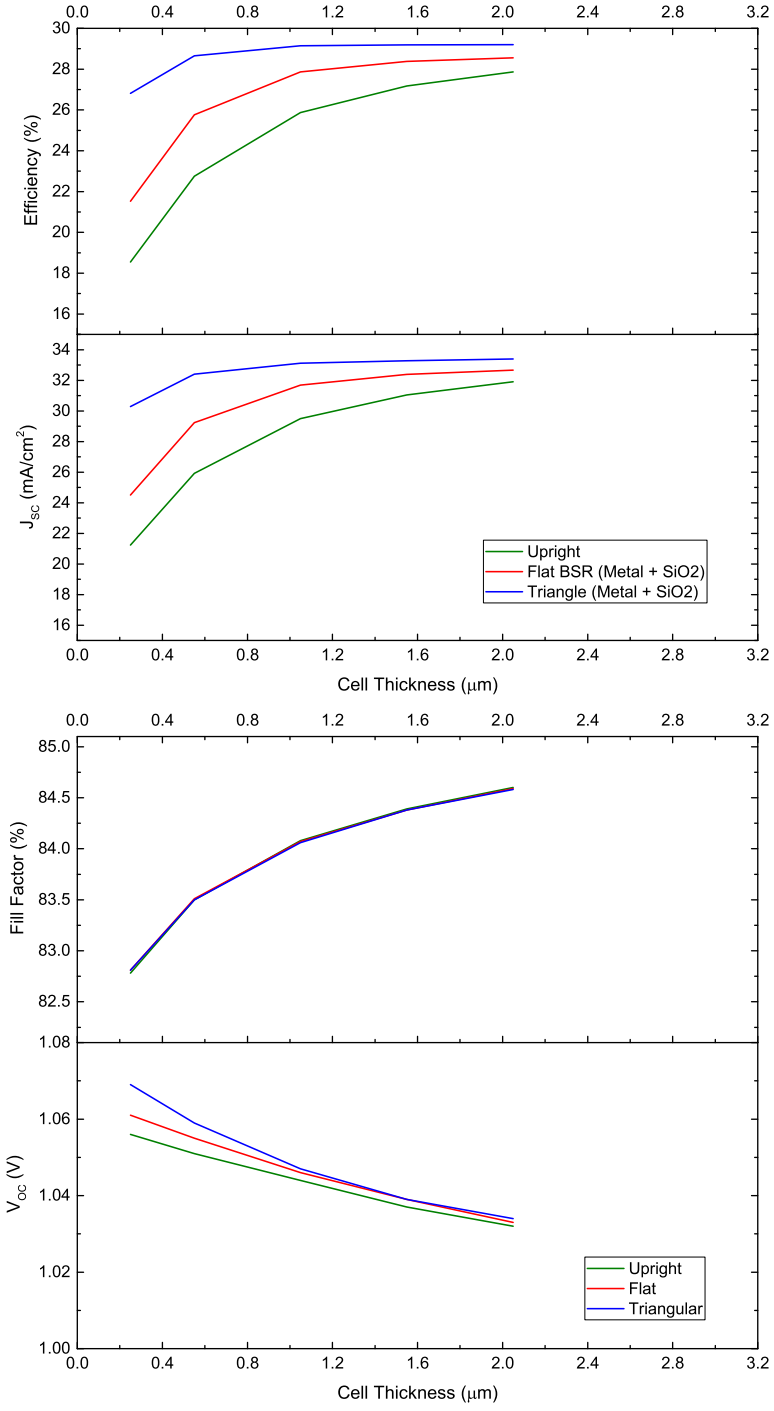


Figure C.2: Cell efficiency, $J_{SC}$, FF, and $V_{OC}$ under AM0 as a function of total cell thickness.

# Appendix D

# IMM Space Solar Cell Model and Damage Coefficient Fitting

Previous experimental results by Adams *et al.* [38] on irradiated 3-J IMM cells provided an opportunity to validate simulations before progressing to predictive irradiated IMM modeling. It was possible to extract a rough value for the damage coefficient for InGaAs (1.0 eV) using 1 MeV electrons by fitting the experimental data. Electron radiation damage coefficients for 1.0 eV-InGaAs could not be found in the literature and are reported here.

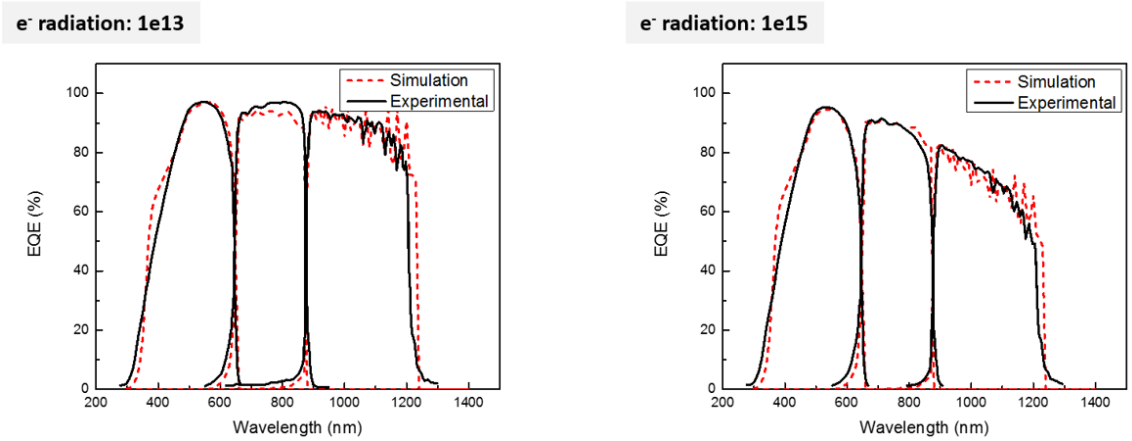


Figure D.1: EQE plots of the fitted triple-junction IMM cells for two different fluences of 1 MeV electrons, $1 \times 10^{13}$ cm$^{-3}$ (left) and $1 \times 10^{15}$ cm$^{-3}$ (right).

Table D.1: Radiation parameters used to model damage in each of the three subcells.

| Material | $K_L$ (cm$^2$) | $R_C$ |
|---|---|---|
| InGaP | $1.0 \times 10^{-7}$ | 1.1 |
| GaAs | $3.0 \times 10^{-9}$ | 2.6 |
| $In_{0.3}Ga_{0.7}As$ | $8.0 \times 10^{-8}$ | 2.6 |

A Sentaurus TCAD IMM model was fit to the experimental data. Adjustments were made

in the radiation damage coefficients for the InGaP, GaAs, and InGaAs subcells to optimize the fitting. The plots of EQE as a function of radiation fluence shown in Figure D.1 are the result of this fit. Excellent match between experiment and simulation can be seen for $e^-$ radiation fluence of $1 \times 10^{13}$ and $1 \times 10^{15}$ $cm^{-2}$. The final radiation parameters used in the fit are listed in Table D.1

# Bibliography


[1] ZTJ space solar cell datasheet, SolAero Technologies. http://solaerotech.com/solaerotech/wp-content/uploads/2018/04/ZTJ-Datasheet-Updated-2018-v.1.pdf.

[2] Photovoltaic Research | NREL. https://www.nrel.gov/pv/.

[3] M. Woodhouse and A. Goodrich. Manufacturing Cost Analysis Relevant to Single-and Dual-Junction Photovoltaic Cells Fabricated with Iii-Vs and Iii-Vs Grown on Czochralski Silicon (presentation). Technical Report NREL/PR-6A20-60126, National Renewable Energy Laboratory (NREL), Golden, CO., May 2014.

[4] K. Horowitz, M. Woodhouse, H. Lee, and G. Smestad. Bottom-Up Cost Analysis of a High Concentration PV Module; NREL (National Renewable Energy Laboratory). Technical Report NREL/PR-6A20-63947, National Renewable Energy Lab. (NREL), Golden, CO (United States), April 2015.

[5] Shin-ichiro Sato, Kenneth J. Schmieder, Seth M. Hubbard, David V. Forbes, Jeffrey H. Warner, Takeshi Ohshima, and Robert J. Walters. Defect characterization of proton irradiated GaAs pn-junction diodes with layers of InAs quantum dots. *Journal of Applied Physics*, 119(18):185702, May 2016.

[6] María González, Ngai Chan, Nicholas J. Ekins-Daukes, Jessica G. J. Adams, Paul Stavrinou, Igor Vurgaftman, Jerry R. Meyer, Joshua Abell, Robert J. Walters, Cory D. Cress, and Phillip P. Jenkins. Modeling and analysis of multijunction solar cells. In *Physics and Simulation of Optoelectronic Devices XIX*, volume 7933, page 79330R. International Society for Optics and Photonics, February 2011.

[7] R.J. Walters, M. Gonzalez, J. G. Tischler, M. P. Lumb, J. R. Meyer, I. Vurgaftman, J. Abell, M. K. Yakes, N. Ekins-Daukes, J. G J Adams, N. Chan, P. Stavrinou, and P.P. Jenkins. Design of an achievable, all lattice-matched multijunction solar cell using InGaAlAsSb. In *2011 37th IEEE Photovoltaic Specialists Conference (PVSC)*, pages 000122–000126, June 2011.

[8] A. Mesli, L. Dobaczewski, K. Bonde Nielsen, Vl. Kolkovsky, M. Christian Petersen, and A. Nylandsted Larsen. Low-temperature irradiation-induced defects in germanium: In situ analysis. *Phys. Rev. B*, 78(16):165202, October 2008.

[9] Bor-Chau Juang, Ramesh B. Laghumavarapu, Brandon J. Foggo, Paul J. Simmonds, Andrew Lin, Baolai Liang, and Diana L. Huffaker. GaSb thermophotovoltaic cells grown

on GaAs by molecular beam epitaxy using interfacial misfit arrays. *Applied Physics Letters*, 106(11):111101, March 2015.

[10] Martin A. Green. The path to 25% silicon solar cell efficiency: History of silicon cell evolution. *Progress in Photovoltaics: Research and Applications*, 17(3):183–189, May 2009.

[11] T. Inoue, K. Watanabe, K. Toprasertpong, H. Fujii, M. Sugiyama, and Y. Nakano. Enhanced Light Trapping in Multiple Quantum Wells by Thin-Film Structure and Backside Grooves With Dielectric Interface. *IEEE Journal of Photovoltaics*, 5(2):697–703, March 2015.

[12] Antonio Musu, Federica Cappelluti, Timo Aho, Ville Polojärvi, Tapio K. Niemi, and Mircea Guina. Nanostructures for light management in thin-film GaAs quantum dot solar cells. In *Light, Energy and the Environment (2016), paper JW4A.45*, page JW4A.45. Optical Society of America, November 2016.

[13] A. Mellor, N. P. Hylton, S. A. Maier, and N. Ekins-Daukes. Interstitial light-trapping design for multi-junction solar cells. *Solar Energy Materials and Solar Cells*, 159:212–218, January 2017.

[14] R. Rehm, M. Walther, J. Schmitz, J. Fleissner, J. Ziegler, W. Cabanski, and R. Breiter. Dual-colour thermal imaging with InAs/GaSb superlattices in mid-wavelength infrared spectral range. *Electronics Letters*, 42(10):577–578, May 2006.

[15] I. Pouchet, V. Zéninari, B. Parvitte, and G. Durry. Diode laser spectroscopy of CO2 in the 1.6$\mu$m region for the in situ sensing of the middle atmosphere. *Journal of Quantitative Spectroscopy and Radiative Transfer*, 83(3):619–628, February 2004.

[16] M. Muneeb, A. Vasiliev, A. Ruocco, A. Malik, H. Chen, M. Nedeljkovic, J. S. Penades, L. Cerutti, J. B. Rodriguez, G. Z. Mashanovich, M. K. Smit, E. Tourni, and G. Roelkens. III-V-on-silicon integrated micro - spectrometer for the 3 μm wavelength range. *Opt. Express, OE*, 24(9):9465–9472, May 2016.

[17] Gunther Roelkens, Amin Abassi, Paolo Cardile, Utsav Dave, Andreas de Groote, Yannick de Koninck, Sören Dhoore, Xin Fu, Alban Gassenq, Nannicha Hattasan, Qiangsheng Huang, Sulakshna Kumari, Shahram Keyvaninia, Bart Kuyken, Lianyan Li, Pauline Mechet, Muhammad Muneeb, Dorian Sanchez, Haifeng Shao, Thijs Spuesens, Ananth Subramanian, Sarah Uvin, Martijn Tassaert, Kasper van Gasse, Jochem Verbist, Ruijun Wang, Zhechao Wang, Jing Zhang, Joris van Campenhout, Xin Yin, Johan Bauwelinck, Geert Morthier, Roel Baets, and Dries van Thourhout. III-V-on-Silicon Photonic Devices for Optical Communication and Sensing. *Photonics*, 2(3):969–1004, September 2015.

[18] A. Rogalski, P. Martyniuk, and M. Kopytko. InAs/GaSb type-II superlattice infrared detectors: Future prospect. *Applied Physics Reviews*, 4(3):031304, September 2017.

[19] Martin A. Green, Yoshihiro Hishikawa, Ewan D. Dunlop, Dean H. Levi, Jochen Hohl-Ebinger, Masahiro Yoshita, and Anita W. Y. Ho-Baillie. Solar cell efficiency tables (Version 53). *Progress in Photovoltaics: Research and Applications*, 27(1):3–12, 2019.

[20] Kunta Yoshikawa, Hayato Kawasaki, Wataru Yoshida, Toru Irie, Katsunori Konishi, Kunihiro Nakano, Toshihiko Uto, Daisuke Adachi, Masanori Kanematsu, Hisashi Uzu, and Kenji Yamamoto. Silicon heterojunction solar cell with interdigitated back contacts for a photoconversion efficiency over 26%. *Nature Energy*, 2(5):nenergy201732, March 2017.

[21] F. Dimroth, T. N. D. Tibbits, M. Niemeyer, F. Predan, P. Beutel, C. Karcher, E. Oliva, G. Siefer, D. Lackner, P. Fuß-Kailuweit, A. W. Bett, R. Krause, C. Drazek, E. Guiot, J. Wasselin, A. Tauzin, and T. Signamarcheix. Four-Junction Wafer-Bonded Concentrator Solar Cells. *IEEE Journal of Photovoltaics*, 6(1):343–349, January 2016.

[22] Maike Wiesenfarth, Simon P. Philipps, Andreas W. Bett, Kelsey Horowitz, and Sarah Kurtz. Current Status of Concentrator Photovoltaic (CPV) Technology. Technical Report TP-6A20-63916, Fraunhofer ISE; National Renewable Energy Laboratory, April 2017.

[23] Vijit Sabnis, Homan Yuen, and Mike Wiemer. High-efficiency multijunction solar cells employing dilute nitrides. *AIP Conference Proceedings*, 1477(1):14–19, October 2012.

[24] M. Feifel, J. Ohlmann, J. Benick, M. Hermle, J. Belz, A. Beyer, K. Volz, T. Hannappel, A. W. Bett, D. Lackner, and F. Dimroth. Direct Growth of III–V/Silicon Triple-Junction Solar Cells With 19.7% Efficiency. *IEEE Journal of Photovoltaics*, 8(6):1590–1595, November 2018.

[25] Elisabeth L. McClure and Seth M. Hubbard. The effects of silicon substrate thickness and annealing temperature on surface coverage for aluminum-induced crystallization of germanium films. *Materials Science in Semiconductor Processing*, 94:22–27, May 2019.

[26] Kelsey A. Horowitz, Timothy W. Remo, Brittany Smith, and Aaron J. (ORCID:0000000309978964) Ptak. A Techno-Economic Analysis and Cost Reduction Roadmap for III-V Solar Cells. Technical Report NREL/TP-6A20-72103, National Renewable Energy Lab. (NREL), Golden, CO (United States), November 2018.

[27] J. Simon, K. L. Schulte, N. Jain, S. Johnston, M. Young, M. R. Young, D. L. Young, and A. J. Ptak. Upright and Inverted Single-Junction GaAs Solar Cells Grown by Hydride Vapor Phase Epitaxy. *IEEE Journal of Photovoltaics*, 7(1):157–161, January 2017.

[28] H. Chen, A. Cattoni, R. De Lépinau, A. Walker, O. Hoehn, D. Lackner, G. Siefer, N. Vandamme, J. Goffard, B. Behaghel, C. Dupuis, N. Bardou, F. Dimroth, and S. Collin. 19.9mirror for multi-resonant absorption and enhanced luminescence extraction. In *Photovoltaic Specialists Conference (PVSC), 2018 IEEE 45th*, June 2018.

[29] Telmo Adão, Jonáš Hruška, Luís Pádua, José Bessa, Emanuel Peres, Raul Morais, and Joaquim Sousa. Hyperspectral Imaging: A Review on UAV-Based Sensors, Data Processing and Applications for Agriculture and Forestry. *Remote Sensing*, 9(11):1110, October 2017.

[30] G. Milinevsky, Ya. Yatskiv, O. Degtyaryov, I. Syniavskyi, M. Mishchenko, V. Rosenbush, Yu. Ivanov, A. Makarov, A. Bovchaliuk, V. Danylevsky, M. Sosonkin, S. Moskalov, V. Bovchaliuk, A. Lukenyuk, A. Shymkiv, and E. Udodov. New satellite project Aerosol-UA: Remote sensing of aerosols in the terrestrial atmosphere. *Acta Astronautica*, 123:292–300, June 2016.

[31] Michael MacDougal, Jon Geske, Chad Wang, Shirong Liao, Jonathan Getty, and Alan Holmes. Low dark current InGaAs detector arrays for night vision and astronomy. In *Infrared Technology and Applications XXXV*, volume 7298, page 72983F. International Society for Optics and Photonics, May 2009.

[32] S. R. Messenger, G. P. Summers, E. A. Burke, R. J. Walters, and M. A. Xapsos. Modeling solar cell degradation in space: A comparison of the NRL displacement damage dose and the JPL equivalent fluence approaches. *Progress in Photovoltaics: Research and Applications*, 9(2):103–121, 2001.

[33] Shinichiro Sato, Takeshi Ohshima, and Mitsuru Imaizumi. Modeling of degradation behavior of InGaP/GaAs/Ge triple-junction space solar cell exposed to charged particles. *Journal of Applied Physics*, 105(4):044504, February 2009.

[34] A. J. Ptak, S. W. Johnston, Sarah Kurtz, D. J. Friedman, and W. K. Metzger. A comparison of MBE- and MOCVD-grown GaInNAs. *Journal of Crystal Growth*, 251(1):392–398, April 2003.

[35] D. J. Chmielewski, K. Galiano, P. Paul, D. Cardwell, S. Carnevale, J. A. Carlin, A. R. Arehart, T. J. Grassman, and S. A. Ringel. Comparative study of 2.05 eV AlGaInP and metamorphic GaInP materials and solar cells grown by MBE and MOCVD. In *2016 IEEE 43rd Photovoltaic Specialists Conference (PVSC)*, pages 3411–3414, June 2016.

[36] Xiaoli Ji, Baiqing Liu, Hengjing Tang, Xuelin Yang, Xue Li, HaiMei Gong, Bo Shen, Ping Han, and Feng Yan. 2.6 μm MBE grown InGaAs detectors with dark current of SRH and TAT. *AIP Advances*, 4(8):087135, August 2014.

[37] C. Sah, R. N. Noyce, and W. Shockley. Carrier Generation and Recombination in P-N Junctions and P-N Junction Characteristics. *Proceedings of the IRE*, 45(9):1228–1243, September 1957.

[38] J. G. J. Adams, V. C. Elarde, G. Hillier, C. Stender, F. Tuminello, A. Wibowo, C. Youtsey, Z. Bittner, S. M. Hubbard, E. B. Clark, M. F. Piszczor, and M. Osowski. Improved radiation resistance of epitaxial lift-off inverted metamorphic solar cells. In *Photovoltaic Specialists Conference (PVSC), 2013 IEEE 39th*, pages 3229–3232, June 2013.

[39] V. M. Emelyanov, N. A. Kalyuzhniy, S. A. Mintairov, M. Z. Shvarts, and V. M. Lantratov. Multijunction GaInP/GaInAs/Ge solar cells with Bragg reflectors. *Semiconductors*, 44(12):1600–1605, December 2010.

[40] J. Hernández-Saz, M. Herrera, F. J. Delgado, S. Duguay, T. Philippe, M. González, J. Abell, R. J. Walters, and S. I. Molina. Atom-scale compositional distribution in InAlAsSb-based triple junction solar cells by atom probe tomography. *Nanotechnology*, 27(30):305402, June 2016.

[41] D. W. Pack, C. M. Coffman, J. R. Santiago, and R. W. Russell. Earth Remote Sensing Results from the CUbesat MULtispectral Observing System, CUMULOS. *AGU Fall Meeting Abstracts*, 41, December 2018.

[42] Ruud W. M Hoogeveen, Ronald J van der A, and Albert P. H Goede. Extended wavelength InGaAs infrared (1.0-2.4 um) detector arrays on SCIAMACHY for space-based spectrometry of the Earth atmosphere. *Infrared Physics & Technology*, 42(1):1–16, February 2001.

[43] Jenny Nelson. *The Physics of Solar Cells*. Imperial College Press, London : River Edge, NJ, 1 edition edition, September 2003.

[44] A. Khanna, T. Mueller, R.A. Stangl, B. Hoex, P.K. Basu, and A.G. Aberle. A fill factor loss analysis method for silicon wafer solar cells. *IEEE Journal of Photovoltaics*, 3(4):1170–1177, October 2013.

[45] D. Pysch, A. Mette, and S. W. Glunz. A review and comparison of different methods to determine the series resistance of solar cells. *Solar Energy Materials and Solar Cells*, 91(18):1698–1706, November 2007.

[46] Solar Spectra.

[47] Zhou Fang and Ce Zhou Zhao. Recent Progress in Silicon Photonics: A Review. *International Scholarly Research Notices*, 2012.

[48] Peter Blood and John Wilfred Orton. *The electrical characterization of semiconductors: majority carriers and electron states*. Academic Press, 1992.

[49] William D. Callister Jr. *Materials Science and Engineering: An Introduction, 7th Edition.* John Wiley & Sons, Limited, September 2007. ISBN: 9780470120323.

[50] E. A. Fitzgerald, Y.-H. Xie, M. L. Green, D. Brasen, A. R. Kortan, J. Michel, Y.-J Mii, and B. E. Weir. Totally relaxed GexSi1-x layers with low threading dislocation densities grown on Si substrates. *Appl. Phys. Lett.*, 59(7):811–813, August 1991.

[51] Tetsuo Soga, Takashi Jimbo, and Masayoshi Umeno. Low etch pit density GaAs on Si grown by metalorganic chemical vapor deposition. *Appl. Phys. Lett.*, 56(15):1433–1435, April 1990.

[52] Soraia Sofia Pascoa. Oxygen and related defects in Czochralski silicon crowns. *71*, 2014.

[53] Christopher Paul Ewels. *Density functional modelling of point defects in semiconductors.* Ph.D., University of Exeter, 1997.

[54] P. J. H. Denteneer. *The pseudopotential-density-functional method applied to semiconducting crystals.* PhD thesis, Technische Hogeschool, 1987.

[55] E. Cartier, J. H. Stathis, and D. A. Buchanan. Passivation and depassivation of silicon dangling bonds at the Si/SiO2 interface by atomic hydrogen. *Appl. Phys. Lett.*, 63(11):1510–1512, September 1993.

[56] D. V. Lang. Deep-level transient spectroscopy: A new method to characterize traps in semiconductors. *Journal of Applied Physics*, 45(7):3023–3032, July 1974.

[57] Armin G. Aberle, Stefan Glunz, and Wilhelm Warta. Impact of illumination level and oxide parameters on Shockley–Read–Hall recombination at the Si-SiO2 interface. *Journal of Applied Physics*, 71(9):4422–4431, May 1992.

[58] B. Chatterjee, S. A. Ringel, R. Sieg, R. Hoffman, and I. Weinberg. Hydrogen passivation of dislocations in InP on GaAs heterostructures. *Appl. Phys. Lett.*, 65(1):58–60, July 1994.

[59] A. R. Peaker, V. P. Markevich, B. Hamilton, G. Parada, A. Dudas, A. Pap, E. Don, B. Lim, J. Schmidt, L. Yu, Y. Yoon, and G. Rozgonyi. Recombination via point defects and their complexes in solar silicon. *physica status solidi (a)*, 209(10):1884–1893, 2012.

[60] L. Dobaczewski, P. Kaczor, M. Missous, A. R. Peaker, and Z. R. Zytkiewicz. Structure of the DX state formed by donors in (Al,Ga)As and Ga(As,P). *Journal of Applied Physics*, 78(4):2468–2477, August 1995.

[61] A. A. Istratov, O. F. Vyvenko, H. Hieslmair, and E. R. Weber. Critical analysis of weighting functions for the deep level transient spectroscopy of semiconductors. *Meas. Sci. Technol.*, 9(3):477, 1998.

[62] O. D. Miller, E. Yablonovitch, and S. R. Kurtz. Strong Internal and External Luminescence as Solar Cells Approach the Shockley-Queisser Limit. *IEEE Journal of Photovoltaics*, 2(3):303–311, July 2012.

[63] T. Grasser and S. Selberherr. Technology CAD: Device simulation and characterization. *Journal of Vacuum Science & Technology B: Microelectronics and Nanometer Structures Processing, Measurement, and Phenomena*, 20(1):407–413, January 2002.

[64] T. Grasser, Ting-Wei Tang, H. Kosina, and S. Selberherr. A review of hydrodynamic and energy-transport models for semiconductor device simulation. *Proceedings of the IEEE*, 91(2):251–274, February 2003.

[65] Kevin F. Brennan. *The Physics of Semiconductors: With Applications to Optoelectronic Devices*. Cambridge University Press, February 1999. Google-Books-ID: 6JElXbZpX3IC.

[66] Synopsys Sentaurus manual, 2017.

[67] John David Jackson. *Classical Electrodynamics*. Wiley, 2007. ISBN: 978-81-265-1094-8.

[68] Dragica Vasileska. Drift-Diffusion Model, Part A: Introduction. June 2006.

[69] Martin-Thomas Vasicek. *Advanced Macroscopic Transport Models*. PhD Dissertation, Technical University Vienna, 2009.

[70] Spectrolab :: The World's leading provider of compound semiconductor and lighting products. http://www.spectrolab.com/solarcells.htm.

[71] J. F. Geisz, Sarah Kurtz, M. W. Wanlass, J. S. Ward, A. Duda, D. J. Friedman, J. M. Olson, W. E. McMahon, T. E. Moriarty, and J. T. Kiehl. High-efficiency GaInP/GaAs/InGaAs triple-junction solar cells grown inverted with a metamorphic bottom junction. *Applied Physics Letters*, 91(2):023502, July 2007.

[72] Kazuaki Sasaki, Takaaki Agui, Katsuya Nakaido, Naoki Takahashi, Ryusuke Onitsuka, and Tatsuya Takamoto. Development of InGaP/GaAs/InGaAs inverted triple junction concentrator solar cells. volume 1556, pages 22–25, September 2013.

[73] R. M. France, J. F. Geisz, I. García, M. A. Steiner, W. E. McMahon, D. J. Friedman, T. E. Moriarty, C. Osterwald, J. Scott Ward, A. Duda, M. Young, and W. J. Olavarria. Quadruple-Junction Inverted Metamorphic Concentrator Devices. *IEEE Journal of Photovoltaics*, 5(1):432–437, January 2015.

[74] Wolfgang Guter, Jan Schöne, Simon P. Philipps, Marc Steiner, Gerald Siefer, Alexander Wekkeli, Elke Welser, Eduard Oliva, Andreas W. Bett, and Frank Dimroth. Current-matched triple-junction solar cell reaching 41.1% conversion efficiency under concentrated sunlight. *Applied Physics Letters*, 94(22):223504, June 2009.

[75] N. Karam, R. Sherif, P. Pien, G. S. Kinsey, D. D. Krut, S. Mesropian, W. Hong, A. Zakaria, M. Haddad, C. Fetzer, D. C. Law, H. Yoon, M. J. Romero, K. M. Edmondson, A. Boca, and R. King. Raising the Efficiency Ceiling With Multijunction III-V Concentrator Photovoltaics. *23rd European Photovoltaic Solar Energy Conference and Exhibition, 1-5 September 2008, Valencia, Spain*, pages 24–29, November 2008.

[76] M. Stan, D. Aiken, B. Cho, A. Cornfeld, V. Ley, P. Patel, P. Sharps, and T. Varghese. High-efficiency quadruple junction solar cells using OMVPE with inverted metamorphic device structures. *Journal of Crystal Growth*, 312(8):1370–1374, April 2010.

[77] P. Patel, D. Aiken, A. Boca, B. Cho, D. Chumney, M. B. Clevenger, A. Cornfeld, N. Fatemi, Y. Lin, J. McCarty, F. Newman, P. Sharps, J. Spann, M. Stan, J. Steinfeldt, C. Strautin, and T. Varghese. Experimental Results From Performance Improvement and Radiation Hardening of Inverted Metamorphic Multijunction Solar Cells. *IEEE Journal of Photovoltaics*, 2(3):377–381, July 2012.

[78] Matthew P. Lumb, María Gonzalez, Igor Vurgaftman, Jerry R. Meyer, Joshua Abell, Michael Yakes, Raymond Hoheisel, Joseph G. Tischler, Phillip P. Jenkins, Paul N. Stavrinou, Markus Fuhrer, Ned J. Ekins-Daukes, and Robert J. Walters. Simulation of novel InAlAsSb solar cells. volume 8256, pages 82560S–82560S–13, 2012.

[79] M. P. Lumb, M. González, J. Abell, K. J. Schmieder, J. G. Tischler, D. A. Scheiman, M. K. Yakes, I. Vurgaftman, J. R. Meyer, and R. J. Walters. Characterization, modeling and analysis of InAlAsSb Schottky barrier solar cells grown on InP. In *2014 IEEE 40th Photovoltaic Specialist Conference (PVSC)*, pages 0243–0246, June 2014.

[80] M. González, M. P. Lumb, L. C. Hirst, S. Tomasulo, J. G. Tischler, W. Yoon, J. Abell, I. Vurgaftman, M. F. Bennett, K. J. Schmieder, N. A. Kotulak, M. K. Yakes, J. R. Meyer, and R. J. Walters. Rapid thermal annealing of InAlAsSb lattice-matched to InP for top cell applications. In *2015 IEEE 42nd Photovoltaic Specialist Conference (PVSC)*, pages 1–4, June 2015.

[81] Louise C. Hirst, Matthew P. Lumb, Josh Abell, Chase T. Ellis, Joseph G. Tischler, Igor Vurgaftman, Jerry R. Meyer, Robert J. Walters, and María González. Spatially indirect radiative recombination in InAlAsSb grown lattice-matched to InP by molecular beam epitaxy. *Journal of Applied Physics*, 117(21):215704, June 2015.

[82] Haruki Yokoyama, Hiroki Sugiyama, Yasuhiro Oda, Michio Sato, Noriyuki Watanabe, and Takashi Kobayashi. Metalorganic Vapor Phase Epitaxy Growth of InAlAsSb on InP. *Japanese Journal of Applied Physics*, 43(8A):5110–5113, 2004.

[83] N. L A Chan, N.J. Ekins-Daukes, J. G J Adams, M.P. Lumb, M. González, P.P. Jenkins, I. Vurgaftman, J.R. Meyer, and R.J. Walters. Optimal Bandgap Combinations

#x2014;Does Material Quality Matter #x003f;. *IEEE Journal of Photovoltaics*, 2(2):202–208, April 2012.

[84] Michael Slocum, David V. Forbes, Glen C. Hillier, Brittany L. Smith, Jessica G. J. Adams, and Seth M. Hubbard. Development of InAlAsSb growth by MOVPE. *Journal of Crystal Growth*, 471:15–20, August 2017.

[85] Brittany Smith. *Development and Life Cycle Assessment of Advanced-Concept III-V Multijunction Photovoltaics*. Ph.D., Rochester Institute of Technology, Rochester, New York, USA, June 2018.

[86] G. T. Nelson, Z. S. Bittner, B. Smith, D. V. Forbes, and S. M. Hubbard. Study of deep levels in InAlAsSb grown via organometallic vapor phase epitaxy. In *2014 IEEE 40th Photovoltaic Specialist Conference (PVSC)*, pages 1168–1173, June 2014.

[87] Angelo Scotty Gilmore, James Bangs, and Amanda Gerrish. Current voltage modeling of current limiting mechanisms in HgCdTe focal plane array photodetectors. *Journal of Elec Materi*, 34(6):913–921, June 2005.

[88] J. F. Geisz, D. J. Friedman, J. M. Olson, S. R. Kurtz, and B. M. Keyes. Photocurrent of 1ev GaInNAs lattice-matched to GaAs. *Journal of Crystal Growth*, 195(1):401–408, December 1998.

[89] Wyatt H. Strong, David V. Forbes, and Seth M. Hubbard. Investigation of deep level defects in electron irradiated indium arsenide quantum dots embedded in a gallium arsenide matrix. *Materials Science in Semiconductor Processing*, 25:76–83, September 2014.

[90] S. W. Johnston, S. R. Kurtz, D. J. Friedman, A. J. Ptak, R. K. Ahrenkiel, and R. S. Crandall. Observed trapping of minority-carrier electrons in p-type GaAsN during deep-level transient spectroscopy measurement. *Applied Physics Letters*, 86(7):072109, February 2005.

[91] E. N. Agafonov, U. A. Aminov, A. N. Georgobiani, and L. S. Lepnev. Observation of minority-carrier traps in Schottky diodes with a high barrier and a compensated near-contact region using deep-level transient spectroscopy. *Semiconductors*, 35(1):48–53, January 2001.

[92] F. Buchali, F. Scheffer, C. Heedt, I. Gyuro, P. Speier, W. Prost, and F-J Tegude. Evidence of oxygen in undoped InAlAs MOVPE layers. In *, Fourth International Conference on Indium Phosphide and Related Materials, 1992*, pages 534–537, April 1992.

[93] M. P. Lumb, M. GonzÃ¡lez, C. G. Bailey, I. Vurgaftman, J. R. Meyer, J. Abell, M. Yakes, R. Hoheisel, J. G. Tischler, P. N. Stavrinou, M. Fuhrer, N. J. Ekins-Daukes, and R. J.

Walters. Drift-diffusion modeling of InP-based triple junction solar cells. volume 8620, pages 86201G–86201G–9, 2013.

[94] B. L. Smith, G. T. Nelson, Y. Dai, M. A. Slocum, A. Wibowo, R. Tatavarti, and S. M. Hubbard. Development of back surface texture for light management in epitaxial lift off (elo) quantum dot solar cells. In *2017 IEEE 44th PVSC*, June 2017.

[95] G. J. Bauhuis, P. Mulder, E. J. Haverkamp, J. C. C. M. Huijben, and J. J. Schermer. 26.1% thin-film GaAs solar cell using epitaxial lift-off. *Solar Energy Materials and Solar Cells*, 93(9):1488–1491, September 2009.

[96] Zachary Bittner. *Development and Characterization of Novel III-V Materials for High Efficiency Photovoltaics*. Ph.D., Rochester Institute of Technology, Rochester, New York, USA, December 2018.

[97] C. A. Wang, S. Salimand, K. F. Jensen, and A. C. Jones. Low oxygen and carbon incorporation in AIGaAs using tritertiarybutylaluminum in organometallic vapor phase epitaxy. *Journal of Electronic Materials*, 25(5):771–774, May 1996.

[98] Robert M. Biefeld, Andrew A. Allerman, and Kevin C. Baucom. Method of making AlInSb by metal-organic chemical vapor deposition, June 2000. U.S. Classification 427/255.34, 427/255.11, 117/105, 117/104; International Classification C23C16/30; Cooperative Classification C23C16/301; European Classification C23C16/30B.

[99] Christopher D. Yerino, Baolai Liang, Diana L. Huffaker, Paul J. Simmonds, and Minjoo Larry Lee. Review Article: Molecular beam epitaxy of lattice-matched InAlAs and InGaAs layers on InP (111)A, (111)B, and (110). *Journal of Vacuum Science & Technology B*, 35(1):010801, December 2016.

[100] C. L. Andre, D. M. Wilt, A. J. Pitera, M. L. Lee, E. A. Fitzgerald, and S. A. Ringel. Impact of dislocation densities on n+/p and p+/n junction GaAs diodes and solar cells on SiGe virtual substrates. *Journal of Applied Physics*, 98(1):014502, July 2005.

[101] Beatriz Galiana, Ignacio Rey-Stolle, Mathieu Baudrit, Ivan Garcia, and Carlos Algora. A comparative study of BSF layers for GaAs-based single-junction or multijunction concentrator solar cells. *Semicond. Sci. Technol.*, 21(10):1387–1392, August 2006.

[102] C. L. Schilling, O. HÃ¶hn, D. N. Micha, S. Heckelmann, V. Klinger, E. Oliva, S. W. Glunz, and F. Dimroth. Combining Photon Recycling and Concentrated Illumination in a GaAs Heterojunction Solar Cell. *IEEE Journal of Photovoltaics*, 8(1):348–354, January 2018.

[103] Shigeya Naritsuka, Takao Noda, Aki Wagai, Shinobu Fujita, and Yasuo Ashizawa. Influence of V/III Molar Ratio on Deep Traps in Metalorganic Chemical Vapor Deposition

Grown InAlAs Layers. *Japanese Journal of Applied Physics*, 32(Part 2, No. 7A):L925–L927, 1993.

[104] M. M. Ben Salem S. Bouzgarrou. DLTS and PL study of defects in InAlAs/InP heterojunctions grown by metal organic chemical vapor deposition. *Materials Science and Engineering: B*, 116(2):202–207, 2005.

[105] Shu Goto, Takashi Ueda, Tomoyuki Ohshima, and Hiroaki Kakinuma. Effect of Growth Conditions on Electrical Properties of Si-Doped In$_**0.52**$Al$_**0.48**$As Grown by Metalorganic Vapor Phase Epitaxy. *Japanese Journal of Applied Physics*, 38(Part 1, No. 2B):1048–1051, 1999.

[106] N. Yu Ganushkina, I. Dandouras, Y. Y. Shprits, and J. Cao. Locations of boundaries of outer and inner radiation belts as observed by Cluster and Double Star. *Journal of Geophysical Research: Space Physics*, 116(A9), 2011.

[107] D. Heynderickx, B. Quaghebeur, J. Wera, E. J. Daly, and H. D. R. Evans. New radiation environment and effects models in the European Space Agency's Space Environment Information System (SPENVIS). *Space Weather*, 2004.

[108] Chunlei Yu, Xue Li, Bo Yang, Songlei Huang, Xiumei Shao, Yaguang Zhang, and Haimei Gong. Noise characteristics analysis of short wave infrared InGaAs focal plane arrays. *Infrared Physics & Technology*, 85:74–80, September 2017.

[109] C. P. Skrimshire, J. R. Farr, D. F. Sloan, M. J. Robertson, P. A. Putland, J. C. D. Stokoe, and R. R. Sutherland. Reliability of mesa and planar InGaAs PIN photodiodes. *IEE Proceedings J - Optoelectronics*, 137(1):74–78, February 1990.

[110] Y. Arslan, F. Oguz, and C. Besikci. Extended wavelength SWIR InGaAs focal plane array: Characteristics and limitations. *Infrared Physics & Technology*, 70:134–137, May 2015.

[111] G. J. Shaw, S. R. Messenger, R. J. Walters, and G. P. Summers. Radiation-induced reverse dark currents in In0.53ga0.47as photodiodes. *Journal of Applied Physics*, 73(11):7244–7249, June 1993.

[112] H. Ohyama, J. Vanhellemont, Y. Takami, K. Hayama, T. Kudou, T. Hakata, S. Kohiki, and H. Sunaga. Degradation and recovery of In/sub 0.53/Ga/sub 0.47/As photodiodes by 1-MeV fast neutrons. *IEEE Transactions on Nuclear Science*, 43(6):3019–3026, December 1996.

[113] P. W. Marshall, C. J. Dale, and E. A. Burke. Space radiation effects on optoelectronic materials and components for a 1300 nm fiber optic data bus. *IEEE Transactions on Nuclear Science*, 39(6):1982–1989, December 1992.

[114] H. Ohyama, K. Kobayashi, J. Vanhellemont, E. Simoen, C. Claeys, K. Takakura, T. Hirao, and S. Onoda. Induced lattice defects in InGaAs photodiodes by high-temperature electron irradiation. *Physica B: Condensed Matter*, 340-342:337–340, December 2003.

[115] H. Ohyam, T. Kudou, E. Simoen, C. Claeys, Y. Takami, and H. Sunaga. Radiation damage of In0.53ga0.47as photodiodes by high energy particles. *Journal of Materials Science: Materials in Electronics*, 10(5):403–405, July 1999.

[116] T. Kudou, H. Ohyama, E. Simoen, C. Claeys, Y. Takami, K. Shigaki, A. Fujii, and H. Sunaga. Radiation Damage Of InGaAs Photodiodes By High Energy Particles. *MRS Online Proceedings Library Archive*, 487, 1997.

[117] S. A. Goodman, F. D. Auret, and W. E. Meyer. The effect of alpha-particle and proton irradiation on the electrical and defect properties of n-GaAs. *Nuclear Instruments and Methods in Physics Research Section B: Beam Interactions with Materials and Atoms*, 90(1):349–353, May 1994.

[118] R. Schifano, K. Gościński, E. Przeździecka, and T.A. Krajewski. Zurich instruments application note: Laplace deep level transient spectroscopy using the MFIA. `https://www.zhinst.com/sites/default/files/zi_mfia_appnote_dlts.pdf`, 2017.

[119] Michaël Verdun, Grégoire Beaudoin, Benjamin Portier, Nathalie Bardou, Christophe Dupuis, Isabelle Sagnes, Riad Haïdar, Fabrice Pardo, and Jean-Luc Pelouard. Dark current investigation in thin P-i-N InGaAs photodiodes for nano-resonators. *Journal of Applied Physics*, 120(8):084501, August 2016.

[120] Masafumi Yamaguchi and Koushi Ando. Mechanism for radiation resistance of InP solar cells. *Journal of Applied Physics*, 63(11):5555–5562, June 1988.

[121] Masafumi Yamaguchi, Yoshio Itoh, and Koushi Ando. Room-temperature annealing of radiation-induced defects in InP solar cells. *Appl. Phys. Lett.*, 45(11):1206–1208, December 1984.

[122] G. J. Shaw, R. J. Walters, S. R. Messenger, and G. P. Summers. Time dependence of radiation-induced generation currents in irradiated InGaAs photodiodes. *Journal of Applied Physics*, 74(3):1629–1635, August 1993.

[123] S. W. S. McKeever, R. J. Walters, S. R. Messenger, and G. P. Summers. Deep level transient spectroscopy of irradiated p-type InP grown by metalorganic chemical vapor deposition. *Journal of Applied Physics*, 69(3):1435–1439, February 1991.

[124] A. Broniatowski, A. Blosse, P. C. Srivastava, and J. C. Bourgoin. Transient capacitance measurements on resistive samples. *Journal of Applied Physics*, 54(6):2907–2910, June 1983.

[125] S. H. Huang, G. Balakrishnan, A. Khoshakhlagh, A. Jallipalli, L. R. Dawson, and D. L. Huffaker. Strain relief by periodic misfit arrays for low defect density GaSb on GaAs. *Applied Physics Letters*, 88:131911, March 2006.

[126] A. Jallipalli, G. Balakrishnan, S. H. Huang, A. Khoshakhlagh, L. R. Dawson, and D. L. Huffaker. Atomistic modeling of strain distribution in self-assembled interfacial misfit dislocation (IMF) arrays in highly mismatched III–V semiconductor materials. *Journal of Crystal Growth*, 303(2):449–455, May 2007.

[127] Matthew P. Lumb, Shawn Mack, Kenneth J. Schmieder, María Gonzalez, Mitchell F. Bennett, David Scheiman, Matthew Meitl, Brent Fisher, Scott Burroughs, Kyu-Tae Lee, John A. Rogers, and Robert J. Walters. GaSb-Based Solar Cells for Full Solar Spectrum Energy Harvesting. *Advanced Energy Materials*, 7(20):1700345, 2017.

[128] M. P. Lumb, M. Meitl, K. J. Schmieder, M. Gonzalez, S. Mack, M. K. Yakes, M. F. Bennett, J. Frantz, M. A. Steiner, J. F. Geisz, D. J. Friedman, M. A. Slocum, S. M. Hubbard, B. Fisher, S. Burroughs, and R. J. Walters. Towards the ultimate multi-junction solar cell using transfer printing. In *2016 IEEE 43rd Photovoltaic Specialists Conference (PVSC)*, pages 0040–0045, June 2016.

[129] C. Alibert, A. JoulliÃ©, A. M. JoulliÃ©, and C. Ance. Modulation-spectroscopy study of the ${\mathrm{Ga}}_{1\ensuremath{-}x}{\mathrm{Al}}_{x}\mathrm{Sb}$ band structure. *Phys. Rev. B*, 27(8):4946–4954, April 1983.

[130] K. C. Nunna, S. L. Tan, C. J. Reyner, A. R. J. Marshall, B. Liang, A. Jallipalli, J. P. R. David, and D. L. Huffaker. Short-Wave Infrared GaInAsSb Photodiodes Grown on GaAs Substrate by Interfacial Misfit Array Technique. *IEEE Photonics Technology Letters*, 24(3):218–220, February 2012.

[131] Charles J. Reyner, Jin Wang, Kalyan Nunna, Andrew Lin, Baolai Liang, Mark S. Goorsky, and D. L. Huffaker. Characterization of GaSb/GaAs interfacial misfit arrays using x-ray diffraction. *Applied Physics Letters*, 99(23):231906, December 2011.

[132] Shenghong Huang, Ganesh Balakrishnan, and Diana L. Huffaker. Interfacial misfit array formation for GaSb growth on GaAs. *Journal of Applied Physics*, 105(10):103104, May 2009.

[133] George T. Nelson, Bor-Chau Juang, Michael A. Slocum, Zachary S. Bittner, Ramesh B. Laghumavarapu, Diana L. Huffaker, and Seth M. Hubbard. GaSb solar cells grown on GaAs via interfacial misfit arrays for use in the III-Sb multi-junction cell. *Appl. Phys. Lett.*, 111(23):231104, December 2017.

[134] E. Kessler, M. Slocum, and S. Hubbard. Unpublished results. 2018.

[135] Dante DeMeo, Corey Shemelya, Chandler Downs, Abigail Licht, Emir Salih Magden, Tom Rotter, Chetan Dhital, Stephen Wilson, Ganesh Balakrishnan, and Thomas E. Vandervelde. GaSb Thermophotovoltaic Cells Grown on GaAs Substrate Using the Interfacial Misfit Array Method. *Journal of Electronic Materials*, 43(4):902–908, February 2014.

[136] E. J. Renteria, A. Mansoori, S. J. Addamane, D. M. Shima, C. P. Hains, and G. Balakrishnan. Development of thin film metamorphic GaSb cells by epitaxial lift-off from GaAs substrates. In *2016 IEEE 43rd Photovoltaic Specialists Conference (PVSC)*, pages 2310–2312, June 2016.

[137] L. M. Fraas, J. E. Avery, P. E. Gruenbaum, V. S. Sundaram, K. Emery, and R. Matson. Fundamental characterization studies of GaSb solar cells. In *, Conference Record of the Twenty Second IEEE Photovoltaic Specialists Conference, 1991*, pages 80–84 vol.1, October 1991.

[138] Thomas Schlegl. *GaSb-Photovoltaikzellen für die Thermophotovoltaik*. PhD Dissertation, Universität Regensburg, January 2006.

[139] J. Tournet, S. Parola, A. Vauthelin, D. Montesdeoca Cardenes, S. Soresi, F. Martinez, Q. Lu, Y. Cuminal, P. J. Carrington, J. Décobert, A. Krier, Y. Rouillard, and E. Tournié. GaSb-based solar cells for multi-junction integration on Si substrates. *Solar Energy Materials and Solar Cells*, 191:444–450, March 2019.

[140] Omer Salihoglu, Abdullah Muti, Kutlu Kutluer, Tunay Tansel, Rasit Turan, Coskun Kocabas, and Atilla Aydinli. Atomic layer deposited Al2o3 passivation of type II InAs/GaSb superlattice photodetectors. *Journal of Applied Physics*, 111(7):074509, April 2012.

[141] A. Nainani, T. Irisawa, Ze Yuan, B. R. Bennett, J. B. Boos, Y. Nishi, and K. C. Saraswat. Optimization of the Interface and a High-Mobility GaSb pMOSFET. *IEEE Transactions on Electron Devices*, 58(10):3407–3415, October 2011.

[142] Gregory C. DeSalvo, Ron Kaspi, and Christopher A. Bozada. Citric Acid Etching of GaAs(1-x)Sb(x), Al0.5ga0.5sb , and InAs for Heterostructure Device Fabrication. *J. Electrochem. Soc.*, 141(12):3526–3531, December 1994.

[143] Najah J. Kadhim, Stuart H. Laurie, and D. Mukherjee. Chemical Etching of Group III - V Semiconductors. *Journal of Chemical Education*, 75(7):840, July 1998.

[144] J. G. Buglass, T. D. McLean, and D. G. Parker. A Controllable Etchant for Fabrication of GaSb Devices. *Journal of The Electrochemical Society*, 133(12):2565–2567, December 1986.

[145] Kanji Yoh, Kazumasa Kiyomi, Akira Nishida, and Masataka Inoue. Indium Arsenide Quantum Wires Fabricated by Electron Beam Lithography and Wet-Chemical Etching. *Japanese Journal of Applied Physics*, 31(12S):4515, December 1992.

[146] P. S. Gladkov, Ts Marinova, V. Krastev, and Sh Dinkov. Study of a New Chemical Etchant for GaSb (100) and (111) Substrate Preparation for Epitaxial Growth. *Journal of The Electrochemical Society*, 142(7):2413–2417, July 1995.

[147] S. Johnston, I. Repins, N. Call, R. Sundaramoorthy, K. M. Jones, and B. To. Applications of imaging techniques to Si, Cu(In,Ga)Se2, and CdTe and correlation to solar cell parameters. In *2010 35th IEEE Photovoltaic Specialists Conference*, pages 001727–001732, June 2010.

[148] O. S. Romero, A. A. Aragon, N. Rahimi, D. Shima, S. Addamane, T. J. Rotter, S. D. Mukherjee, L. R. Dawson, L. F. Lester, and G. Balakrishnan. Transmission Electron Microscopy-Based Analysis of Electrically Conductive Surface Defects in Large Area GaSb Homoepitaxial Diodes Grown Using Molecular Beam Epitaxy. *Journal of Electronic Materials*, 43(4):926–930, March 2014.

[149] George A. Patterson and James S. C. Chang. Characterization and Control of Surface Morphology and Defect Density for MBE GaAs Surfaces in the Production MBE Environment. *MRS Online Proceedings Library Archive*, 340, January 1994.

[150] Masafumi Yamaguchi and Yoshio Itoh. Efficiency considerations for polycrystalline GaAs thin-film solar cells. *J. Appl. Phys.*, 60(1):413–417, July 1986.

[151] Alan S. Teran, Eunseong Moon, Wootaek Lim, Gyouho Kim, Inhee Lee, David Blaauw, and Jamie D. Phillips. Energy Harvesting for GaAs Photovoltaics Under Low-Flux Indoor Lighting Conditions. *IEEE Trans. Electron Devices*, 63(7):2820–2825, July 2016.

[152] E. H. Aifer, J. H. Warner, C. L. Canedy, I. Vurgaftman, E. M. Jackson, J. G. Tischler, J. R. Meyer, S. P. Powell, K. Olver, and W. E. Tennant. Shallow-Etch Mesa Isolation of Graded-Bandgap "W"-Structured Type II Superlattice Photodiodes. *J. Electron. Mater.*, 39(7):1070–1079, February 2010.

[153] G. Stollwerck, Oleg V. Sulima, and A.W. Bett. Characterization and simulation of GaSb device-related properties. *IEEE Transactions on Electron Devices*, 47(2):448–457, February 2000.

[154] O. V Sulima and A. W Bett. Fabrication and simulation of GaSb thermophotovoltaic cells. *Solar Energy Materials and Solar Cells*, 66(1–4):533–540, February 2001.

[155] Masafumi Yamaguchi and Chikara Amano. Efficiency calculations of thin-film GaAs solar cells on Si substrates. *J. Appl. Phys.*, 58(9):3601–3606, November 1985.

[156] Eiichi Kuramochi, Naoto Kondo, Yoshifumi Takanashi, and Masatomo Fujimoto. Observation of deep levels in undoped GaSb grown by molecular beam epitaxy. *Applied Physics Letters*, 63(19):2664–2666, November 1993.

[157] Tatsuya Takamoto, Eiji Ikeda, Hiroshi Kurita, Masamichi Ohmori, Masafumi Yamaguchi, and Ming-Ju Yang. Two-Terminal Monolithic In0.5ga0.5p/GaAs Tandem Solar Cells with a High Conversion Efficiency of Over 30%. *Jpn. J. Appl. Phys.*, 36:6215–6220, October 1997.

[158] C. Algora and V. Díaz. Performance and optimization of monochromatic pn heteroface AlGaAs/GaAs photovoltaic cells. *Solid-State Electron.*, 41(11):1787–1793, November 1997.

[159] E. Vadiee, E. Renteria, C. Zhang, J. J. Williams, A. Mansoori, S. Addamane, G. Balakrishnan, and C. B. Honsberg. AlGaSb-Based Solar Cells Grown on GaAs: Structural Investigation and Device Performance. *IEEE Journal of Photovoltaics*, 7(6):1795–1801, November 2017.

[160] H. Uchida, T. Soga, H. Nishikawa, T. Jimbo, and M. Umeno. Reduction of dislocation density by thermal annealing for GaAs/GaSb/Si heterostructure. *Journal of Crystal Growth*, 150:681–684, May 1995.

[161] M. Aziz, A. Mesli, J. F. Felix, D. Jameel, N. Al Saqri, D. Taylor, and M. Henini. Effect of post-growth annealing treatment on interfacial misfit GaSb/GaAs heterostructures. *Journal of Crystal Growth*, 424:5–10, August 2015.

[162] Ch Giesen, M. M Beerbom, X. G Xu, and K Heime. MOVPE of AlAsSb using tritertiarybutylaluminum. *Journal of Crystal Growth*, 195(1):85–90, December 1998.

[163] D. Whalen. *The Rise and Fall of COMSAT: Technology, Business, and Government in Satellite Communications*. Springer, May 2014. Google-Books-ID: hj7tAwAAQBAJ.

[164] L. G. Napolitano. *A New Era in Space Transportation: Proceedings of the XXVIIth International Astronautical Congress, Anaheim, 10 - 16 October 1976*. Elsevier, October 2013. Google-Books-ID: ztogBQAAQBAJ.

[165] J. Haynos, J. Allison, R. Arndt, and A. Meulenberg. The COMSAT nonreflective silicon solar cell: a second generation improved cell. In *Int. Conf. on Photovoltaic Power Generation*, volume 25, 1974.

[166] M. Wolf. Updating the limit efficiency of silicon solar cells. *IEEE Transactions on Electron Devices*, 27(4):751–760, April 1980.

[167] Eli Yablonovitch. Statistical ray optics. *Journal of the Optical Society of America*, 72(7):899, July 1982.

[168] K. Masuko, M. Shigematsu, T. Hashiguchi, D. Fujishima, M. Kai, N. Yoshimura, T. Yamaguchi, Y. Ichihashi, T. Mishima, N. Matsubara, T. Yamanishi, T. Takahama, M. Taguchi, E. Maruyama, and S. Okamoto. Achievement of More Than 25 #x0025; Conversion Efficiency With Crystalline Silicon Heterojunction Solar Cell. *IEEE Journal of Photovoltaics*, 4(6):1433–1435, November 2014.

[169] Zachary C. Holman, Stefaan De Wolf, and Christophe Ballif. Improving metal reflectors by suppressing surface plasmon polaritons: a priori calculation of the internal reflectance of a solar cell. *Light Sci Appl*, 2(10):e106, October 2013.

[170] Dimitre Z. Dimitrov and Chen-Hsun Du. Crystalline silicon solar cells with micro/nano texture. *Applied Surface Science*, 266:1–4, February 2013.

[171] Dong Liang, Yangsen Kang, Yijie Huo, Yusi Chen, Yi Cui, and James S. Harris. High-Efficiency Nanostructured Window GaAs Solar Cells. *Nano Lett.*, 13(10):4850–4856, October 2013.

[172] Emily D. Kosten, Jackson H. Atwater, James Parsons, Albert Polman, and Harry A. Atwater. Highly efficient GaAs solar cells by limiting light emission angle. *Light Sci Appl*, 2(1):e45, January 2013.

[173] N. L. A. Chan, T. Thomas, M. FÃ¼hrer, and N. J. Ekins-Daukes. Practical Limits of Multijunction Solar Cell Performance Enhancement From Radiative Coupling Considering Realistic Spectral Conditions. *IEEE Journal of Photovoltaics*, 4(5):1306–1313, September 2014.

[174] M. A. Steiner, J. F. Geisz, I. García, D. J. Friedman, A. Duda, and S. R. Kurtz. Optical enhancement of the open-circuit voltage in high quality GaAs solar cells. *Journal of Applied Physics*, 113(12):123109, March 2013.

[175] Antonio Luque and Antonio Martí. Increasing the Efficiency of Ideal Solar Cells by Photon Induced Transitions at Intermediate Levels. *Physical Review Letters*, 78(26):5014–5017, June 1997.

[176] Y. Okada, N. J. Ekins-Daukes, T. Kita, R. Tamaki, M. Yoshida, A. Pusch, O. Hess, C. C. Phillips, D. J. Farrell, K. Yoshida, N. Ahsan, Y. Shoji, T. Sogabe, and J.-F. Guillemoles. Intermediate band solar cells: Recent progress and future directions. *Applied Physics Reviews*, 2(2):021302, June 2015.

[177] Yushuai Dai. Development of High Efficiency III/V Photovoltaic Devices. *Theses*, September 2017.

[178] Hyun Kum, Yushuai Dai, Taketo Aihara, Michael A. Slocum, Takeshi Tayagaki, Anastasiia Fedorenko, Stephen J. Polly, Zachary Bittner, Takeyoshi Sugaya, and Seth M.

Hubbard. Two-step photon absorption in InP/InGaP quantum dot solar cells. *Appl. Phys. Lett.*, 113(4):043902, July 2018.

[179] Andrea Cattoni. Multi-resonant light trapping in ultra-thin solar cells (Conference Presentation). In *Photonics for Solar Energy Systems VII*, volume 10688, page 106880I. International Society for Optics and Photonics, May 2018.

[180] Synopsys RSoft manual, 2017.

[181] Steven J. Byrnes. Multilayer optical calculations. *arXiv:1603.02720 [physics]*, March 2016. arXiv: 1603.02720.

[182] Kane Yee. Numerical solution of initial boundary value problems involving maxwell's equations in isotropic media.

[183] B. L. Smith, M. A. Slocum, Z. S. Bittner, Y. Dai, G. T. Nelson, S. D. Hellstroem, R. Tatavarti, and S. M. Hubbard. Inverted growth evaluation for epitaxial lift off (ELO) quantum dot solar cell and enhanced absorption by back surface texturing. In *2016 IEEE 43rd PVSC*, pages 1276–1281, June 2016.

[184] Yushuai Dai, Stephen J. Polly, Staffan Hellstroem, Michael A. Slocum, Zachary S. Bittner, David V. Forbes, Paul J. Roland, Randy J. Ellingson, and Seth M. Hubbard. Effect of electric field on carrier escape mechanisms in quantum dot intermediate band solar cells. *Journal of Applied Physics*, 121(1):013101, January 2017.

[185] Zachary C. Holman, Miha Filipič, Antoine Descoeudres, Stefaan De Wolf, Franc Smole, Marko Topič, and Christophe Ballif. Infrared light management in high-efficiency silicon heterojunction and rear-passivated solar cells. *Journal of Applied Physics*, 113(1):013107, January 2013.

[186] F.-J. Haug, T. Söderström, O. Cubero, V. Terrazzoni-Daudrix, and C. Ballif. Plasmonic absorption in textured silver back reflectors of thin film solar cells. *Journal of Applied Physics*, 104(6):064509, September 2008.

[187] Corsin Battaglia, Ching-Mei Hsu, Karin Söderström, Jordi Escarré, Franz-Josef Haug, Mathieu Charrière, Mathieu Boccard, Matthieu Despeisse, Duncan T. L. Alexander, Marco Cantoni, Yi Cui, and Christophe Ballif. Light Trapping in Solar Cells: Can Periodic Beat Random? *ACS Nano*, 6(3):2790–2797, March 2012.

[188] Yi Zou, Xing Sheng, Kun Xia, Huayu Fu, and Juejun Hu. Parasitic loss suppression in photonic and plasmonic photovoltaic light trapping structures. *Opt. Express, OE*, 22(104):A1197–A1202, June 2014.

[189] Aurélien David, Brendan Moran, Kelly McGroddy, Elison Matioli, Evelyn L. Hu, Steven P. DenBaars, Shuji Nakamura, and Claude Weisbuch. GaN/InGaN light emitting diodes with embedded photonic crystal obtained by lateral epitaxial overgrowth. *Appl. Phys. Lett.*, 92(11):113514, March 2008.

[190] I. García, C. F. Kearns-McCoy, J. S. Ward, M. A. Steiner, J. F. Geisz, and S. R. Kurtz. Back reflectors based on buried Al2o3 for enhancement of photon recycling in monolithic, on-substrate III-V solar cells. *Applied Physics Letters*, 105(13):133507, September 2014.

[191] S. Kicin, V. Cambel, M. Kuliffayová, D. Gregušová, E. Kováčová, J. Novák, I. Kostič, and A. Förster. Fabrication of GaAs symmetric pyramidal mesas prepared by wet-chemical etching using AlAs interlayer. *Journal of Applied Physics*, 91(2):878–880, December 2001.

[192] Xing Sheng, Lirong Zeng Broderick, Juejun Hu, Li Yang, Anat Eshed, Eugene A. Fitzgerald, Jurgen Michel, and Lionel C. Kimerling. Design and fabrication of high-index-contrast self-assembled texture for light extraction enhancement in LEDs. *Optics Express*, 19(104):A701–A709, July 2011.